IAEA-TECDOC-1589

Industrial Process Gamma Tomography

Final report of a coordinated research project
2003–2007

IAEA
International Atomic Energy Agency

May 2008

IAEA-TECDOC-1589

Industrial Process Gamma Tomography

Final report of a coordinated research project
2003–2007

IAEA
International Atomic Energy Agency

May 2008

The originating Section of this publication in the IAEA was:

Industrial Applications and Chemistry Section
International Atomic Energy Agency
Wagramer Strasse 5
P.O. Box 100
A-1400 Vienna, Austria

INDUSTRIAL PROCESS GAMMA TOMOGRAPHY
IAEA, VIENNA, 2008
IAEA-TECDOC-1589
ISBN 978–920–0–104508–9
ISSN 1011–4289

Printed by the IAEA in Austria
May 2008

FOREWORD

Gamma computed tomography (CT) is complementary to radiotracer and gamma sealed source techniques largely used for analyzing industrial process units. Relevant target areas for gamma CT applications are generally known. Although the methodology is generic and applicable across broad industrial specimen and facilities, a number of specific items have been identified as the most appropriate target beneficiaries of these applications: distillation columns; packed beds; risers; fluidized beds and other multiphase processing units. These industrial process units present significant technical challenges to CT investigations in terms of the complexity of the multiphase flows that occur in them.

In order to address these needs, the IAEA implemented a Coordinated Research Project (CRP) on Industrial Process Gamma Tomography with the overall objective of testing and validating CT techniques for diagnosing industrial multiphase processes. CT laboratories from Argentina, Brazil, Czech Republic, France, Republic of Korea, Malaysia, Norway, Poland, United Kingdom and the United States of America have participated. The specific objectives of the CRP were assessment of the tomographic methods, evaluation of them for investigation of multiphase engineering processes, and design of prototypes of simple CT systems for industrial processing, which can be transferred to other developing countries. The CRP has generated an active network, which also included other groups engaged in the CT field. The round robin test has played an important role in validation of techniques and software.

This TECDOC is prepared based on the findings and achievements of the CRP. It is a comprehensive technical report containing valuable information, not readily available in any single publication elsewhere. The participants' reports and software developed by them are compiled in a CD-ROM and attached to the back cover. The guidelines and software packages described in this report can be used as an introduction and brief user manual for working with the CT technique. This publication can be a valuable reference for developers and users of industrial process gamma tomography systems. It will also be useful for all radioisotope laboratories working on industrial applications.

The IAEA wishes to thank all CRP participants for their valuable contributions. The IAEA officer responsible for this publication is Joon-Ha Jin of the Division of Physical and Chemical Sciences.

EDITORIAL NOTE

This publication has been prepared from the original material as submitted by the authors. The views expressed do not necessarily reflect those of the IAEA, the governments of the nominating Member States or the nominating organizations.

The use of particular designations of countries or territories does not imply any judgments by the publisher, the IAEA, as to the legal status of such countries or territories, of their authorities and institutions or of the delimitation of their boundaries.

The mention of names of specific companies or products (whether or not indicated as registered) does not imply any intention to infringe proprietary rights, nor should it be construed as an endorsement or recommendation on the part of the IAEA.

CONTENTS

1. INTRODUCTION

The potentials of imaging with ionizing radiation were discovered almost at the same time as the ionizing radiation itself in the late 1890s. At that time and for many years thereafter photographic film was used because efficient position sensitive detectors were not developed until more recently. The imaging modality first applied was radiography, and this is still important for nondestructive (NDT) applications and of course in medicine. This is so-called projective imaging and may be considered as a large number of separate transmission measurements onto one plane (Fig. 1).

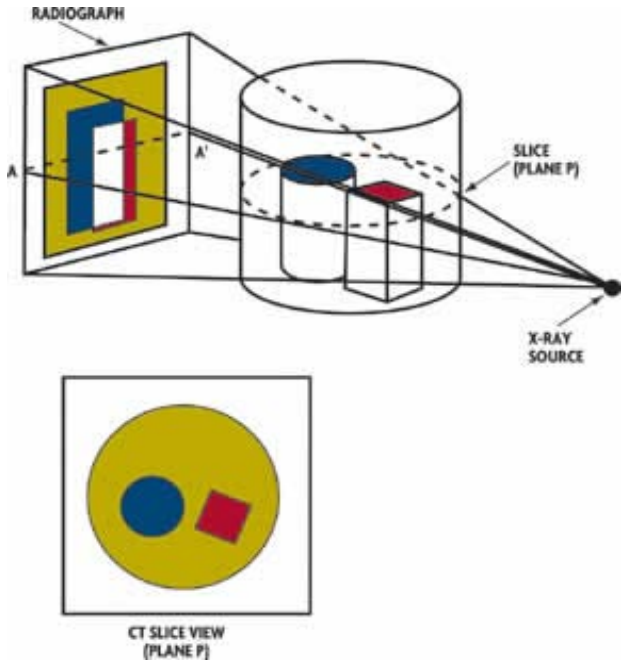

FIG. 1. Principle of radiography and tomography.

For industrial processes another imaging modality is of higher interest; namely tomographic imaging which is cross-sectional imaging (Fig. 1). Most people associate tomography with medical X ray tomography, so-called CT (computed tomography). With tomographic imaging multiple measurements are carried out at different directions through the object being investigated, followed by an image reconstruction where a 2D distribution of parameters is produced. Several sequential 2D images may also be stacked together to form a 3D image.

Process tomography is a non-intrusive technique, which is capable of measuring the phase distribution inside multiphase equipment without disturbing normal operations. Tomography provides unique technique for quantification of multiphase opaque flow fields, which cannot be accomplished by any other means. Multiphase systems are encountered in many modern industrial and environmental processes. The multiphase flow systems, vastly used in industrial production of polymers, minerals, pharmaceuticals, food and feed are the major targets of computed tomography (CT). These multiphase systems consisting of gas – liquid, liquid – solid, gas – solid, gas – liquid – solid, and liquid – liquid – solid – gas mixtures are major processing units of modern industry.

Multiphase mixtures have to be transported in pipes, mixed in tanks, separated in settlers, crystallizers, distillation columns, packed bed absorbers, bubble column absorbers, reacted in stirred slurries, bubble columns, packed beds and other reactors. In each case the available theories are insufficient to predict the phase distribution, flow pattern and mixing in the process equipment used.

Considerable savings in capital expenditures and in operating costs would result if these process units could be designed and operated more efficiently. In the United States alone multi-phase processing contributes more than 650 million dollars to the national economy. Currently, the design is very conservative due to the lack of understanding of flow patterns and phase distributions in processing vessels causing sub-optimal operation of industrial units. It is therefore essential to have available suitable means of investigating them, from the point of view of troubleshooting and process optimization. Multiphase systems can be difficult to measure and control using "conventional" instrumentation, so CT techniques are frequently employed. The impact of the CT technique on the design, scale-up and troubleshooting of equipment has been profound.

A Coordinated Research Project (CRP) on Industrial process gamma tomography was operational during 2003–007 period. The overall objective of the CRP was testing and validating computer tomography (CT) techniques for diagnosing industrial multiphase processes.

This TECDOC summarizes the main achievements in research and development during the four year period. The guidelines and software packages described in this report can to be used as an introduction and brief user manual for working with the CT techniques. This comprehensive technical document can be a valuable reference for potential designers and users of gamma tomography systems. It will be useful for all radioisotope applications laboratories working on industrial process gamma CT.

This TECDOC is organized into 7 chapters. The characteristics of various CT methods are described in chapters 1 and 2. It is shown that gamma CT method is the most suitable and competitive for on-line investigation of industrial processes, in particular for visualization of multiphase systems. Gamma CT technique provides a good spatial resolution and is well adapted to harsh environments of many industrial processes.

Experimental design and data processing for gamma transmission tomography is described in chapter 3, while Chapter 4 presents the gamma emission tomography method and gives the principles and basic knowledge for radioactive particle tracking method, which is complementary to the gamma CT. Chapter 5 provides the results of the phantom tests. Very compatible results were obtained by almost all participants. Chapter 6 describes the practical aspects of the industrial process tomography, including mechanical and electronic hardware.

Chapter 7 provides the available software packages for image reconstruction in CT, especially for gamma CT and electrical capacitance CT.

Annex 1 summarizes the main activities and achievements obtained by the CRP participants' laboratories.

2. INDUSTRIAL PROCESS TOMOGRAPHY

Tomography is derived from the Greek words "τομοσ" (tomos) which means "sharp" in the sense of making a sharp cut, and "γραφειν" (graphein) which means "to write". Industrial process tomography (IPT) is thus cross sectional imaging of parameters of industrial processes, very often a function of time. The foundation of IPT is to conduct several measurements around the periphery of a multiphase process, and use these measurements to unravel the cross sectional distribution of the process components in time and space. This information is used in the design and optimization of industrial processes and process equipment, and also to improve accuracy of multiphase system measurements in general.

There has been tremendous development within measurement science and technology over the past couple of decades. New sensor technologies and compact versatile signal recovery electronics are continuously expanding the limits of what can be measured and with what accuracy this can be done. Miniaturization of sensors and the use of nano-technology push these limits further. Also, thanks to powerful and cost-effective computer systems, sophisticated measurement algorithms previously only accessible in advanced laboratories are now available for in situ on-line measurement systems.

Industrial tomography methods have taken advantage of the general progress in measurement science, and aim at providing more information, both quantitatively and qualitatively, on multiphase systems and their dynamics. In many cases, the traditional approach for such systems has been to carry out one local or bulk measurement and assume this is representative for the whole system. In some cases, this is sufficient. However, there are many complex systems where the component distribution varies continuously and often unpredictably in space and time.

Industrial process tomography has several similarities to medical tomography: Several sensors or detectors are used to provide multiple measurement data at the boundary process which can be used to reconstruct the cross-sectional component distribution. Unlike medical systems, many IPT technologies are fast in order to also unravel the dynamics of the processes. Some IPT systems provide several thousand data sets or images per second.

A large number of IPT measurement principles have been, and are still being, developed: electrical methods, such as the measurement of capacitance, inductance and resistance, optical and radiation-based methods ranging from infrared, microwave, X rays, gamma-rays and even neutrons, magnetic resonance, ultrasound and acoustic methods to mention a few. The sensor technology for a specific application is primarily selected to achieve sensitivity to a physical property which is different for the components of the process, e.g. density, or electrical permittivity. For the measurement or imaging of more than two components, multi-modality systems are often employed, either by measuring with one principle at several wavelengths or energies, or by combining several independent sensor principles. IPT is inherently interdisciplinary, so that R&D requires skills in process engineering (chemical, combustion, pharmaceutical, etc), physics and electronic engineering for the sensor system, and mathematics and computer science for data processing algorithms.

It is difficult if not impossible to perform a comparison of the different tomography principles because it is so dependent on the application in question. The first consideration is to choose a sensing principle which is sensitive to a parameter where the components in the multiphase process have different values. For tomographic imaging of gas/ solid or gas/ liquid systems one obvious parameter would be the density because of the high contrast between gas and solids (liquids). Next one needs to consider whether the so-called sensor head can be installed in the process, whether a special wall material is required, and so forth. Furthermore, the process need to be compatible with the sensing principle to make sure it is not blinded. There is also a question of measurement resolutions to time (speed of response), matter (e.g. density which defines the contrast in each pixel) and space (spatial resolution which defines how detailed the image is).

The most mature sensing principles today are:

- Electrical capacitance tomography (ECT) which is sensitive to the electrical permittivity of the process components. This principle has a limitation in that it cannot be applied to processes which have a conductive component, such as water, as the continuous component.
- Electrical capacitance tomography (ERT) which is sensitive to the electrical resistance (conductance) of the process components.
- Electromagnetic tomography (EMT) which, depending on the configuration, is sensitive to the permeability or the electrical conductivity of the process components.

All the electrical methods require a non-conductive liner or process wall material, and also a screen (Faraday cage). These are fast imaging methods available at a relatively low cost. Because of fringe effects related to electrical and electromagnetic fields, the spatial resolution is limited to about 10% of the process dimension such as the diameter. These methods are often referred to as soft-field sensing methods whereas radiation based methods are hard-field methods. For the latter, the contribution to the actual measurements only depends on the process medium inside the volume defined by the source and detector. Provided correct collimation is applied, it will not be influenced by what is on the outside of this volume as is the case with soft-field methods because of the fringe field which causes the measurement volume boundaries to be fuzzy.

The most common hard-field methods are:

- Optical transmission tomography which basically is sensitive to the transparency of the process medium at the selected wavelength(s). This is a relatively low cost method with one drawback in that it requires transparent windows into the process.

- Gamma tomography and X ray tomography which, depending on the energy are sensitive to the density or the atomic composition (effective Z number) of the process medium. These are often the only methods left for demanding applications where the other fails due to limitations. Regarding spatial resolution these ionizing radiation methods covers a huge span from nm to cm, and it is also possible to obtain fast speed of response. The limitation is actually the system costs, not the technology.

The output of an IPT imaging system need not be an image: it is just as often merely a few parameters describing the component distribution in the process. Actually, the complexity of an IPT system depends very much on the application: full imaging systems are most often encountered in the development of multiphase processes or the equipment for these, whereas in situ on-line process measurement systems frequently use a limited number of sensors and only a few parameters as output. In some chemical processes, the degree of component mixing is important; in others, it is the other way around and the degree of separation is the issue.

Generally, the process industries increasingly require more process related information, motivated by key issues such as improved process control, process utilization and process yields, ultimately brought forward by cost effectiveness, quality assurance, environmental and safety demands. Also considering the increasing complexity of industrial processes running at smaller margins, more information and insight are important, particularly on multiphase processes where the spatial and temporal distribution of the components often is of paramount importance.

There are two categories of sensor systems: Hard-field where the sensitivity is equal in all positions throughout the measurement volume independent of the distribution of the measured parameter inside and outside the measurement volume. Then there are soft-field systems where the sensitivity depends on the position in the measurement volume and the distribution of the parameter inside and outside the measurement volume. A gamma system using relatively narrow beams through source and detector collimation is a typical hard-field.

A capacitance system is in the soft-field category because, even though guard electrodes can be used to reduce the fringe fields. This also has consequences for the image reconstruction. Soft-field systems are more complex because their measurements produce sets of non-linear equations, whereas hard-field systems produce sets of linear equations and are simpler.

2.1. PRINCIPLE OF GAMMA PROCESS TOMOGRAPHY

The foundation of all industrial nuclear measurement systems is the combination of one or several radiation sources and one or several radiation detection units (Fig. 2). Important process or system parameters are then derived from the measurement of interactions between the ionizing radiation and the process or system under investigation.

Tomography systems based on scatter and characteristic X ray emission have been developed, however, these suffers from relatively low response intensity, particularly the latter.

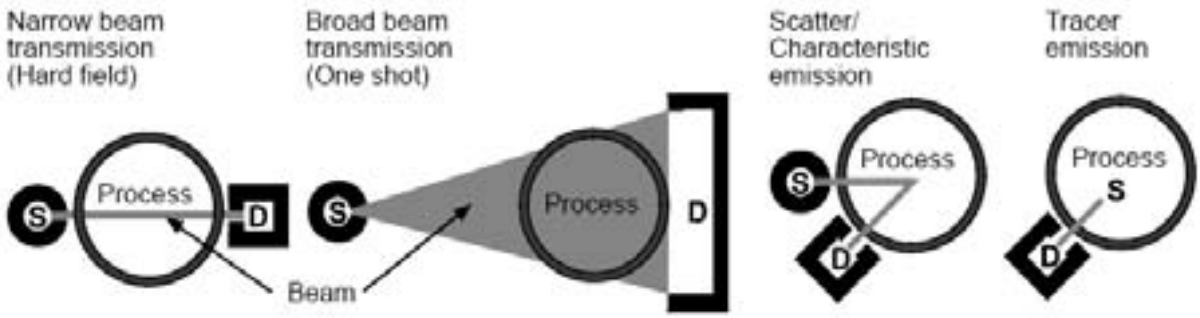

FIG. 2. Measurement modalities used in industrial gauging systems. The radiation source (S) is shielded and collimated except in the case of tracers where the source is an integral part of the process. Likewise collimation and shielding are applied to the detector(s) (D).

Radioisotope tracing is a powerful tool for process diagnostic and laboratory measurements. For process diagnostics, tracer studies are frequently used for measurement of flow rate and residence time and for leakage detection. Radiotracers are also the foundation of a range of advanced laboratory methods primarily used to provide experimental process data otherwise not available. These data provide improved understanding of various processes and their dynamics and are often the key for the development of accurate process models and their validation. The most widely known method is positron emission tomography (PET), where a short-lived β^+-emitter, such as ^{18}F, is used as the tracer isotope. PET imaging of industrial processes uses instruments developed for medical imaging. This is also true for industrial transmission tomography where the X ray scanner has found widespread use since the first commercial scanner was introduced by EMI in 1972.

On the other hand there have been developed a large number of dedicated tomography systems based on gamma-ray transmission, often because the relatively higher energies enables imaging of processes hidden behind thick process vessel walls.

2.2. DUAL GAMMA ENERGY CT

The need for component fraction measurements in multiphase processes lead to the development of so-called dual energy meters. Here energy sensitive detectors are used and the transmission is measured at two energies. The highest energy is chosen where Compton scattering is the dominant attenuation mechanism in the mixture. The linear attenuation coefficients of the components are then proportional to their densities.

The lowest energy is in the range dominated by photoelectric absorption where the linear attenuation coefficients are strongly dependent on the effective atomic number or composition. The result is two independent measurements enabling determination of the volumetric fractions of three components in a closed system. This principle was first developed for gas/oil/water measurements, and later also for ash in coal measurements.

The difference in dependency of photoelectric and Compton attenuation to the process density and atomic composition may also be measured by the dual modality principle using one low radiation energy (e.g. using ^{241}Am sources). Here one transmission measurement responding to both photoelectric and Compton attenuation, are combined with one scatter measurement from which the Compton response is derived. A dual modality system based on scatter and annihilation radiation for measurement of ash in coal has also been developed. Low-energy systems require low attenuation vessel walls (or windows therein) and are often used as part of a multiple measurement system such as in conjunction with other measurement principles (e.g. electrical capacitance or conductivity) and volumetric flow measurements in multiphase flow meters. There are on the other hand limited examples on tomographic systems utilizing these methods.

2.3. MULTIPLE MODALITY CT

There are also multiple modality systems utilizing different sensing principles which are sensitive to different parameters of the process components to be measured. Nuclear principles are most often used for measurement of density, atomic composition (Z) or hydrogen density. Electrical methods are used to measure electrical conductance, permittivity, and permeability; ultrasound methods for sound velocity and density, and so forth. In multiphase measurements of gas/ oil/ water pipe flow combination of several measurement principles has been used for decades, however, for industrial tomographic measurement it has only been a few developments on this type of multi modality technology. Examples on developments are multiphase flow imaging using measurements based on gamma-ray transmission and electrical capacitance, gamma ray transmission and electrical conductance, optical transmission and electrical capacitance. The only systems commercially available are those applied for medical imaging based on X ray transmission tomography (CT) in combination with magnetic resonance imaging (MRI) or PET.

3. GAMMA TRANSMISSION TOMOGRAPHY

3.1. SYSTEM DESIGN

Generally, a good knowledge of the system helps very much in designing a CT system. The experimental design for applying gamma-ray tomography in industry should first consider and identify the most important process properties, for a tomographic acquisition, which are:

- size or diameter of the system,
- densities, composition of different materials present in the system, including vessel wall properties (type, thickness, form),
- bandwidth of the phenomena to be studied. If a periodic phenomenon occurs, it should be considered for phase-averaged acquisition.

These are important because most often the process properties dictate the system requirements. Other important parameters are related to the environment: temperature, humidity, dust, location of the measurement, available place, hazardous atmosphere etc..

The purpose of process tomography is to provide cross sectional information. This means that the following parameters need to be considered:

Spatial resolution. This parameter is strongly linked to the collimation of detectors, the number of detectors per projection and the number of projections. For example, with 64 detectors x 128 projections, the spatial resolution can be as low as 2.3% of the object diameter, which is more than that could be expected (1/64=1.6%). Figure 3 presents what can be obtained in different configurations, depending on the number of detector per projection and the number of projections.

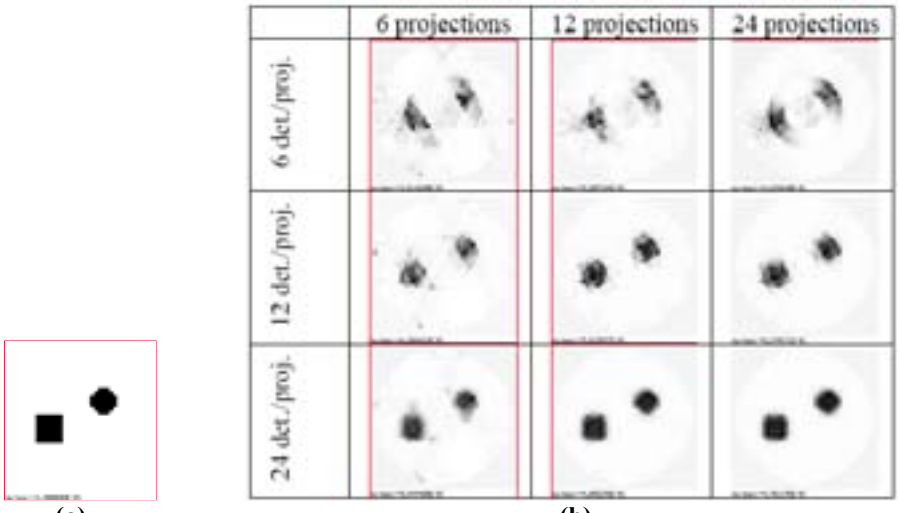

FIG. 3. (a) Original image and (b) comparison of reconstructed images with different numbers of detectors per projection (6, 12 and 24) and different numbers of projections (6, 12 and 24).

Contrast (measurement accuracy), i.e. the lowest detectable density difference. A CT system should be considered as a set of individual nucleonic control systems [NCS]. Specific software can also be used to select the energy source, the activity and the detector type.[1].

[1] Monte Carlo codes, like Macalu7 software can be used to reduce trial error in selection of detector and source when designing the NCS system. Expert system like Janu gives preliminary results, while Monte Carlo gives more accurate result taking into account scattering and energy resolution of the detector.

The difference between basic NCS and tomography is final value in a pixel is, approximately, a weighted sum of individual signals where the statistical error in a pixel of interest can be estimated considering the ray sums going through the considered pixel. This is almost true when using analytical method for the reconstruction of the data. When algebraic algorithms are used, error due to the algorithm itself can be important also. Problems with linearity overshoot, high frequency noise can arise with such algorithm and one must pay lot of attention to the algorithm. As it is quite difficult to predict these problems, the only solution is to make Monte Carlo simulations with numerical phantom.

Temporal resolution, which is related to the bandwidth of the phenomena to be studied and thus will be different for:

- Static processes,
- Dynamic objects where only temporal averaging of the process dynamics is required,
- Dynamic objects where the process dynamics need to be imaged.

It is important to be realistic when specifying the parameters listed above, because they are all interrelated and affect the cost of the CT system, as shown graphically in Fig.4.

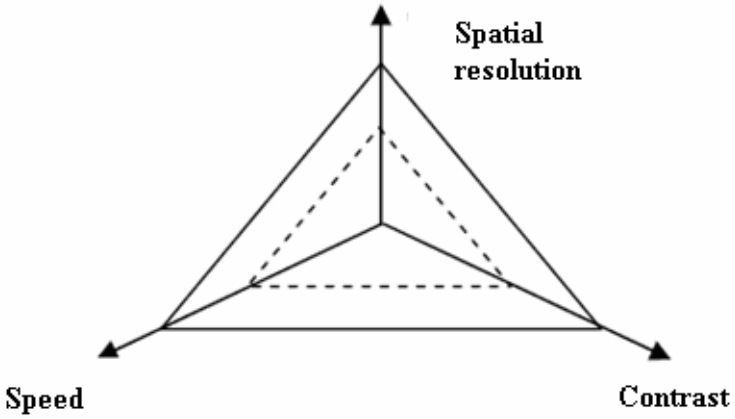

FIG. 4. The cost is proportional to the area of the triangle.

This means that it is necessary to make a compromise between speed, contrast and spatial resolution. A simultaneous performance increase in all parameters is possible, but this will rapidly increase the cost of the system.

The physical process parameters are interrelated when it comes to designing the tomography system. Also, with this information it is possible to decide if the object under study can be brought to the laboratory or if the tomographic equipment has to be armed around the object at its operational place. The dimensional aspects can be roughly categorized with respect to the radiation penetration capability as shown in Table I.

TABLE I. RECOMMENDED TYPICAL SOURCES DEPENDING ON VESSEL DIMENSIONS.

Vessel dimensions	Approximate range	Energy	Approximate range	Typical source
Small	< 150 mm	Low	< 200 keV	241-Am / X ray
Medium	150 – 600 mm	Medium	200 – 800 keV	137-Cs
Large	600 – 1500 mm	High	> 800 keV	60-Co
Extra large	>1500 mm	High	> 800 keV	60-Co

3.2. HARDWARE

3.2.1. Scanning system

The design of hardware for scanning system is related to CT generation. The term CT generation refers to the geometrical arrangement of the combination of detectors, the source of radiation and the method adopted for acquiring the data for the requisite number of projections. In principle, it involves rotating the source-detector arrangement synchronously with respect to the object under investigation.

There are four methods of scanning commonly used. Figure 5 shows the different gantry based on CT generation developed in history of the medical CT. The gantry also has been applied to industrial CT.

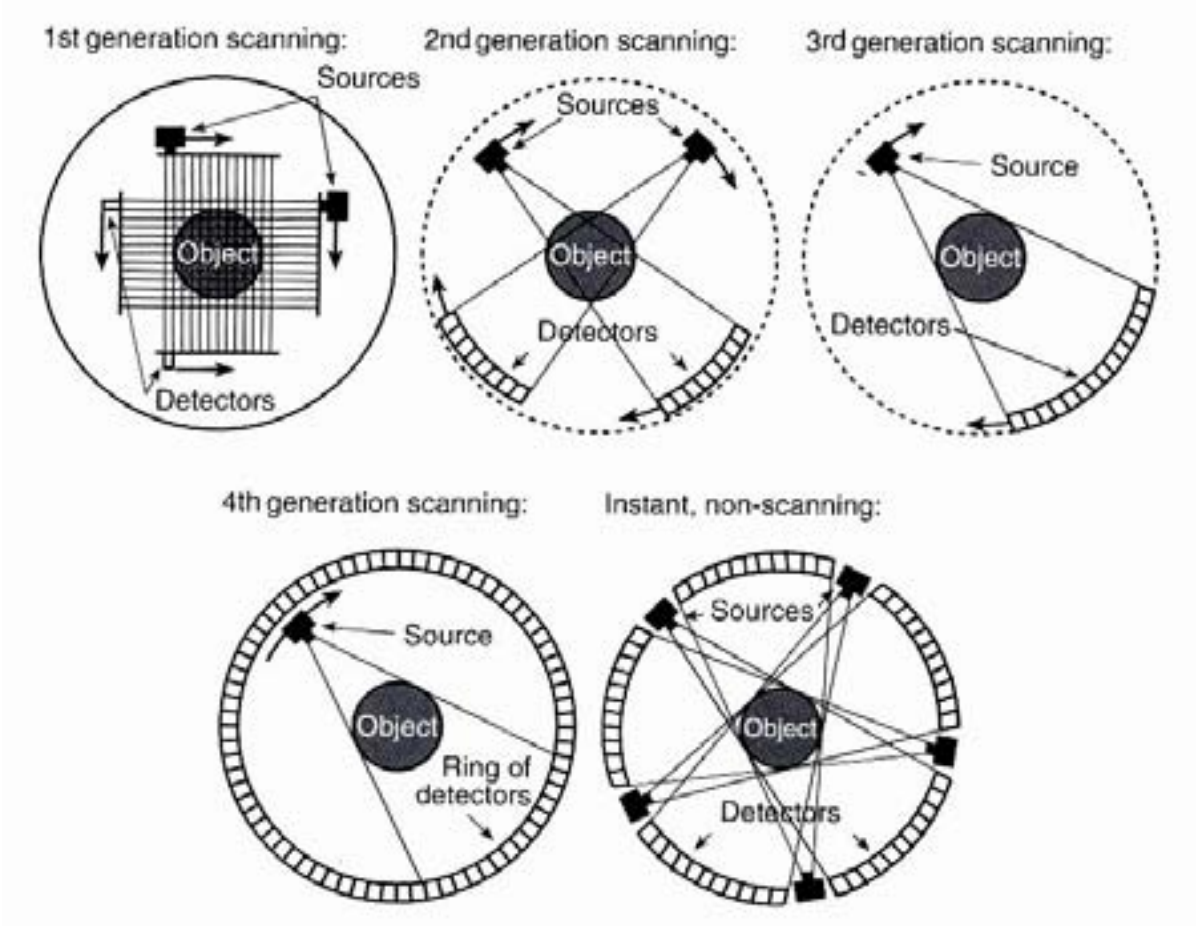

FIG. 5. The development of measurement geometry for γ or x ray CT scanners from the first to the fourth generation. Also shown is the instant configuration in which all ray-sum measurements are carried out simultaneously.

First generation. The simplest of these is parallel scanning in which a source, emitting a single pencil beam of radiation, and a detector are coupled together so that the detector is always facing the source as illustrated in Figure 5. The source and detector are linearly translated to acquire individual measurement. After the completion of the linear measurement, both source and the detector are rotated to the next angular position to acquire the next set of measurements.

Second generation. The second method has an array of detectors facing a single source. The source is collimated in such a way that the pattern of the beam is a fan with a thickness of about 5 to 10 mm. Although this is still a translation-rotation scanner, the number of rotation steps is reduced by the use of multiple pencil beams. In Figure 5 is depicted a design, in which seven detector modules are used. The angle between the pencil beams is 1°. Therefore, for each translation scan, the projections from seven different angles are acquired. This allows the source and detector to rotate 7° at a time for data acquisition, representing a reduction factor of 6 in the acquisition time.

Third generation. One of the most popular scanner types is the third-generation CT illustrated in Figure 5. In this configuration, a large number of detectors are located on an arc concentric to the source. The size of the detector is sufficiently large so that the entire object is within the detector field of view at all times. The source and then detector remain stationary with respect to each other while the entire apparatus rotates about the object. Linear motion is eliminated to significantly reduce the data acquisition time.

Fourth generation. Is the fixed detector-rotating source arrangement in which a large number of detectors are mounted on affixed ring as shown in figure 5. In this design, the detector forms an enclosed ring and remains stationary during the entire scan, the radiation beams sweep across the object. The projection, therefore, forms a fan with its apex at the detector. One of the advantages of the fourth-generation scanner is the fact that the spacing between adjacent samples in a projection is determined solely by the rate at which the measurements are taken. This is in contrast to the third-generation scanning, in which the sample spacing is determined by the detector cell size.

The configuration of fourth generation medical CT scanner has also been applied for imaging of industrial processes such as pipe flows, however, a mechanically rotating radiation source restricts the speed of response. If the rotation is too slow compared to the process dynamics, the reconstructed image will become motion blurred because process features enter and leave the image plane before the data acquisition is completed. In order to avoid this type of inconsistent measurement, all measurements should be carried out simultaneously. This also improves the measurement accuracy at a given speed of response. For these reasons, an approach incorporating several fixed radiation sources each of which faces an array of detectors on the opposite side of the process, as in the instant configuration in figure 5. The number of so-called views in such a system hence equals the number of sources, and the number of ray-sums in each view equals the number of detectors in each array. Each ray-sum is thus one transmission measurement. The requirement for high-speed response does not apply when the required information is temporal averaging of the process dynamics.

The following examples present different designs of the hardware for scanning systems. The systems developed, either portable or permanently installed gamma-ray scanners, were used for investigating of process materials in riser pipes, pipe-works and process columns. Among advantages of using CT techniques in industrial process are that they are rapid, reliable, and, for most applications, can be used in places where no other techniques are applicable such as in aggressive environments or in remote areas.

3.2.2. Portable CT scanner for riser pipes (1st Generation configuration)

The motion control of the CT system in Figure 6 consists of two servo-motors, a data logger and a PC. One motor simultaneously moves the source and the detector for a parallel beam scanning, whereas the other motor rotates the scan table at a preset projection angle. The motor is controlled through a driver linked to a data logger for PC control. The driver makes the motor finish a rotation by 12000 input pulses. The input pulse is generated from the data logger. The data logger transmits the acquired data to a PC and controls the two servo motor drivers for the rotating and scanning motions. It processes the measured radiation counts as two-dimensional data, the rows and columns which indicate the index for the location of a detector bin and the projection angle, respectively.

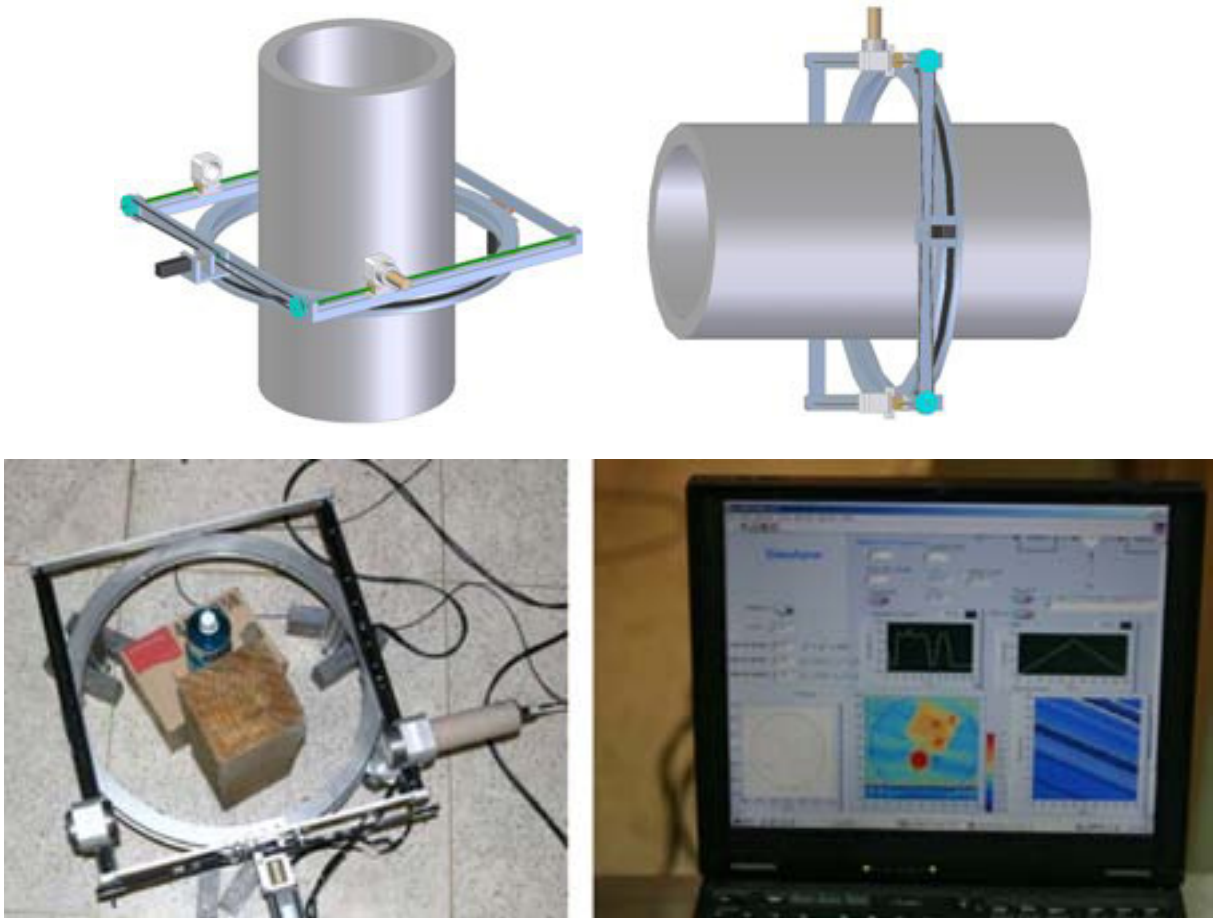

FIG. 6. 1st generation portable gamma CT scanner.

3.2.3. Portable gamma-ray CT scanner for pipeworks (3rd Generation configuration)

A portable gamma ray scanner for industrial pipe inspection has been developed at the Nuclear Agency in Malaysia, formerly known as Malaysian Institute for Nuclear Technology Research (MINT). The mechanical system design for the scanner is based on a third generation fan-beam gamma-ray CT systems but data acquisition procedure is manipulated so that the ray-sum data is acquired in such a way to be essentially equivalent to a first generation sinogram. The scanner has a large potential to be used to determine the extent of corrosion under insulation, to detect blockages, to measure the thickness of deposit/materials built-up on the walls and to improve understanding of material flow in pipelines. It is based on third generation system employing gamma-ray beam and a curved array detector system.

The concept of the portable gamma CT scanner is similar to a pack-and-go system, which could be easily set-up in remote areas with limited accessibility. Several design criteria were established for the CT scanner as described below.

- Small, light weight and battery-powered for use in remote locations (hand carried by one or two operators)
- Rapid scan and fast image reconstruction time without slowing down the normal pipe inspection process
- Good accuracy to provide meaningful data concerning the size and extent of corrosion under insulation (CUI) or the thickness of deposit/materials built-up within the pipe
- Low cost by using small number of detectors (e.g. five CsI(Na) scintillation detectors)

Figure 7 shows the schematic diagram and the photograph of the portable gamma-ray scanner for pipe investigation. Gamma-ray source and five CsI(Na) detectors are mounted on separate rings, individually driven by sprocket wheels meshing onto gear chains.

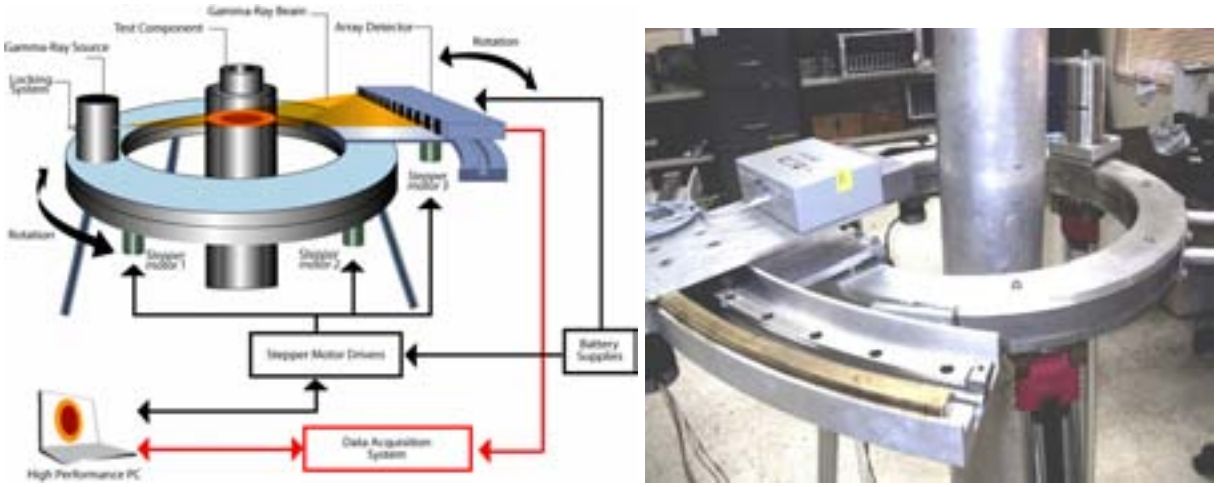

FIG. 7. 3rd generation CT for pipe inspection.

The rotary movement of its mechanical gantry is aided by sets of angular linear bearing and is driven by stepper motors. Gear was designed to give a positioning accuracy of 0.1º. The scanner can be manipulated by using two axes which optimize the data collection. At the major axis, on which the detector and source are placed to be always opposite each other, the main frame rotates in 360°. At a minor axis that has the detector module traveling at any steps with respect to the gamma-ray source, within the 20° fan beam angle. By this way, the number of ray-sum can be selected to suit the investigation requirement. This mechanism design imitates the capability of a multiple detector system (curved array detector bank).

3.2.4. Investigation of multiphase flow in process column (3rd Generation configuration)

Gas-liquid flow through packed beds is an important operation with numerous applications in petroleum and petrochemical industries, wastewater treatment plants, air-pollution control and for conducting chemical and biochemical reactions. These types of industries are under pressure to utilize resources more efficiently and to satisfy demand and legislation for better product quality and reduced environmental emission. Hence, there is an increasing need to know more about the exact behavior of the internal flows in process equipment. Owing to the complexity of two-phase flow through a packed bed, a thorough understanding of the hydrodynamics involved has not been achieved yet.

Several flow regimes can occur in packed beds, depending on the operating mode (co- or counter-current flow), on the physico-chemical properties and the flowrates of the fluid phases and on the geometry of the bed.

Figure 8 illustrates a dedicated computed tomography X ray scanner. It has been developed as a tool for the analysis of the spatial distribution of gas, liquid and solid phases in different types of packed columns such as absorption columns or trickling filters. The basic idea was to obtain quantitative 2D or 3D maps of the solid and of the liquid hold-up distributions in these devices. Thus it should be noted that measured quantities correspond to surface distributions and not to volume distributions.

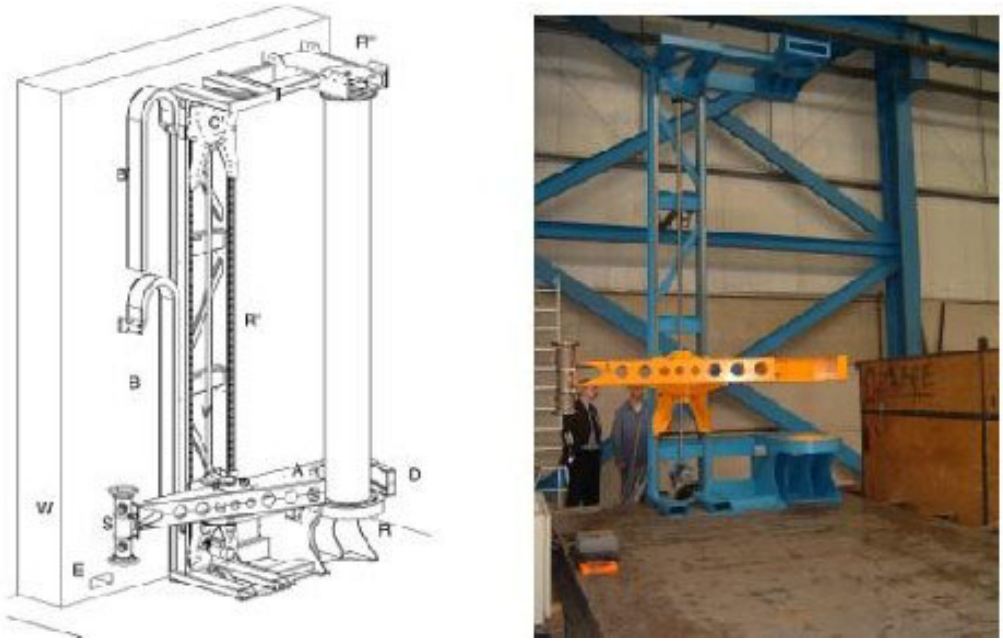

FIG. 8. X ray computed tomography set-up. A: arm; B, B': cable channel lower and upper positions; C, C : carriage lower and upper positions; D: detector bank; E: baffle; O: arm rotation vertical axis; R, R'': rotating table; R': rails; S: X-ray source; V: helicoidal screw; W: 0.6 m concrete wall.

Figure 9 shows a gamma ray CT scanner set-up developed in CEA, France for investigation of two-phase gas/liquid flows in trickle bed reactor of large diameter. It is the third generation scanner (fan beam geometry) mainly composed of a radiation source and a curved-array bank detector. The source and the detector bank are both mounted on a rigid metallic gantry that can be rotated around the vertical axis of a fixed plate on which rests the irradiated column.

FIG. 9. 3rd CT system developed by CEA for IFP, based on 32 shiftable detectors making it equivalent to 64 detectors per projection.

3.2.5. Instant, non-scanning configuration

The use of tomographic techniques for imaging multiphase flow produce a challenge not faced in most industrial or medical imaging applications; that is the process being imaged moves quickly (typically up to 10 ms^{-1}) and can change structure continuously. As a result large amounts of data need to be processed quickly if a real-time system is to be feasible.

For this purpose, a non-scanning or an instantaneous configuration could give real-time imaging of flow in pipelines. This design was achieved through arrangement of multiple modules similar to that of third generation configuration.

Figure 10 presents a laboratory scale of a dual sensor tomography system for multiphase pipe flow imaging developed at the University of Bergen, Norway. The CT system combines an eight-electrode capacitance tomograph with a gamma tomograph of five 18.5 GBq ^{241}Am γ-ray sources and five detector banks each with 17 CdZnTe detectors, which gives a total number of 85 views. The sensor and read-out system are capable of producing images at rates of several hundred frames per second, provided sufficient computing power is available for reconstruction and visualization.

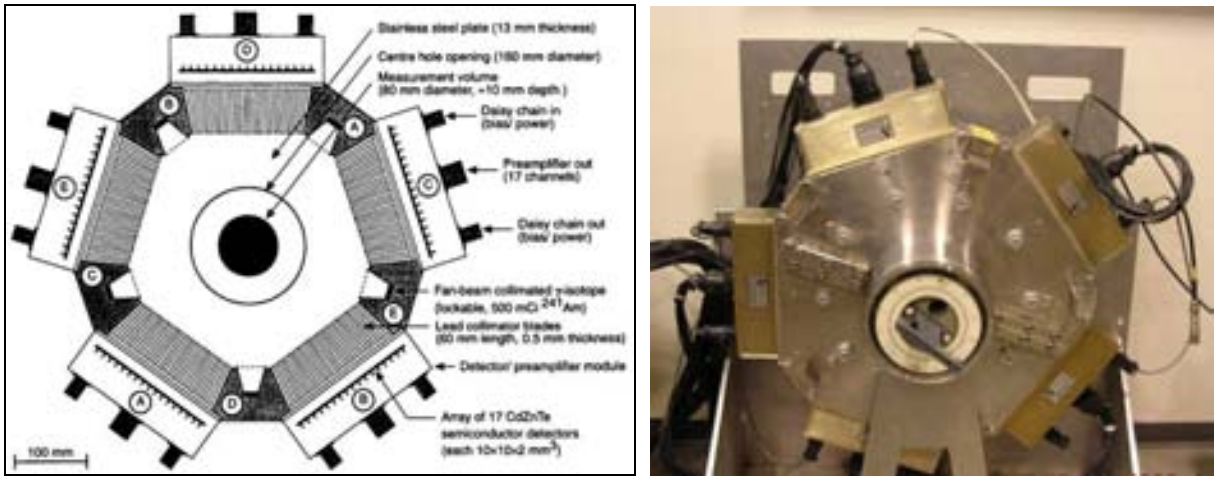

FIG. 10. A dual sensor tomography system for multiphase pipe flow imaging developed at the University of Bergen, Norway.

3.2.6. Detector read-out and data acquisition

Figure 11 shows the general outline of a tomography system. The process to be imaged is surrounded by a set of sources and detectors in the case of gamma transmission tomography, and a set of detectors in the case of tracer emission tomography. The number and size of detectors basically determines the spatial resolution of the system. Scanning may be used to avoid large numbers of sources and detectors; however, mechanical scanning will reduce the system's speed of response.

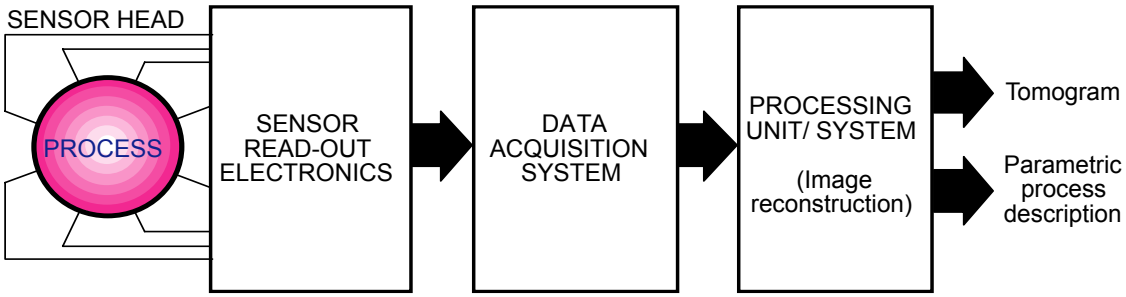

FIG. 11. General arrangement of a tomography system including sensors, read-out electronics, data acquisition and data processing.

The so-called sensor head is connected to the sensor read-out electronics for signal conditioning and analogue to digital conversion. In the case of a gamma radiation tomography system this is typically preamplifiers, shaping amplifiers (filter), triggers and counters. The data integration (counting) time is often controlled by software.

Data acquisition system often uses pipe-lining of data that are taken from the sensor domain, stored, and then transferred to the reconstruction unit at the same time as the sensor domain starts capturing the new data set. Data entering the reconstruction unit may either be stored for later off-line reconstruction, or be reconstructed in real time. The latter is of course only possible when there is sufficient computing power for the reconstruction algorithm that is used.

Gamma transmission tomography allows measuring spatial distributions of material based on its attenuation properties. The attenuation properties take into account the nature of material (atomic number) and the density. It means that transmission CT can distinguish phases with significant different attenuation properties due to density (liquid-gas or solid-gas) and/or atomic number (iodide, tungsten). Tracer emission tomography allows monitoring the fluid of interest by labeling it with radioisotope so that a liquid-liquid mixer can also be investigated.

3.2.7. Selection of radiation source

For transmission tomography it is useful to start with the selection of radiation source and decide what is required with respect to:

- Energy
- Activity

The energy basically has to be selected according to the dimension and composition of the process vessel as indicated in the Table II. The activity has to be selected according to process design (such as walls materials, thickness, materials and phases inside the walls, etc. and the required information) to meet the demands of spatial resolution, speed and contrast, all these should be done according to the ALARA-principle. Then it is necessary to consider what type of system or strategy to choose. This is explained in the Table II, again by regarding the object properties and the information requirement:

TABLE II. RECOMMENDED GEOMETRIES AND EQUIPMENTS DEPENDING ON THE DYNAMIC OF THE OBJECT.

Approach	Equipment*	Speed of response	Dynamics	Cost
Parallel scanning	1S-1D	Low	Static object or temporal averaging	Low
Fan-beam scanning	1S-MD	⇑ ⇓		⇑ ⇓
Instantaneous	MS-MD	High	Dynamic	High

*: S= source, D= detector, 1= one and M= multiple

This means that mechanical scanning cannot be used to image the dynamics of a process unless the scanning time is much smaller than the time constant of the process. Another important parameter in this context is the detector technology. The most realistic alternatives are presented in the Table III.

TABLE III. MORE REALISTIC DETECTORS TECHNOLOGIES FOR CT SYSTEMS.

Detector technology		Radiation energy	Robustness Stability	Speed of response	Stopping efficiency	Cost
Scintillation-crystal with read-out:	PMT*	High	0	+	+	-
	PD*	⇑	+	-	+	0
	APD*		-	+	+	-
CdZnTe		⇓	+	+	+	0
Si			+	+	-	+
Gaseous (e.g. HP Xe)		Low	0	+	-	0

* PMT= Photomultiplier tube, PD= Photodiode, APD= Avalanche photodiode += good, 0= neutral, -= bad .

Finally, detector collimation has to be considered to reduce the effect of scattered radiation:

- Electronic collimation (not possible for low energy systems, due to natural count background)
- Mechanical collimation
- Combination of electronic and mechanical collimation
- Position sensitive detectors

Position sensitive detectors can be used in tomography technology due to their capacity to identify the position where the radiation interaction occurred inside the detector. There are several versions on this kind of detectors (Fig. 12) such as, the Anger camera, multi-wire array spike and scintillator. Scintillator bars coupled to two light sensors have been described in the literature as an alternative to overcome the electronic complexity required by multi-detectors system. Usually, the position sensitive detectors are also so-called linear detector tomography systems. The attenuation of the light along the detector is an essential requirement for a detector to be used in a CT linear detector. In another words, the number of photons initially generated in the radiation interaction point should be decreased along their pathway to reach the light sensor.

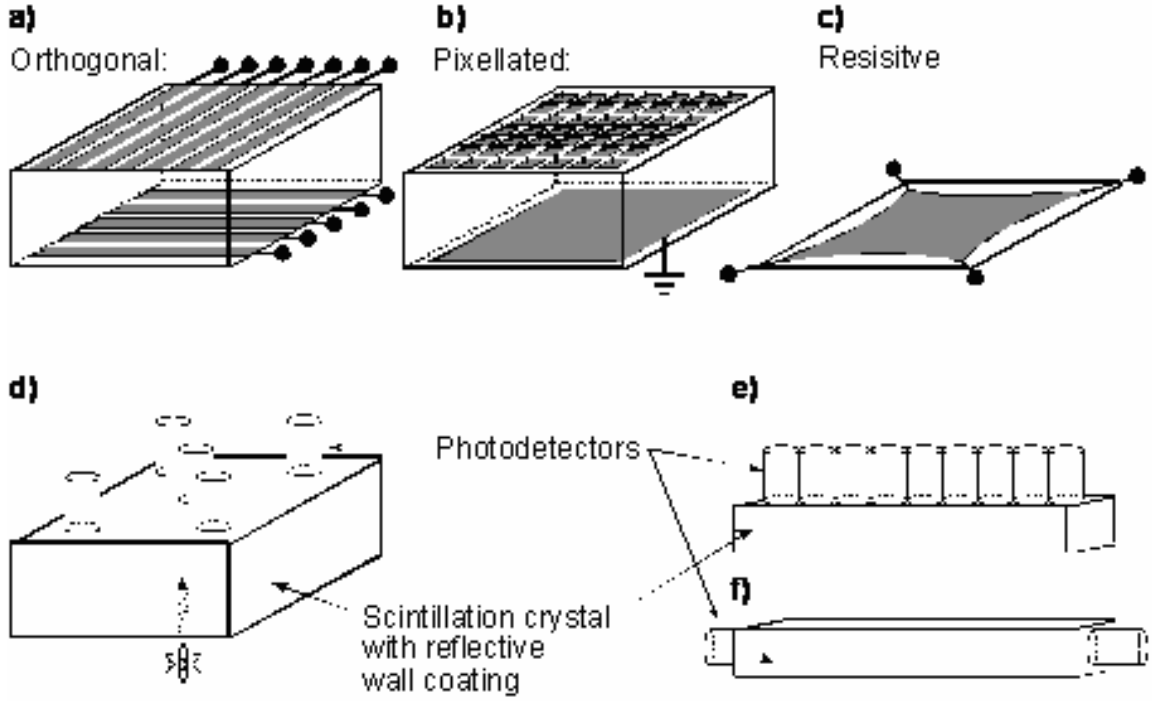

FIG. 12. The most common principles used in inherent position sensitive detectors [Johansen and Jackson, 2004].

The attenuation of the light photon quantity can occur due to self-quenching (a phenomenon where the light is absorbed inside the own material) and/or the escape of photons due to optical effects (mainly due to the differences of refraction index between the detector material and its surrounding). Both processes are responsible by the decrease of the pulse height as shown in Figure 13.

When the radiation interacts with the detector, the light photons scatter inside the detector and reach two detector extremities, generating two different signals: I_1 and I_2 (except for the middle detector position, which generates identical signals). As farther the events occur from the photomultiplier, lower signals are generated.

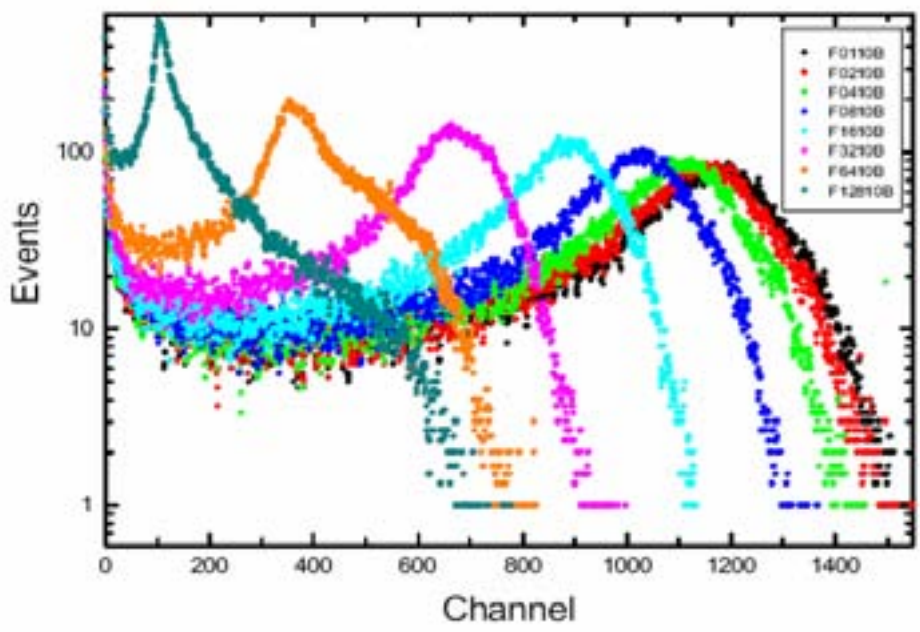

FIG. 13. Energy spectra as a function of the distance between the interaction point in the plastic scintillator and the phototube for cesium source. Distances are 40 (grey curve), 30, 18, 10, 7.5, 5, 2, 1 and 0 cm (black curve).

Basically, hardware (electronic development) takes into account the differentiation of the signal size generated in the light sensor to foresee the radiation interaction position. Otherwise, the use of two sensors coupled to both detector extremities is required for tomography purpose. If the light attenuation obeys a logarithm function, the position of the radiation interaction can be predicted by the function:

$$X = \frac{X_{37}}{2} \times Log_e(I_1 / I_2) \qquad \text{(Eq.1)}$$

where, X is the distance between the interaction point and the centre of the detector, X_{37} is a detector parameter, it means, the length size to attenuate e^{-1} (~37%) of the light produced in the interaction point and I_1 and I_2 is the pulse height from each phototube.

After the definition of the detector type, for example, plastic scintillator or CsI (Tl) bar, the sensor type to be coupled to the scintillator should be selected. This choice depends on the energy profile from the photons produced and the sensor quantum efficiency curve. Another criterion for the choice of the light sensor is related to the safety. Photomultipliers work at high voltage and sparkles could be generated in an eventual accident, putting in risk environments containing combustible material. Particularly, for CsI(Tl) the photodiode can be a good alternative because it works at low voltage and fits adequately to the quantum efficiency curve of the detector.

Usually, photomultipliers with voltage divider chain are capable to generate primary signals suitable to be inputted directly in amplifiers modules. On the other hand, if the distance of the phototube is far from the amplifier module, a good practice recommends the use of a preamplifier connected to the photomultiplier in order to fit the input-output impedances. Photodiodes generate low signals and require a charge-sensitive preamplifier that is used to convert fast current pulse to voltage pulses. Definitively, the modern tomography depends on the computer, thus it is necessary to convert the analogical signal from the light sensor to a digital value. This is made using ADC (Analog Digital Converter). There are several ADC chips available commercially. They are found in different options, such as: precision or resolution (number of bits) and conversion time. These characteristics require special attempting.

The ADC resolution (number of bits per word) is related to the energetic resolution (FWHM, Full Width at Half Maximum) of the detector. Usually, the scintillation present resolution values (FWHM) are in the order of 5 to 20%. For an ADC of 8 bits (256 channels) the photopeak region will be fitted in approximately 30 channels. On the other hand, the photopeak in an ADC of 12 bits resolution will be fitted in approximated 480 channels. In both cases, the photopeak will be well defined. In the first case (8 bits resolution) the photopeak fitting is relatively spaced, however the number of counts/channel shows better precision. In the opposite, the photopeak fitting for a 12 bits ADC is enhanced but the counts/channel will be worse. In such case, the best criterion to ADC selection will be its conversion time. Only as an example, the time for the ADC0820 (8 bits resolution) to make the analog to digital conversion is of 800 ns, while the AD574A (12 bits resolution) requires 35000 ns to make the same conversion. Undoubtedly, in such case, the best option could be the ADC0820 if a fast data acquisition is required.

Often, large detectors are noisy because they are susceptive to the background or have lower signal/noise ratio. Thus, it is essential to include a circuit to check the signals coincidence in both light sensors. The radiation incidence position is proportional to the logarithm of the pulse height ratio S1/S2. It is necessary to assure that S1 and S2 are produced from the same event since one sensor can generate a signal (noise) without the correspondent signal from the other sensor.

3.3. TOMOGRAPHIC IMAGE RECONSTRUCTION

The most critical part is the tomographic inversion process. The choice of the algorithm is a trade-off between noise in measurements, computation time, number of measurements and a priori knowledge. Algorithms are available whatever the number of measurements is, except for the classical FBP algorithm. The latter one requires thin line integral measurements and constrains the number of projections to the number of detectors in each projection.

The objective of CT algorithms is to inverse a set of equations relating the measurements to the image. The estimated parameters are linear attenuation coefficients in CT. These values have ideally to be converted into chemical parameters, mainly gas – liquid – solid fractions for instance. This requires a calibration stage in the CT procedure, which is not always achievable in industrial situation. In that case, a pre-calibration of the system with partial or full modeling is an alternative. However, error measurement, while being larger is difficult to estimate.

A well-suited class of inversion process for industrial CT is algebraic method. The main assumption of these algorithms is the “pixelisation” of the object. Two steps are required:

- Definition of the objective function to minimize,
- Definition of the algorithm that minimizes the objective function.

Objective functions are usually the quadratic distance between measurements and re-projected image or the conditional probability to get the image from the projection. A very efficient algorithm (EM) takes into account the Poisson statistical nature of gamma emission. In addition, this algorithm can take into account “a priori” knowledge on the reconstructed image (MAP-EM). For instance the parabolic velocity profile or any sort of “simple” information provided by chemical engineering knowledge could be used. This algorithm are relatively time consuming for on line imaging. In such a case, iterative algorithm with faster convergence properties should be used (ILST algorithm).

An important part of CT that needs particular attention is the estimation of error in the reconstructed image. The total error combines noise measurements and reconstruction algorithm errors and is therefore hard to estimate without Monte Carlo simulations. However, new techniques such as boot-strap techniques allow estimating error without numerous simulations. This technique can also be used to optimize the design of a CT system.

In transmition tomography, beams of gamma radiation are passed through the equipment or section of a tube being imagined from various positions and at various angles. Each beam is detected on the equipment opposite side from the beam source, and its detected intensity is compared to its intensity at the source. If g, the transmittance of the object, is defined as the logarithm of the ratio of the intensity of the detected beam to the intensity of the emitted beam, then g is given by the linear transformation:

$$g = \int_L \mu(x,y)dl \qquad \text{(Eq. 2)}$$

where μ(x,y) is the linear attenuation coefficient of the object at the point (x,y) and L is the line along which the beam travels.

Most classical algorithms are described here after.

3.3.1. Analytical algorithm – Filtered Back Projection (FBP)

The Filtered Back Projection (FBP) method is a well-known classical technique, if the fast Fourier algorithm is use then the data should be obtained in 2^n parallel rays and use of the Radon transformation, the scheme of this algorithm is shown in Figure 14.

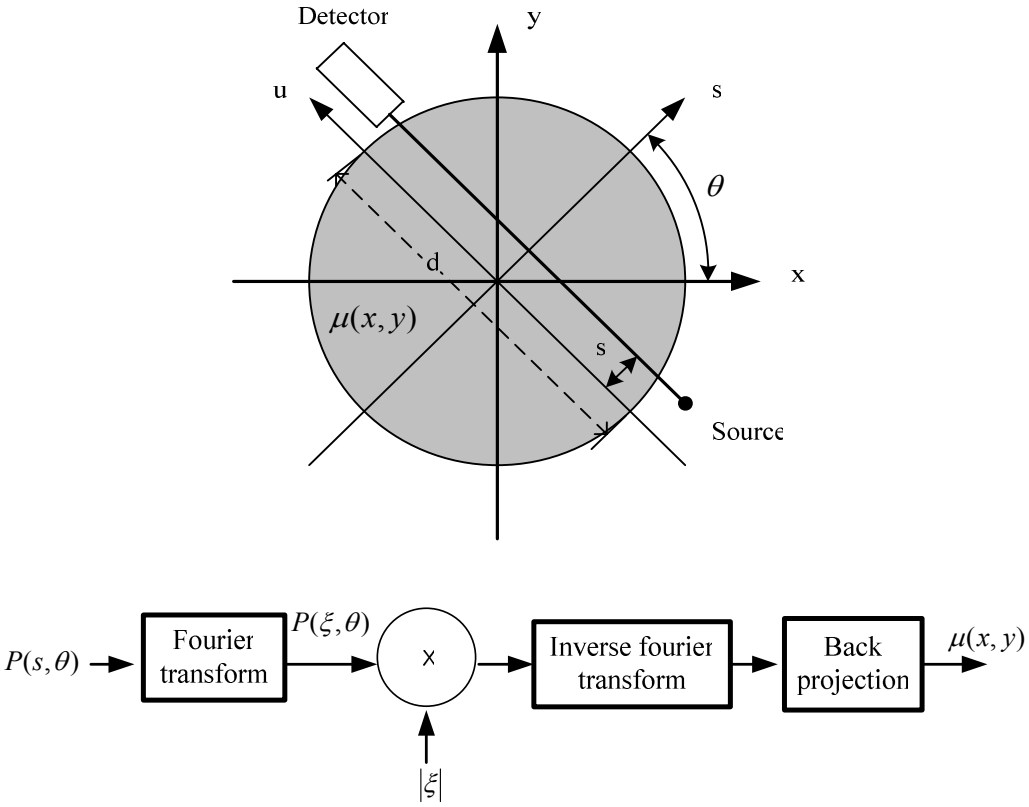

FIG. 14. Filtered back projection process.

In FBP, the ray-sum defined as equation 3.

$$p(s,\theta) = \frac{1}{d}\ln\left(\frac{\rho_\theta^0(s)}{\rho_\theta(s)}\right) \qquad \text{(Eq. 3)}$$

where $\rho_\theta^0(s)$ is measured count with empty object, $\rho_\theta(s)$ is measured count, d is diameter of ROI.

In Fig. 14, $P(\xi,\theta)$ denotes the Fourier transform of $p(s,\theta)$. Mathematically, it is written as:

$$P(\xi,\theta) = \int_{-\infty}^{\infty} p(s,\theta)\exp(-j2\pi\xi s)ds \qquad \text{(Eq. 4)}$$

where $\hat{p}(s,\theta)$ denotes the inverse Fourier transform of $P(\xi,\theta) \bullet |\xi|$.

Mathematically, it is written as:

$$\hat{p}(s,\theta) = \int_{-\infty}^{\infty} |\xi| P(\xi,\theta)\exp j2\pi\xi s d\xi \qquad \text{(Eq. 5)}$$

The reconstructed image can be obtained from a back projection of $\hat{p}(s,\theta)$. That is,

$$\mu(x,y) = \int_{0}^{\pi} \hat{p}(x\cos\theta + y\sin\theta,\theta)d\theta \qquad \text{(Eq. 6)}$$

This method is called filtered back projection (FBP). The FBP algorithm is well established process and strictly based on mathematical theory. The advantage of FBP is that it needs less computation demands when compared to the iterative method.

3.3.2. Algebraic algorithm

To reconstruct an image and produce a graphical representation of the distribution of the process parameters it is necessary to limit the spatial resolution and define a function μ(x,y). This is an array of cells or pixels (picture elements) in which each the linear attenuation coefficient is assumed to be constant (Fig. 15).

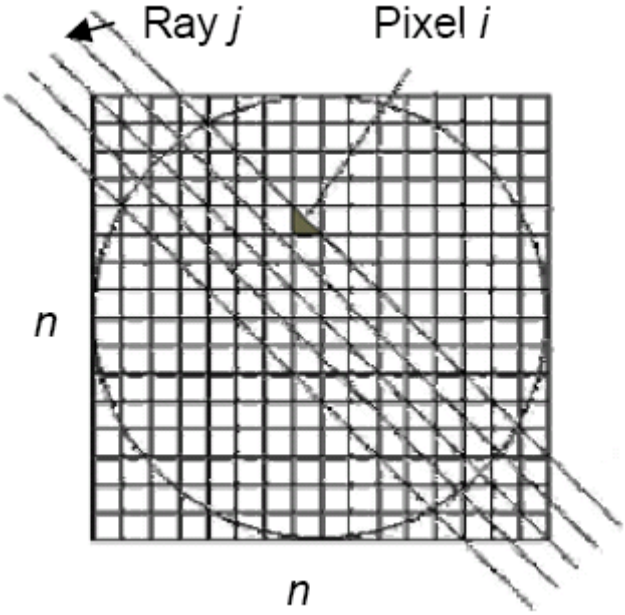

FIG. 15. The reconstruction grid consisting of a total of n x n pixels.

The raysum for each ray *j* is then expressed by the following summation:

$$p_j = \sum_{i=1}^{N} w_{ji}\mu_i \qquad \text{(Eq. 7)}$$

where w_{ij} is the contribution to raysum *j* from pixel *i*, μ_i is the attenuation coefficient of the pixel *i* and *N* is the number of pixels. The terms w_{ij} constitute the elements of the weight matrix W.

This is most often defined as the intersectional area between the j^{th} ray and the i^{th} pixel divided by area between the j^{th} ray and the sample. This may be summarized as follows:

$$
\begin{array}{lll}
p = [p_j] & j = 1,....., M & \text{Raysum vector, M raysums} \\
\mu = [\mu_i] & i = 1,....., N & \text{Attenuation coefficient vector, N pixels} \\
W = [w_{ji}] & \begin{cases} j = 1,....., M \\ i = 1,....., N \end{cases} & \begin{array}{l} \text{Weight matrix,} \\ \text{MxN elements} \end{array}
\end{array}
$$

There are several other methods by which the weight matrix values may be defined:

- 1/0: Beam crossing pixel; weight = 1, otherwise 0
- Measurement path length in one pixel divided by the total measurement length
- Distance of measurement area to the pixel centre
- Measurement path length in one pixel divided by the pixel hypotenuse
- Measurement area inside a pixel divided by the total pixel area
- Measurement volume inside a voxel (volume element) divided by the total voxel volume.

1. Algebraic reconstruction techniques (ART)

One of the first iterative image reconstruction techniques is known as the Algebraic Reconstruction Technique (ART). It is a direct implementation of the Kaczmarz algorithm. This method, introduced by Gordon in 1970, can be stated as;

$$\mu_k^{(n+1)} = \mu_k^{(n)} + \frac{p_i - \widetilde{p}_i}{\sum_{m=1}^{N} w_{im}^2} \; w_{ik} \qquad \text{(Eq. 8)}$$

where $\widetilde{p}_i$ is given by:

$$\widetilde{p}_i = \sum_{k=1}^{N} w_{ik} \mu_k^{(n)} \qquad \text{(Eq. 9)}$$

In these equations, the index *i* corresponds to the different rays of the system and *k* refers to the pixels. It is important to note that in the Eq. 8 a correction to the attenuation map is applied directly after considering each ray-sum. This is known as *ray-by-ray correction.* By using ray-by-ray correction a large number of pixels can be updated in only one iteration, which makes the technique computationally efficient. The ART, however, is known to be sensitive to inconsistencies in the system of equations. Due to inconsistencies, ART reconstructions usually suffer from *salt and paper noise.*

It has been shown by Herman and Lent that the ART convergences to be *maximum entropy* solution of $\vec{p} = W \; \vec{\mu}$.

2. Simultaneous algebraic reconstruction technique (SART)

In 1984, the Simultaneous Algebraic Reconstruction Technique (SART) was proposed as a major refinement of ART. Instead of sequentially updating pixels on a ray-by-ray basis, the SART simultaneously applies to a pixel the average of the corrections generated by all rays. This approach offers a reduction in the amplitude of salt and pepper noise as compared to the ART, however, this goes at the expense of an increase in computation time. The SART algorithm is given by:

$$\mu_k^{(n+1)} = \mu_k^{(n)} + \frac{w}{w_{+,k}} \sum_{i=1}^{M} \left[\frac{p_i - \tilde{p}_i}{w_{i,+}} \; w_{ik} \right] \qquad \text{(Eq. 10)}$$

with

$$w_{i,+} = \sum_{k=1}^{N} w_{i,k} \qquad \text{(Eq. 11)}$$

and

$$w_{+,k} = \sum_{i=1}^{M} w_{i,k} \qquad \text{(Eq. 12)}$$

By using Eq. 10, the summation of corrections generated by the different rays can be recognized, however, for the simultaneous case the normalization factors are different, $w_{+,k}$ represents the total contribution of the k_{th} pixel to all raysums, and the fraction $w_{ij}/w_{i,+}$ can be interpreted as the relative contribution of the k_{th} pixel to the i_{th} raysum.

Convergence of the SART has been proved only in recent years. For example, Jiang and Wang have shown that the SART converges to a weighted least squares solution, under the condition that the coefficients of the system are non-negative. More specifically it converges to a minimizer of the following functional:

$$L(\mu) = \sum_{i=1}^{M} \left[\frac{(p_i - \tilde{p}_i(\mu))^2}{\sum_k w_{ik}} \; w_{ik} \right] = \left\| \tilde{p} - W\mu \right\|_w^2 \qquad \text{(Eq. 13)}$$

Historically, the SART is reckoned to be an algebraic reconstruction method. However, Jiang and Wing have also given a statistical interpretation of the SART. The SART produces a maximum likelihood estimate for the attenuation map for the case where errors are pure stochastic and have a Gaussian or Poisson distribution. Maximum likelihood estimates will be discussed in more detail in the next section.

3.3.3. Estimation Maximization (EM) and Alternating Minimization (AM) Algorithms

Estimation Maximization (EM) and Alternating Minimization (AM) algorithms are based on models that account for the stochastic nature of the gamma ray photons. Algebraic algorithms described earlier and algorithms such as Fourier/convolution techniques when applied to determine the phase holdup distribution either assume the system to be azimuthally symmetric or consider the gamma ray transmission process to be deterministic hence ignoring the true stochastic nature of the data. Thus Estimation Maximization and Alternating Minimization algorithms have been shown to be more suitable image reconstruction methods for determining the phase holdup distribution. We briefly review here the basics of these algorithms.

1. Estimation Maximization (EM):

Lange and Carson defined the image reconstruction for tomography as a maximum likelihood estimation problem and derived the EM algorithm to obtain the maximum likelihood image estimate. The EM algorithm has found extensive applications in emission tomography and a comprehensive description of the algorithm has been presented by Dempster. In experiments where gamma ray counts statistics is high (~ 500 counts/projection), ignoring the true statistical nature of the observations is not a serious limitation because Poisson counting noise is only a component of the total system noise. It is precisely in the low counts experiments (<100 counts/projection) that the EM algorithm is expected to provide the greatest improvement in the reconstruction quality.

Usually in the transmission tomography experiments with the amount of shielding provided at the detectors end (to increase the spatial resolution), the counts recorded are bound to be small (~ 100 counts/projection), which forces one to use an EM algorithm. Further discussion of the superiority of the EM algorithms over Fourier techniques and iterative algebraic methods due to the incorporation of non-negativity constraints and objective measure of quality of reconstruction (e.g. log-likelihood, least squares, maximum entropy) are discussed in detail by Lange and Carson.

The EM algorithm is a general iterative technique for computing maximum likelihood estimates in any measurement of statistical quantities. Its use in image reconstruction for transmission tomography is only a specific application. Each iteration of the EM algorithm consists of two steps: estimation (E step) and maximization (M step). Some key elements related to the derivation and use of the E and M steps for transmission tomography are discussed here. In the estimation step (E-step), the conditional expectation of the statistical model for the process of transmission of the gamma ray photons is determined on the basis of the measured data (counts data from the detector) and a parameter set (attenuation values).

The transmission of photons through a pixel x (Figure 16) has two outcomes: absorption of photons and survival of the photons. If M(y/x) is defined as the intensity (or counts) of the photons that enter a given pixel indexed by x along a projection y and N(y/x) as the intensity of the photons that would survive and leave the given pixel x, then the statistical model in terms of M and N is given as equation 14.

$$p_{N(y|x)} = \binom{M(y|x)}{N(y|x)} \left[\exp\left(-h(y|x)\mu(x)\right)\right]^{N(y|x)} \left[1-\exp\left(-h(y|x)\mu(x)\right)\right]^{M(y|x)-N(y|x)} \quad \text{(Eq.14)}$$

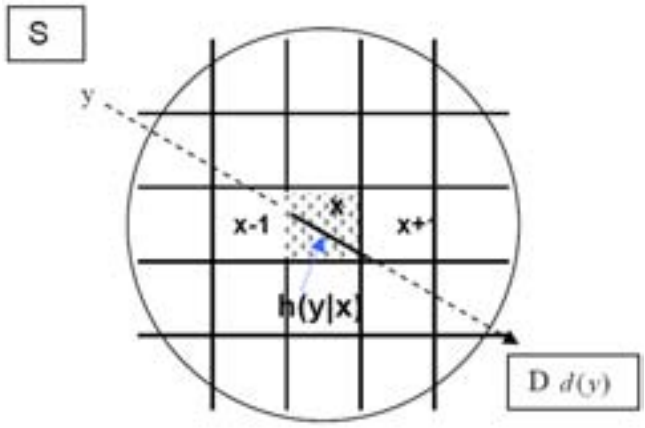

FIG. 16. Schematic of the representation of a transmission tomography domain, the boxes represent the pixels. Here S source, D detector,y projection index, pixel index is the segment of projection y in pixel, d(y) counts measured by detector.

The first pixel along any projection receives the photons emitted from the gamma source. This is a Poisson process with mean λ which represents the intensity of the source, its probability is given by

$$p\left(M(y|1)\right) = \frac{\lambda^{N(y|1)}\exp(-\lambda)}{M(y|1)!}. \quad \text{(Eq.15)}$$

Since the pixels are independent, the likelihood function of the statistical model can be represented as the product of the individual likelihood functions of each pixel that lies along a projection y . This likelihood function is represented as equation 16.

$$f(N(y):\mu)=\frac{\lambda^{N(y|1)}\exp(-\lambda)}{M(y|1)!}\prod_{x\in X}\binom{M(y|x)}{N(y|x)}\left[\exp(-h(y|x)\mu(x)\right]^{M(y|x)}\left[1-\exp(-h(y|x)\mu(x)\right]^{(M(y|x)-N(y|x))} \quad \text{Eq16}$$

Given the current estimate of the attenuation function $\mu^{(k)}(x)$, the estimation step computes the expectation of the statistical model conditional to the data $d(y)$ (measured by detector D). Lange and Carson showed that this can be represented as

$$E\left[N(y|x)\middle|d(y)\right]=d(y)+E\left[N(y|x)\right]-E\left[d(y)\right]. \qquad \text{(Eq.17)}$$

In the M-step, this conditional expectation is maximized with respect to the parameter set $\mu(x)$. Equation 17 is used to determine the expectation values for each pixel in the image which is then summed over all projections and substituted in the likelihood function (Eq.16). The natural logarithm of this equation gives equation 18.

$$\ln\left(f(N(y):\mu)\right)=\sum_{y\in Y}\sum_{x\in X}\left\{N(y|x)\ln\left[\exp(-h(y|x)\mu(x)\right]+\left(M(y|x)-N(y|x)\right)\ln\left[1-\exp(-h(y|x)\mu(x)\right]\right\}+R \quad \text{Eq.18}$$

Here *R* represents all the terms that are not dependant on $\mu(x)$. Maximizing equation 18 yields a transcendental equation:

$$\sum_{x\in X}-N(y|x)h(y|x)+\sum_{x\in X}\left[M(y|x)-N(y|x)\right]\frac{h(y|x)}{\exp\left[h(y|x)\mu(x)\right]-1}=0. \qquad \text{(Eq.19)}$$

Since equation 19 cannot be solved exactly due to the exponential terms, the authors suggest an approximation for it (Eq.20):

$$\frac{1}{\exp\left[h(y|x)\mu(x)\right]-1}=\frac{1}{h(y|x)\mu(x)}-\frac{1}{2}+\frac{h(y|x)\mu(x)}{12}+O\left\{\left[h(y|x)\mu(x)\right]^3\right\}. \qquad \text{(Eq.20)}$$

This approximation is valid for small values of $\left(h(y|x)\mu(x)\right)$ and seriously limits its application as it causes errors in the regions of high density or high attenuation. This in turn may lead to a decrease in the log-likelihood function from one iteration to the other instead of an increase. The alternating minimization algorithm discussed below over comes this

2. Alternating Minimization (AM) Algorithm

The AM algorithm, proposed by O'Sullivan and Benac is a reformulation of the maximum likelihood problem as a double minimization of I-divergence to obtain a family of image reconstruction algorithms. It has been studied extensively in the applications involving x-ray based medical imaging. I-divergence, introduced by Csiszár is a measure of discrepancy between two functions a and b, which is given as:

$$I(a\|b)=\sum_{y\in Y}\left\{a(y)\ln\left[\frac{a(y)}{b(y)}\right]-\left[a(y)-b(y)\right]\right\}. \qquad \text{(Eq.21)}$$

where *y* is a finite dimensional space.

Csiszár examined a wide variety of discrepancy measures (e.g. least squares, entropy) including I-divergence measure between two functions and concluded that if the functions involved are all real valued, and required to be non-negative, then minimizing the I-divergence is a consistent choice.

The I-divergence measure was first employed in image reconstruction by Snyder. Each step of minimization in the AM algorithm is claimed to be an exact process, without any approximation, which as seen above, is not the case in EM (Eq.20). The AM algorithm is guaranteed to monotonically increase the log-likelihood function at every iteration. The AM algorithm when applied to gamma ray tomography improves the quality of the phase hold up images.

In the AM algorithm for CT image reconstruction a statistical model is used for the measured data based on Beer's law and a realistic model for the known point spread function. The reconstruction problem is formulated as an optimization (maximum likelihood) problem in statistical estimation theory. In the expression for the I-divergence (Eq.21), the function a(y) is taken to be the measured data represented by d(y), and b(y) is taken to be a nonlinear model q(y) (dependant on the attenuation parameter set $\hat{\mu}(x)$) which govern the transmission of the photons by Beer-Lambert's law:

$$q(y) = \lambda(y)\exp\left[-\sum_{x\in X} h(y|x)\hat{\mu}(x)\right] \qquad \text{(Eq.22)}$$

The objective of the algorithm is to find the minima of $I(d\|q)$ with respect to $\hat{\mu}(x)$.

The terms in the log likelihood function that depend on the parameter set $\hat{\mu}(x)$ are negative of the corresponding terms in the I-divergence. Thus, minimizing the I-divergence over the parameter set $\hat{\mu}(x)$ is equivalent to maximizing the log-likelihood function. The final expression for updating the parameters derived on the basis of the minima of $I(d\|q)$ is:

$$\hat{\mu}^{(k+1)}(x) = \hat{\mu}^{(k)}(x) - \frac{1}{Z(x)}\ln\left(\frac{\tilde{b}(x)}{\hat{b}^{(k)}(x)}\right). \qquad \text{(Eq.23)}$$

Here $\tilde{b}(x)$ and $\hat{b}^{(k)}(x)$ are the back projections of $d(y)$ and the current estimates of $\hat{q}^{(k)}(y)$, respectively. In other words, they are the back projections of the measured data and the nonlinear model employed (based on Beer-Lamberts law). Their expressions are given by:

$$\tilde{b}(x) = \sum_{y\in Y} h(y|x)d(y) \qquad \text{(Eq.24)}$$

$$\hat{b}^{(k)}(x) = \sum_{y\in Y} h(y|x)\hat{q}(y) \qquad \text{(Eq.25)}$$

$$\hat{q}^{(k)}(y) = \lambda(y)\exp\left[-\sum_{x\in X} h(y|x)\hat{\mu}^{(k)}(x)\right] \qquad \text{(Eq.26)}$$

The iterative process for computing the image goes backwards from equation 26 to 23. An initial guess for $\mu^{(k=0)}(x)$ is chosen based on which the quantities in equations 26 to 24 are determined which are then used to calculate $\mu^{(k+1)}(x)$ from equation 23. A non-negativity constraint is applied on the values of attenuation. Hence at any iteration *k* if $\hat{\mu}^{(k+1)}(x) < 0$, then $\hat{\mu}^{(k+1)}(x) = 0$.

$Z(x)$ in equation 23 is an appropriate scaling function chosen for the x^{th} pixel such that the following criteria is satisfied:

$$\sum_{x\in X}\left(\frac{h(y|x)}{Z(x)}\right) \le 1 \qquad \text{(Eq.27)}$$

In a detailed analysis by Varma the AM algorithm was found to perform far better, in terms of image quality and error, in determining phase holdup images in two phase systems.

3.3.4. Function decomposition and optimization procedures-based algorithm

The algorithms that are described are valid for the limited number of gamma beams. The simplest arrangement consists in using several shielded γ emitters and collimated detectors, monitoring attenuation of rays due to absorption in material. Such a situation is shown in shown in the Figure 17 (circular cross-section, surrounded by 7 emitters and 5 detectors).

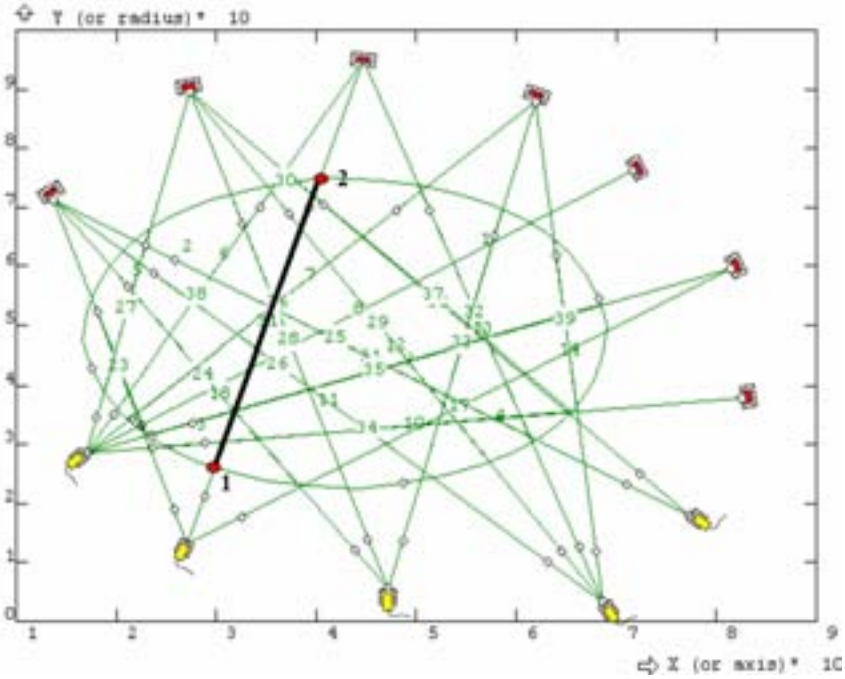

FIG. 17. Example of the beams configuration.

Let us assume, that the measured signal of an arbitrary pair emitter-detector can be expressed as a mean value of unknown density ρ(x,y) along the ray (e.g. along the abscissa 1-2 in the Figure 17),

$$\rho_m = \frac{1}{L_{12}} \int_1^2 \rho(x,y)dl \qquad \text{(Eq. 28)}$$

Experimental data are therefore represented by M values $\rho_{m1}, \rho_{m2}, \ldots, \rho_{mM}$, which enable to identify a density (or volume fraction) distribution ρ(x,y) by the model function:

$$\rho(x,y) = \sum A_i \varphi_i(x,y) \qquad \text{(Eq.29)}$$

where A_i are constants (i.e. parameters of the model)- and $\varphi_i(x,y)$ are basis function.

The next function, as example, has been selected accidentally and has only 3 parameters which are to be identified.

$$\rho(x,y) = A + B((x-0.5)^2 + (y-0.5)^2) + C(x-0.4)(y-0.4) \qquad \text{(Eq.30)}$$

First of all processing of experimental data and evaluation of measured mean density ρ_{mi} along a specific ray must be performed: Assuming linear relationship between density and linear attenuation coefficient the detected intensity of radiation along i-th ray can be expressed by

$$I(\rho_m, L_i) = I_{i0} e^{-a\rho_m L_i}, \qquad \text{(Eq.31)}$$

where the coefficient a is determined from independent experiments or theoretically from tabulated absorption coefficients and densities of individual components of e.g. solid-liquid mixtures.

The incident intensity I_{i0} is a parameter, which is to be calculated for each ray independently using results of calibration measurement when material density ρ_{ref} is uniform and constant (for example measurement with empty apparatus or with apparatus completely filled by a liquid) – this calibration experiment yields values I_{refi}. Using these values the mean density along the i-th ray can be evaluated from the detected signal I_i as follows

$$\rho_{mi} = \rho_{ref} - \frac{1}{aL_i} \ln \frac{I_i}{I_{refi}} \qquad \text{(Eq.32)}$$

The model function is selected according to the presumed distribution of the density. A different pattern is used for an unknown arbitrary distribution, another for distribution, which is e.g. symmetrical around vertical axis or for discontinuous mass distributions. The n values of the constants a_i are determined from measured attenuation of at least m = n different beams.

Different optimization procedures can be used to find proper values of the constants. OPTIMA and SOMA are two examples of this procedure (Fig. 18).

Optimization procedure (operation OPTIMA and SOMA)

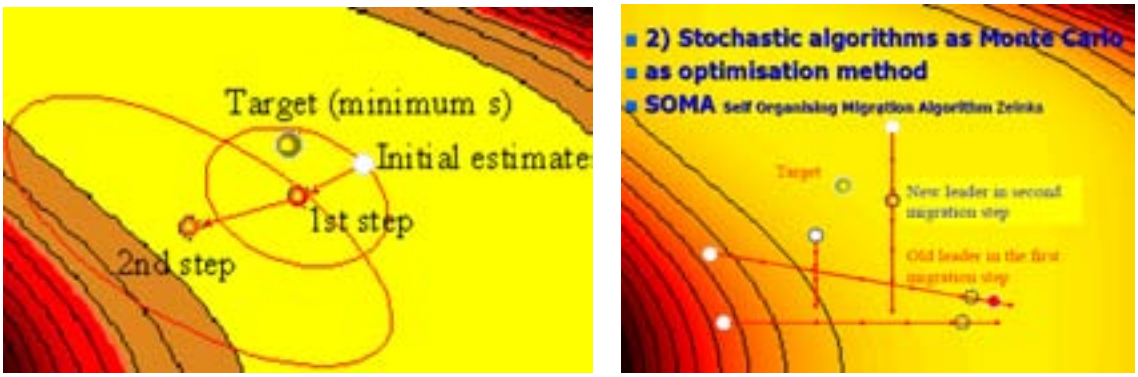

FIG. 18. Procedures of optimization (Optima – left and Soma – right).

The basic method used for optimization of a general mathematical model OPTIMA is in principle the same as the method used for nonlinear regression – Marquardt Levenberg. The method is based upon linearization of optimized model $f(x_i,p_1,\ldots,p_M)=fi$, where xi are independent variables of the i-th observation point and $p_1,\ldots,p_M$ are optimised parameters of model. The least squares criterion is used for optimization

$$s^2 = \sum_i (y_i - f_i)^2 w_i \qquad \text{(Eq.33)}$$

$$\frac{\partial s^2}{\partial p_j} = 2\sum_i (y_i - f_i) \frac{\partial f_i}{\partial p_j} w_i \equiv 0 \qquad \text{(Eq.34)}$$

$$\sum_i (y_i - f_{i0} - \sum_k \frac{\partial f_i}{\partial p_k} \Delta p_k) \frac{\partial f_i}{\partial p_j} w_i \equiv 0 \qquad \text{(Eq.35)}$$

where $\Delta p_k = p_k - p_{k0}$ is the sought increment of k-th parameter in current iteration step. Therefore we arrive to the system of linear algebraic equations for the vector of increments

$$\sum_k C_{jk} \Delta p_k = B_j \qquad \text{(Eq.36)}$$

where:

$$C_{jk} = \sum_i \frac{\partial f_i}{\partial p_j} \frac{\partial f_i}{\partial p_k} w_i \quad , \quad B_j = \sum_i \frac{\partial f_i}{\partial p_j} (y_i - f_{i0}) w_i \qquad \text{(Eq.37)}$$

In the case, that the model is linear with respect to calculated parameters, with this algorithm one iteration is needed. However, even if some parameters are non-linear iterations are necessary: first the values of linear parameters are calculated from reduced system for fixed values of nonlinear parameters and after the full system of equations for linear and nonlinear parameters is solved, with modified matrix of the system, where a positive value λ is added to all diagonal entries of the matrix. Before adding the parameter λ the whole system of equations is scaled, which represents matrix transformation giving equivalent system of equations with matrix having ones on diagonal (this scaling is optional but recommended):

$$\sum_k C^*_{jk} \Delta p^*_k = B^*_j \qquad \text{(Eq.38)}$$

$$C^*_{jk} = \frac{C_{jk}}{\sqrt{C_{jj} C_{kk}}} \quad , \quad C^*_{jj} = 1 + \lambda \quad , \quad B^*_j = \frac{B_j}{\sqrt{C_{jj}}} \quad , \quad \Delta p^*_k = \Delta p_k \sqrt{C_{kk}} \qquad \text{(Eq.39)}$$

Gauss Jordan reduction is used for solution of (Eq.35) and calculated vector of increments is unscaled

$$\Delta p_k = \frac{\Delta p^*_k}{\sqrt{C_{kk}}} \qquad \text{(Eq.40)}$$

and added to the vector of optimized parameters from the previous iteration.

In some case is recommended to use an alternative method to the deterministic Marquardt Levenberg method, especially when there are many relative maximum, for this is recommended to use the stochastic method SOMA, which will give a rough estimate of optimal parameters. The method SOMA (Self Organising Migration Algorithm) need not calculate model derivatives, and therefore is much more simpler, robust but also significantly slower. This is so called memetic algorithm, modelling movement of several specimen in a hyperspace (under the term specimen we have in mind a collection of parameters that may conduct to the optimization of the mathematical model).

The structure of this algorithm is as follow:

- First several specimen NSPEC is generated by using pseudorandom number generator. All specimens must be within the specified range of model parameters.
- The best specimen, called LEADER, is selected.
- Iterations, in SOMA terminology called migration laps, begin. In each lap each of NSPEC specimen is moving towards LEADER in small steps of the length STEP (the parameter STEP is relative length of step with respect to the initial distance between specimen and leader), number of steps is MASS (MASS is specified control parameter, like STEP and NSPEC). In the space of parameter the trajectories of specimen are lines which aiming toward leader. Not exactly, the direction specimen-leader is perturbed intentionally by using random number generator. The measure of perturbation is specified by parameter PRT: if PRT=1 no disturbance is applied and the smaller (but still positive) is PRT, the greater is the deviation of direction toward the leader (this is realized in fact so that some randomly fixed parameters are fixed, and the smaller is PRT, the more parameters is fixed). Migration lap ends by transfer of all specimens to their best position and by election of new LEADER.

For more details see FEMINA Manuals (http://www.fsid.cvut.cz/~zitny/fem3ai1.pdf).

3.3.5. Evaluation strategy for tomography images

The goal of industrial CT imaging system is to non-destructively produce internal images of object with sufficient detail to detect crucial features. The task of the CT user is to specify the system that will satisfy a particular need and to verify that the specification is met. The visibility of a feature in a CT image depend on the difference in gamma or X rays attenuation between the features and its background, size of the feature, size of the background object, number of sample collected, radiation exposure and numerous other factors.

A systematic evaluation of experimental results obtained with different tomographic systems or different tomographic configurations for optimization require setting common experimental basic references; that will allow realize measurable comparisons between tomographs obtained under different hardware, geometrical arrangements, algorithms, sensor system, etc.

To do such evaluation it is necessary to consider several aspects, some of which are:

- Reference phantoms
- Spatial resolution
- Contrast
- Temporal resolution
- Linearity

Reference phantoms. Phantom is a test object containing features of known size, spacing and contrast, which can be scanned to determine spatial or density resolution. The use of a set of reference polypropylene phantoms will allow the possibility to evaluate their tomographic images obtained with different tomographic systems or different tomographic configurations for optimization using the same reference object. Once selected the reference phantom the tomographic image is obtained for each tomographic system or configuration, then they are compared using a four evaluation criteria, namely: spatial resolution, temporal resolution, contrast and linearity.

Spatial resolution. The finite number and width of X ray or gamma ray beams causes the blurring of a feature, which can alter both the shape of the feature and the resolvability of multiple features. This blurring also affects the perceived contrast, especially of small features. Spatial resolution is generally quantified in terms of the smallest separation at width two points can be distinguished as separate entities. The limiting value of the spatial resolution is determined by the design and construction of the system and by the amount of the data and sampling scheme used to interrogate the object of interest. The precision of the mechanical system determines how accurately the views can be backprojected.

For this purpose, two metrics are employed, both metrics use the root mean square error (RMSE) of the reconstructed attenuation coefficient minus the known attenuation coefficient of the phantom at each pixel, the first metric is obtained dividing the RMSE by the total number of pixels, N, in the model and in the second metrics is the division of RMSE by root of the sum of squares of known attenuation coefficient at each pixel. The procedure described can be said that it is RMSE space resolution, since it compares results in base of their spatial values. The mathematical formulations of the metrics are:

$$RMSE = \sqrt{\sum \left(\mu_{reconstructed,i} - \mu_{known,i} \right)^2} \qquad \text{(Eq. 41)}$$

First metric RMSE with respect to N:

$$RMSE_N = \frac{RMSE}{N} \qquad \text{(Eq. 42)}$$

Second metric RMSE with respect to μ:

$$RMSE_{\mu} = \frac{RMSE}{\sqrt{\sum_{i=1}^{N} \mu_{known,i}^{2}}} \qquad \text{(Eq. 43)}$$

Here $\mu_{known,\,i}$ and $\mu_{reconstructed,i}$ are known and reconstructed attenuation mean values at pixel i and N is the total number of pixels. For systems operating in the Compton range with ^{137}Cs (661.6 keV), μ can be replaced with ρ; the density. Likewise, for capacitance tomograph μ must be replaced with ε_R; the relative dielectric permittivity.

A graphical procedure of the spatial resolution is described by making comparisons of source-detector geometries using the image intensity (grey scale) along selected perpendicular lines to X or Y coordinate, at specific points. Each one of these profiles can be used to compare spatial resolution.

For example to compare the results obtained using three different geometries, figure 19, such as parallel beam configuration, equilinear beam configuration and equiangular beam configuration.

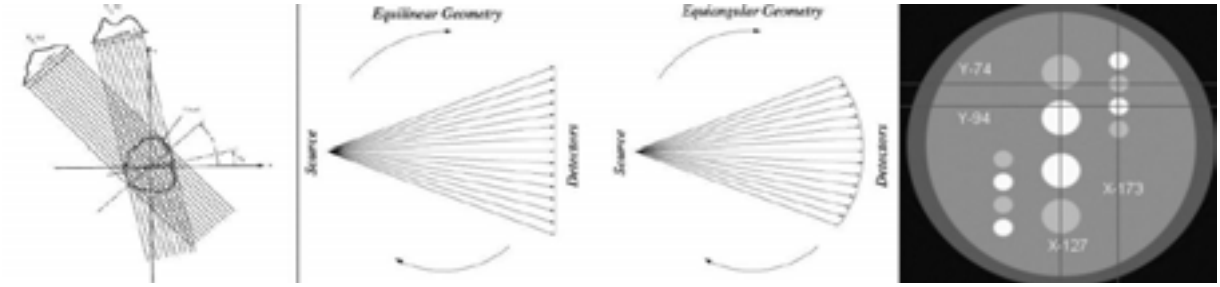

FIG. 19. Diagrams of three different geometries: parallel beam (l.), equilinear (l.m.) and equiangular (r.m.); and phantom with pixel lines Y-74, Y-94, X-127 and X-173.

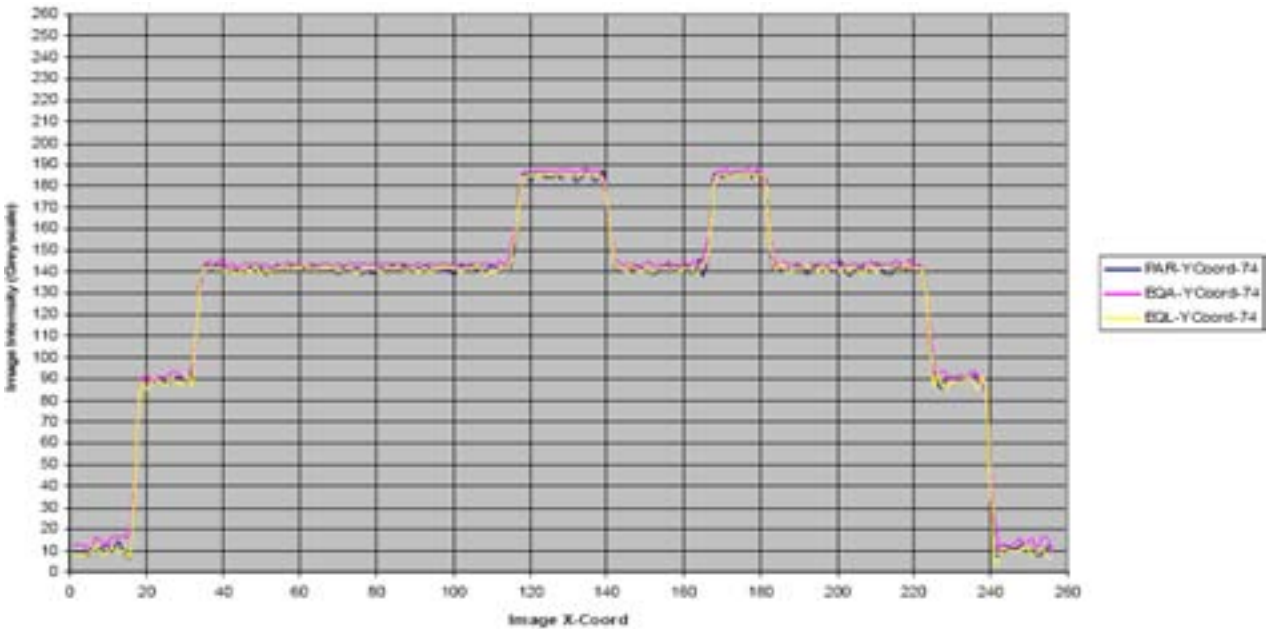

FIG. 20. Graphical comparation of three different geometries: parallel beam (blue), equilinear (red) and equiangular (yellow); Intensity (grayscale) vs pixel location on the line Y-74.

Contrast. The quantity that is reconstructed in X ray CT imaging is the linear attenuation coefficient, μ, usually within a two-dimensional slice defined by the thickness of the x-ray beam. It is measured in units of cm^{-1} and is directly proportional to the electron density of the material. To be distinguished, a feature must have a linear attenuation coefficient, μ_f, that is sufficiently different from the linear attenuation coefficient of its background material, μ_b.

Contrast could also be analyzed using number of pixels versus attenuation coefficient histograms. A qualitative evaluation can be made using the histograms of the number of pixels in each class in which is divided the total linear attenuation coefficient values obtained with the computed tomographic system (observed linear attenuation coefficient) and the theoretically calculated linear attenuation coefficient of standard polypropylene phantom (μ_{poly}= 0.91 cm^{-1}) with two holes ($\mu = \mu_{air} \approx 10^{-5}$ cm^{-1}). In the ideal case, the histogram should show two narrow peaks, one close to zero, μ_{air}, and the other close to μpoly. However, in real case, due to Poisson noise, pixel size and reconstruction error, these histogram peaks are broad.

Below are some attenuation coefficient histograms, where ideal data was obtained from the designed value of phantom. Figure 21 shows the difference between the reconstruction algorithms SIRT and EM. It is important to note that even with ideal data the two materials (polyethylene and air) gives two peaks, since the attenuation coefficient of air is much smaller than the one of polypropylene, its peak is close to zero; these peaks are different due to the reconstruction error inherent to the algorithm

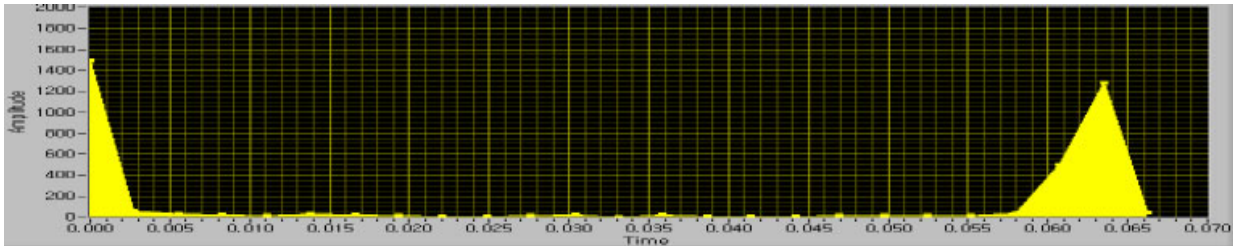

a.

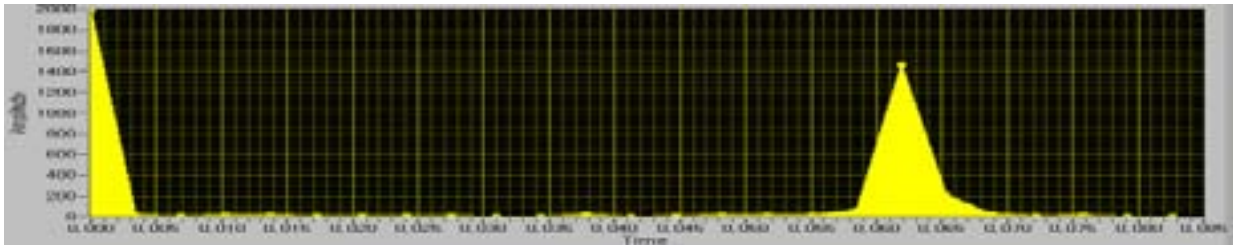

b.

FIG. 21. Attenuation coefficient histograms of the SIRT (a.) and EM (b.) reconstructed SIRT (a.) and EM (b.) algorithms using ideal data.

Two attenuation coefficient histograms in Figure 22 were reconstructed with EM algorithm, using a 1 second and with 10 seconds counting time where the base of the peaks are broader in the short counting time, so it has a less contrast resolution.

Other evaluation example of contrast resolution was used an oil-water-gas mixture. In this case, the materials observed as three peaks that represent each linear attenuation value are shown in Figure 23, which represents the different values of linear attenuation coefficient.

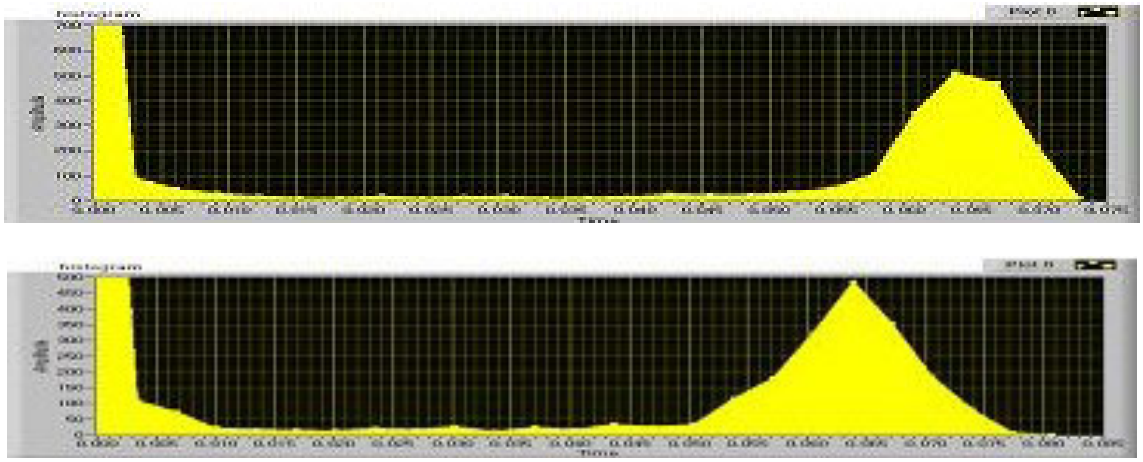

FIG. 22. Attenuation coefficient histogram of the EM reconstructed image using 10 s (a) and 1 s (b) counting time

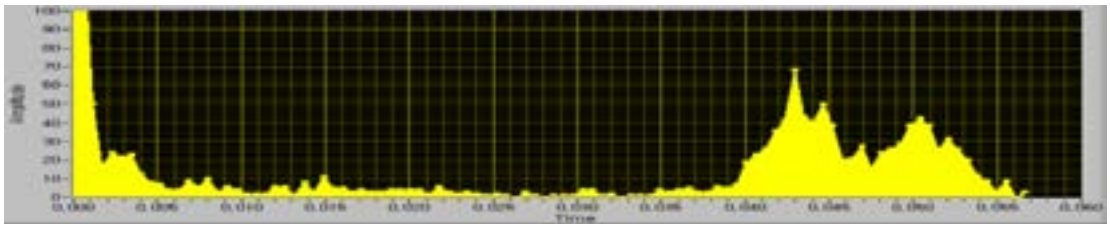

FIG. 23. Attenuation coefficient histogram of the EM reconstructed image using oil-water-gas mixture.

Another application of this method is shown in figure 24, where the tomographic image and attenuation coefficient histogram were obtained using EM algorithm when for two different sources ^{137}Cs and ^{60}Co for the oil-water-gas mixture phantom.

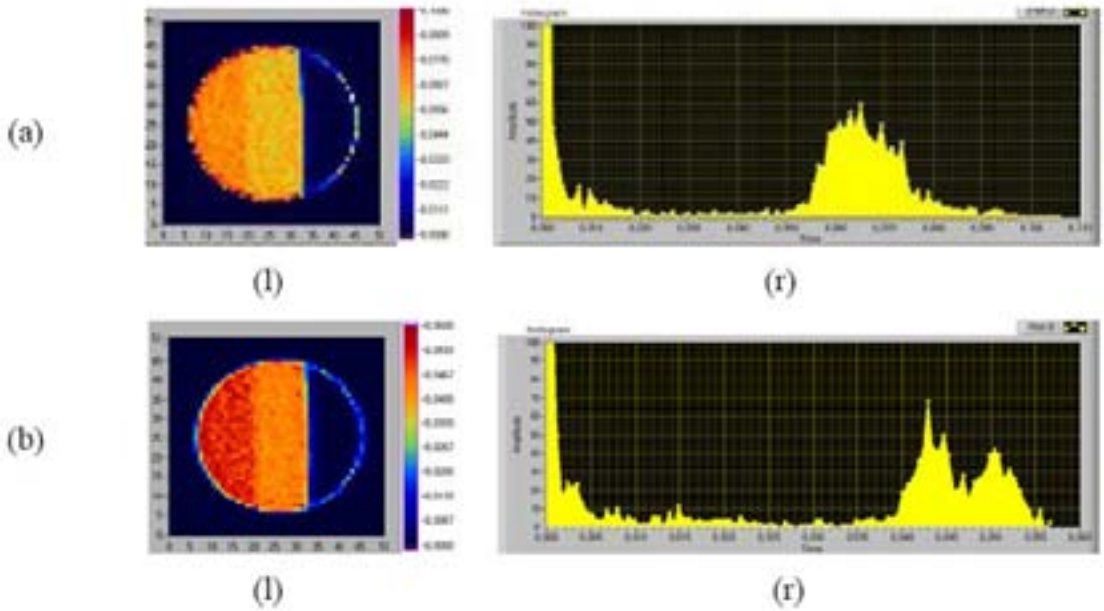

FIG. 24. Tomographic image (l) and attenuation coefficient histogram (r) using ^{137}Cs (a) and (b) ^{60}Co source.

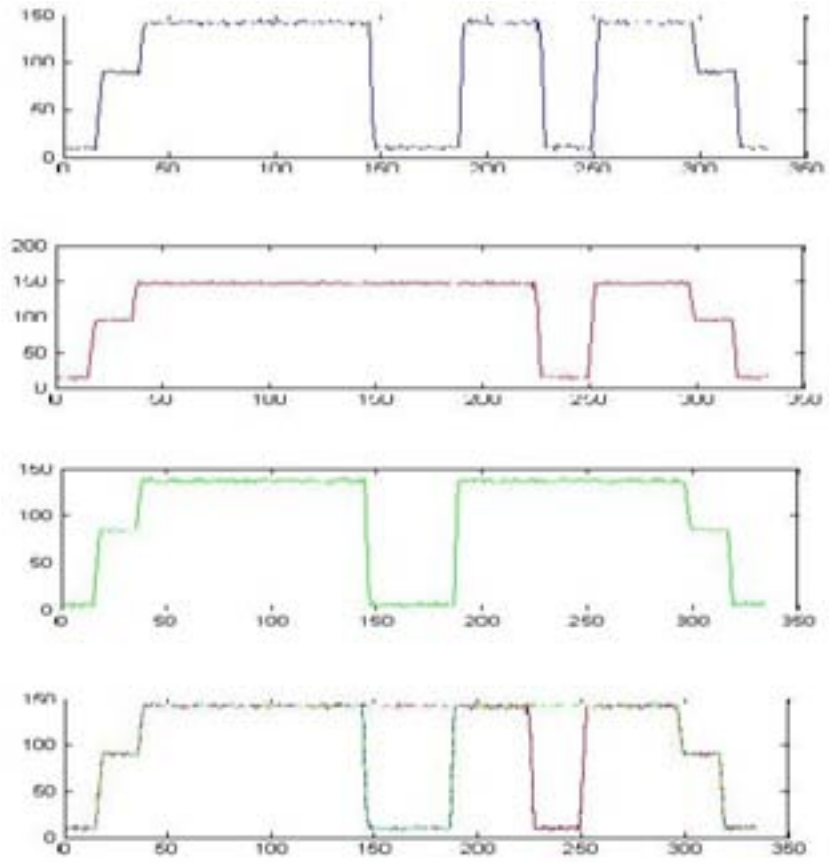

FIG. 25. Linearity using image intensity diagram along a selected line: (a) Phantom with two holes (b) Phantom with one hole, (c) Phantom with one hole in middle (d) Superposition of (a), (b) and (c).

Linearity. In tomography exists at least two different types of linearity, a) due to the path (or area) along which the integration of the attenuation property distribution take place, under this definition it is said that the tomography is not linear if the path does not follow a straight line or if it is not known and b) due to tomographic reconstruction algorithm of two of more abnormalities at different spatial locations (for examples holes) when the tomographic image is obtained for each abnormality separated and together, if the tomographic image when they are superposed match then it is said that the tomography is linear (Figure 25). At this figure was used the same phantom, fulfilling one hole at the time.

Artifact. An artifact is something in an image that does not correspond to a physical feature in the test object. All imaging systems, whether CT or conventional radiography, exhibit artifacts. Examples of artifacts common to conventional radiography are blotches of underdevelopment on a film or scattering produced by high-density objects in the X or gamma ray field. In both cases, familiarities with these artifacts allow the experienced operators to discount their presence quantitatively.

3.3.6. Dual modality software

The measurements obtained by gamma ray tomography depend on the density distribution. Therefore the images reconstructed from these measurements illustrate the density distribution within a measured volume with a high spatial resolution (Fig. 26). On the other hand electrical tomography provides high speed imaging (at a rate of up to 300 frames per seconds) with lower spatial resolution than gamma ray tomography. Combination of two tomographic techniques provides for dual modality tomography (DMT) with good spatial and temporal resolutions.

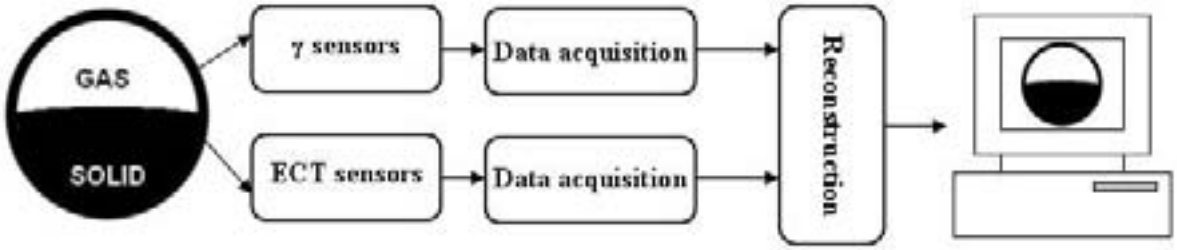

FIG. 26. Schema of DMT aplication.

The mathematical model of the dual mode tomograph can be presented in the following manner:

$$p_i^C(\Delta t) = c_i(\Delta t) \pm N_i(\Delta t)$$
$$p_i^G(\Delta T) = A(c_i(\Delta t) + c_i(2\Delta t) + \ldots + c_i(n\Delta t)/n$$
$$\Delta T = n\Delta t$$

where:

- $c_i(\Delta t)$ is a mean temporal material concentration for the *ith* pixel of a pipe cross section on a time interval Δt, $p_i^C(\Delta t)$ is the corresponding pixel value in the reconstructed image from data captured by an ECT tomograph, $N_i(n\Delta t)$ is reconstruction error,
- $p_i^G(\Delta T)$ is corresponding pixel value in the reconstructed image from data captured by a gamma tomograph, where ΔT is a sampling interval of a gamma tomograph.
- *n is a number of ECT frames*
- *A* stands for the solid density .

We proposed the following mathematical model (equations) of a dual tomographic system. The model includes the higher spatial resolution of a gamma tomograph and the higher temporal resolution of a ECT tomography. Pixel values of $p_iG(\Delta T)$ and $p_iC(\Delta t)$, $p_iC(2\Delta t),\ldots,p_iC(n\Delta t)$ are known. We seek unknown values of $c_i(\Delta t),c_i(2\Delta t),\ldots,c_i(n\Delta t)$. For seeking $c_i(\Delta t),c_i(2\Delta t),\ldots,c_i(n\Delta t)$ the Dual Modality Reconstruction (DMR) algorithm was developed. The DMR algorithm is based on adjusting pixel values of $p_iG(\Delta T)$ according to the pixels $p_iC(\Delta t)$, $p_iC(2\Delta t),\ldots$, $p_iC(n\Delta t)$.

A new algorithm was developed using a priori knowledge provided by gamma-ray and capacitance tomography and it should be emphasized that the DMR (Dual Mode Reconstruction) algorithm is a mixture of deterministic and stochastic approaches. The scheme of the algorithm can be presented in the following steps. On the basis of the ILST Iterative Least Square Technique) pixel values, the set is calculated, which consists of the pixel values which meet three criterions:

- the average of pixels values must be more or less equal to ILST pixel
- the improved pixel values obtained by means of the DMR algorithm should not significantly differ from the value of the equivalent pixel obtained using the IBP algorithm (IBP criterion)
- the calculated pixel values should not significantly differ from the neighboring pixels, obtained using the k-NN rule (neighborhood criterion)

The next step is to select pixel values from the set which have the largest number of representations in the set. These values are the final pixels values in the output frame. The final effect of the DMR algorithm is *n* improved IBP frames by means of one ILST frame.

Values of improved pixels must meet the condition: $p_i^{\,G} - \Delta s \le \dfrac{\left(\sum_{j=1}^{n} c_{i,j}\right)}{n} \le p_i^{\,G} + \Delta s$

where:
n – the number of IBP frames,
i – the number of pixels,
j – the number of frames,
Δs – the constant,

The concept of the proposed algorithm is described by processing a hypothetical set of four images each consisting of nine pixels. In the first step k= 1 a set of four arbitrary chosen numbers (within the range 0-1) was assigned to four pixels as shown in Figure 27. The value assessed from gamma-ray tomography was constant $p_5^{G}(\Delta T) = 0.5$.

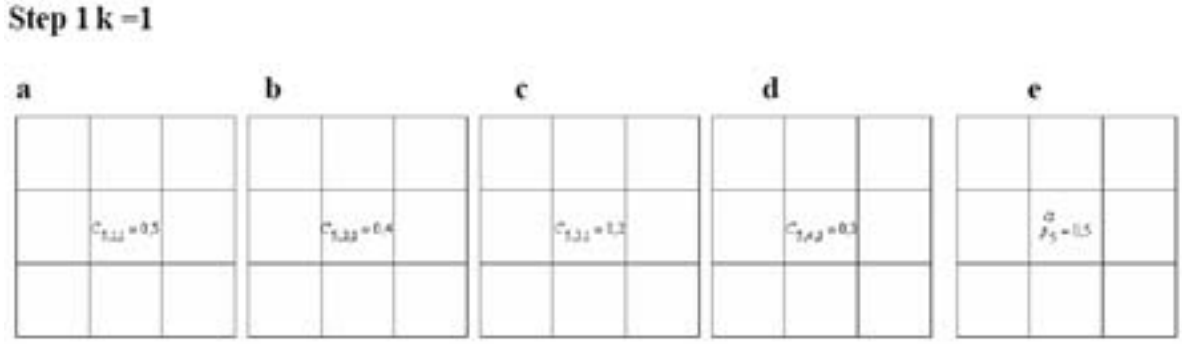

FIG. 27. Pixel combination no. 1 (k = 1)

Next the condition is checked if the average $\sum_{j=1}^{n} c_{5,j,1}(j\Delta t)/n$ is within the range $p_5^{\,G}(\Delta T) \pm \delta_1$. In this way the interaction between the measurements provided by both modalities on the image quality is introduced. The condition that the average is less than the predetermined condition is the starting point of this algorithm as shown later. For the assumed value of $\delta_1 = 0.1$ this condition is not met. Therefore during this step k becomes k = 2 and the next set of $c_{i,j,k}(j\Delta t)$ is generated as illustrated in Figure 28.

FIG. 28. Pixel combination no. 2 (k = 2)

The average for this data set is within the range $p_5^{\,G}(\Delta T) \pm \delta_1$. Repeating step 1 a large set of potential solutions can be generated. Let Z determine the set of potential solutions. To limit a number of potential solutions, additional constrains were applied on this data set.

Step 2

In step 2 only the values of $c_{i,j,k}(j\Delta t)$ from a set *Z* are chosen which do not significantly differ from the values of $p^{C}{}_{i,j}(j\Delta t)$ as described by the IBP (iterative back projection) criterion:

$$p^{C}_{i,j}(j\Delta t) - \Delta c \le c_{i,j,k}(j\Delta t) \le p^{C}_{i,j}(j\Delta t) + \Delta c$$

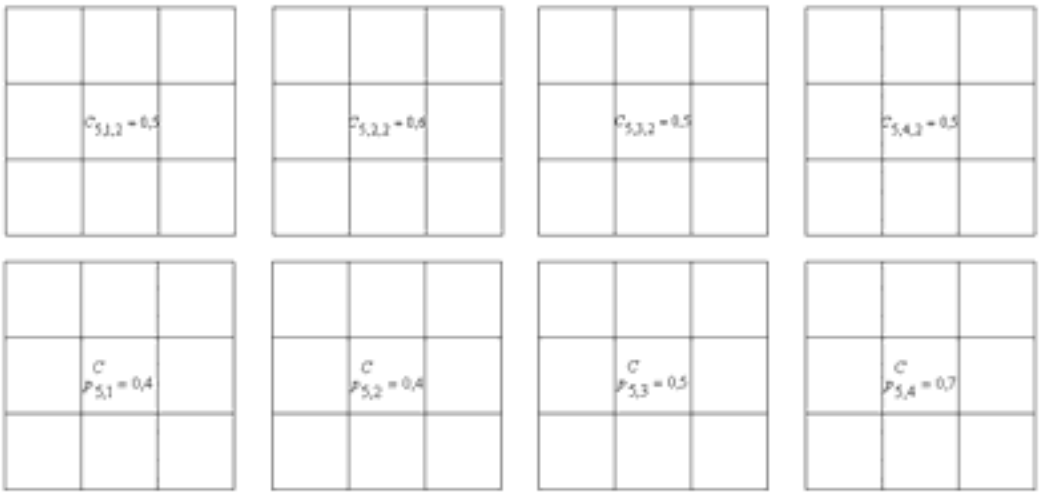

FIG. 29. IBP criterion

Step 3

In this step an additional criterion was introduced based on the k-NN rule (neighborhood criterion). The criterion is expressed by the following equation:

$$p^{C}_{i+s,j}(j\Delta t) - \Delta d \le c_{i,j,k}(j\Delta t) \le p^{C}_{i+s,j}(j\Delta t) + \Delta d$$

where Δd – constant, s – the number of neighbor pixels.

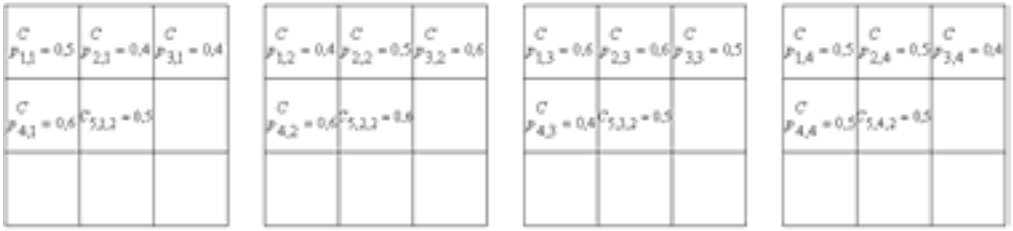

FIG. 30. Neighbourhood criterion

Step 4

In this step from the set *Z*, the values of $c_{i,j,k}(j\Delta t)$ with the largest number of representations were chosen. These are the final $c_{i,j}(j\Delta t)$ values.

The DMR algorithm was also applied to imaging a gas/solid flow in a vertical channel. As shown in Figure 31, the images obtained by means of the DMR algorithm are characterized by a greater sharpness than those obtained from the IBP (Iterative Back Projection) algorithm. In addition, the effect of blurring that occurs in IBP images has significantly been reduced.

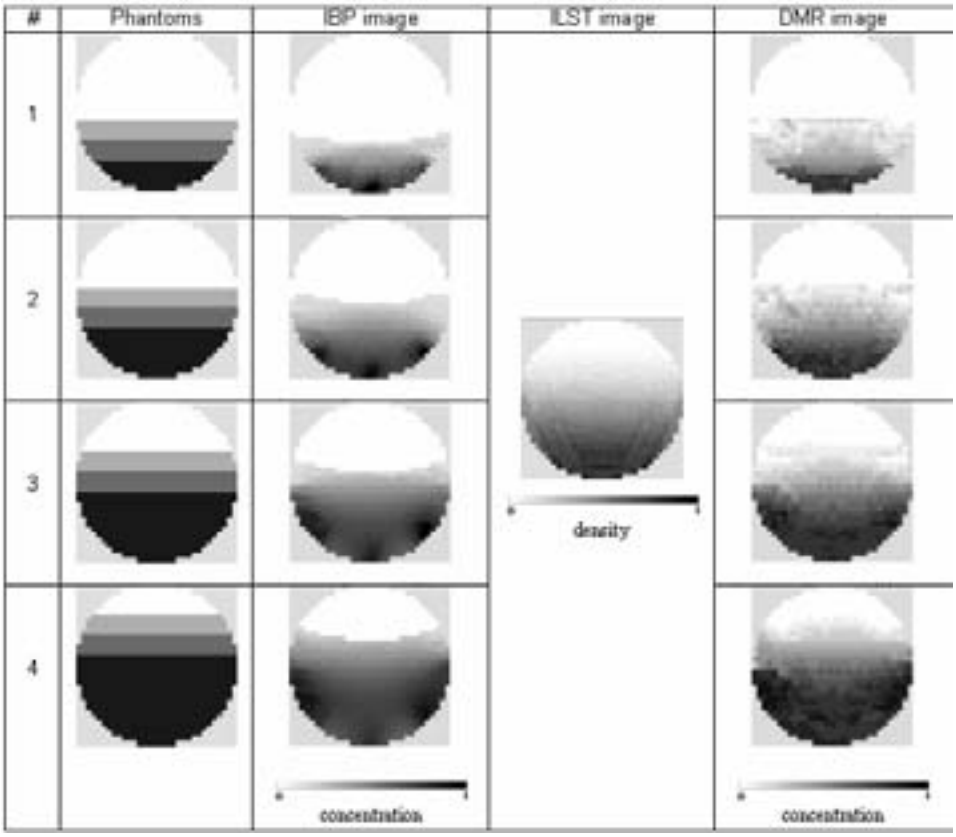

FIG. 31. Example of image reconstruction by DMT software.

4. GAMMA EMISSION TOMOGRAPHY

Imaging systems are most suitable for in situ system inspection with control purpose, diagnosis of a system or modeling for CFD validation. The field of applications of emission tomography for tracer visualization extends from chemical engineering, oil recovery, geochemistry or hydrogeology. In chemical engineering for instance, experts would like to visualize the behavior of individual phases in multi phase flow reactors, such as fluidized beds, slurry reactors, bubble columns, or any kind of system involving multi phase flows or not, like mixers, separators, etc. The tracer approach for the study of these systems can generally be defined as follows: the objective being to get information on a specific phase in a multi phase flow, an additional flow that conveys the tracer is added to the phase of interest. From the analysis of the labeled flow, some information can be recovered. In some case, the tracer is natural in the process but in most cases, the tracer is added to flow. Classical approach, based on transfer function analysis uses spatio-temporal information. By this way, it is possible to estimate Residence Time Distribution [RTD], and thus flow rate, dead volume, loops, dispersivity, and diffusion coefficient for porous media analysis.

Numerous methods based on particle tracking exist to characterize a flow, and specifically in aerodynamics for wing, car, wing mill or pump design. In case of opaque flow systems or systems involving bubbles like gas phase or vapor phase, optical methods can no longer be used. As such, ionizing radiation based methods are required. Two types of methods can be used to investigate such flows. The first one is based on the use of particles opaque to X ray photons. In such experiments, 2 X ray sources with the corresponding 2D detectors are assembled to 90° one of the other. The stereo vision allows the tracking of the particles. The second method makes used of radioactive sources and the techniques are called positron emission particle tracking (PEPT) and gamma ray emission radioactive particle tracking, quite frequently known as radioactive particle tracking (RPT).

Both SPECT and RPT use the detection and counting of highly penetrating gamma rays emitted by a single radio labeled flow follower (tracer), which is dynamically similar to the tracked phase. The detected gamma-rays are used to estimate the instantaneous coordinates of the moving tracer. The number of photons registered depends mainly on the distance between the tracer and the detector, but also on the attenuation of the media between the particle and the detector and the intrinsic properties of the detector. Accurate tracking requires detection of large number of photons to reduce statistical fluctuations. Since the tracking of fast moving phases has to be done at high sampling frequencies, up to 200 Hz, the tracers should generally have relatively high intensity, and the detection system requires high rate counting capability.

Both fluid and solid flows can be followed with appropriate tracers, provided they match in size, density, shape and buoyancy the characteristics of the tracked phase. From these measurements, the instantaneous and local Lagrangian velocities can be estimated by successive time differentiation. From sufficiently long experiments, transient and steady state information can be determined. For instance, the 3D Eulerian velocity field, local velocity distributions, turbulence intensities, kinetic energy, shear stress, dispersion coefficients, phase holdups, trajectory length distributions, mixing times, circulating times, residence time distributions can be obtained. Information obtained from CARPT is especially valuable for validation of CFD models.

Industrial imaging method based on emission has been developed for fluid flow monitoring in chemical engineering for trickled bed reactor [COLARGOL] or fluidised bed [IFP], diffusion of tracers in rock sample [ANDRA], or flow stratification in nuclear power plant. 2D tracer distribution imaging is described in this document. The acceptable sampling time is constrained mainly by the dynamics of the flow, the available tracer activity and the number of detectors.

4.1. SINGLE PHOTON EMISSION COMPUTED TOMOGRAPHY (SPECT)

The specificity of single photon emission computed tomography (SPECT) is related to the choice of the tracer, the activity to inject and the processing of waste after experiment. Tracers usually used are, as radioisotope generators, Mo/^{99m}Tc, Sn/^{113m}In, Cs/^{137m}Ba, and as radioisotope, ^{82}Br or ^{140}La. The choice of the energy of the tracer is related to the absorption of the different elements that constitute the system: flow(s), internal parts if exist, the wall of the pipe. The amount of activity of tracer is related to the size of the vessel, the distance from detectors to the flow and the dynamic of the flow. In case of porous media analysis, low activity can be used; some experiments have been conducted with activity as low as few tenth of kBq. Conversely, in case of high velocity flows, higher amounts of activity need to be injected. For SPECT measurement of water distribution in a T mixer where the flow rate was 1 m^3/s with a section of the pipe equal to 0.2 m^2, 200 GBq of ^{99m}Tc was injected. Attenuation of material and dynamics of the flow are usually connected since high flow rate also means thick wall of the pipe.

In SPECT tomography, the general problem can be set as a following, in the 2D case (Fig. 32). The tracer distribution is estimated from projections by a reconstruction technique. The projection process can be set as following. Let decompose the image to reconstruct on a N^2 matrix. Let denote λ_j the unknown intensity of pixel j. Let denote y_i the measure in the i^{th} detector. If A_{ij} represents the probability that a photon emitted from pixel j is detected in detector i then it arises:

$$y_i = \sum_{j=1}^{N^2} A_{ij}\lambda_j + \varepsilon_i$$

and for the set of measurements, by a matrix notation:

$$y = A\lambda + \varepsilon$$

where y is the set of measurements, λ is the set of unknown intensities and A is the projection matrix of the system.

The aim of computed tomography is to inverse former equation providing that matrix A is a sufficient approximation of the projection process. Matrix A includes solid angle, gamma scattering, attenuation, lead penetration and detector response. The estimation of the projection matrix is described below. Many methods can be used to inverse the equation. Due to the lack of statistics, ML-EM is generally well suited. Statistical algorithms are more intensively used in nuclear medical imaging, due to the available computing power. This algorithm is a statistical approach that takes into account the statistical nature of photon detection.

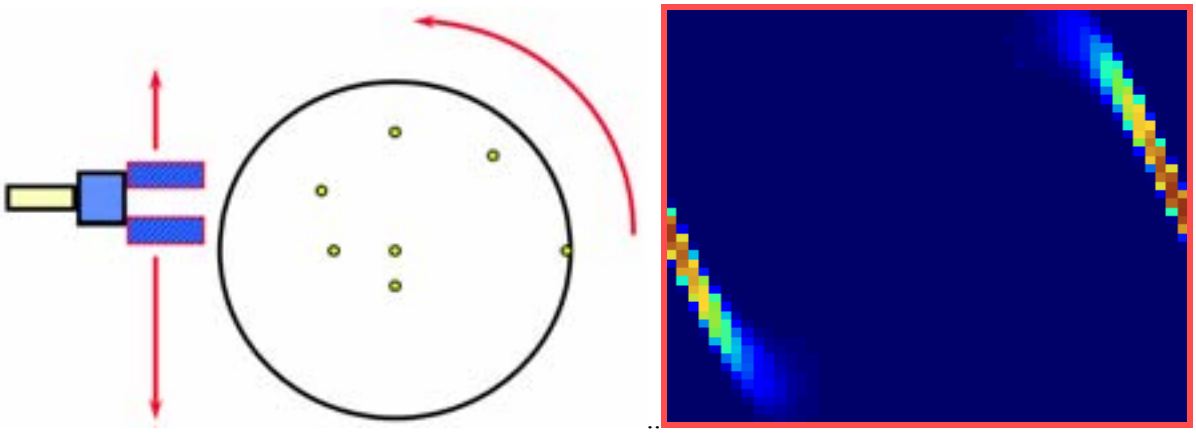

FIG. 32. General description of 2D SPECT system showing the collimated detector, the projection and rotation displacements (left). Obtained sinogram for a source located on the edge where horizontal axis represents the projection angles (right).

4.1.1. Estimation of the A matrix

Regarding the 2D SPECT tomography, we have to consider that the reconstructed image is unfortunately an approximation of the signal in a thick slice of the pipe under inspection. Matrix coefficients are best estimated by Monte Carlo approach, in order to take into account all phenomena, and particularly scattered events. To estimate the projection matrix, we consider source lines, perpendicular to the detection plane define by the set of detectors. The coefficients of the A matrix become the probability that photons emitted from the source line located in the pixel j are detected by detector i. Source line should be long enough to consider that the probability of detection of photons emitted from the extremities are very low (Fig. 33). A 95% or 99% criterion should be used, ie find the length of the source that leads to 95% of the signal obtained with an infinite length source.

A two stages process is applied to estimate the A matrix. For rapid evaluations, calculation based on direct model of the acquisition process is used. In that case, scattering is ignored. The coefficients of the matrix are computed as follow. An elementary function computes the solid angle and the attenuations from any points in the vessel to the detectors. This calculation is easy when basic geometrical objects are used (cylinder, parallelepipeds…).

In case of more sophisticated geometry, the stereo lithography (STL) format can be used. Once the rough parameters are designed, the second step is the computation of the matrix transport by Monte Carlo software, to take into account all the phenomena. MCNP, Geant or more specific software like Inspect (from CEA-Saclay) can be used.

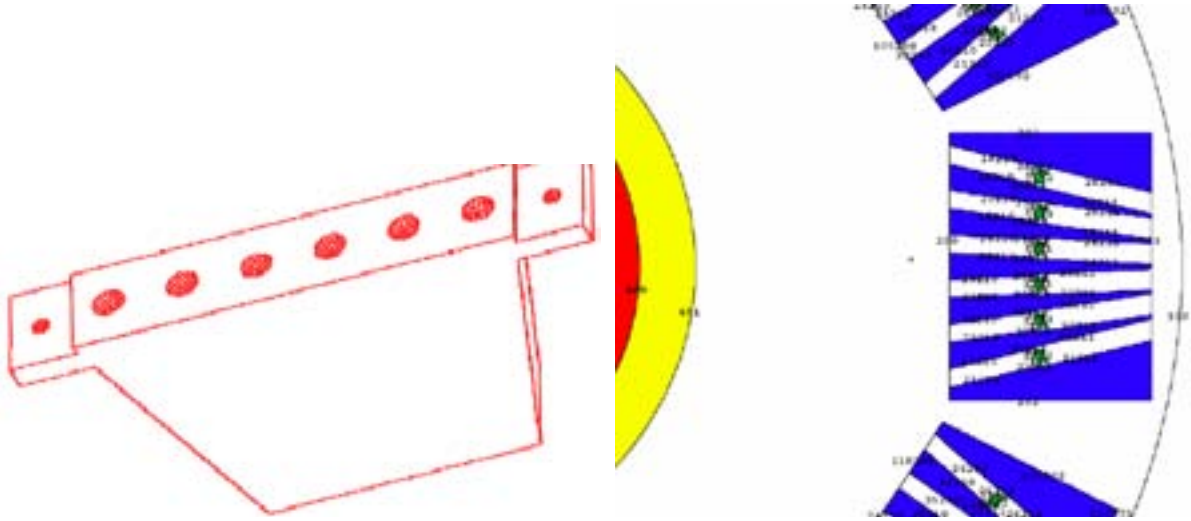

FIG. 33. Divergent collimator (l.) and MCNP model (r.).
In green the 16x16x10 mm scintillator.

Due to the long computation time required by simulation software, not all the coefficients of the matrix are simulated. We only consider some line source locations as depicted below, as an example. Density distribution of source increases while approaching the detector (Figs. 34-36). Once simulations are completed, an interpolation is applied to estimate the coefficients of the matrix.

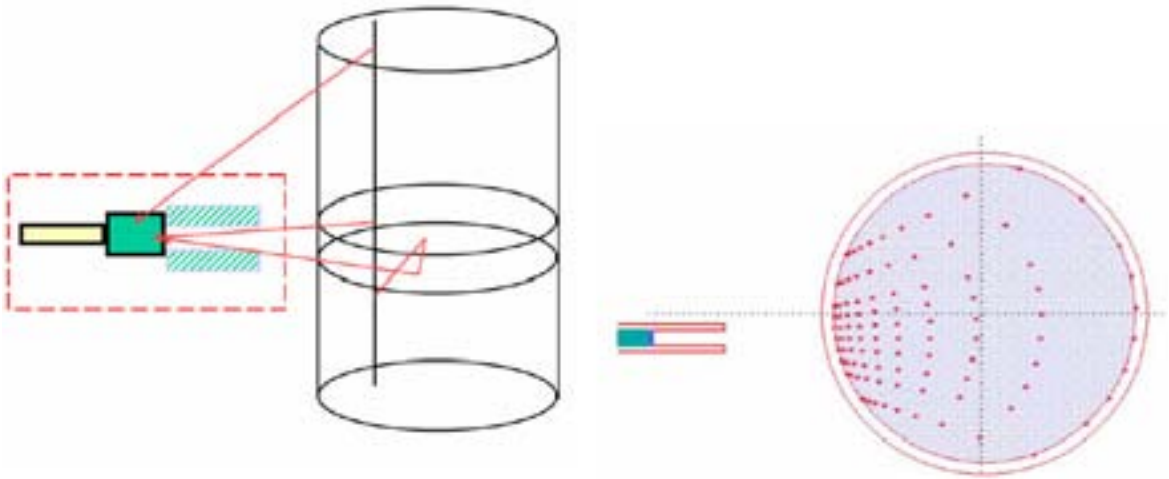

FIG. 34. Description of line source locations used for simulations with "Marilin" software.

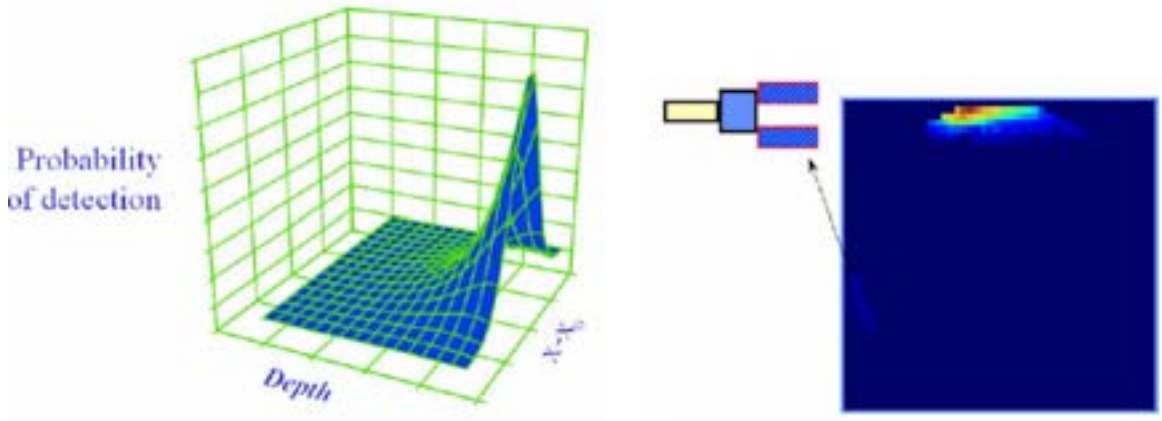

FIG. 35. Probability of detection for source located in reconstruction plane for one detector (2 representations). On the right, figure shows that photons can be detected through collimator (arrow)..

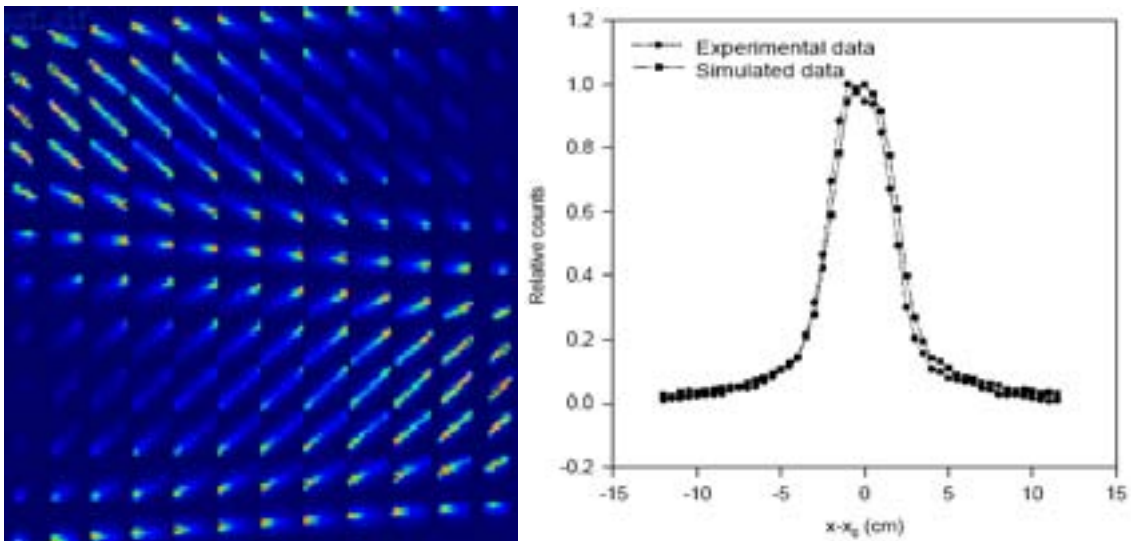

FIG. 36. View of the full matrix for a SPECT system based on 12 projections with 12 detectors per projection. The colour map scales the probability of detection: black blue value is 0 and brown value is 0.0001 (Left). Validation of simulated data with experimental measurements (right).

4.1.2. Scanning system for SPECT

There are two kind of scanning system in gamma emission tomography. One is rotational scanning system (Fig. 37) and the other is non rotational scanning system (Fig. 38). The gamma emission tomography needs array detectors at different angles. The rotating scanning system has one array detector and rotating it to generate several views. The rotating scanning system is less expensive because it need only one array detector but it has poor temporal resolution. Non rotating scanning system is expensive because it needs many detectors but it is suitable for high speed flowing imaging.

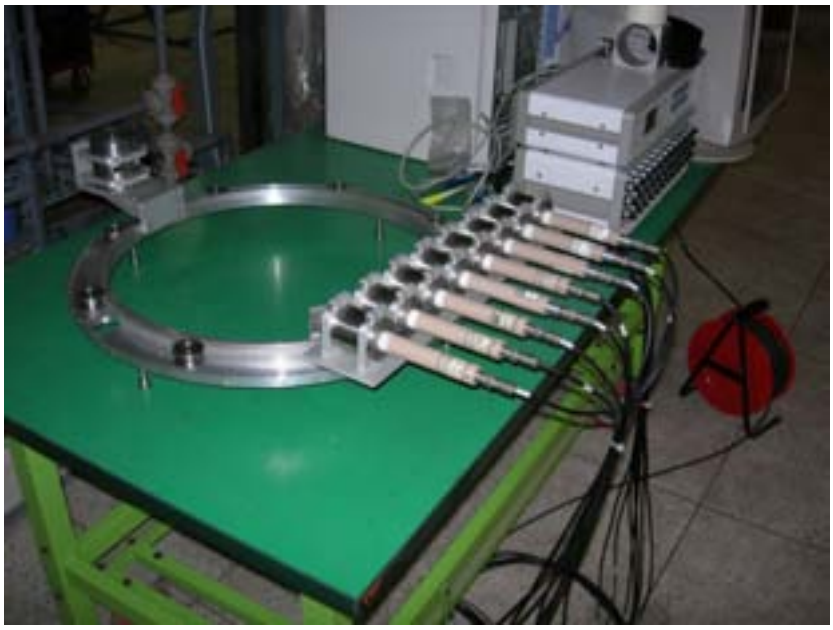

FIG. 37. The rotating scanning system for emission CT.

FIG. 38. Fixed SPECT system for dynamic measurements (l.), mounted on a trickle bed mock-up reactor (r.).

4.2. RADIOACTIVE PARTICLE TRACKING (RPT)

Design of radioactive particle tracking (RPT) depends on the interaction of the gamma rays with the materials of the detectors and of the system. In designing the RPT, it has to be considered that the position of the tracer should be “observed” with good signal to noise ratio by as many detectors as possible, to take advantage of information redundancy in the reconstruction procedures.

It is advisable to take into account the theoretical number of photopeak counts that would be recorded by a detector during a sample time interval T, form a point source of strength R placed within a dense medium. The factors determining the number of counts recorded by the detectors will be responsible for the different aspects of the design. According to Tsoulfanidis, the number of photopeak counts C can be expressed as done by Chaouki:

$$C=\frac{T\nu R(\phi\varepsilon)}{1+\tau\nu R(\phi\varepsilon)}$$

where μ is the number of gamma rays emitted per disintegration, τ is the dead time per recorded pulse, Φ is the peak to total ratio and ε is the total efficiency, defined as:

$$\varepsilon=\iint_{\Omega}\frac{\mathbf{r}\bullet\mathbf{n}}{r^3}\exp\left[(-\mu_m e_m-\mu_w e_w)(1-\exp(-\mu_d d)\right]d\Sigma$$

where r is the distance between the source and the outer surface of the detector crystal, e_m the distance travelled by the gamma ray within the dense medium where the tracer is immersed, e_w, the distance crossed through the wall and d, the thickness of the crystal in the direction given by the vector r. Ω is the subtended solid angle between detector and tracer and μ_m, μ_w and μ_d are the linear attenuations of the media, the vessel wall and the detector material, respectively.

Therefore, the most important factors to be considered for the design of a RPT facility are:

i) The characteristics of the radionucleide used for preparing the tracer (energy spectrum, half life, intensity, etc.). The choice of the radionucleide to be used and its required intensity is determined by the need to get a statistically significant number of counts by all the detectors. As tracers are generally beta-emitters prepared by neutron bombardment, purity of the radionucleide is important and enough time after activation, to let impurities decay, is required. The tracer should have a sufficient intensity to be detected by the whole array of detectors in short sample periods. However, saturation of the detector while the source is close should be avoided. It is advisable that the half life of the radionucleide used be an order of magnitude larger than the duration of the tracking experiment, to have a source with practically constant activity.

Radionuclide that have been used are ^{22}Na (2.6 yr), ^{24}Na (15.1h), ^{60}Co (5.27 y), ^{198}Au (2.69 d) and remarkably ^{46}Sc (83.3 d), due to its convenient half life and high energy gamma disintegrations (0.89 and 1.12 MeV). Less penetrative low energy gamma rays are inadequate, since the number of counts registered by detectors located far away from the source will be too low for resolving the signal from the background, and the information provided by these detectors will be lost.

ii) The solid angle subtended by the irradiated surface of the detectors as viewed by the tracer. The system should contain as many detectors as possible since they must be close in between to allow all the zones of the equipment that the tracer will inspect to be in the region of highest sensitivity of at least one detector. As far as possible, arrange the detectors in a way so that they are symmetrically distributed around the equipment.

iii) The detection efficiency, the photopeak fraction and the dead time of the acquisition system. Gamma rays undergo photoelectric absorption and Compton scattering while crossing a dense material. Build-up caused by Compton scattering of photons by the media external to the detector and single Compton scattering in the detector cause the spectrum to broaden. These effects have to be filtered since they decrease the fraction of genuine unscattered gamma rays that follow a straight line from the tracer to the detector, contributing to the photo peak fraction.

iv) The tracer features. The ideal tracer is a perfect flow follower of the motion of the phase of interest in the flow being studied. It should be compatible with the fluids or other materials involved. It should be thermally stable and sufficiently rigid and resistant. To track the solid, the tracer must have the same size, shape, and density as the rest of the solid inventory.

It should also have the same collisional properties. For fluidized systems, the tracer is frequently prepared by using one of the particles within the solid inventory, by introducing inside a small amount of the element that can be turned active by neutron bombardment, for example ^{45}Sc as Sc_2O_3. It is advisable to coat the particle with a thick polymer to protect the radioactive material from abrasion. After the coating, the tracer should match the density and shape of the rest of the solids to be fluidized. To follow the liquid, the tracer should be totally wettable, neutrally buoyant and sufficiently small to avoid low-pass filtering of high frequency fluctuations. A spray-coated polypropylene sphere, containing a tiny air hole to match the density of the liquid has been used as tracer for water.

4.2.1. Detectors distribution for RPT

The detection of radiation in computer automated radioactive particle tracking (RPT) does not use collimators and shields as accessories. Detectors are distributed all over the "observed" equipment so as to have information from every region, as illustrated in the schematic of Figure 39.

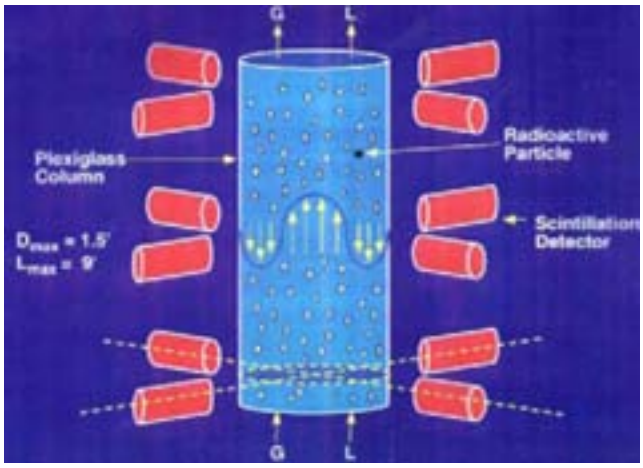

FIG. 39. Schematics of the detectors distribution in a RPT facility.

Figure 40 shows one of the RPT facilities currently in operation at the Chemical Reaction Engineering Laboratory (CREL), Washington University in St. Louis, USA.

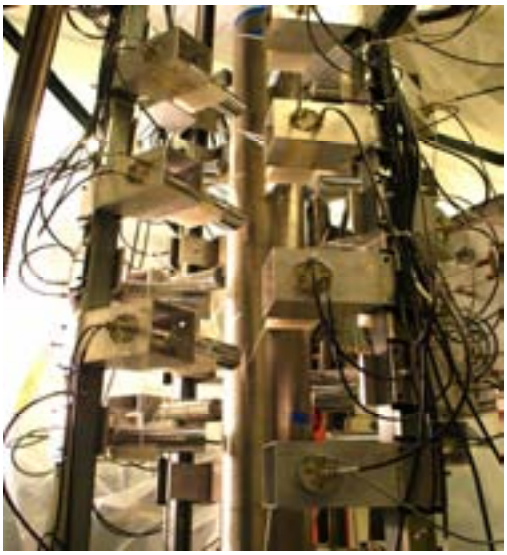

FIG. 40. Photograph of one of the CARPT facilities in the Chemical Reaction Engineering Laboratory (CREL) at the Washington University in St. Louis, USA.

A limitation to the accuracy of RPT lies in the error associated with the reconstruction of the tracer particle position, which affects the space resolution capability of the technique. This error can be reduced by choosing an appropriate distribution of the RPT detectors array, which has been largely based on experience. RPT is not an "off-the-shelf" technique that can be implemented easily on relatively large pilot plant scale equipments or even on a new system in the laboratory. There is no easy a priori assessment of the optimal experimental protocol for positioning the detectors; with any new system, a trial and error experimental procedure is normally required. An optimal protocol for implementing RPT; i.e., maximizing accuracy, minimizing cost and maximizing implementation feasibility can rely on using indicators to quantify the performance of a RPT setup (Roy et al. 2002) have proposed two such indicators, namely resolution and sensitivity, which can be used to assess the uncertainty in position reconstruction caused by the above and other less important sources of error.

Resolution, R, refers to the sphere of uncertainty around the exact particle position. It can also be viewed as the minimum distance between two neighboring positions of the tracer particle that can be discriminated as two different particle positions. Confined to the z-direction, this is expressed as:

$$R(z)=\sigma_{counts}\frac{dz}{dC}$$

where σ_{counts} refers to the variance in photon counts due to source fluctuations and the derivative represents the rate of reconstructed position change as a function of the recorded photon counts, C.

Sensitivity is the fractional change in counts recorded at the detector with a small change in position of the tracer particle. For unidirectional movement in z-direction of the tracer particle, sensitivity can be defined as:

$$S(z)=\frac{1}{C}\frac{dC}{dz}$$

Some basic recommendations given (Roy et al. 2002) for a multidetector system arrangement are:

- On a single plane, three is the optimal number of detectors to be used.
- As far as possible, detectors should be symmetrically distributed around the observed equipment.
- Rotate adjacent planes so that detectors on alternate planes are farthest from each other.
- One recommended choice is to have three detectors per plane arranged in an equilateral triangle. Locate adjacent planes 10 cm apart and stagger the triangles.
- The limits of the observed area (lower and upper) have relatively poor resolution and sensitivity; it is advisable to place a few more detectors in the vicinity of these regions.
- Although of secondary importance, the central plane of column may develop relatively poor resolution and sensitivity. This effect can be overcome by setting more detectors off central plane.

4.2.2. Calibration of detectors

Before performing the RPT experiment, calibration of all detectors used must be performed *insitu*, preferably at the same operating conditions as used in the actual experiment, to obtain the calibration curve (the relationship between intensity and the positions of the detector and the radioactive particle) for each detector. Two types of calibration methods can be used:

- *External:* calibration using an automated device with the advantage of the possibility of using a large number of calibration points (several hundreds).
- *Internal*: calibration (insitu), using an intrusive rod for holding the radioactive tracer. The advantage of this method is its simplicity and versatility to be transported and located in places of difficult accessibility. However, it provides only a few calibration points within reasonable time; this limitation requires extrapolation to more calibrations points by Monte-Carlo based simulations. It is also necessary to manually repeat the calibration for each different experimental operating condition.

4.2.3. Detector read out

Detector read out for emission tomography and RPT is equivalent to detector read out for gamma CT. The main difference with gamma CT is that, generally, due to the limitation of the injected activity, there is a strong need to maximize the efficiency of detection. This consideration has many impacts. The first one is that all the surface of the detector should be used, i.e. the aperture of the collimation should be equal to the detector section, and for RPT no collimation is used. To keep a sufficient good spatial resolution, one would design a long collimator, but limiting again the efficiency. Depending on the application, the balance must be kept between sufficiently good spatial resolution and low statistic noise (Fig. 41).

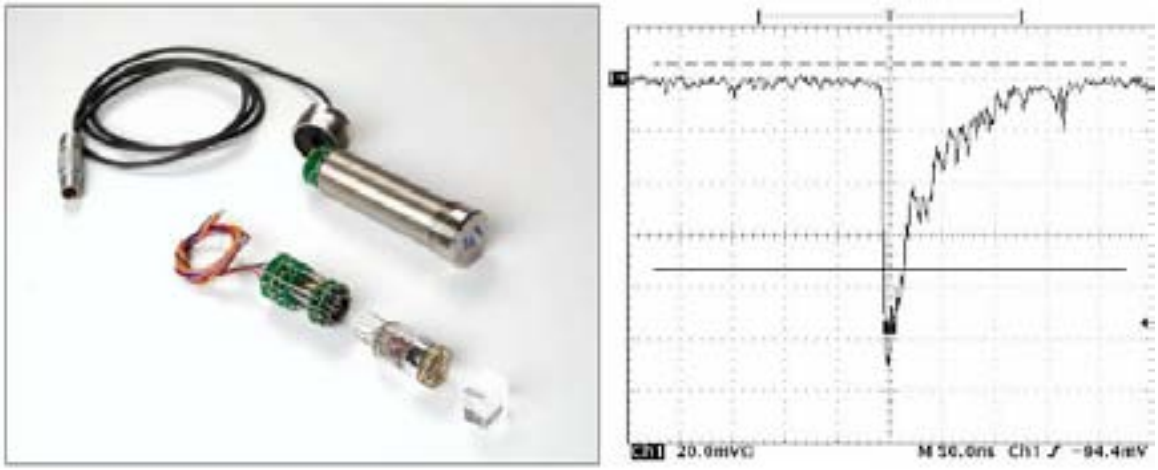

FIG. 41. LYSO scintillator (16x16x10 mm) with PMT and electronics embedded in a stainless cylinder (27x110 mm) (l.) and corresponding pulse for 662 keV photons (r.) with a duration of 50 ns for high count rates measurement.

The second impact is the selection of photons. Keeping photons in the photo peak energy range leads to sharper images, since scattering photons wide spread and enlarge the impulse response of the system, but increases also the statistic noise. Usually, then, it is worthwhile to consider lower energy threshold to increase the photon statistic, while degrading the sharpness of the image. This means that scattered photons are welcome to contribute to the image formation. For RPT, since the goal is to get the precise location of a single particle, the energy range is restricted to the photo peak region to reduce the uncertainty in the reconstruction.

A feature of detector used in SPECT experiment, like in RPT and RTD, is that the detector has to afford high gradient flux that appears when the peak of the RTD curve reaches the detector. The pulse pile up leading to counts losses have to be estimated accurately for all the detectors since it can differ from one detector to the other. In transmission measurement, the data injected in the reconstruction algorithm are calibrated by the measurements obtained with and without the phase of interest (or an equivalent in term of average Z number). In the emission case, this calibration procedure does not exist: the whole detection efficiency of each detector must be estimated accurately in properly defined conditions.

4.2.4. Collimator design

The number of detectors, their distribution and the collimator geometry define the projection matrix. The figure below presents the RMS error that can be obtained for a specific tracer distribution, depending on the number of detectors per projection and the number of projections. These results have been obtained by simulation, with free noise data. The RMS error represents the noise due to the projection matrix and the reconstruction algorithm (Fig. 42).

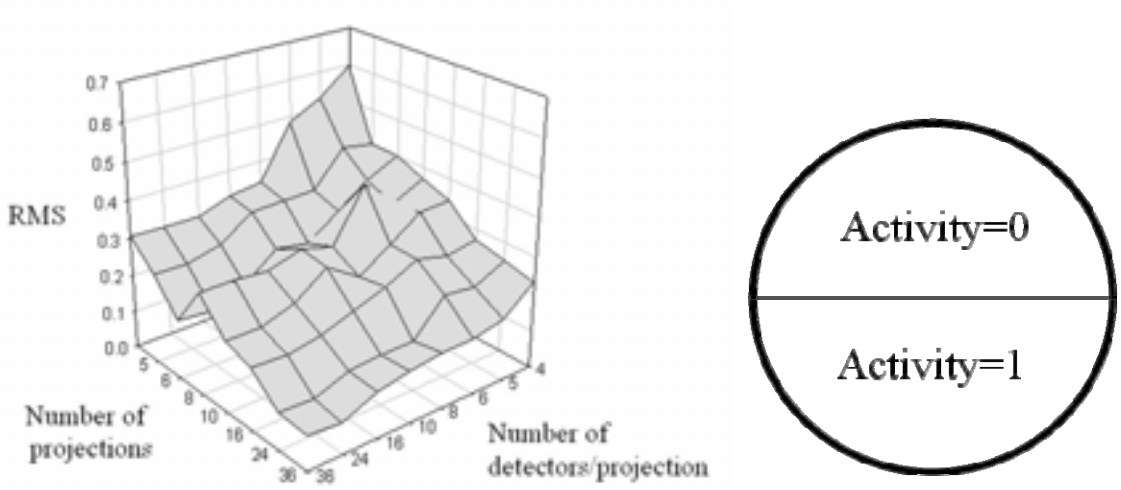

FIG. 42. Variation of RMS error with number of detectors per projection and number of projections. The phantom image used to make this evaluation looks like a stratified flow (right).

A general rule to design the collimator is to consider the profile obtained with a source moving along the diameter of the vessel, parallel to the projection, i.e. the y axis as depicted below. The relevant parameter is the FWHM of the measured profile P(y). A good criterion is to design the collimator such that:

$$1 \le \frac{FWHM \times (number\ of\ \det ectors)}{2R} \le 2$$

where R is the vessel radius.

Figure 43 shows the source displacement procedure and obtained profile from a detector located on X axis.

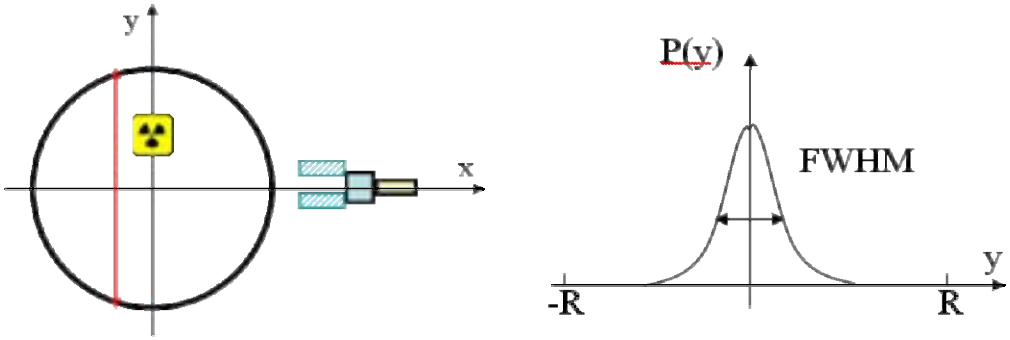

FIG. 43. Source displacement procedure (l.) and obtained profile from a detector located on x axis (r.).

4.2.5. Position reconstruction for RPT

Considering a point source in a multiphase emulsion observed externally by a detector, the intensity of the radiation detected is related to the radioactive source activity and position and to the intervening medium attenuation. Under the assumption of constant production rate for a source of constant activity, implying constant photon density, constant velocity of the photons and mono-energetic beams, the counts recorded by a detector with its crystal centered on $\mathbf{x}_d$, from a point source at $\mathbf{x}$, can be expressed as:

$$C(\mathbf{x_d}) = q(\mathbf{x})\, exp\left(\iiint_{R^3} \mu(x,y,z,t)\, \delta(l - x\cos\theta\sin\phi - y\sin\theta\sin\phi - z\cos\phi)\, dx\, dy\, dz \right)$$

where q(**x**) is the production rate of photons, x, y and z are the spatial coordinates, t is time, l is the perpendicular distance from the origin to the line joining **x** to $\mathbf{x_d}$, θ and ϕ are the angles that the perpendicular makes with the x and z axes, respectively (Fig.44), and δ is the Kronecker delta.

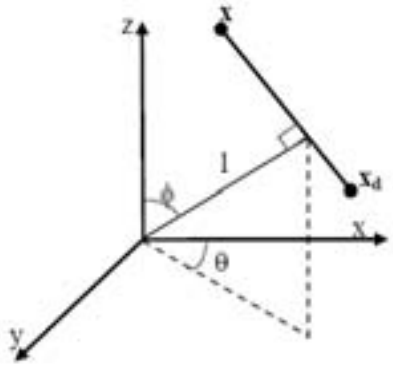

FIG. 44. Geometrical position of the tracer, x, and the center of the crystal, x_d within the reference coordinates.

The inverse problem of position rendition is to evaluate the value of **x**, given the values of $\mathbf{x_d}$ and C. Since the triple integral contains the value of **x**, an analytical solution for this inverse problem cannot be accomplished. In an actual RPT experiment, the problem is more complicated because one needs to integrate the counts or intensity values obtained along many different lines connecting the source and each detector within the solid angle subtended by the detector crystal at the source position. Moreover, the linear attenuation coefficient is a function of the distribution of the phases in the system.

In a RPT experiment, the particle is left free to move around the vessel, and the position of the particle is determined by an array of scintillation detectors that monitor the emitted γ-rays. In order to estimate the position, a calibration is performed prior to the RPT experiment by placing the tracer particle at various known locations, which yields a calibration map relating counts and particle positions for each detector. Then, with the number of counts measured by each detector during the actual RPT experiment, the inverse problem can be solved to get the instantaneous position of the particle. Time differentiation of the successive particle positions yields instantaneous Lagrangian particle velocities as a function of time and position. Hence, it is necessary to have as precise position reconstruction as possible to avoid propagation of error to the velocities and turbulence parameters.

Several methods for identification of particle position in RPT are available:

(a) Data reduction scheme
(b) Monte-Carlo model based method
(c) Neural network model based method and
(d) Cross correlation search based method.

The data reduction scheme assumes that the intensity of radiation or counts received by a detector is only proportional to the distance between the centre of the detector crystal and the tracer location (since tracer is small, it is assumed to be a point source). The calibration curve relating counts versus distance for every detector is fitted with splines. While four detectors in principle identify the tracer location exactly, due to the statistical nature of the experiments, the redundancy of detectors is required to apply the weighted least-squares method in identifying particle position.

Based on the distances obtained from the spline fit for each detector, the most probable location is identified from a weighted least-squares regression, applied to the counts registered by all detectors. This method suffers in accuracy and resolution in dense flows even after improvements due to the basic assumption that counts recorded depend only on the particle-detector distance and are independent of the geometry of the system, medium attenuation and solid angle.

The second method available is a model employing Monte Carlo simulations that accounts for the geometry and radiation effects in a RPT experiment. This method generates a very fine grid and the counts for each detector from the source located in every position within the grid are obtained from the calibration data by modelling the intervening medium attenuation with a time-averaged holdup distribution profile. In order to reconstruct the tracer particle position, experimentally obtained counts for each detector are compared to those predicted by the model for the points in the generated grid, thus searching for the best grid position with the least error between model and measured counts. A model to estimate the photopeak counts for each detector, originally proposed by Tsoulfanidis is used. This model accounts for the detector dead time; the detector total efficiencies need to be calculated using Monte Carlo simulations for given tracer positions in the reactor.

In order to estimate the total detector efficiency, one needs to evaluate the probabilities of interaction of photons with the reactor medium and with the detector crystal, and the solid angles. Several thousand directions must be sampled from Monte Carlo simulations and a statistical weight is assigned to each direction. Generation of the database for detector total efficiencies with a refined mesh is computationally expensive.

Alternate methods of approximation are discussed by Larachi and Gupta. However, the change in the medium attenuation due to the flow is either taken as a constant or estimated using a time-averaged holdup profile. A constant holdup profile, where the constants of the holdup profile are obtained by regression, introduces errors into the computationally expensive sophisticated Monte Carlo based model. This is one of the drawbacks of this method. The change in the number of counts with changes in the holdup variations can be large, particularly for gas-solid flows, preventing the use of a mean linear attenuation for gas-solid suspensions.

The third method relies on capturing the dependence of radiation intensity with position by a black-box model, employing a neural network as done by Godfroy. In this method, part of the calibration data is used as training data set to estimate the neural network constants and gain confidence while using the remaining calibration data as test to check for the accuracy achieved. The drawback of this method is that the model does not have physical significance, and employs a huge number of fitting parameters (~160) which can restrict the applicability to a narrow range. However, the method can be used for real time visualization of trajectories.

Recently, Bhusarapu has proposed another procedure that uses a cross correlation based search algorithm for locating the tracer particle position, and a semi-empirical model relating the counts recorded (C) to the position of the emitting tracer particle (**x**), accounting for the geometry and radiation effects. Prior to the actual RPT experiment, detectors are calibrated by placing the particle at various known locations and obtaining the counts for all the detectors (typically, N_d = 16 to 30) at the required operating condition. Hence, each calibration position is mapped to a unique series of counts recorded on N_d detectors. Conversely, an inverse mapping should exist relating a series of counts at N_d detectors to a unique position. Such an inverse mapping will exist if, and only if, the mapping is one-to-one. This is the premise on which a RPT experiment is founded.

Considering the series of counts obtained on all detectors at a given tracer particle location during calibration $\{C_{calib}(i): i = 1, N_d\}$, and a similar series of counts obtained during the actual experiment at a given instant $\{C_{run}(j): j = 1, N_d\}$, the zero lag of the cross-correlation between these two series provides an estimate of how well the counts from the corresponding detectors match. As the zero lag of the cross-correlation function is the auto-correlation function, the key property exploited here is that the auto-correlation function always peaks at the zero lag.

Hence, when the zero lag of the normalized cross-correlation function equals one, the unknown tracer position during the run at that instant is quite close to the calibration position. Therefore, the approach to finding an unknown tracer position is reduced to matching the counts series from that position received by detectors, to the counts received from known calibration positions.

The values for the cross-correlation function are found for the *k* calibration positions. The nearest known location is identified to be the calibration position where the cross-correlation peaks. This gives the best estimate of the closest known position. Further refinement of this position is performed in a second step by searching around this "initial best estimate" (IBE). All the nearest neighboring positions in the calibration map around this identified IBE of tracer location are located to form a closed surface with the identified IBE of tracer location at the centre. Using a model for the counts, the mesh is refined within this closed surface and a similar search procedure is followed iteratively until the convergence criterion is met. The details about the mesh refinement and the iterative procedure can be consulted in Bhusarapu' paper given in the bibliography. The model for the photopeak counts is obtained by modeling the total efficiency of the detector, defined as the probability that γ-rays will emerge from the reactor without scattering and will interact with the detector. The model used for counts recorded (C) is given by:

$$C=\frac{k_1}{d^2}exp\left(\left(-k_2 d_x - k_3 d_y - k_4 d_z\right)\left(1-exp(-\mu_d k_5)\right)\right)$$

where d_x, d_y and d_z are the x, y and z directional distances between any position in the reactor and the centre of the detector crystal, d is the distance between the tracer position and the centre of the detector crystal, μ_d is the attenuation coefficient for the detector material, and $k_{1,2,3,4,5}$ are constants. The second step provides a new calibration set at a refined mesh level and the cross-correlation based search for the "best position estimate" is resumed within this refined mesh. Steps one and two are alternatively followed to meet a convergence criterion.

In the counts-position model given by the equation above, the solid angle subtended by the detector at any location, varying over small displacements (within the sphere of nearest neighbors) was modeled as k_1/d^2, where k_1 corresponds to the view area of the detector from that position.

The exponential terms in the three directions correspond to the attenuation due to the medium between the tracer location and the detector, and the constants $k_{2,3,4}$ correspond to the effective mass attenuation coefficients in the three directions. Following Chaouki the probability of interaction of these γ-rays inside the crystal of the detector is modeled as $\left(1-exp(-\mu_d k_5\right)$, where k_5 corresponds to the length of the ray along the crystal, assumed to be a constant within the sphere of nearest neighbors. Constants are found by an optimization method within the sphere of nearest neighbors.

4.2.6. Analysis of RPT data

The relevance of RPT relies in its capability of measuring key hydrodynamic parameters for multiphase flows under conditions where all other techniques fail. Hence, it is the best tool to validate CFD models. Parameters of interest include local instantaneous and average velocities, structural boundaries in the flow, such as in core-annulus flow, features of the flow fluctuations, like eddy diffusion coefficients and turbulence intensities, turbulent shear stress, etc.

Therefore, typical analysis of RPT data involves calculation of instantaneous velocities to get features of the traced phase motion from Eulerian and Lagrangian approaches. The reactor is first divided into sampling compartments depending on the column diameter and the height of the expanded liquid when in operation. Each instantaneous velocity is evaluated from two sequential particle positions and assigned to the compartment into which the mid-point of the two positions falls, as described in the Figure 45.

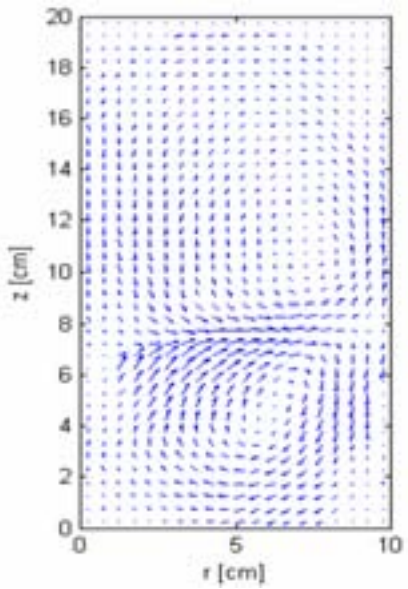

FIG. 45. Velocity vector plot: 1% Solids, 1000 RPM.

The velocity vector is given by the time derivative of the particle position vector (i.e. particle trajectory), assuming that the particles travels in a straight line between the two successive points considered. To construct the velocity map, the time averaged velocities are computed from the number of instantaneous realizations that are obtained for each compartment over the time the experiment is carried out (typically 12-15 hours).

As an example, the time-averaged solids velocity vector plot in a solid-liquid stirred tank obtained using RPT is shown in Figure 45. The overall solids holdup is 1% and the impeller used is Rushton turbine rotating at 1000 RPM. The radial solids jet from the impeller and the two circulating loops, one above and one below the impeller, characteristic of radial impeller driven flow.

TABLE IV. TYPICAL APPROACHES TO CALCULATE HYDRODYNAMIC PARAMETERS FROM RPT (1/2).

Eulerian

1. Instantaneous tracer coordinates at instants "t_i" and "$t_i + T$":

Cartesian: $\mathbf{x}_i = (x_i, y_i, z_i)$ and $\mathbf{x}_{i+1} = (x_{i+1}, y_{i+1}, z_{i+1})$

Cylindical: $\mathbf{x}_i = (r_i, \theta_i, z_i)$ and $\mathbf{x}_{i+1} = (r_{i+1}, \theta_{i+1}, z_{i+1})$

2. Coordinates of the assigned mid-point:

Cartesian: $\mathbf{x}_m = (x_m, y_m, z_m) = \frac{1}{2}(x_i + x_{i+1}, y_i + y_{i+1}, z_i + z_{i+1})$

Cylindical: $\mathbf{x}_m = (r_m, \theta_m, z_m) = \left(\sqrt{x_m^2 + y_m^2}, \mathrm{atan}(y_m / x_m), z_m\right)$

3. Local instantaneous velocities assigned to the grid cell j that contains the middle point:

Cartesian: $\mathbf{u} = \mathbf{u}(\mathbf{x_j}) = (u_x, u_y, u_z) = \frac{1}{T}(x_{i+1} - x_i, y_{i+1} - y_i, z_{i+1} - z_i)$

Cylindical: $\mathbf{u} = \mathbf{u}(\mathbf{x_j}) = (u_r, u_\theta, u_z) = \frac{1}{T}(r_{i+1} - r_i, r_m(\theta_{i+1} - \theta_i), z_{i+1} - z_i)$

4. Local time(ensemble)-averaged velocity for the grid cell j, in the case of P events:

$$\left\langle \mathbf{u}(\mathbf{x_j}) \right\rangle = \frac{1}{P}\sum_{k=1}^{P} \mathbf{u}(\mathbf{x_j}) = \frac{1}{P}\sum_{k=1}^{P} \mathbf{u}(x_j, y_j, z_j)$$

5. Eulerian fluctuating velocities:

$$\mathbf{u'}(\mathbf{x_j}) = \mathbf{u}(\mathbf{x_j}) - \left\langle \mathbf{u}(\mathbf{x_j}) \right\rangle = \mathbf{u'}(x_j, y_j, z_j) = \mathbf{u}(x_j, y_j, z_j) - \left\langle \mathbf{u}(x_j, y_j, z_j) \right\rangle$$

The fluctuating velocity components are obtained by subtraction of the mean velocities from the instantaneous velocities. The Root Mean Square (RMS) velocities are then computed as described in the Tables IV and V, and the intensity and kinetic energy of turbulence can also be computed from the fluctuating velocities. The stress tensor is symmetric and consists of the normal and shear components, which are computed considering the occurrences in each cell within the column, and then averaging the product over all occurrences.

TABLE V. TYPICAL APPROACHES USED TO CALCULATE HYDRODYNAMIC PARAMETERS FROM RPT (2/2).

Lagrangian

1. Mean position calculated from P events crossing through a grid cell j at a given instant. Crossing instants $t_{0,k}$ are considered as an initial time t_0:

$$\Xi_0 = \frac{1}{P}\sum_{k=1}^{P}(\mathbf{x}_k) = \frac{1}{P}\sum_{k=1}^{P}(x_k, y_k, z_k)$$

2. Excess displacement with respect to □ for a relative time $t > t_0$:

$$\mathbf{X}(\Xi_0, t) = \mathbf{x}(\Xi_0, t) - \Xi_0$$

3. Instantaneous Lagrangian velocities calculated from the trajectories corresponding to the P events considered to calculate □t is generally one sample period T for the approximations to be valid):

$$\mathbf{v}(\Xi_0, t) = \left(v_r(\Xi_0, t), v_\theta(\Xi_0, t), v_z(\Xi_0, t)\right) = \frac{1}{(t - t_0)}\left[\mathbf{x}(\Xi_0, t) - \mathbf{x}(\Xi_0, t_0)\right]$$

4. Ensemble-averaged Lagrangian velocity for □:

$$\left\langle \mathbf{v}(\Xi_0, t) \right\rangle = \frac{1}{P}\sum_{k=1}^{P}\mathbf{v}(\Xi_0, t)$$

5. Fluctuating Lagrangian velocities:

$$\mathbf{v}'(\Xi_0, t) = \mathbf{v}(\Xi_0, t) - \left\langle \mathbf{v}(\Xi_0, t) \right\rangle = \left(v_r'(\Xi_0, t), v_\theta'(\Xi_0, t) v_z'(\Xi_0, t)\right)$$

6. Root mean square (RMS) velocities:

$$\mathbf{v}_{RMS} = \sqrt{\frac{1}{P}\sum_{k=1}^{P}\left(\mathbf{v}'(\Xi_0, t)\right)^2}$$

7. Turbulent Reynolds stress tensor:

$$\left\langle \mathbf{v}'(\Xi_0, t) \cdot \mathbf{v}'(\Xi_0, t) \right\rangle = \frac{1}{P}\sum_{k=1}^{P}\mathbf{v}'(\Xi_0, t) \cdot \mathbf{v}'(\Xi_0, t)$$

Normal: $\left\langle v_r' v_r' \right\rangle = \frac{1}{P}\sum_{k=1}^{P}\left(v_r'(\Xi_0, t) v_r'(\Xi_0, t)\right)$; $\left\langle v_\theta' v_\theta' \right\rangle$; $\left\langle v_z' v_z' \right\rangle$

Shear: $\left\langle v_r' v_\theta' \right\rangle = \frac{1}{P}\sum_{k=1}^{P}\left(v_r'(\Xi_0, t) v_\theta'(\Xi_0, t)\right)$; $\left\langle v_r' v_z' \right\rangle$; $\left\langle v_\theta' v_z' \right\rangle$

7. Intensity of turbulence

Radial: $I_r = \frac{\sqrt{\left\langle (v_r')^2 \right\rangle}}{\left\langle v_r \right\rangle}$ Axial: $I_z = \frac{\sqrt{\left\langle (v_z')^2 \right\rangle}}{\left\langle v_z \right\rangle}$

8. Turbulent kinetic energy:

$$k = \frac{1}{2}\left[\left\langle (v_r')^2 \right\rangle + \left\langle (v_\theta')^2 \right\rangle + \left\langle (v_z')^2 \right\rangle\right]$$

Finally, the radial and axial dispersion coefficients can also be calculated as:

$$D(\mathbf{x}) = v_{RMS} T_L$$

where $\mathbf{v}_{RMS}$ is the root mean square (RMS) velocity calculated from the Lagrangian fluctuating velocities in the direction under consideration, and T_L is the Lagrangian integral time scale, defined by:

$$T_L = \frac{\int_0^\infty t' R_L(\mathbf{x},t')dt'}{\int_0^\infty R_L(\mathbf{x},t')dt'}$$

and the autocorrelation coefficient, $R_L(\mathbf{x},t')$, is defined as:

$$R_L(\mathbf{x},t') = \frac{\langle v'(\Xi_0,t)v'(\Xi_0,t+t')\rangle}{(v_{RMS})^2}$$

The autocorrelation of Lagrangian fluctuating velocity is obtained from CARPT experiments for each coordinate by:

$$\langle v'(\Xi_0,t)v'(\Xi_0,t+t')\rangle = \frac{1}{P}\sum_{k=1}^{P}\left(v'(\Xi_0,t)v'(\Xi_0,t+t')\right)$$

where P is the number of statistically independent experiments observed in the given compartment.

Thus, the RPT technique provides useful insights into the flow pattern of the reactor being studied along with information that quantifies the mean flow field, fluctuating flow field, and the turbulent parameters. Given the complex, and generally chaotic, characteristics of the multiphase flows tracked, alternative analyses have also been conducted to get further insight in the dynamical features of the motion of the traced phase, using tools borrowed from the theory of nonlinear dynamics, symbolic dynamics and from the theory of information.

4.2.8. EM-ML algorithm for SPECT reconstruction

The ML-EM probabilistic method was initiated in 1982 by Shepp and Vardi for the reconstruction of TEP images. It was then applied for tomography by transmission by Lange in 1984 et finaly in SPECT by Miller in 1985. In a general way, the reconstruction by iterative methods consists in searching an estimator who minimizes an error between calculated projections and acquired projections, for instance in the quadratic form:

$$\varepsilon = \|y - A\lambda\|^2$$

λ is estimated by minimizing this error at each iteration. Due to the Poisson noise in *y*, the ML-EM algorithm minimizes the quadratic error by maximizing the likelihood, eg the probability that the estimated activity distribution *f* produces the acquired projection. For computational consideration, the log-likelihood is used instead of the likelihood. Its expression is given as follow :

$$\ln(L(\lambda)) = \sum_j \left\{ -\sum_i A_{ij}\lambda_j + y_i \ln\left(\sum_i A_{ij}\lambda_j\right) - \ln(p_j!) \right\}$$

The ML-EM algorithm is given by:

$$\lambda_i^{n+1} = \lambda_i^n \frac{1}{\sum_i A_{ij}} \sum_j A_{ij} \frac{y_j}{\sum_i A_{ij}\lambda_i^n}$$

λ_i^n is the estimated activity in pixel i for iteration n.

Thus, the estimation of the distribution of λ in iteration n+1 is calculated from the estimation in the iteration n multiplied by a corrective factor. Main properties of this algorithm are conservation of positivity of the solution, conservation of the number of events, i.e. detected photons. The stopping criteria is important because divergence can be obtained after a given number of iterations, depending on the statistics in data, the geometry and the number of detectors in the experiment. It means that the algorithm reconstructs mainly the noise in the data. During first iterations, low spatial frequencies are reconstructed. It means that balance has to be finding between the possible reconstructed frequency and "noise" reconstruction. Statistical criteria might be used like the distance between the experimental values y_j and the «reprojected» data $y_j^{rec} = \sum_i A_{ij} \lambda_i^n$. The iterations are stopped if y and y^{rec} are statistically equal.

5. PHANTOM TESTS

5.1. STANDARD PHANTOMS FOR INDUSTRIAL GAMMA CT

Normally a gamma CT system should be calibrated with a standard specimen, so called "phantom". In contrast to medical CT, where there is a medical phantom designed according to the shape and density of human body, in industrial process tomography there is no standard phantom. In industrial field the object or process can be everything. Nevertheless, in chemical and petrochemical industries the most spread are oil and gas, plastics and polymers, water and air, as well as metallic constructions. A typical standard phantom is presented in the fig. 46. The phantom is composed of solid polypropylene with 400 mm diameter with two 50 mm diameter holes.

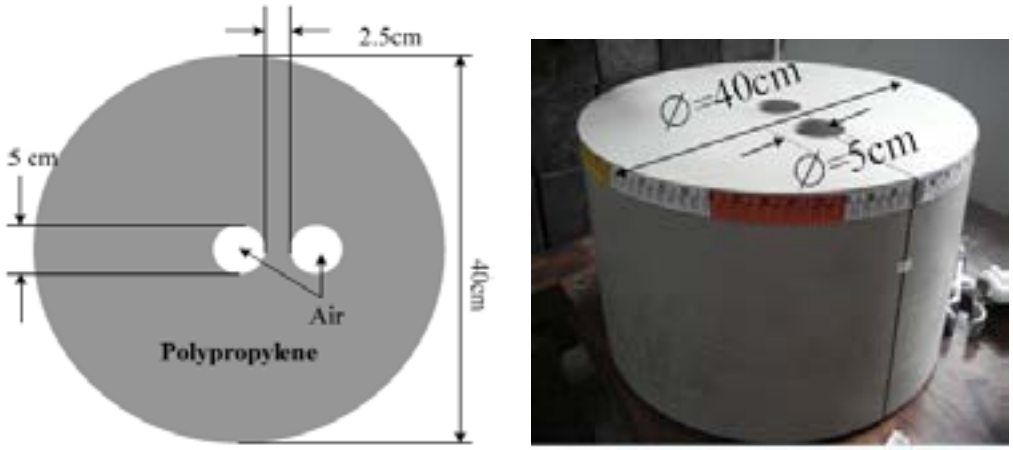

FIG. 46. A typical standard phantom.

Experiments were carried out with several data acquisition or counting times separated with one order of magnitude, such as 10 ms, 100 ms, 1 s, 10 s and 100s. This allows studying the effect of Poisson noise on the results. The images were reconstructed on a square pixel grid of 16×16, 32×32, 64×64 or 128×128.

For the sake of comparison it was recommended to use several reconstruction algorithms:

- Algebraic Reconstruction Technique (ART)
- Multiplicative ART (MART)
- Iterative Least Square Technique (ILST)
- Maximum Likelihood - Expectation Maximization (ML-EM)

For quantification of the results two error specifications were employed, which seem to be developed as some sort of standard:

1. The Root Mean Square Error with respect to N:

$$RMSE_N = \sqrt{\frac{\sum_{i=1}^{N}(\mu_{true,i} - \mu_{reconstructed,i})^2}{N^2}}$$

2. The Root Mean Square Error with respect to μ:

$$RMSE_\mu = \sqrt{\frac{\sum_{i=1}^{N}(\mu_{true,i} - \mu_{reconstructed,i})^2}{\sum_{i=1}^{N}\mu_{true,i}^2}}$$

Here $\mu_{true,i}$ are true pixels values and $\mu_{reconstructed,i}$ the reconstructed ones. N is the total number of pixels.

These errors were plotted as a function of counting time. This gave an indication of how much the Poisson counting error and the reconstruction error contributes to the total error.

5.2. TEST OF CRP PARTICIPANTS' LABORATORIES

In order to make it possible to compare test results and thus study effects of geometries and hardware set-up of different gamma-ray transmission tomography systems, a standard phantom has been defined to be used as reference (Figure 47). The phantom is made of polypropylene which has a density of 0.91 g/cm^3, and it has two holes drilled in it which either can be empty under test, of filled with another material Because different systems are designed for different process vessel diameters, positions and diameters of these holes are specified relative to the phantom diameter. The mechanical workshop at Department of Physics and Technology at the University of Bergen (Norway) was in charge of the phantom production. A total of 10 phantoms were produced for the participating laboratories with specifications as given in table VI.

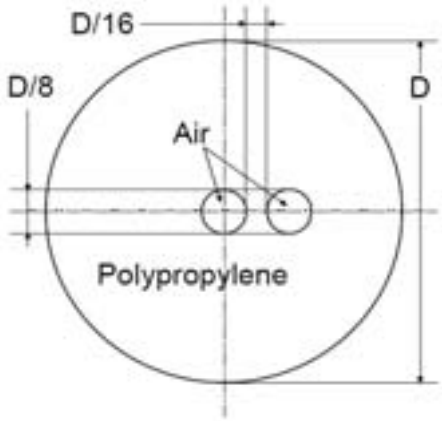

FIG. 47. Definition of the IAEA standard phantom for the experiments.

TABLE VI. PHANTOM SPECIFICATION FOR THE DIFFERENT LABORATORIES:

Test laboratory	Diameter [cm]	Length [cm]	Volume [cm^3]	Tolerance specification
Brazil	40	22	27 646	h10, 0/-0.23, D/8=50, D/16=25
Czech Republic	30	22	15 551	h10, 0/-0.21, D/8=37.5, D/16=18.75
France	50	22	43 197	h10, 0/-0.25, D/8=62.5, D/16=31.25
Republic of Korea	40	22	27 646	h10, 0/-0.23, D/8=50, D/16=25
Malaysia	45	22	34 989	h10, 0/-0.25, D/8=56.25, D/16=28.125
Norway	8	22	1 106	h10, 0/-0.12, D/8=10, D/16=5, D/16=5
Poland	6.99	22	844	h10. 0/-0.12, D/8=10, D/16=5, D/16=5
	8	22	1 106	h10, 0/-0.12, D/8=8.74, D/16=4.37
Mexico	8	22	1 106	h10, 0/-0.12, D/8=10, D/16=5, D/16=5
USA	20.32	22	7 134	h10, 0/-0.185, D/8=25.4, D/16=12.7

Because the number of design variables in gamma ray and capacitance tomographs is very high, certain limitations were agreed on to limit the experiment, and also to enable comparison. The intention was not that all laboratories should carry out everything as specified below:

- No vessel wall material is to be used in the standard tests, i.e. measurements are carried out on naked phantoms.
- All participants use the tomography systems they have. Those who have mechanical systems which allow the number of sources (views) and detectors (ray-sums) to be chosen, may agree on a common geometry for the test.
- All systems must be calibrated without the phantom present and with a "full" phantom. For the latter the holes in the phantoms should be filled by rape seed oil which has density about similar polypropylene. To limit the error of this approach it is possible to do several "full" phantom calibrations and rotate the phantom 90° between each. In this way there are be measurements available with all beams in the polypropylene only. The errors in doing this will be related to mechanical precision (which always will be present in scanning systems) and to difference in scatter contribution from the holes. The latter will be negligible since these are filled with oil with almost similar density as polypropylene.
- Experiments should be carried out with several data acquisition or counting times separated with one order of magnitude, such as 10 ms, 100 ms, 1 s, 10 s and 100s. Exactly which times to use, depends on the activity of the source. This will allow us to study the effect of Poisson noise on the results.
- The images should be reconstructed on a square pixel grid of 16×16, 32×32, 64×64 or 128×128. The true value of the attenuation coefficient (or dielectric permittivity) of each and every pixel may then be calculated form the fractional area covered by air/ polypropylene when the grid is projected onto the phantom cross section.

5.2.1. Brazil

1. Experimental setup.

A first generation parallel beam computed tomography (CT) scanner system was used for the experiments carried out using an IAEA standard phantom composed of solid polypropylene of 400 mm diameter with two holes, designed and prepared by the University Bergen. The computed tomography (CT) scanner system consisted of a NaI(Tl) detector with a 5.08 cm diameter and an encapsulated ^{60}Co radioactive source located opposite to the center of the detector.

The detector and the source were mounted on a fixed support and the phantom can be rotated and dislocated by two stepper motors controlled through a microprocessor. The detector side collimator provides 5mm width collimated gamma rays to the detector. In each movement, the phantom rotates 6°. The experimental setup, schematically shown in Figure 48 was developed to study the IAEA phantom (diameter 400 mm).

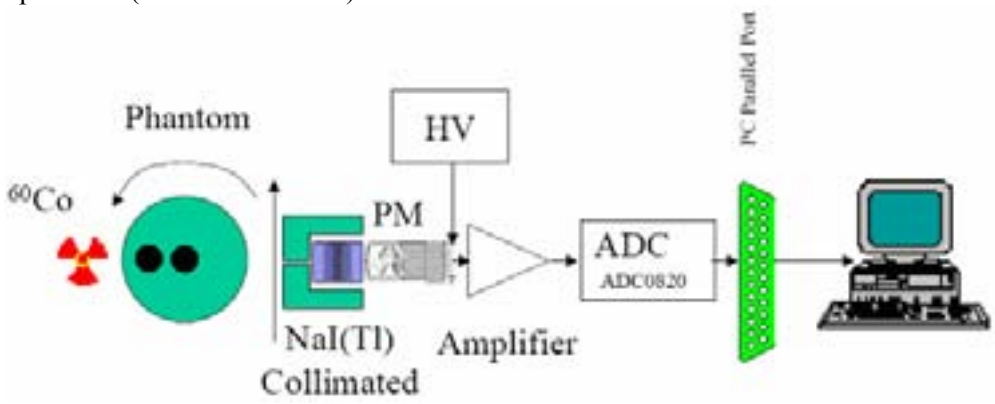

FIG. 48. Schematic diagram of the computed tomography.

Figure 48 shows the data acquisition board and the mechanical control developed and used in this CT system. The data acquisition board is constituted of two 8 bit ADC with corresponding to 256 channels positions (0 to 5V) for each one. It can be used versatility for multipurpose applications, so that, it can be used for one detector (CT1st) version, a multi-detector array (1 board for each 2 detectors) or as well as in linear detector CT with a position sensitive detector (CTLD).

For the optimization of the ^{60}Co source activity, the source activity suitable was calculated using JANU simulation software. For this phantom, the minimal effective required activity was 12.02 MBq with a confidence level of 95 % and 1% relative error for 10s counting time. The reconstruction algorithm used was the filtered back projection technique and was developed in the MATLAB code. The software uses the filtered back-projection algorithm to perform the inverse Radon transform for parallel projection data. The filter is designed directly in the frequency domain and then multiplied by the FFT of the projections. The projections are zero-padded to a power of 2 before filtering to prevent spatial domain aliasing and to speed up the FFT. The computational program reconstructs the image from projection data in two-dimensional array using a matrix where the columns are parallel beam projection data for different angles (in degrees) at which the projections were taken. The software assumes that the center of rotation is the center point of the projections. Linear interpolation and the cropped Ram-Lak are used in this software.

2. Results and discussion

The results are showed in the following reconstructed tomograms cases including the root mean square errors (RMSE) respective to N (total pixels number) and μ (attenuation coefficient) and the specific conditions. In all cases 0.5 cm lead collimators for the source and the detector were used. The experiments were carried out with the phantom holes empty and filled with materials of different densities.

Figure 49 represents sinogram examples in 2D and 3D for the results obtained from the IAEA standard phantom with the holes empty, here named Case 1.

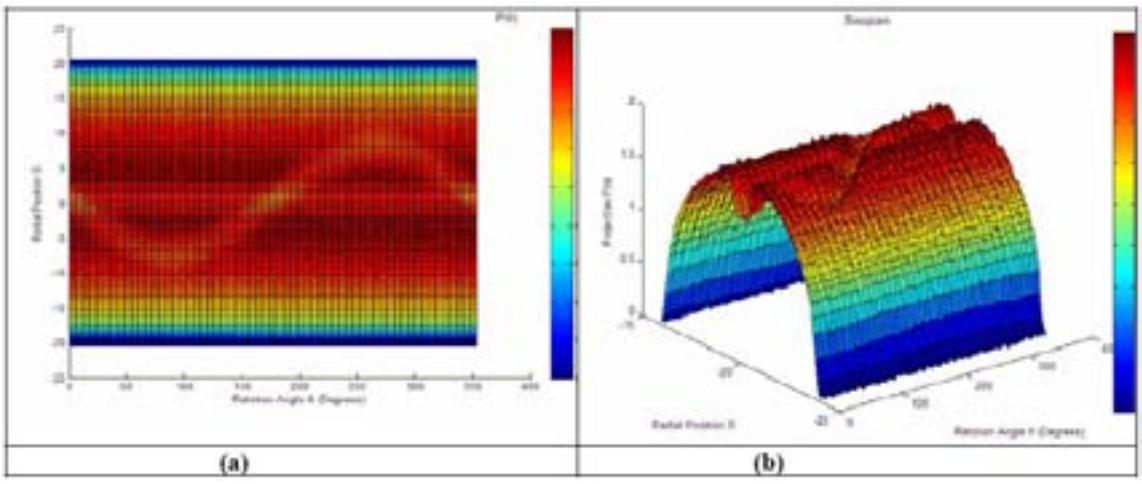

FIG. 49. Example of sinogram surface plots in 2D (a) and 3D (b) for empty holes.

Figure 50 shows the reconstructed tomograms of the phantom with air, rape seed oil and lead. For all measurements shown in this figure, the counting time for each rotation was 15 s, the rotation angle was 6° and lead collimator width was of 0.5 cm.

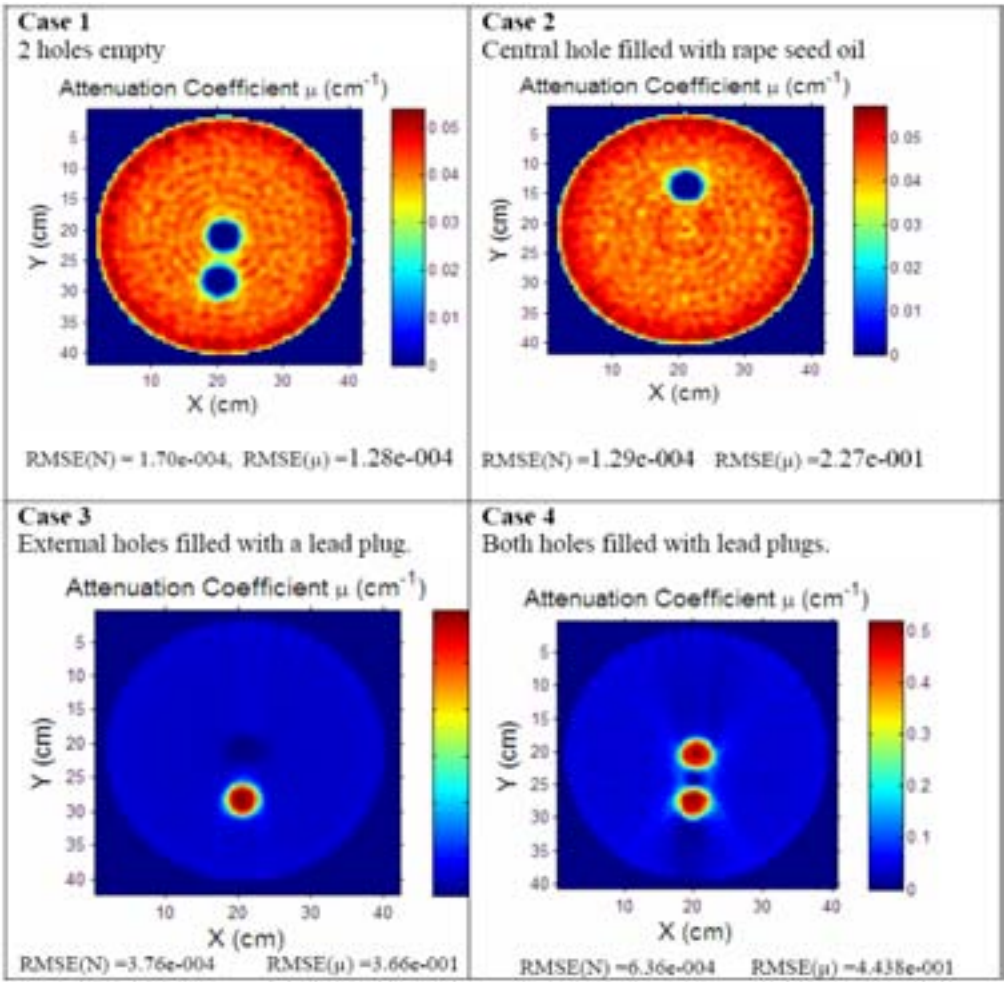

FIG. 50. Reconstructed images of the standard phontom filled with different density materials.

Table VII summarizes the root mean square errors for all reconstructed images, while Table VIII presents the values of the attenuation coefficient obtained experimentally compared to the theoretical values.

TABLE VII. ROOT MEAN SQUARE ERRORS (RMSE) RELATED TO N (TOTAL PIXELS NUMBER) AND μ (ATTENUATION COEFFICIENT).

Materials used to fill phantom holes	RMSE(N)	RMSE(μ)
Air (empty)	1.7045 e-004	1.2864 e-004
Oil	1.2864 e-004	2.2710 e-001
Lead (one)	3.7587 e-004	3.6584 e-001
Lead (two)	6.3555 e-004	4.4298 e-001

TABLE VIII. ROOT MEAN SQUARE ERRORS (RMSE) RELATED TO N (TOTAL PIXELS NUMBER) AND μ (ATTENUATION COEFFICIENT)

Materials used to fill phantom holes	Linear Attenuation Coefficient	
	Experimental Value (cm^{-1})	Theoretical Value (cm^{-1})
Oil	0.055	(0.0572)*
Lead	0.649	0.669
Polypropylene	0.055	0.0572

* Considered the same theoretical value of the Polypropylene

A good resolution was observed for all images, as shown in Figure 51. The density of the rape seed oil used was determined as being 0.92 ± 0.01 g/cm^3, which is similar to 0.91g/cm^3 of the polypropylene used for the phantom. As expected, the attenuation found for the oil was the same of the polypropylene (Table VIII). The attenuation coefficient found experimentally for the air, lead and polypropylene are comparable to the theoretical values described in the literature for these materials [8]. Figure 51 shows the surface reconstructed tomogram from the results obtained for the phantom with holes empties.

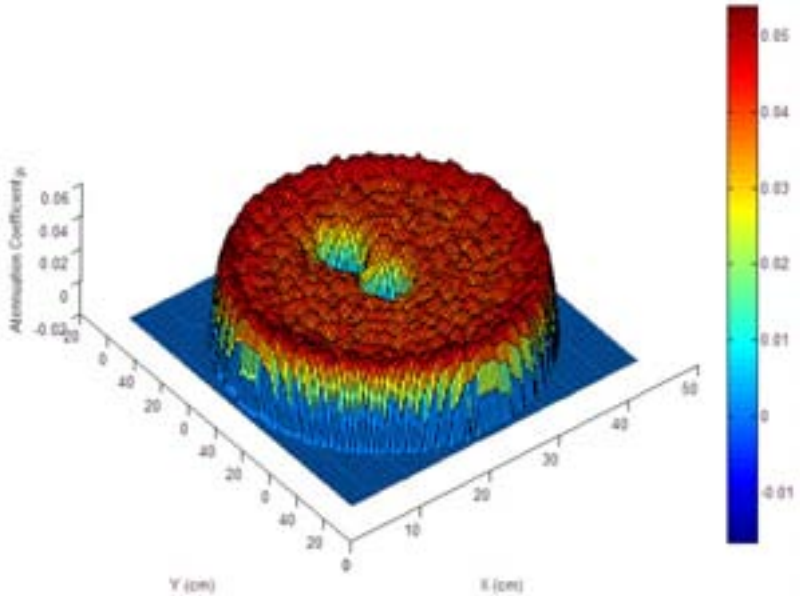

FIG. 51. An example of surface reconstructed tomogram.

Figure 52 shows the tomograms obtained for phantom with external hole filled with a lead plug measured at different counting times.

Case 1 Counting Time: 5 s	**Case 2** Counting Time: 15 s	**Case 3** Counting Time: 20 s
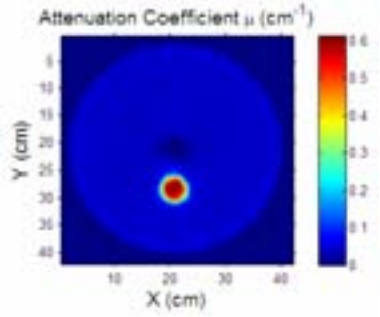	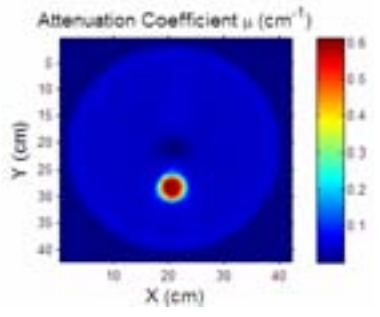	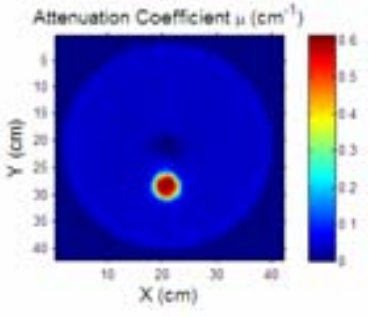
RMSE(N)=4.2045e-004 RMSE(μ) = 3.9864e-001	RMSE(N)=3.7587e-004 RMSE(μ)=3.6584e-001	RMSE(N) =3.7868e-004 RMSE(μ) =3.6955e-001

FIG. 52. Reconstructed images of the Standard phantom at different counting time.

As it can be observed in Figures 53 and 54 the error was higher for the image with counting time of 5s compared to that of 15s and 20s.

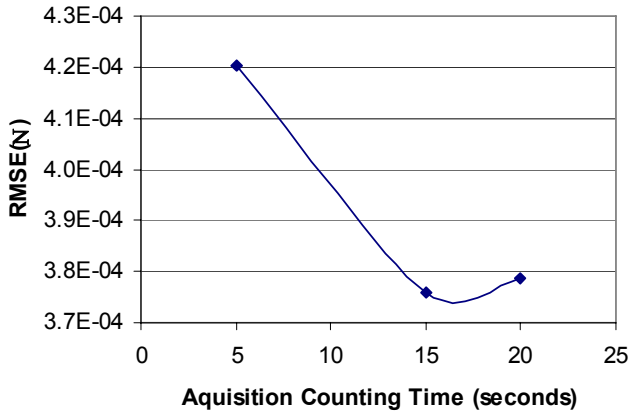

FIG. 53. RMSE errors related to the pixel total number (N) as a function of couting time.

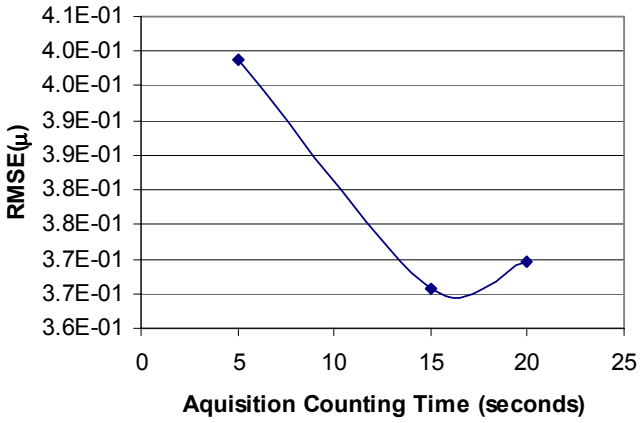

FIG. 54. RMSE errors related to the attenuation coefficient (μ) as a function of counting time.

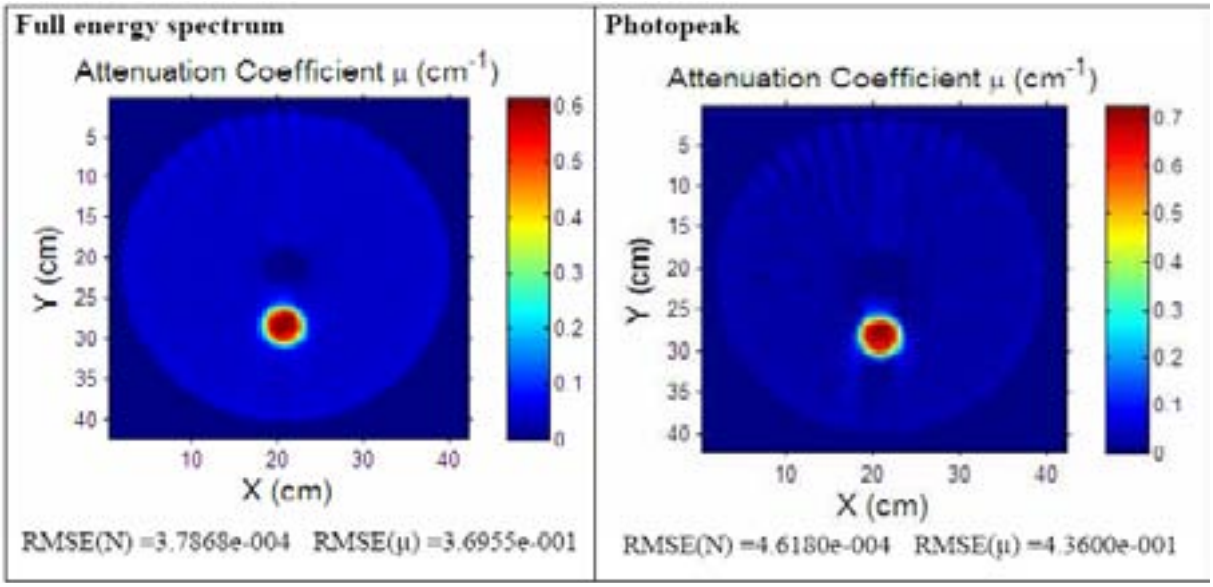

FIG. 55. Reconstructed images of the standard phantom in photopeak and all energy.

Figure 55 presents the reconstructed tomograms obtained from the results of measurements carried out selecting only the photopeak region and compared to the image reconstructed from the results obtained from full energy spectrum. No significant result was observed for both images. The image obtained for photopeak region could be improved, using a source with higher activity.

3. Additional plots

Figures 56, 57 and 58 show the plots of 3D- volumetric reconstructions using different 2D slices data under the same conditions. The images were reconstructed with the box – Gaussian convolution kernel smoothing voxel method.

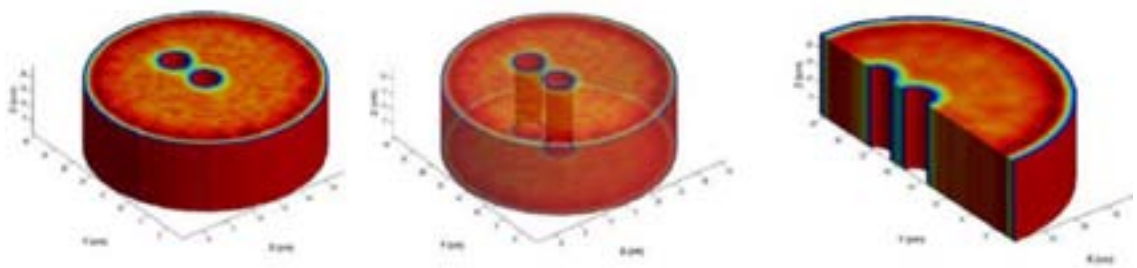

FIG. 56. IAEA Standard phantom with empty holes using 3D image reconstruction, b) transparent 3D image reconstruction, and c) cross sectional 3D image reconstruction.

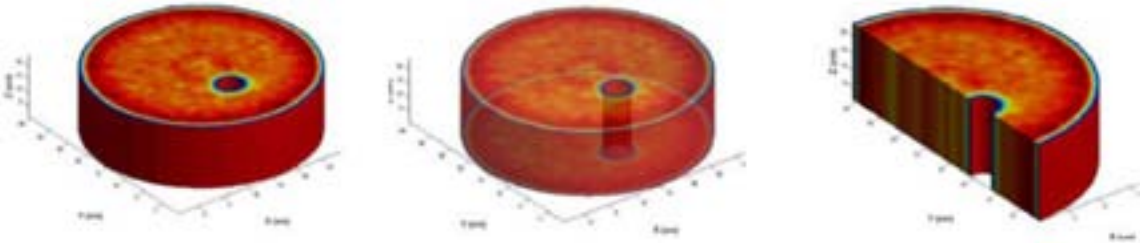

FIG. 57. IAEA Standard phantom with empty hole and one filled with oil using 3D image reconstruction, b) transparent 3D image reconstruction, and c) cross sectional 3D image reconstruction.

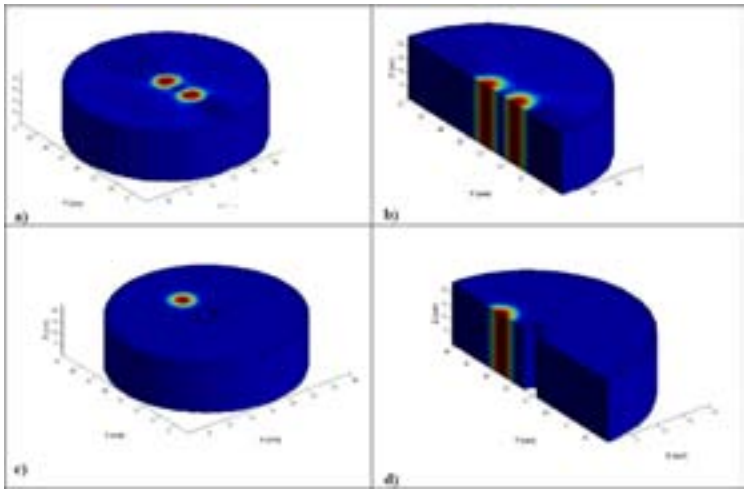

FIG. 58. IAEA Standard phantom with both holes filled with lead (a and b) and one hole filled with lead and one empty (c and d) using 3D image reconstruction.

5.2.2. Czech Republic

1. Introduction

The procedure of analytical transmission tomography (ATT) was tested on a phantom of polypropylene drum with two empty tubes. The positions and diameters of the tubes are evaluated by suggested analytical model used in reconstruction procedure. The comparison of the results with known reality were done with experiments which were realized for different counting time and different sequence of rotation of basic system with seven detectors and two collimated sources. As even simple models for discontinuity regions have more than three constants the values of which have to be identified by optimization procedure, more than seven positions of gamma beams will be needed.

If the stability of the discontinuity regions can be assumed, the simple way of increasing number of beams can be realized by rotation of the measured system that is by rotation of fixed configuration of two collimated sources and seven detectors. It is suitable to situate the middle of rotation out of the middle of object when it is not known whether the discontinuity is in the middle of the object. Results are presented as figures presented real and reconstructed dimensions and positions of the holes and quantifications ware done by the least squares criterion.

2. Measurement set-up

Cylindrical polypropylene phantom with two holes were used for testing ATT procedure. In the laboratory scale it is simpler to rotate the object instead of measured system. Phantom was eccentrically situated on the table, which rotates. Test rig with configuration of radioactive sources and detectors is shown in Figure 59. Collimation of the radioactive source and scintillation detectors are shown in Figure 60.

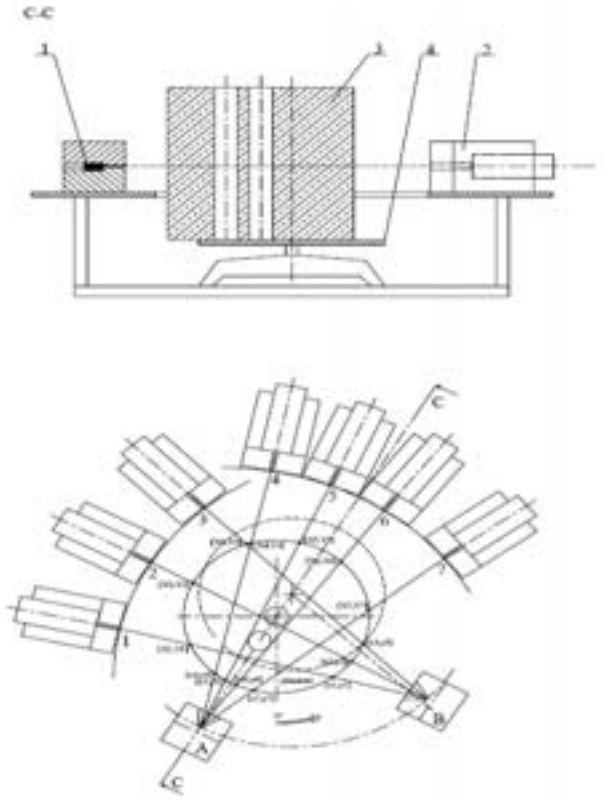

FIG. 59. Phantom measurement, a) 1-radioactive source ^{137}Cs, 2-scintillation detector, 3-measured object (phantom), 4-rotated table; b) A, B radioactive sources, (1-7) detectors.

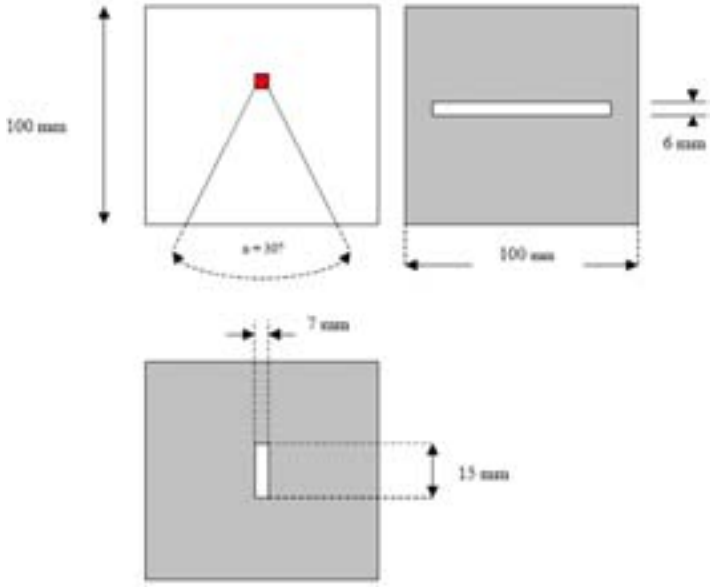

FIG. 60. Collimation of radioactive source (top) and detectors (bottom).

Seven collimated scintillation detectors and single radioactive source ^{137}Cs (460 MBq) were used separately in two collimated position. The multiple detectors system comprised a Nucleus Digital Multiplexer Router II – with 7 scintillation detectors and amplifiers, a Digital Multiplexer Router Unit: DMR-108, and Multichannel Analyzer Card. NDMR enable to eliminate scattered radiation by measuring in the energy windows.

3. Measurement and evaluation

The table desk with phantom was rotated by step of 30° and so with seven detectors;76 useful beams were used. Rotation is evident from the Figure 65.

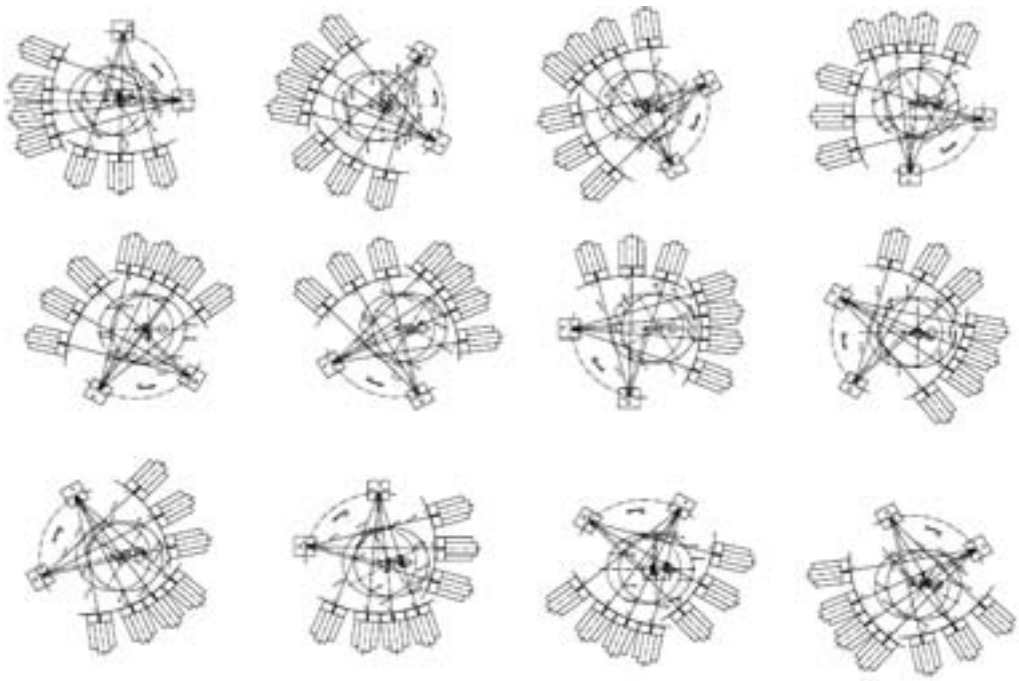

FIG. 61. Rotation of the phantom in steps of 30º.

Two measurements were realized for any configuration, calibration i.e. measurement of phantoms with any discontinuities (the holes were full with the liquid which had the same density as phantom)- N_{ref} -and measurement of phantom with the empty holes –*N*-. Simple equation can be found for evaluation of length of the beam in side of the hole L_{ih}:

$$L_{ih} = \frac{1}{\mu} \ln \frac{N_{ref}}{N}$$

From this simple evaluation, so call **active** (red line) or **inactive** (blue line) beams, (that is beams which go through the discontinuity) or not can be distinguished. The situation is evident from Figure 62.

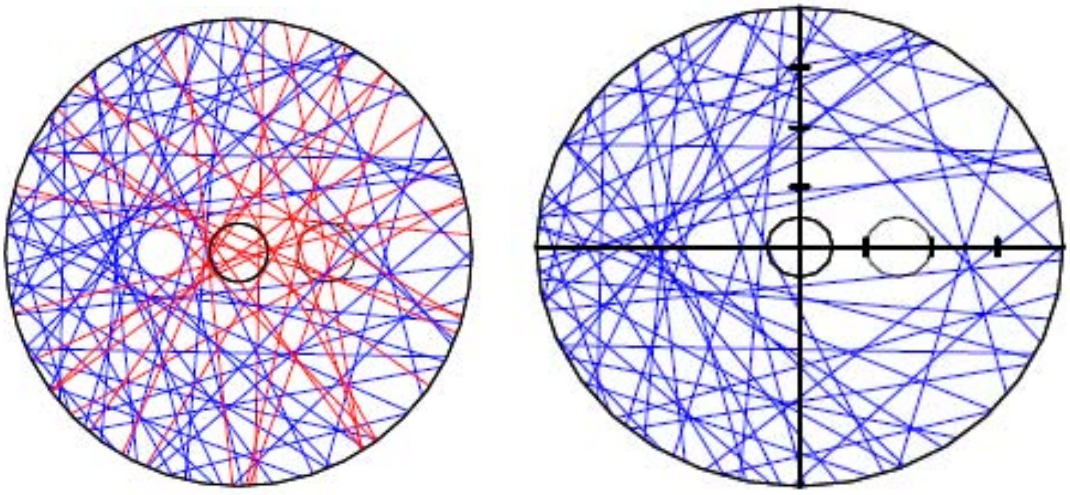

a) **b)**

FIG. 62. Positions of active and inactive beams in phantom with two he holes; a) all 76 beams, b) inactive beams.

The positions of inactive beams are used for estimation of the dimensions and positions of the holes. The measured signal L_m of an arbitrary pair emitter-detector can be expressed as a mean value of unknown volume fraction L (x,y) along the beam,

$$L_m = \frac{1}{L_{12}} \int_1^2 L(x, y)\, dl$$

Experimental data are therefore represented by M values Lm1, Lm2, …, LmM , which enable to identify a active length L(x,y) by the model function. The model function is

$$L(x,y) = \sum \varphi_i (A_i, x,y)$$

where $\varphi_i (x,y)$ are basis function and A_i are constants.

Model of two circular holes: coordinates of 1 and 2:

$\varphi_1 = (x - \mathbf{A_1})^2 + (y - \mathbf{A_2})^2$ $q_2 = (x - \mathbf{A_3})^2 + (y - \mathbf{A_4})^2$ radius of 1 and 2: $A_5 = r1$, $A_6 = r2$

The model has six parameters, two coordinates of the middle of the holes (x_1, y_1; x_2, y_2; and radius r_1 and r_2. The optimisation procedure SOMA, which is included to FEMINA software was used. for identification of parameters of the model.

SOMA (Self Organizing Migration Algorithm) belongs to the group of stochastic algorithms as Monte Carlo. (More details about procedures are given in on-line user manuals FEM3AI1.pdf (content, introduction), FEM3AI2.pdf (tutorial), FEM3AI3.pdf (quick reference), as well as in theoretical manual FEM3AII.pdf).

A success and time required for the evaluation strongly depends on the default values of parameters and their limits. These are estimated from the diagram of the inactive beams. 76 beams which go through the object were obtained after 12 sequences with 30 degree of revolution, while 38 beam after 6 sequences with 60 degree of revolution. These results are presented in Figures 63 and 64.

a) **b)** **c)**

FIG. 63. Results of evaluation from the 76 beams, with counting time a) 2.4s, S=0.015; b) 24 s, LS=0.088 and c) 240 s, LS=0.0082.

a) **b)** **c)**

FIG. 64. Results of evaluation from the 38 beams, with counting time a) 2.4s, LS=0.0122; b) 24 s LS=0.012 and c) 240 s LS=0.011.

Quantifications of the reconstruction results can be done by the least squares criterion evaluated on the basis of measured and reconstruction length of beams in the holes.

$$LS_m = \sum_{i=1}^{i=N} (l_{measured,i} - l_{reconstruted,i})^2$$

From the results which are presented in the figures 67 and 68 it follows that the best results were received when 76 beams were used and time of counting was in the region of 24-240 sec. Higher values were received when only 38 beams were used. When in evaluation were used exact length inn 76 beams LS = 0.0033, which can be judge as reconstruction errors.

For quantification of the results mostly two error specifications as some sort of standard are used, which can be adapt for ATT procedure as:

The Root Mean Square Error with respect to N:

$$RMSE_N = \sqrt{\frac{\sum_{i=}^{i=N} (L_{true,i} - L_{reconstructed,i})^2}{N^2}}$$

The Root Mean Square Error with respect to L:

$$RMSE_\mu = \sqrt{\frac{\sum_{i=}^{i=N} (L_{true,i} - L_{reconstructed,i})^2}{\sum_{i=1}^{N} L_{true,i}^2}}$$

Here $L_{true,\ i}$ are true values and $L_{reconstructed,\ i}$ the reconstructed ones. N is the total number of beams used in evaluation. $L_{true,\ i}$ were received from the graphical evaluation of beams going through the holes. The results are presented in figure 69.

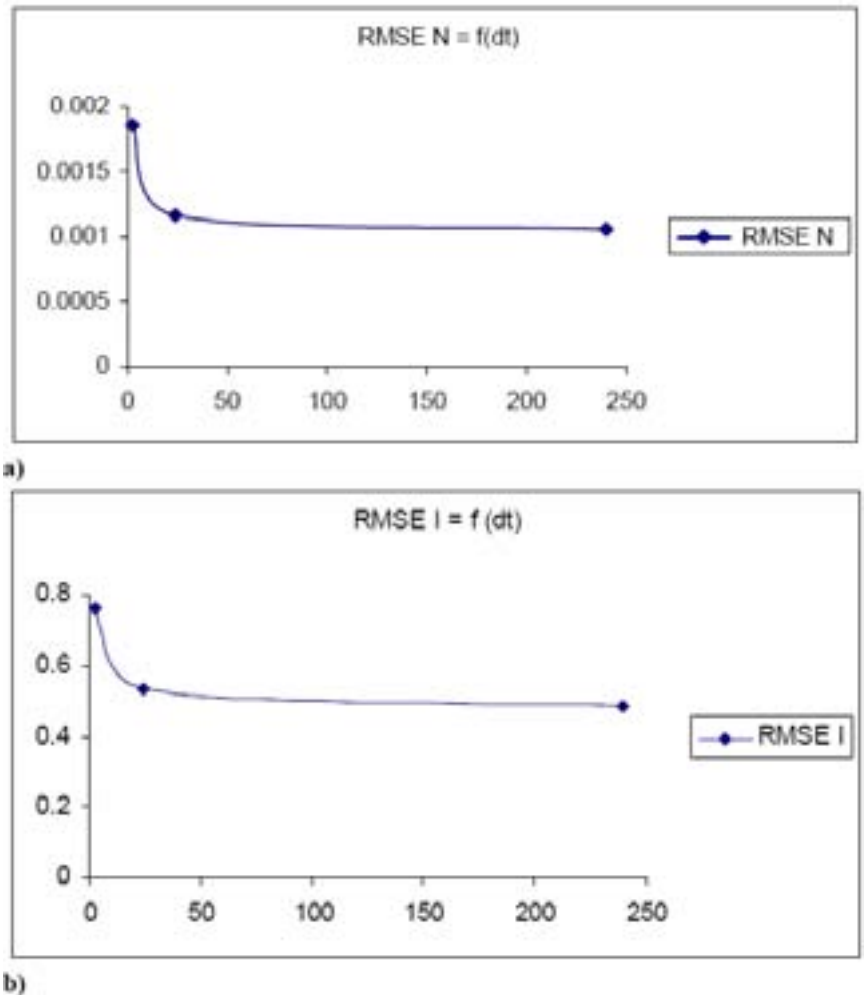

FIG. 65. The Root Mean Square Error evaluation for 76 beams and different counting time 2.4s, 24s and 240s a) with respect to N and b) with respect to I.

5.2.3. France

1. Measurements

Two systems have been evaluated to reconstruct the phantom provided by IAEA. The external diameter of the phantom is 50 cm with 2 holes. The first system is the CT scanner developed for French Institute of Petrol (IFP) in France. The main parameters of the system are:

- BGO scintillator h=39mm x diam=19mm
- 64 measurements/projection
- 64 projections
- Sampling time=1sec./projection
- ^{137}Cs source with activity=13 GBq
- Reconstruction algorithm=OS-EM
- Projector calculation: line crossing pixels
- Number of subsets=32 - Number of iterations=200

Figure 66 presents the average number of gamma-ray paths crossing each pixel. An homogeneous distribution of the parameter is a good criteria to avoid numerical problem during the reconstruction process. Figure 67 presents the sinogramm obtained for the phantom test, the reconstructed image and the reconstructed sinogramm. The $RMSE_{\mu}$ error is 0.007 in that case.

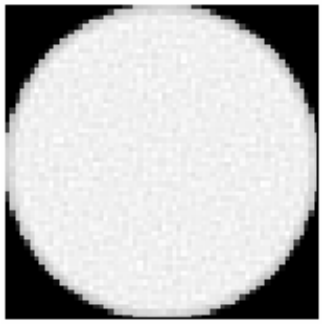

FIG. 66. Average number of gamma-ray paths crossing each pixel.

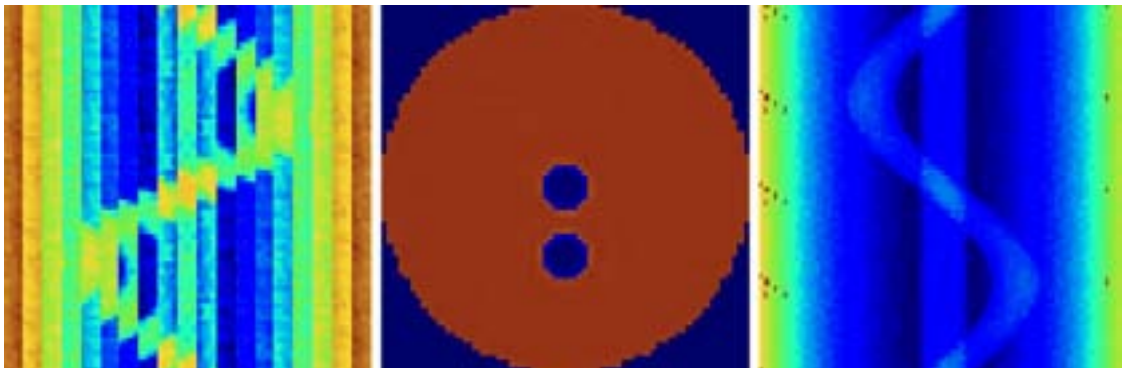

FIG. 67. Sinogram, reconstructed image and reconstructed sinogram in the noise free case.

Figure 68 shows the evolution of the reconstructed image as a function of the number of detected photons without object (I_0). This value is 37000 photons for the 13 GBq source. In that case, $RMSE_{\mu}$ error is 0.04. The value of 0.007 is approached for I_0=700000, i.e. for a counting time or source activity 19 times higher.

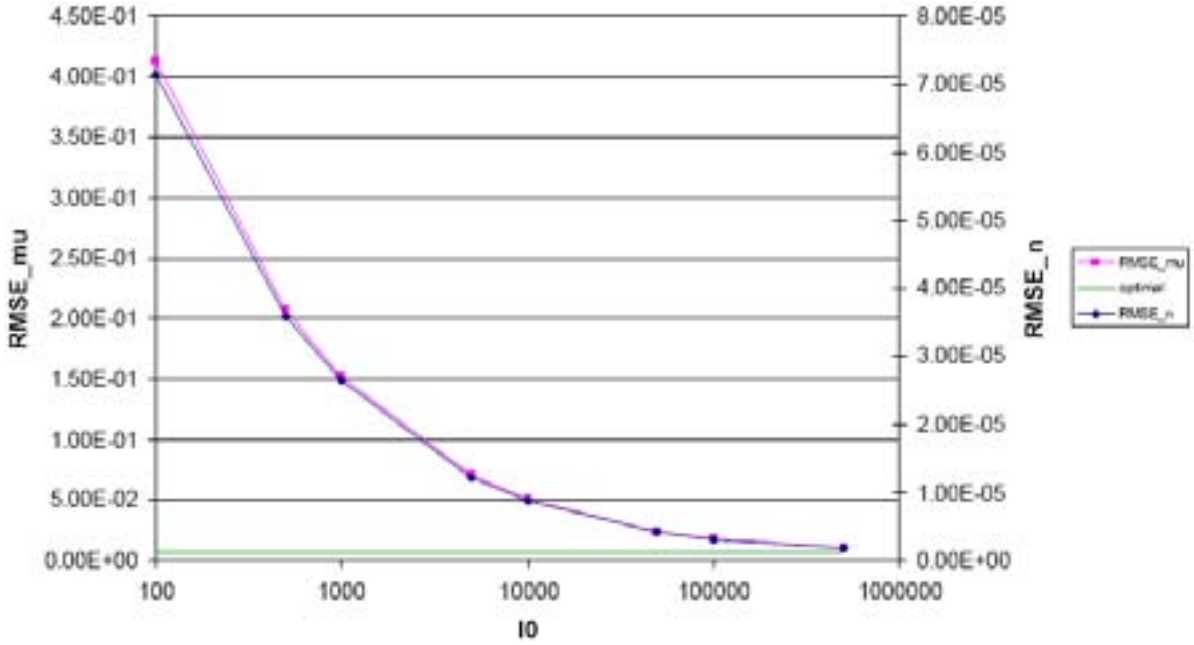

FIG. 68. Variation of $RMSE_{\mu}$ as a function of activity of the source for the "IFP" solution.

The second system evaluated is described in the Figure 69 and is based on the use of 19 uncollimated BGO detectors located on a ring and equi-distributed in a sector defined by the θ angle. Axes of scintillators are collinear to vessel axis. The specificity of this geometry is that the source is located on the same ring than detectors' one. This geometry makes the system very light since no collimation is used. Instead, to avoid scattering, only photopeak events are collected. The loss of events due to loss of photons scattered in the scintillator is compensated by the fact that distance between source and detectors is smaller. Comparison between this solution and IFP solution is presented in the Table IX in terms of counting efficiency. The global efficiency is almost the same for the two solutions.

TABLE IX. COMPARISON BETWEEN IFP AND COMPACT SOLUTIONS

Parameter	IFP Solution	Compact solution
Source – detectors distance	120 cm	60 cm
BGO efficiency	85%	53%
Threshold	10 keV	550 keV
Spectrum counting efficiency	90%	20%
Surface of detector	2.8 cm²	4.8 cm²
Global efficiency	1.48×10^{-4}	1.41×10^{-4}

2. Results

Simulations have been realized to estimate the influence of θ on reconstruction. The values 90°, 135°, 160°, 180° and 225° have been evaluated. Figure 70 presents the results.

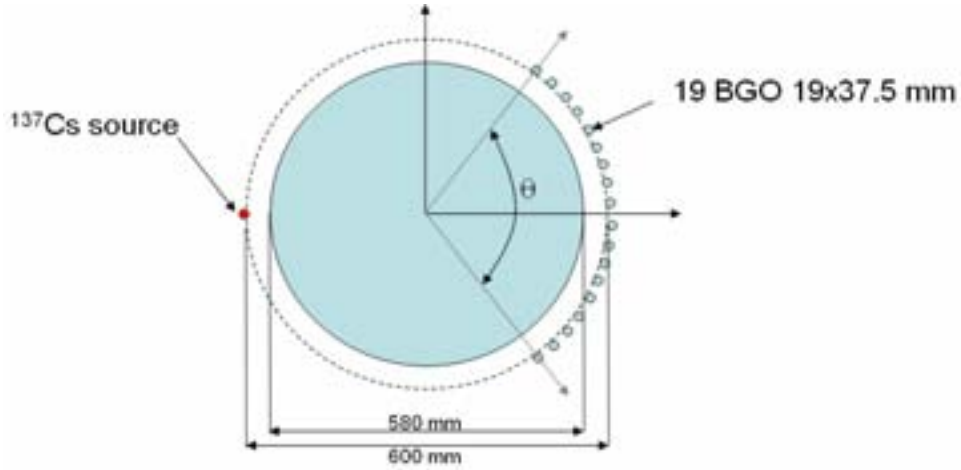

FIG. 69. Description of a compact gamma CT for industrial gamma-CT.

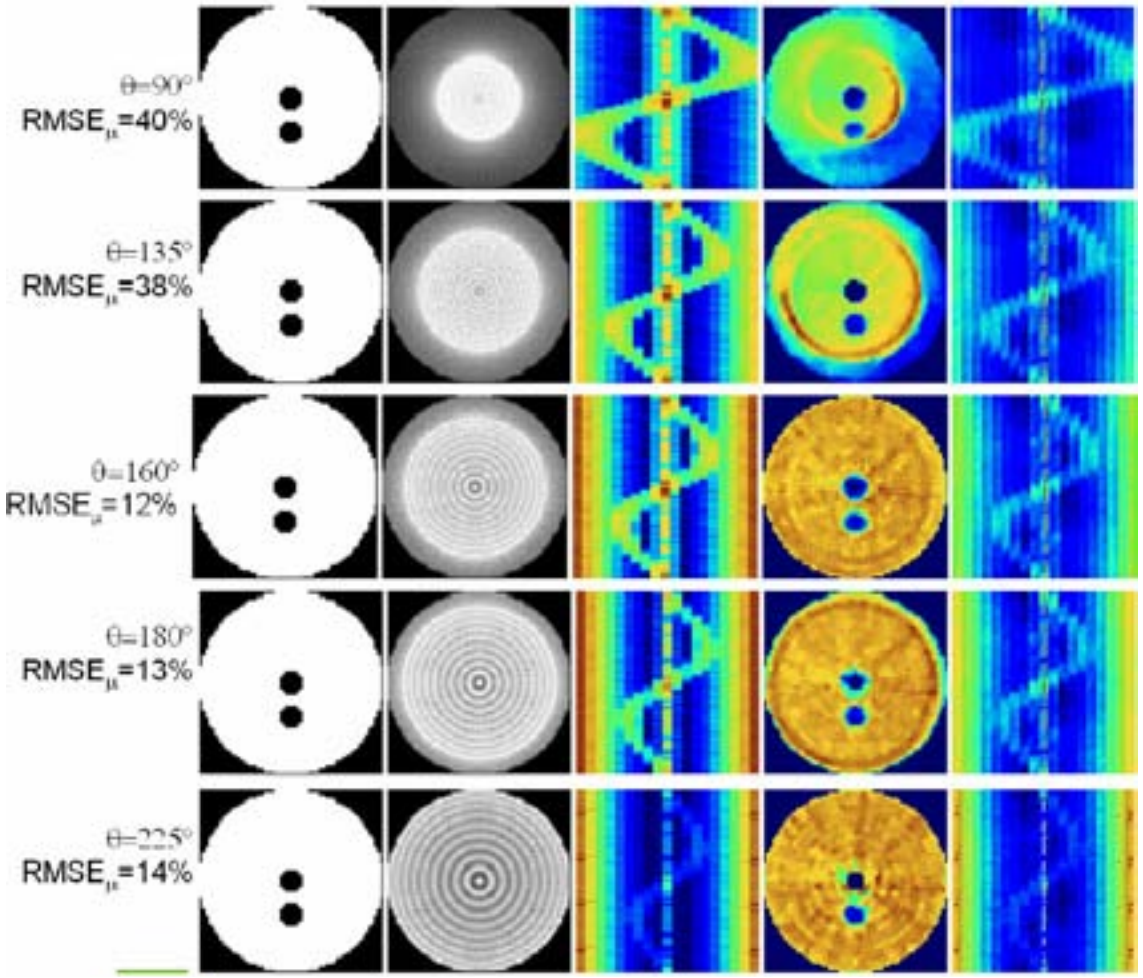

FIG. 70. Variation of reconstructed images as a function of θ.

For each value of θ, the number of projections crossing each pixel (2nd raw, [NPCP] image), the sinogram, the reconstructed image and the "reconstructed" sinogram are presented. The best configuration is obtained for θ=160°. However, the image obtained for θ=225° presents also a good quality. The corresponding RMSEμ is a little bit higher due to the fact that holes have not been properly reconstructed. This optimization has been realized for a given phantom but it does not mean this is true for a different distribution in the image. In the general case, the optimization must be done, when possible, with distribution or phantom close to the real case. The NPCP image gives information on the quality of image that may be obtained; a configuration that leads to a homogeneous distribution will most likely produce better images. In this example, for θ=90°, the homogeneity in the whole image is very poor. However, if we consider the central part of the image, the homogeneity is quite good. As a result, the hole in the middle is qualitatively well reconstructed, while the image on the frontier of the region and outside this region is badly reconstructed. Same conclusion can be obtained from image obtained for θ=135°. In that case, the second hole located close to the center of the phantom, is properly reconstructed, due to the fact that it is located inside the area which presents a good homogeneity. This approach is interesting when considering "local tomography", i.e. the reconstruction of information in a region of interest of the object.

For θ=180° and 225°, the NPCP image presents some rings in the image. These rings appear clearly in the reconstructed image for θ = 225°. The presence of rings is due to the acquisition procedure where projections are obtained for discrete positions of the source. Another solution would consist in considering continuous displacement of the source to limit the "ring artifact", while, probably, limiting the spatial resolution.

Figures 71 and 72 present the evolution of the RMSEμ estimator as a function of activity. For the 13 GBq of Cesium source, a value of RMSEμ = 0.15 is obtained for a measurement time of one second. Finally, Figure 73 presents 3 examples of reconstruction obtained for an average number of detected photons equal to 55, 273 and 547 and leading to RMSEμ equal to 0.50, 0.30 and 0.23 respectively.

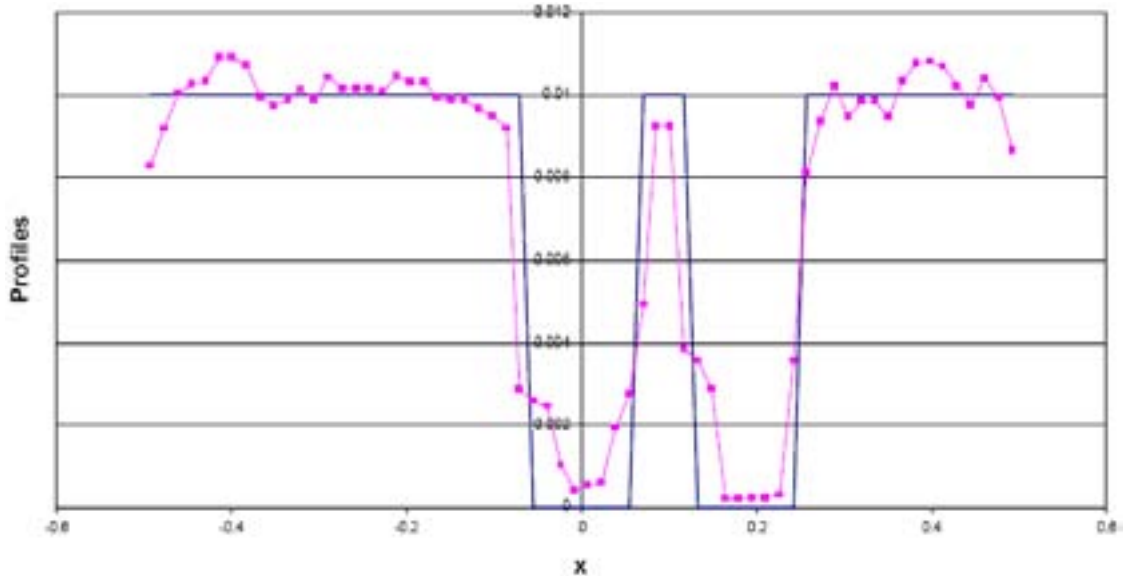

FIG. 71. Profile in the image obtained for the compact system in the best configuration (θ=160°, RMSE$_\mu$=0.12)

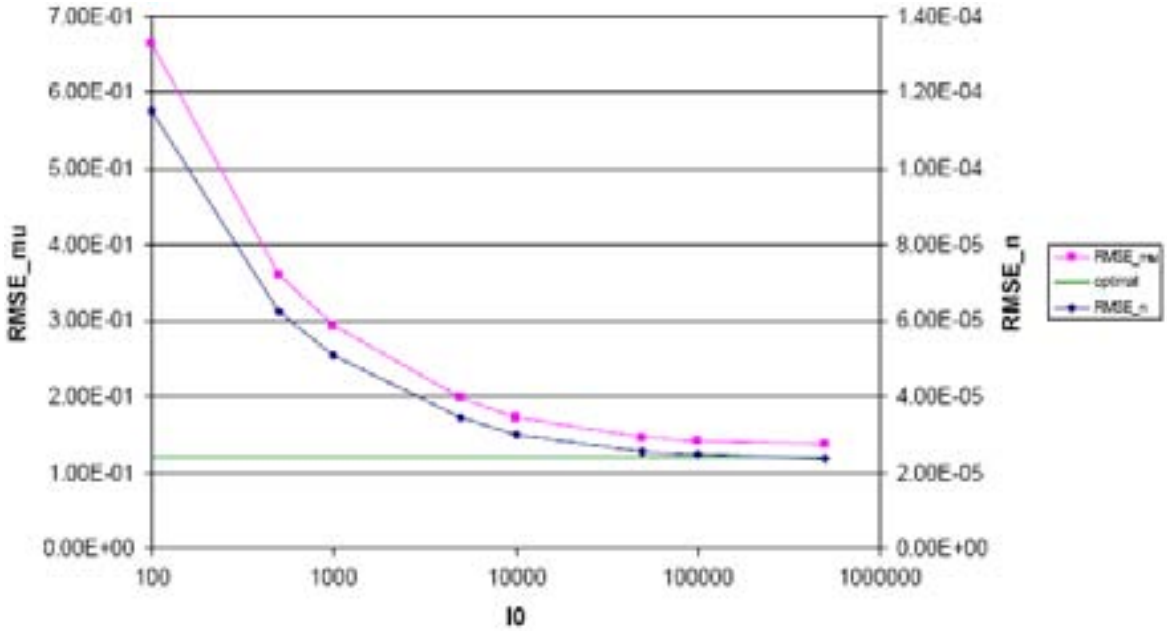

FIG. 72. Variation of $RMSE_{\mu}$ as a function of activity of the source for the compact solution.

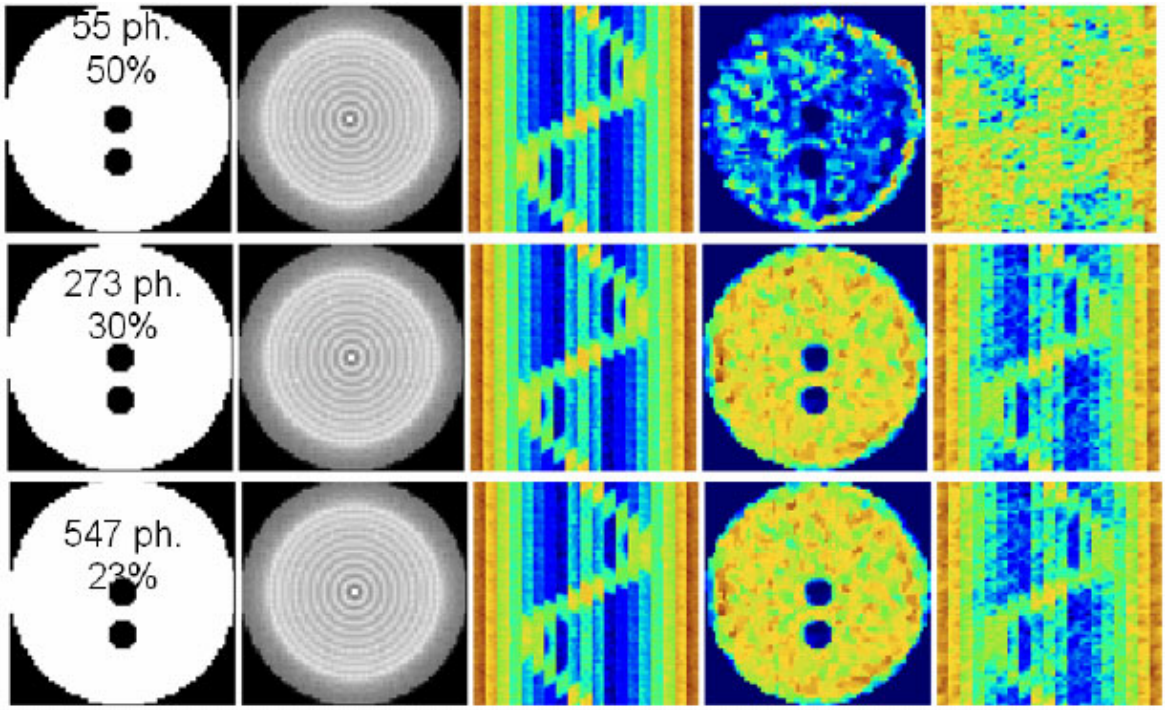

FIG. 73. 3 examples of reconstruction obtained with an average number of detected photons equal to 55, 273 and 547.

5.2.4. Korea, Republic of

IAEA supplied the standard phantom (Fig. 74) to compare test results from the different geometries and hardware set-up.

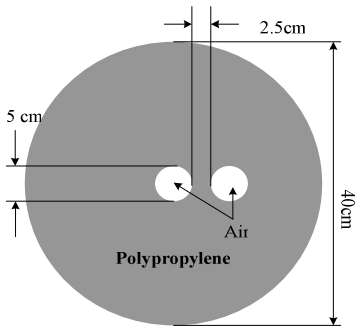

FIG. 74. The design specification of phantom.

The density of polypropylene is known to be 0.91g/cm^3. Experiment has been carried out with 1s, 5s, 10s. Each experiment also carried out with 16×16, 32 ×32 and 64×64 grid. Each result for visual evaluation is plotted (Figs. 75-81).

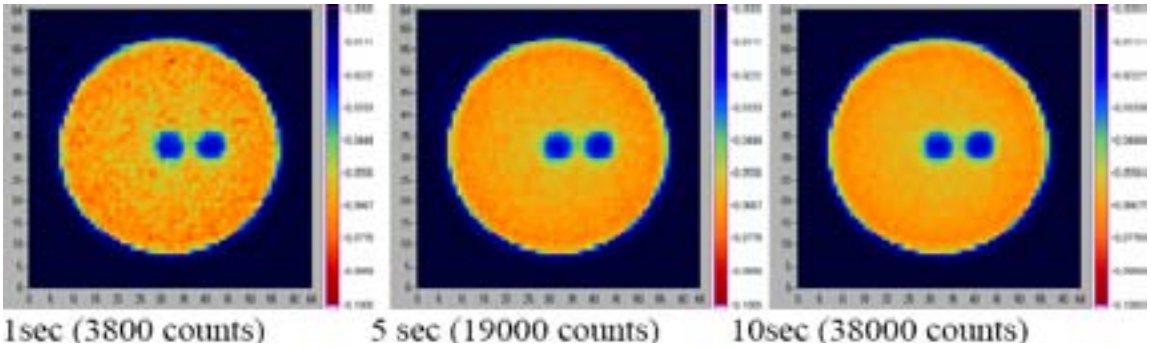

FIG. 75. Reconstructed images -vs- data acquisition time using 4096 (64 ×64) pixels.

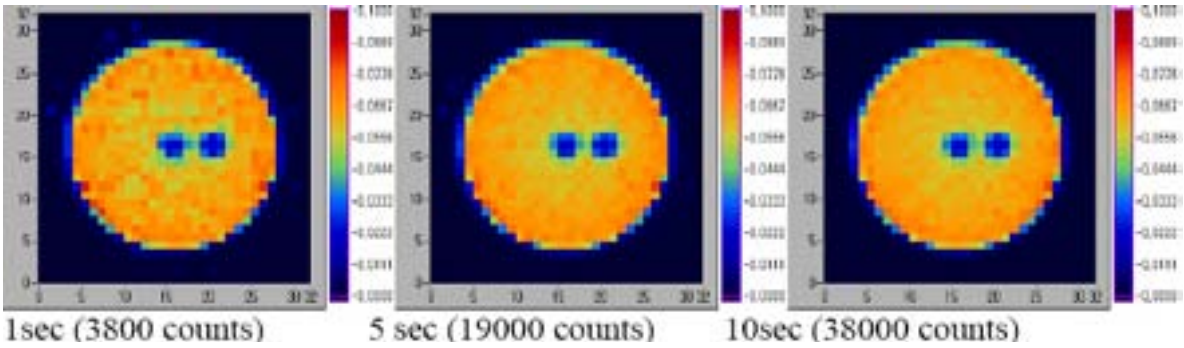

FIG. 76. Reconstructed images -vs- data acquisition time using 1024 (32 ×32) pixels.

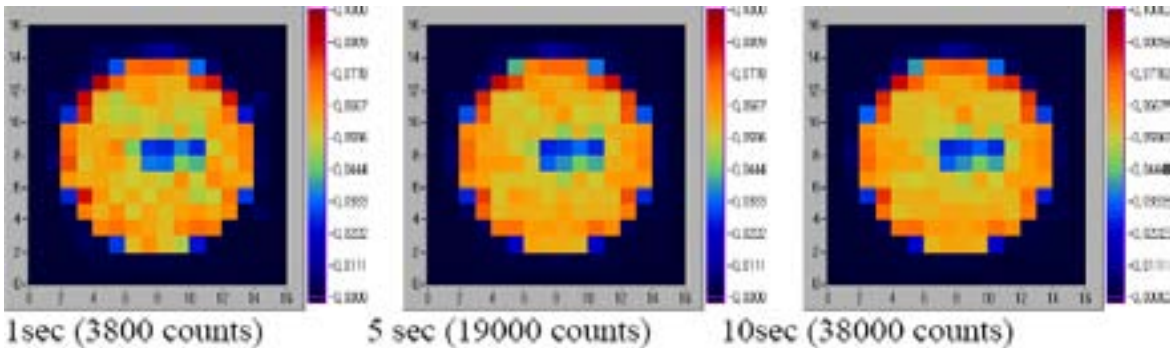

FIG. 77. Reconstructed images -vs- data acquisition time using 256 (16 ×16) pixels.

Counting time	1 sec	5 sec	10 sec
$RMSE_N$	1.686×10^{-3}	1.601×10^{-3}	1.577×10^{-3}
$RMSE_\mu$	0.1572	0.1493	0.1472

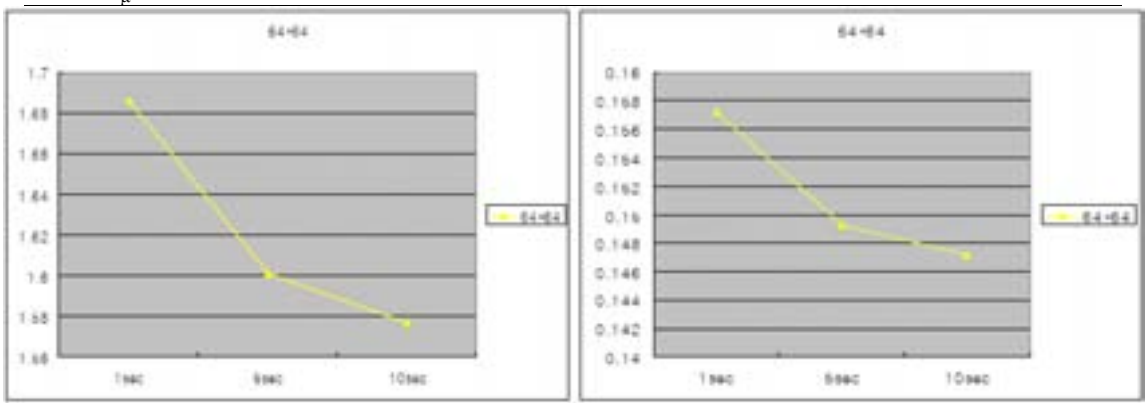

FIG. 78. The errors plotted as a function of counting time for 64×64 pixels.

Counting time	1 sec	5 sec	10 sec
$RMSE_N$	3.758×10^{-3}	3.626×10^{-3}	3.556×10^{-3}
$RMSE_\mu$	0.1772	0.1715	0.1693

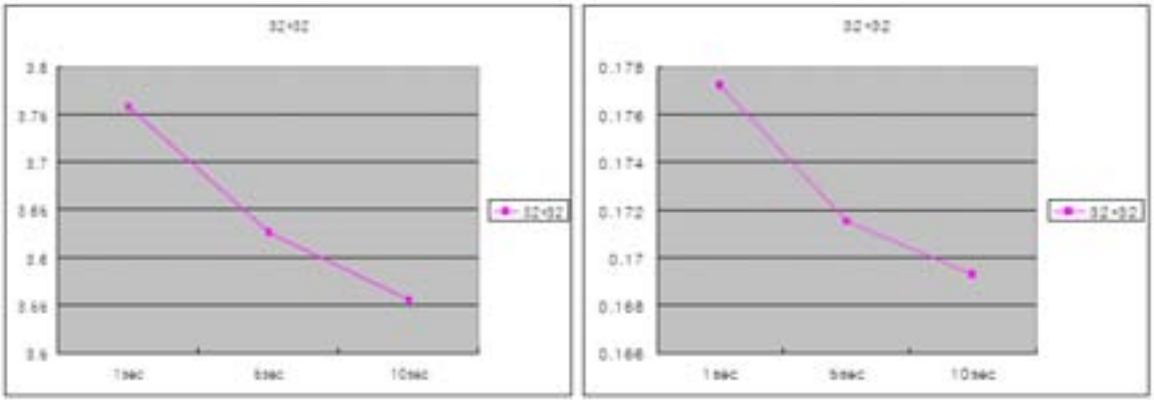

FIG. 79. The errors plotted as a function of counting time for 32×32 pixels.

Counting time	1 sec	5 sec	10 sec
$RMSE_N$	9.030×10^{-3}	8.645×10^{-3}	8.546×10^{-3}
$RMSE_\mu$	0.2194	0.2082	0.2067

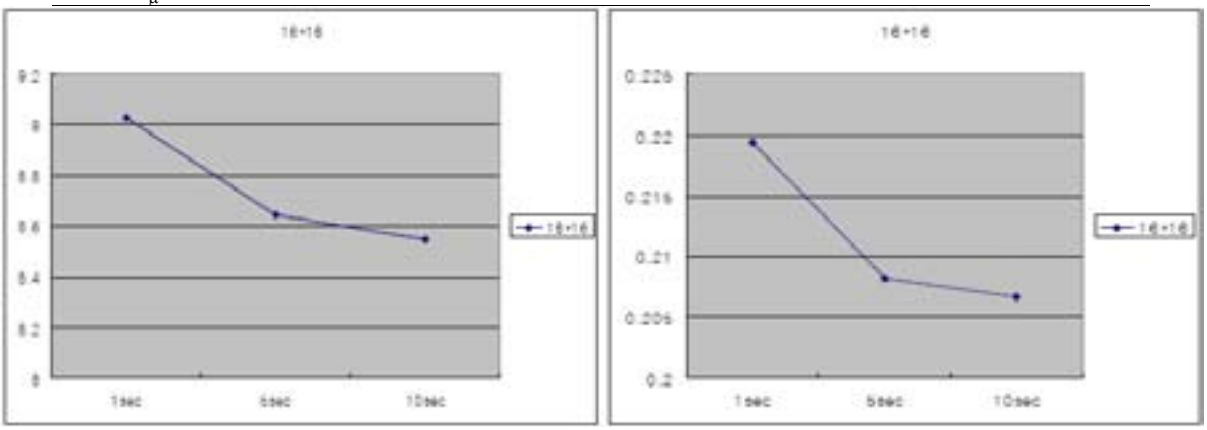

FIG. 80. The errors plotted as a function of counting time for 16×16 pixels.

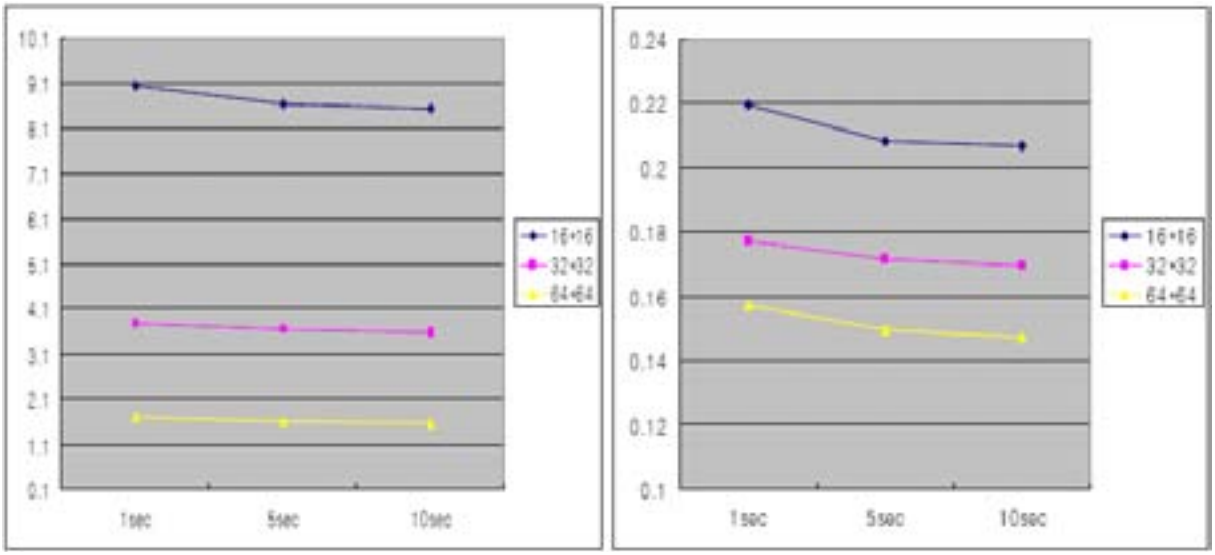

$RMSE_N$ $RMSE_\mu$

FIG. 81. The errors plotted as a function of counting time for all cases.

5.2.5. Norway

1. Measurements

Figure 82 shows a cross section of the high speed gamma ray tomograph developed by Johansen at the University of Bergen.

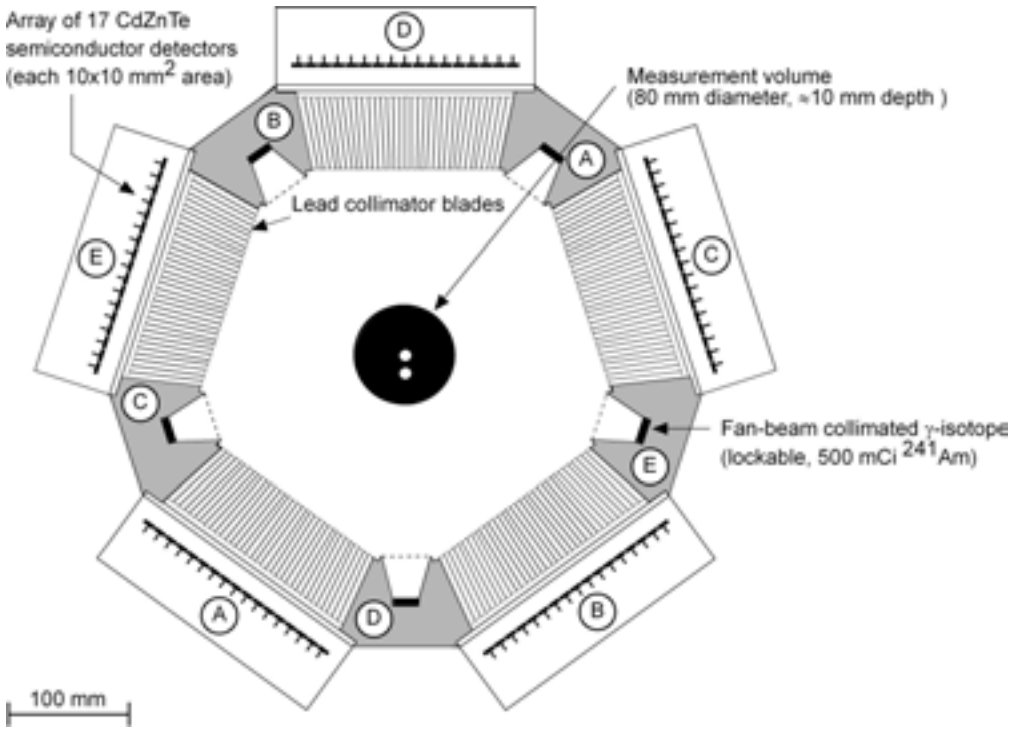

FIG. 82. The UoB high speed tomograph also showing the orientation of the phantom inside the measurement volume.

This tomograph has a fixed geometry optimized for speed of response. It was therefore decided to focus the experiments on image quality, specified in terms of $RMSE_N$, as function of reconstruction time using seven different iterative reconstruction algorithms; five algebraic algorithms: The Algebraic Reconstruction Technique (ART), the Multiplicative ART (MART), the Simultaneous MART (SMART); the Iterative Least Square Technique (ILST) and the Simultaneous Iterative Reconstruction Technique (SIRT), and two statistical methods based on the maximization of the likelihood function; the Alternating Minimization (AM) and the Maximum Likelihood - Expectation Maximization (ML-EM).

The measurements were carried out without wall material in the standard tests in order to limit the number of variables and simplify geometrical and algorithmic performance comparison. All images have been reconstructed on a grid of 32x32 pixels. Several other phantom were also tested for comparison, but only the results of the standard IAEA phantom are plotted in Figure 83. The performance and convergence properties of the tested algorithms are evident from the plot.

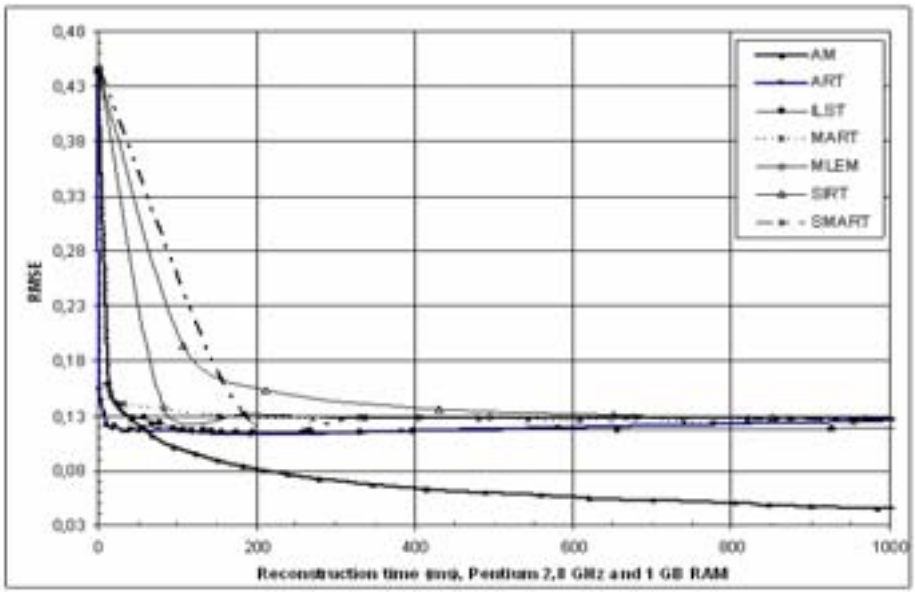

FIG. 83. $RMSE_N$ of the reconstructed images (32x32 pixels) using the standard IAEA phantom and seven different reconstruction algorithms as a function of reconstruction time using a standard PC.

2. Discussion of results

From comparison with other phantoms it is evident that the RMSE depends strongly on the cross sectional pattern of phantom and it complexity in addition to the performance of the measurement system.

AM algorithm is superior to ART, MART, SIRT, ML-EM, ILST and SMART for some cross sectional patterns, but it has approximately the same performance for others. AM has virtually no divergence when increasing the number of iterations although the presence of noise.

ART is a very fast algorithm comparing to MART, SIRT, AM, ML-EM, ILST and SMART. The disadvantage of ART is low resolution performance comparing to AM, and due to the presence of noise, there is a divergence of RMSE even when the number of iterations is very high (>800).

ILST is relatively fast, but it presents a divergence with the reconstruction time. The number of iterations in ILST, which correspond to the minimum value of the RMSE, has a little dependence on the elemental density distribution of the sample.

In practice, the number of iteration is fixed by doing some test on the measurement device. This prefixed number does not correspond to the RMSE's minimum for all samples, but it gives results that are not far from the minimum.

None of these algorithms enable real time high speed reconstruction unless a parallel reconstruction unit is applied. For high speed real time imaging the best option is to stream data to disk for off-line reconstruction.

5.2.6. Poland

The tests on electrical capacitance tomography (ECT) were performed for the phantom of 69.9 mm diameter. Tests were performed for four different rotation angles 0, 90, 180, 270 degrees. Reconstruction of the image was performed for four different resolutions 16x16, 32x32, 64x64 and 128x128 pixels. For calibration of the tomograph holes in the phantom were filled with oil, which has similar to PVC permittivity coefficient and density. Two types of preliminary experiments were performed: with one and two holes filled. Two of reconstruction results are presented in Figure 84. Graph of errors according to $RMSE_\varepsilon$ error specification is given in the Figure 85.

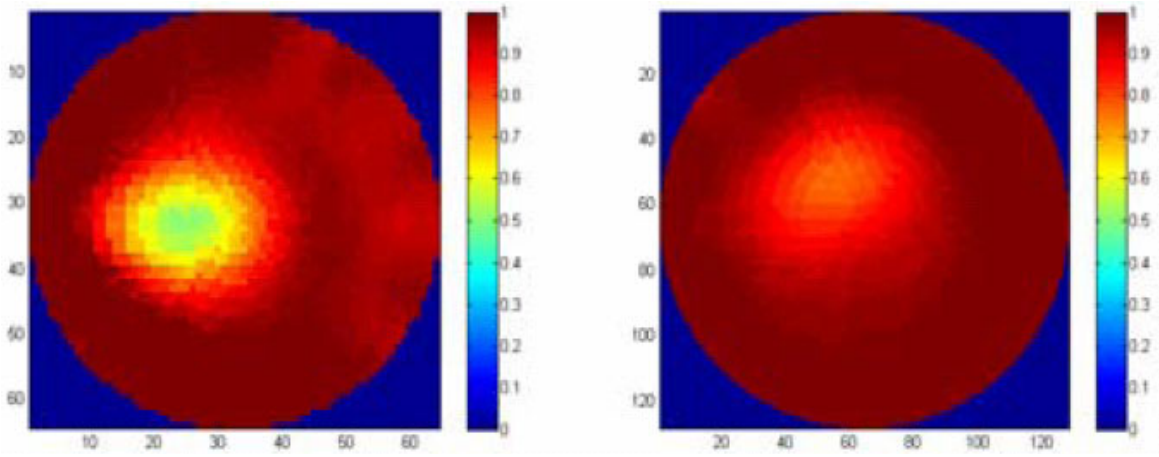

FIG. 84. Reconstructed phantom images for 128x128 resolutions: left – phantom with two holes, right: phantom with one hole.

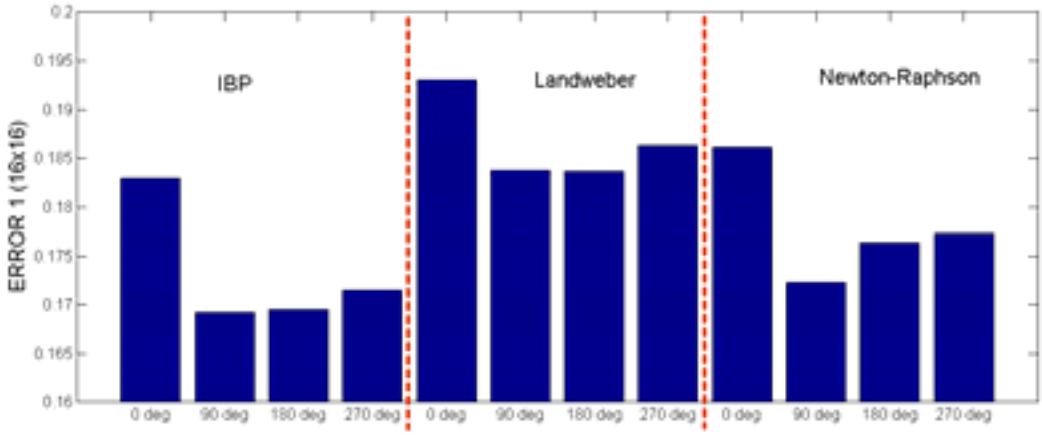

FIG. 85. Graph of errors according to $RMSE_\varepsilon$ error specification.

Regarding the phantom measurements the following remarks are worth to emphasize:

ECT technique is characterized by a low spatial resolution. Linearized problem of image reconstruction is ill-posed, which results in numerical problems.

- The investigated phantom is not well suited for ECT measurements. The holes are small, close to each other and located in the region of the lowest ECT sensor sensitivity.
- We deducted that phantom geometry and type causes problems with correct reconstruction. In order to validate this conclusion the additional experiment was conducted. The new, proposed phantom configuration (with just one hole) confirmed our logic assumptions.

We provide for common use the video clip taken during performed phantom experiments. Video can be accessed from the web page: http://tomo.kis.p.lodz.pl/.

ECT reconstruction results summary

The reconstruction results can reproduce simple objects not quite well. The results show one object inside sensor instead of two objects. The isolated holes of the phantom are not distinguished. The poor quality of the reconstructed images is caused by:

(1) ECT technique is characterized by a low spatial resolution. It is due to the strong non-linearity of the electrical field in ECT sensor conditioned by the Laplace equation [6, 10]. Therefore, linearized problem of image reconstruction is ill-posed, which results in numerical problems.

(2) Numerical problem of image reconstruction is under-determined. A fixed, small number of measurements (i.e. 12 electrodes give 66 linear independent measurements) gives the substantial reconstruction error (images has usually at least 1024 pixels). Mathematically we have great number of unknown values (pixels) with a small number of known data (measurements). It is then advised to use 32x32 pixels in the reconstructed image to get the acceptable image quality.

(3) It was found that the experimental phantom was inappropriate in some cases for the correct reconstruction with ECT technique. The results have shown that it was difficult to reconstruct properly some configurations where the size and the interspacing between holes were too small. Moreover, the reconstruction shows some limitation when holes are situated in the centre of the phantom where the sensor sensitivity is the lowest.

The next problem encountered during the phantom reconstruction was the higher permittivity value of the background (plastic material) comparing to the permittivity of the objects of interest (holes with air). The measurements for such phantom are conducted in the range of few percents of sensitivity scale. Moreover, the measurements are close to the maximal calibration values. Such conditions result in lack of any special unique information about the phantom.

6. PRACTICAL ASPECTS OF IPT SYSTEM DESIGN

When designing and building an industrial process tomography (IPT) system for a particular application, it is important to be as cost effective as possible, while still reliable enough for the intended purpose. In this chapter, some of the practical recommendations for the development of CT system are discussed. We hope that this chapter will help others in setting up a similar system or those who want to improve an existing one. It is particularly useful for those who want to develop or test their own system design for industrial process CT.

6.1. MECHANICAL GANTRY AND AUXILIARIES

The mechanical scanning system provides the relative motion between the test article, the source, and the detectors. It makes no difference, at least in principle, whether the test object is moved systematically relative to the source and detectors, or if the source and detectors are moved relative to the test object. Physical considerations such as the weight or size of the test article should be the determining factors for the appropriate motion to use.

Design of a mechanical system for industrial CT is non-standard. Unlike medical CT system, it is highly dependent on the particular application needed by the user. Design consideration varies in portable and permanently fixed CT systems. The mechanical system for industrial process tomography system must be tailored to its specific application.

6.1.1. Accuracy and repeatability

The mechanical assembly for a CT system plays a critical part in ensuring positional accuracy when acquiring reconstruction data. Acquisition of data for any tomography system usually involves high accuracy and good repeatability. Mechanical assemblies may involve the use of gear system, translator, rotary stage and stepper motor or servomotors. The mechanical system may have specifications, such as 4000 steps per revolution or pulse rates from 0.02 (1 pulse every 50 seconds) to 1500000 pulses per second. There are two kinds of gears normally used to achieve good accuracy, namely spur gear and worm gear. Spur gears are cylindrical gears with teeth that are straight and parallel to the axis of rotation. They are used to transmit motion between parallel shafts. Worm gears are crossed-axis helical gears in which the helix angle of one of the gears (the worm) has a high helix angle, resembling a screw. The use of suitable gears shall give good repeatability for scanning. Repeatability is the ability of a motion control system to return repeatedly to the commanded position. It is influence by the presence of backlash and hysterisis. Consequently, bi-directional repeatability, a more precise specification, is the ability of the system to achieve the commanded position repeatedly regardless of the direction from which the intended position is approached. It is synonymous with precision. However, accuracy and precision are not the same. Backlash is the amount by which the width of a tooth space exceeds the thickness of the engaging tooth measured on the pitch circle. It is the shortest distance between the non-contacting surfaces of adjacent teeth.

One major factor influencing the precision of the CT system is the geometric alignment. It is important to ensure that the array of detectors is horizontally aligned with the gamma source fixture on the same scanning plane. This is because misalignment can cause image artifacts when acquiring data for the object under investigation. Mechanical misalignment in the detectors or gamma-ray source could cause positional uncertainty of ray data in reconstruction. In rotate only systems, the effect is degradation in spatial resolution. Provided that actual positions of all rays are accurately known, the effect may be eliminated by software correction.

6.1.2. Material selection

Strength and rigidity are traditionally key factors considered in the selection of a material. Equally important is the relative reliability and durability of the part when made from alternative materials. When the component is expected to operate at extreme temperatures, this must be considered carefully when selecting the material.

In designing and fabricating a portable CT system, two important aspects to be considered are size and weight. For permanent or fixed types, the structural weight of the system is less crucial but its rigidity and strength are more important. Selection of suitable materials for several aspects of the mechanical gantry and its auxiliary system must be considered. Table X gives some examples of materials that could be used in building the mechanical structure of a CT system. Since gamma ray and X ray CT systems are ionizing radiation, radiological hazards to the operator or user should be minimized. Thus, radiological safety features should be included in the design by using good shielding material and mechanical locking system.

TABLE X. EXAMPLE OF MAIN CONSTITUTIVE PARTS OF MECHANICAL GANTRY IN A CT SYSTEM

Items	Material/Parts
Structural frame	Aluminium or Aluminium alloy, Stainless steel
Source shield	Tungsten, Lead or depleted Uranium
Transmission/ gearing	Brass, Aluminium or HDPE
Motion guide	Angular linear bearing
Gear system	Rack and pinion

6.1.3. Motion control

A modern motion control system typically consists of a motion controller, a motor drive or amplifier, an electric motor, and feedback sensors. The system might also contain other components such as one or more belt-, ball screw-, or lead screw-driven linear guides or axis stages. A motion controller today can be stand-alone programmable controller, a personal computer containing a motion control card, or a programmable logic (PLC).

All of the components of a motion control system must work together seamlessly to perform their assigned functions. Their selection must be based on both engineering and economic considerations. Most motion control systems today are powered by electric motors rather than hydraulic or pneumatic motors or actuators because of the many benefits they offer:

- More precise load or tool positioning, resulting in fewer product or process defects and lower material costs
- Quicker changeovers for higher flexibility and easier product customizing
- Increased throughput for higher efficiency and capacity
- Simpler system design for easier installation, programming, and training
- Lower downtime and maintenance costs
- Cleaner, quieter operation without oil or air leakage

Electric-powered motion control systems do not require pumps or air compressors, and they do not have hoses or piping that can leak hydraulic fluids or air. The motion controller is the “brain” of the motion control system and performs all of the required computations for motion path planning, servo-loop closure, and sequence execution. It is essentially a computer dedicated to motion control that has been programmed by the end user for the performance of assigned tasks. The motion controller produces a low-power motor command signal in either a digital or analog format for the motor driver or amplifier.

In general, a motion controller receives a set of operator instructions from a host or operator interface and it responds with corresponding command signals for the motor driver or drivers that control the motor or motor driving the loop.

The most popular motors for motion control systems are stepping motors or stepper motors and permanent-magnet (PM) DC brush-type and brushless DC servo motors. Stepper motors are selected for systems because they can run open loop without feedback sensors. These motors are indexed or partially rotated by digital pulses that turn their rotors a fixed fraction or a revolution where they will be clamped securely by their inherent holding torque. Stepper motors are cost-effective and reliable choices for many applications that do not require the rapid acceleration, high speed, and position accuracy of a servomotor.

6.1.4. Pitfalls in design

When faced with the task of designing a mechanical system in tomography, there are many points or factors to be mindful of to minimize motion or operational errors and to maximize acquisition performance. Some practical points are highlighted below but these may not cover other unforeseen issues faced in implementation.

- Over-designed on the part of shielding fixture tends to increase total structural weight, which may pose difficulties for a portable type. This can be avoided through suitable selection of materials and reasonable shielding thickness.
- Undesirable backlash on mechanical system especially when gear train reverses - the gantry should be able to return to the original position.
- Gear ratio and motion plays the main contribution an accuracy of system.
- Size of process column or load/weight factor of the object. Must determine the investigation objective and type of specimen before start to fabricate the system.
- Feedback system – The availability of both hardware and software end-of-travel limits could prevent the motor's load from traveling past defined limits. Software and hardware limits are typically positioned in such a way that when the software limit is reached, the motor/load will start to decelerate toward the hardware limit, thus allowing for a much smoother stop.
- Laser alignment – Recommended for accurate positioning of radiation source and detectors
- Avoid collisions during motion
- Rigid design for mechanical gantry is important to eliminate unnecessary vibrations
- Avoid operational noise, if necessary

6.2. DETECTORS AND SENSING HARDWARE

6.2.1. Sensors for ECT

The electrical capacitance tomography system (for example ET1 used for tests) — which is presented in Figure 86 consists of hardware and software.

FIG. 86. ECT system ET-1 manufactured by the Warsaw University of Technology.

One of the hardware components of capacitance tomograph consists of a sensor with appropriate number of electrodes. Their number depends on tomograph construction. Different ECT hardware setups allow using versatile electrode configurations. Some ECT systems allow connecting 12 or 16 electrodes. The most popular configuration is single-plane sensor (Fig. 87). The Computer Engineering Department (Lodz, POLAND) designed single – plane sensors and also 3D sensors with different electrodes configurations. Two planes sensor can be built as 2x8 electrodes sensor or different combination creating fully 3D sensor.

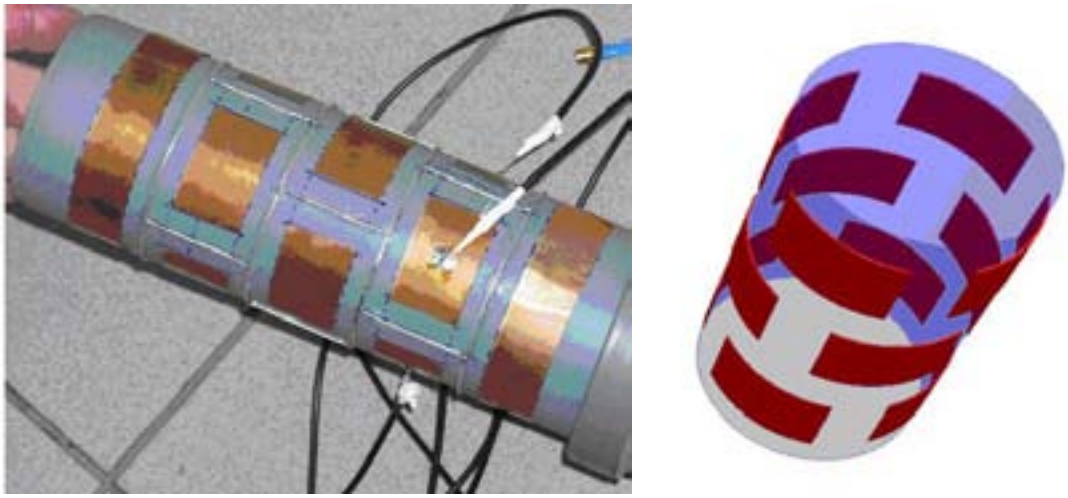

FIG. 87. Example of a 3D sensor: produced example and simulated model.

The sensor consists of assumed number of copper electrodes, which are mounted around the circumference of a PVC (polyvinyl chloride) tube (Fig. 88). The PVC tube has an inner diameter of 70 mm and is located between the electrodes and the measurement area. Thus a real non-invasive measurement is ensured, because there is no mechanical interaction between the investigated material and the electrodes. The guard electrodes are mounted above and below the measurement electrodes of the sensor. The sensor is further protected from electromagnetic stray fields by a copper shield around the whole sensor. Between the electrodes and the shield a layer of PU (polyurethane foam) is mounted. The sensor is connected to the tomograph using coaxial cables of 50 Ohm impedance. The cables are fitted with gold coated SMB connectors (radial). All wires are 1.5 m long. The measurement process in the ECT unit is based on a charge-discharge method. This principle of measurement is well described in the literature.

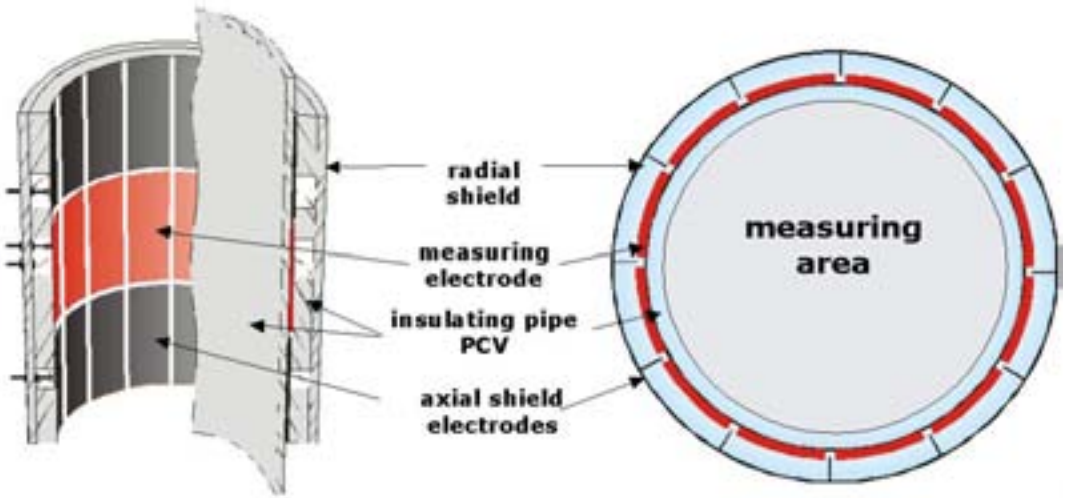

FIG. 88. The cross-section of the 12-electrodes ECT sensor. The electrode length is equal to the pipe diameter (70 mm).

The measurement concept of capacitance tomography is the following (Fig. 89) — one electrode is switched on as the sender or the source electrode and all the other electrodes are chosen to be receivers or sink electrodes. All electrodes are switched on successively clockwise.

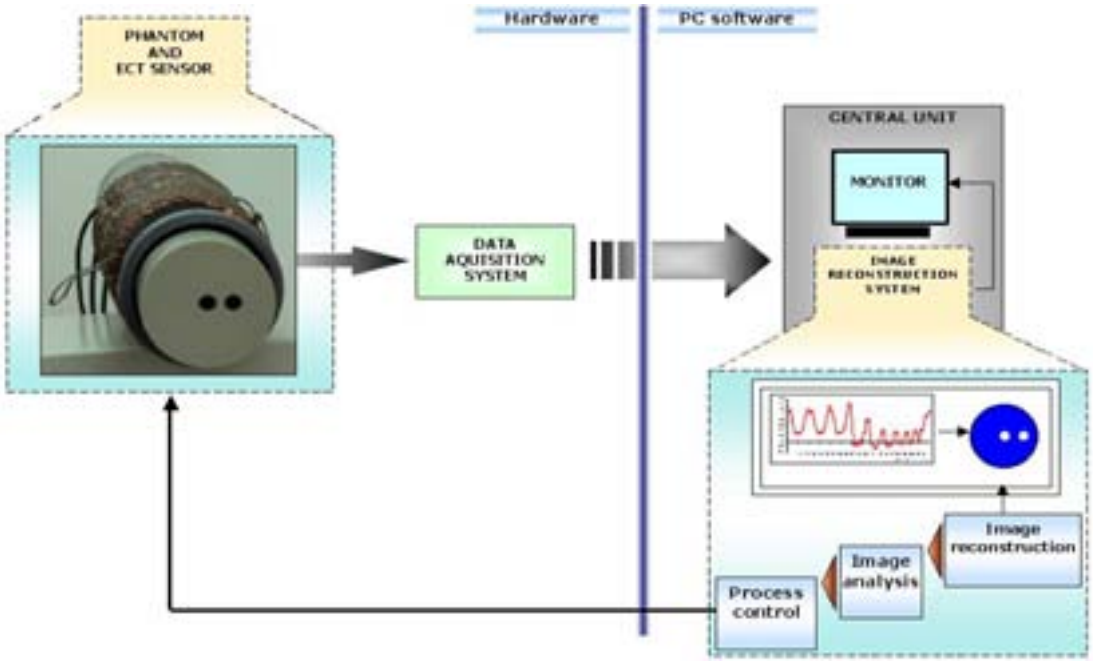

FIG. 89. ECT measurement process.

During the measurement process, every sensor electrode in turn acts as a transmitting (active) electrode. All remaining electrodes of the same sensor work as receiving (passive, detector) electrodes at the same time. The receiving signal cards perform all detected charge measurements in parallel.

The transmitted signal is a rectangular pulse train with 12 V amplitude and 1.5 MHz frequency. It is generated using analogue switches (Analog Devices ADG442BR), connecting the transmitting electrode alternatively to +12 V voltage and to ground potential as described by Isaksen. The measured capacitances range is limited to nano- and femto-Farads. To ensure maximal reliable measurement values the sensor capacitance should be as high as possible. In the case of a sensor it can be achieved by maximizing electrodes area. The optimal sensor size equals to the sensor diameter.

The image data are saved in different matrix formats e.g. 16x16 and 32x32 elements. The pixel values are normalized and the value range is from 0 to 1, i.e. from minimum to maximum permittivity range, if the measurement data were normalized.

6.2.2. Detection systems for gamma tomography

The needs within experimental high energy physics, space physics research and medical imaging have led to substantial advances in the radiation detector technology. Here, detector concepts applicable to gamma-ray tomography systems operated in pulse counting mode are discussed. Dense semiconductor detectors are preferable at low gamma-ray energies, whereas scintillation detectors have to be used at higher energies. The use of VLSI and ASIC read-out electronics improves performance and reduces cost.

Attenuation measurements in most X ray tomographs are performed by detectors operated in current mode, i.e. measurements of the detectors' average signal currents. This is possible since the radiation intensity (number of photons per second) is quite high. The radiation intensity in gamma-ray tomography is normally orders of magnitude lower due to the physical limitations of the isotopic sources.

This is advantageous from a safety point of view since the radiated dose to the environment consequently is lower. The drawback is a higher measurement error due to the random fluctuation in the photon emission. This error is inversely proportional to the square root of the radiation intensity at a given measurement (integration) time as demonstrated by Johansen and Jackson. This time limits the image data capture time and has to be short in many industrial applications to enable imaging of dynamic objects and processes such as flows. The source activity is consequently chosen as high as possible in such cases. Even so, the average signal current in the detectors is not measurable with sufficient accuracy. Gamma ray tomography systems therefore have to be operated in pulse counting mode, where all photons interacting in a detector are separated and individually counted. This puts strict demands to the detectors and the read-out electronics which have to cope with high count rates.

6.2.3. Photon counting systems

Fig. 90 shows a typical photon counting system for detectors without internal gain, which is the case for most semiconductor detectors. The charge liberated in the detector due to the photon interaction is collected at the electrodes and integrated in charge sensitive preamplifier. The preamplifier output signal is fed through a so-called pulse shaper which is a bandpass filter and amplifier. The shaper is characterized by the output signal's peaking time, τ_0, which is proportional to the filter's centre frequency and defined as the time from 1% to 100% of full amplitude.

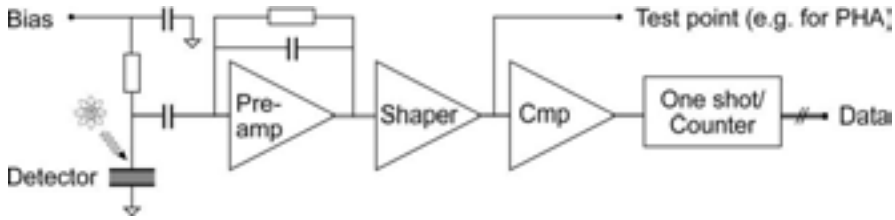

FIG. 90. Outline of gamma counting system with charge integration for optimal signal to noise ratio.

The amplitude of the pulse shaper's output signal is proportional to the radiation energy deposited in the detector. A comparator is therefore used to discriminate and enable counting of full energy events only, i.e. photons with energy close to the emission energy of the applied isotope. Low noise in the detector and preamplifier is critical particularly in low energy systems since the noise level determines the lowest detectable energy. The total noise of a state-of-the-art charge sensitive preamplifier and a silicon detector is shown as function of peaking time in figure 91. It is basically composed of so-called step and delta noise which are proportional to the peaking time and its inverse, respectively. The practical implication of these noise characteristics is that high count rate capability which requires short peaking times, means that the detector system cannot be operated at the lowest noise level. The challenge for detectors without internal gain is then very often to enable detection of the signal above the noise threshold.

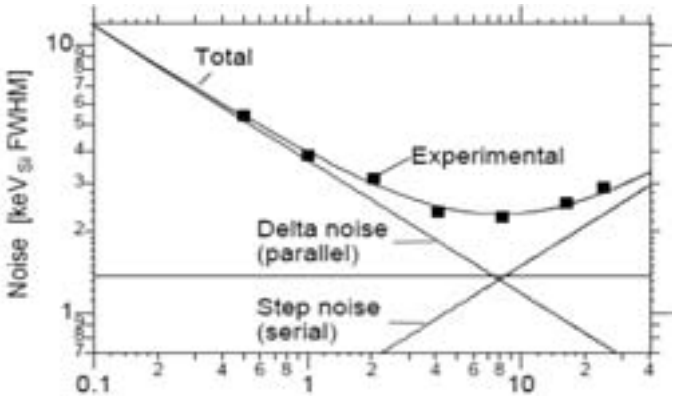

FIG. 91. Measured noise composition at 23°C of a depleted (30 V bias) AE9441 silicon diode and an Amptek A250 charge sensitive preamplifier. A Tennelec TC244 is used for pulse shaping.

Preamplifier charge integration is not required for detectors with internal gain, conventional voltage or current preamplifiers may then be used. In this case, the noise characteristics and the lowest detectable energy are normally defined by the detector alone. Except from that, the read-out is the same.

6.2.4. Radiation detectors

The choice of detector technology is primarily dependent on the radiation energy, which is in turn determined by the application with respect to penetration capability and measurement error. The latter is minimized when the average attenuation between source and detector is close to 86%. Thereafter several detector parameters need to be carefully considered with respect to the following:

- Radiation stopping efficiency close to unity for optimal utilization of the isotope activity.
- Fast speed of response to enable high count rates and thereby short integration time for a given measurement accuracy.
- Compactness, shape, size and weight to allow efficient stacking into arrays. Many of these parameters ultimately depend on the isotope and amount of lead shielding required.
- Ruggedness, reliability, stability and operation at ambient temperature.
- Cost.
- Energy resolution. This is of particular importance in multiple energy systems.

Some of these are related and conflicting requirements making it necessary to compromise when designing real time, high speed imaging systems. Several detector types can be eliminated at once: Gaseous detectors are not suited because of their poor stopping efficiency. Neither are semiconductor detectors requiring cryogenic cooling for noise reduction preferable, since this makes the total assembly complicated and expensive. All together, there are basically two detector categories which are applicable: Room temperature semiconductor detectors and various detectors using scintillation crystals. All these are also available in position sensitive versions. The position sensitivity required in detector systems for industrial gamma-ray tomography is, however, normally less than that offered by typical imaging detectors. Except for those using pixelised read-out, position sensitive detectors are also to slow for high speed counting. Position sensitive detectors are therefore not considered here.

6.2.5. Semiconductor detectors

Semiconductor detectors are particularly attractive in gamma-ray tomography applications because they are compact and easily stacked into arrays. Silicon detectors are due to the low stopping efficiency only applicable at low energies (<20 keV). For several years there has been a search for semiconductor detector materials which combine room temperature operation and high radiation stopping efficiency. Compound materials like HgI_2, CdTe and CdZnTe have received most attention. Detectors which are several mm thick are available; however, thin devices are faster and better suited for counting at high rates. The 85-channel gamma-ray tomograph developed at the University of Bergen uses CdZnTe detectors and 60 keV radiation from five ^{241}Am sources. The short peaking time (τ_0= 250 ns) enables the system to cope with rates above 100 kcps as shown by Johansen. This peaking time is not optimal with respect to noise characteristics as discussed above. The total noise of these detectors shows a similar dependency on the peaking time as shown in Figure 92.

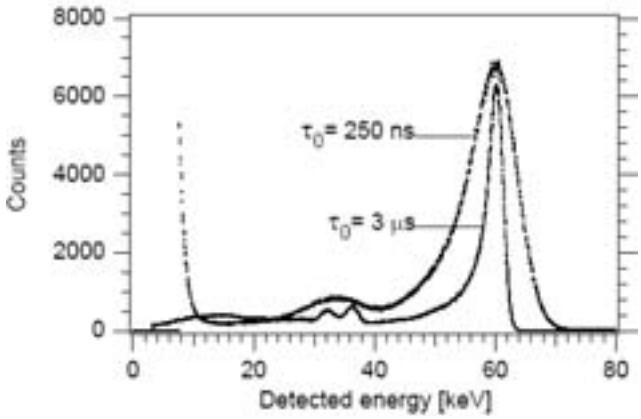

FIG. 92. Pulse height spectra of a 10x10x2 mm^3 CdZnTe detector exposed to 60 keV γ-rays from a ^{241}Am source at 23°C. Energy resolutions are 4,5% with τ_0= 3 μs and 16% with τ_0= 250 ns.

The best suitable detectors for radiation energies above a few hundred keV, however, are those based on scintillation crystals. This is evident from Figure 93, which compares the stopping efficiency of various detectors with realistic shapes and sizes.

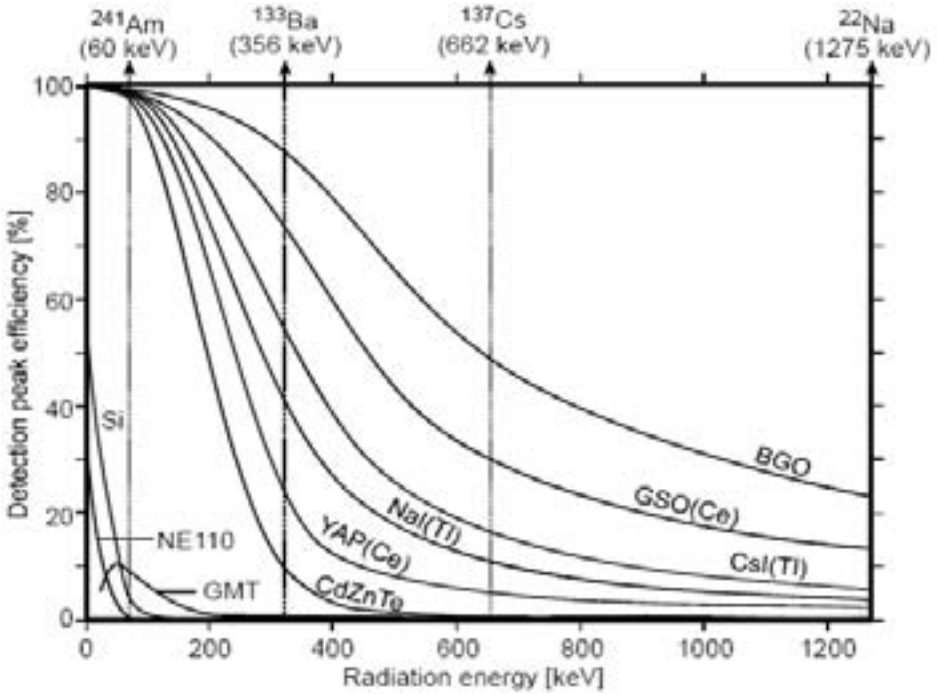

FIG. 93. Full energy stopping efficiency of several detectors at room temperature at 26 and 60 (^{241}Am), 356 (^{133}Ba), 511 (e.g. ^{22}Na), 662 (^{137}Cs) and 1275 keV (^{22}Na) γ-ray energies. Legends represent data calculated by MC simulations of 10x10 mm^2 parallel and monoenergetic beams incident to 10x10 mm^2 detectors. The crystals are 25 mm thick, except for the CdZnTe and Si detectors which are 2 and 1 mm thick, respectively.

6.2.6. Scintillation crystals

Scintillation crystal detectors are composed of two units which need to be considered separately. These are the scintillation crystal which converts gamma rays to visible or UV light, and the scintillation light read-out detector which provides the electrical output signal.

The traditional scintillation detector using a NaI(Tl) crystal optically coupled to a photo multiplier tube (PMT) is still widely used. This is a rugged, reliable and well proven detector, however, it has certain drawbacks related to the stopping efficiency and decay time of the crystal. There are now other attractive crystals and detector alternatives available.

The stopping efficiency of a scintillation crystal is determined by its density and size. Increasing the crystal thickness will, however, increase the loss of scintillation light by self absorption in the crystal and thereby reduce the output signal and the SNR. Hence, it is preferable to use small, dense crystals which also allow tight stacking. The scintillation efficiency or light output, i.e. the fraction of gamma-ray energy which is converted to scintillation light energy, is another important crystal property which affects the signal to noise ratio. The speed of response of a scintillation crystal detector is limited by the decay time of the scintillation signal which thus should be short. The most interesting scintillation crystals for high speed gamma-tomography are presented in Table XI. The NaI and CsI crystals are shown for comparison as these are commonly used scintillation materials.

BGO has been used in high stopping efficiency applications for years; GSO, YAP and LSO have also been used for some years whereas LYSO, LuYAP and $LaBr_3$(Ce) are relatively new crystals. The down side of new crystals is their higher cost. When comparing the crystals in Table XI it should also be kept in mind that there are also other parameters and issues that need to be considered: Some crystals are fragile, some are hygroscopic and require sealed packaging, others have multiple light decays where the longer decays in effect increases the background level of the faster ones. There are several excellent review articles for more information on scintillation crystals and their latest developments written by Weber, van Eijk and Melcher.

TABLE XI. IMPORTANT PHYSICAL PROPERTIES OF SCINTILLATION MATERIALS AT ROOM TEMPERATURE [JOHANSEN AND JACKSON, 2004, VAN EIJK, 2006].

Material	NaI (Tl)	CsI (Tl)	CsI (Na)	BGO[1]	GSO[2]	YAP[4]	LSO[5]	LYSO6[6]	LuAP[7]	$LaBr_3$ (Ce)
Density, ρ [g/cm^3]	3.67	4.51	4.51	7.13	6.71	5.55	7.40	7.1	8.3	5.07
Density, ρ [g/cm^3]										
Light output (γ), Q_C	11.4	11.7	11.5	2.1	2.5	6.4	7.4	3.9	3.9	19.9
Decay time, τ_D [ns]	230	1000	630	300	30-60	28	40	40	18	16
Wavelength, λ_{max} [nm]	415	550	420	480	440	350	420	420	365	380

[1] $Bi_4Ge_3O_{12}$, [2] Gd_2SiO_5(Ce), [3] $CdWO_4$, [4] $YAlO_3$(Ce), [5] Lu_2SiO_5(Ce), [6] $Lu_{1.8}Y_{0.2}SiO_5$(Ce), [7] $LuAlO_3$(Ce).

6.2.7. Scintillation light detectors

In addition to the general requirements in the bullet list above, a scintillation read-out detector needs to have spectral sensitivity matching the emission spectrum of the applied scintillation crystal. Since the latter three crystals in table 1 have their maximum emission (peak wavelength) in the deep blue and UV-region, detectors with UV-windows are needed for optimum performance.

In the world of radiation detectors vacuum technology still has a high standing, particularly in detection of low light levels such as those produced by scintillators. The photomultiplier tube (PMT) is the most frequently employed light detector. This is a photosensitive device consisting of a photo emissive cathode followed by focusing electrodes, an electron multiplier and an electron collector (anode) in a vacuum tube. The PMT is available in different shapes and configurations, including position sensitive devices which are attractive for tomography. A TO-5 metal can package was introduced to the market a few years ago. Its active diameter is 8 mm whilst the can diameter is about 16 mm.

In a more recent detector concept, the Hybrid Photodiode (HPD), the dynodes and anode structure is replaced with a silicon diode which senses the integral energy of the accelerated electrons from the photocathode. The HPD-performance is comparable to that of the traditional PMT, and even better concerning speed of response and gain stability. There are also versions available with pixelised silicon diodes. These could possibly be connected with multiple light guides to an array of scintillation crystals and used for multi channel read-out. The speed of response would be maintained since each pixel is read-out separately; however, there will be a considerable signal loss in the light guides.

The PIN photodiode has several properties making it an attractive scintillation light read-out detector: It is very compact and can virtually be made in any shape, it has stable low voltage operation and low power consumption, and it is very rugged. Even so the PMT by far still is the most common scintillation light detector. This is because of two interconnected disadvantages of the photodiode; it has no internal gain and it has limited surface area. These disadvantages limit the signal-to-noise ratio (SNR):

The lack of internal gain means that a gamma-ray scintillation event leads to a relatively low number of charge carriers in the photodiode. Secondly, because the noise in the diode is proportional to the diode capacitance, which in turn is proportional to the area of the diode any increase in the diode area would increase the noise level. The consequence is a poor SNR and a very good illustration of a case where the low energy detection threshold is noise limited.

UV-enhanced photodiodes (PD) have been investigated and successfully used for scintillation light read-out by Johansen. The result is compact, rugged and stable gamma-ray detectors whose only drawback is a lack of internal gain. This limits the lowest detectable energy and represents a problem, especially when used with scintillation crystals with low scintillation efficiency. This is demonstrated in the pulse height spectra of GSO, BGO and CsI(Tl) crystals in Figure 94. The diode system is used for read-out with those peaking times giving optimal signal to noise ratio for each crystal. The peaking times for GSO and BGO cannot be reduced since the noise then will increase and bury the signal. The situation will be the same for the CsI(Tl) configuration where shorter peaking times also reduce the signal due to long decay time and thereby incomplete light collection. PD read-out is therefore not applicable for high count-rate applications and high speed imaging.

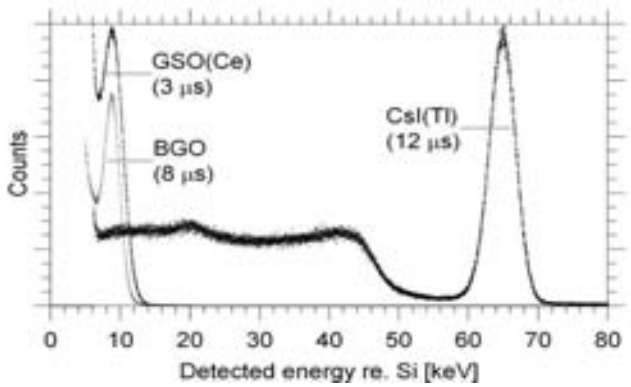

FIG. 94. Pulse height spectra of ^{137}Cs gamma-rays (661,6 keV) acquired with 10x10x25 mm^3 scintillation crystals coupled to the PD. The spectra are calibrated relative to direct absorption of gamma-rays in the PD. The optimal peaking times for each case are shown in parenthesis.

Another alternative is using avalanche photodiodes (APD) for read-out. These are silicon diodes doped to a multilayer structure forming a high electric field region with charge gain when a high voltage bias is applied. The APD is therefore well suited as read-out device for fast scintillation crystals. Devices with a few hundred mm^2 area and gain of about 1000 are available today though at a higher cost than the conventional diodes.

These do not match the specifications of the PMT. However, considering the general advantages of photodiodes, APDs are believed to be increasingly used, particularly for scintillation light detection.

6.2.8. Read-out electronics

Low noise charge sensitive preamplifiers are essential for optimal operation of semiconductor detectors, especially at high count rates since the preamplifier noise is dominated by delta noise short peaking times. The state-of-the-art is devices using surface mounted technology. There are also multi-channel VLSI preamplifiers available, normally in combination read-out electronics.

A preamplifier needs to be placed close to the detector to minimize stray capacitances and thereby noise. The preamplifier performance is less critical for scintillation detectors with internal gain. Independent of preamplifier configuration, the use of VLSI and ASIC technology is recommended for the remaining read-out electronics, i.e. shaper, comparator and digital circuitry. This is due to general advantages like compactness, better stability and noise immunity and less power consumption, in addition to reduced cost.

6.2.9. Complete detector systems

Some manufacturers offer complete system with detectors and read-out electronics such as the one shown in Figure 95. This system has a total of 768 detectors (pixels) with 1 mm pitch and operates in pulse counting mode. The output pulses for each detector channel are sorted in five different programmable energy bins. It uses CdTe or CZT detectors and the ASIC electronics is capable of count rates up towards 1Mcps.

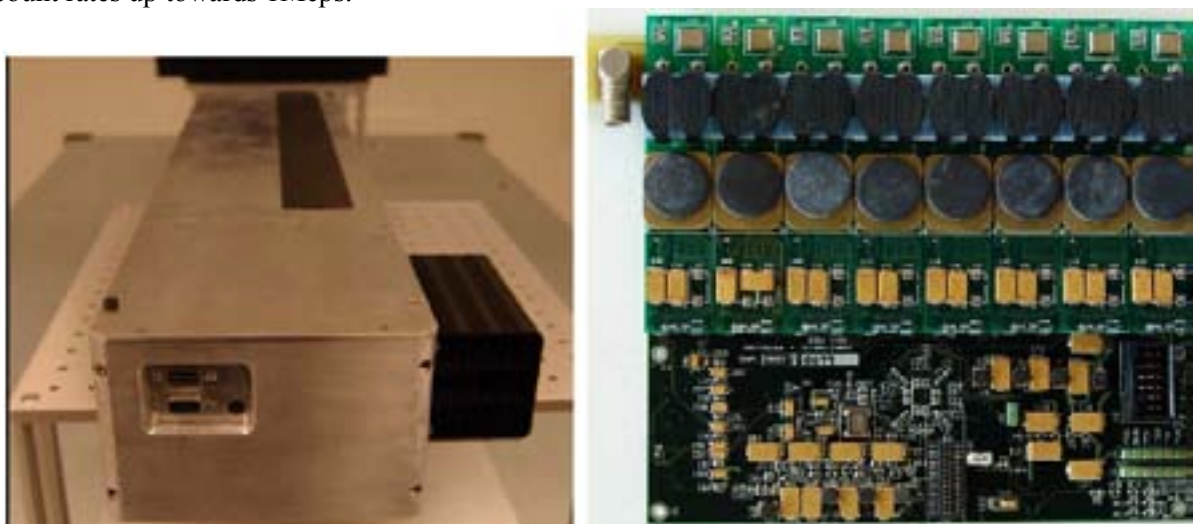

(a) **(b)**

FIG. 95. Example of integrated detector system with the input window on the top of the detector housing (a) and part of the ASIC (b). Courtesy of [Gamma Medica - Ideas].

6.2.10. Recommendations on radiation detectors

Several detector concepts may be used in applications with relaxed requirements to measurement time and image capture rate. For high speed imaging, CdZnTe detectors are the best choice for gamma-ray energies below a few hundred keV. Low energy radiation should be considered for every application since the cost is lower and the safety also is more easily maintained. In many cases this can be done by using wear resistant radiation windows (with low atomic number) e.g. in a steel process vessel. At higher energies detectors based on scintillation crystals must be applied for high stopping efficiency. Here, fast crystals read-out by compact PMTs are presumably the best choice.

Regarding cost and the time it takes to develop and build a gamma-ray tomography system, it is a general recommendation to choose mature detector technology rather than novel systems even though these may perform better if everything works out. For the same reason it is also recommended to purchase complete detector systems in stead of assembling this on your own. The same applies to read-out electronics. This may be more expensive initially, but very often it pays off in the long run. Common challenges in designing tomography systems based on radiation measurement are:

- "Cross talk" caused by scattered radiation from one detector to another. Solution: Proper use of source and detector collimation, possibly electronic discrimination.
- Electronic cross talk between the different detector channels. Solution: Careful design including proper grounding and shielding.
- Drift in detector system gain caused by temperature or ageing. Solution: Electronic monitoring of drift and either correction of this or compensation for it.
- Count rate errors at high count rates. Solution: Apply pile-up correction.
- Microphonics or acoustic noise from process equipment to the radiation detectors. Solution: Avoid physical contact between radiation detector housing and process vessel if possible. If not apply rubber suspension or mount the detectors in rubber or foam in their housing.

6.2.11. Field gamma CT

In the field system, the several factors should be considered in designing hardware. It is recommendable that the scanning geometry should be designed simple as possible. Unlike the turntable system, the self rotating system is strongly recommendable. The designs of field CT systems are shown in Figs. 96 and 97.

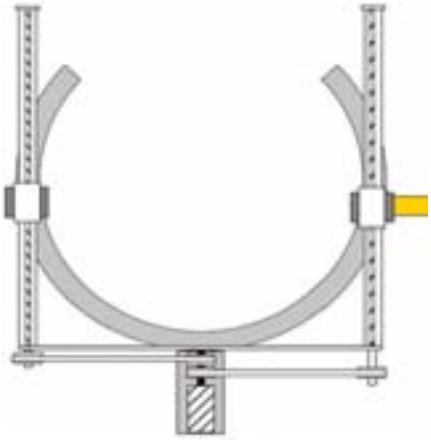

FIG. 96. Example of clamp-on parallel beam type gamma CT system.

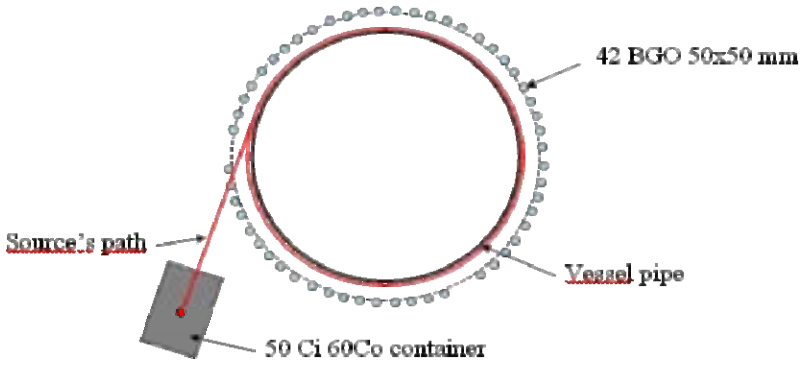

FIG. 97. Example of a compact CT system for on-field CT.

6.3. ALGORITHMS FOR IMAGE RECONSTRUCTION

6.3.1. Gamma CT algorithms

The performance of five different reconstruction algorithms have been investigated regarding the effect of number of sources and detectors on gamma-ray tomographs using fan beam geometry. The image reconstruction algorithms evaluated here are the Algebraic Reconstruction Technique (ART), the Multiplicative ART (MART), the Iterative Least Square Technique (ILST), The Alternating Minimization (AM) and the Maximum Likelihood - Expectation Maximization (ML-EM). The experiments have been carried out using a computer controlled flexible geometry gamma-ray tomograph where different geometries easily are programmed. Based on an analysis of the error of the reconstructed pixel values, it is found that although these algorithms perform different, they agree in that there is virtually nothing to be gained by using more than 7 sources.

In Figure 98, the effect of the number of sources (views) on the error is presented for each algorithm. The distance between the source and the detector is 638 mm, whereas the distance between the source and the object is 312 mm. Detector aperture opening of 10 mm x 10 mm and 3.7 GBq source was used. Further the number of detectors facing each source is fixed to 17, i.e. the total number of raysums increases with the number of sources. Figure 98 shows that error decreases with the number of sources, but also that there is no significant benefit in using more than seven sources.

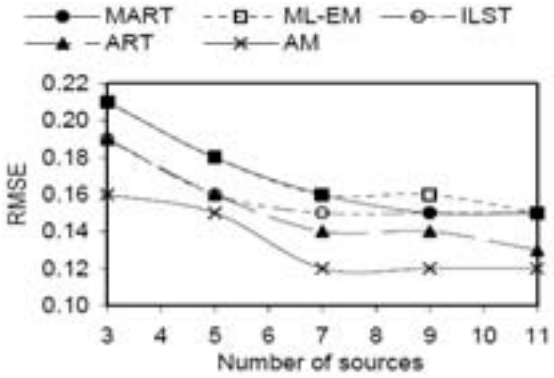

FIG. 98. The RMSE for different number or sources, each with 17 detectors.

The AM algorithm is better than to the other algorithms in this experiment where the influence of number of views and raysums on the pixel error has been evaluated. Each of these algorithms may be optimized for the particular geometries and thus perform better than reported here, however, there are limits in both number of sources (views) and detectors (raysums) beyond which any increase has little effect. This is important in order to design systems with moderate cost and complexity. To decrease the time of reconstruction the ordered subsets algorithms should be applied.

6.3.2. Tool to assess the weight matrix quality

The weight matrix can be computed in many ways. We propose here a simple way to check its quality and avoid troubles during the reconstruction phase, like for instance hot spots. The weight matrix can be observed in Figure 99 where the ray-sums for 2 projection angles (0 and 30°) and 15 detectors for fan beam geometry are presented. It allows checking any computing mistake.

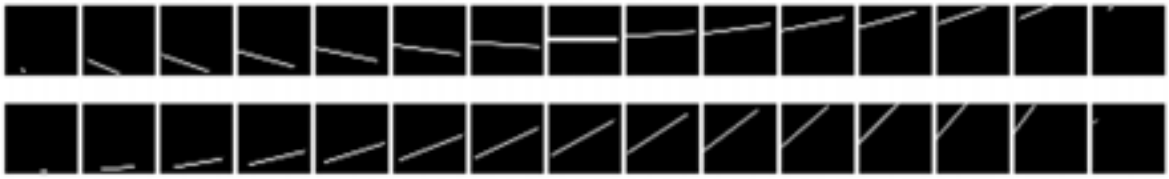

FIG. 99. Ray-sums for 2 projection angles and 15 detectors for fanbeam geometry.

A second method to check weight matrix quality consists in calculating for each pixel of the reconstructed space, the number of ray sums crossing it, the average value of the weight matrix for this pixel and the variance of it. Figure 100 presents the corresponding images for 2 configurations (one per row). The first configuration exhibits “noisy” images, for the 3 representations. In the variance representation, 4 pixels have 0 values meaning that one ray sum cross these pixels. In the second representation, images are smoother leading to better reconstructed images. In the true life, acquisition process is continue and should be kept in mind while estimating the weight matrix. The size of the beam crossing the object and the number of pixels are related one to each other. If the pixel size is lower than the beam size, it is more likely that some pixels may not been crossed by any ray sum.

It leads to discontinuities in the weight matrix and the impossibility to estimate the pixel value! In that case, some black spots appear in the 3 representations of the weight matrix.

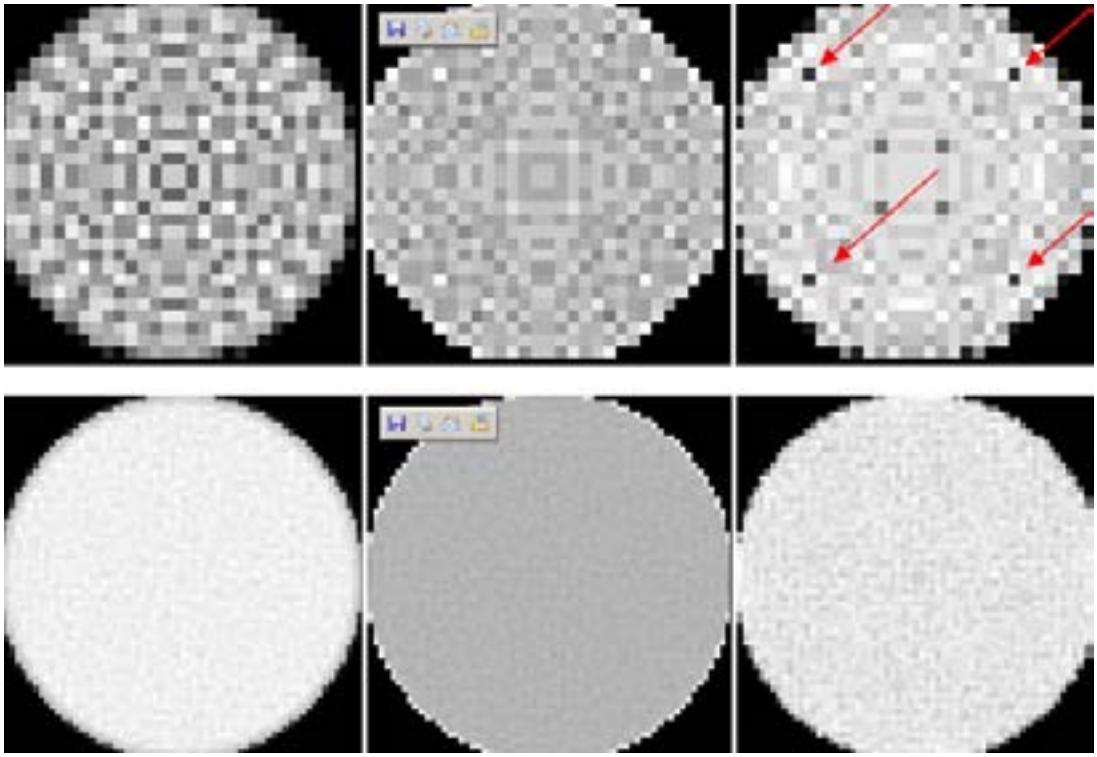

FIG. 100. Images presenting for 2 CT geometries (one per row) the number of ray sums crossing the pixels of an image (left), the average value of the weight matrix (center) and the variance (right). Red arrows show 0 value in the variance representation meaning that 1 ray sum cross these 4 pixels.

6.3.3. Electrical capacitance CT algorithms

The aim of image reconstruction process for Electrical Capacitance Tomography – ECT is to reconstruct the electrical permittivity distribution of the material inside the sensor. This process usually called as “Inverse Problem” is ill-posed and ill-conditioned. The solution of it is very susceptible to the error and to the measurement noise. Relationship between the electrical permittivity and measured capacitance is strongly non-linear. The electrical field is disturbed by the material distribution. This is mostly called as “soft - field” effect. The measured capacitance value depends strongly on the surface of the electrode and on the diameter of the ECT sensor. The length of the electrodes is usually the same as a diameter of the sensor and the width is determined by the total number of electrodes located on a ring. Designing too long layers of the electrodes makes that the final image of the cross-section can be a great averaging of the reality. Simultaneously too short layers affect the small capacitance values and the measurement is susceptible to noise.

The tomography team of the Computer Engineering Department (CED) of Technical University of Lodz (TUL) carried out a lot of preliminary experiments with its own phantoms before the experiments with the phantom provided for the project was started. CED has developed its own software for image reconstruction of ECT. It is developed using C++ programming language and works under Microsoft Windows operating system. The software uses the multithreaded character of the system which allows the full control of the reconstruction process by the user. Additionally the separation of the calculation and visualization modules allows maximizing computing power. Image visualization is powered with the modern 3D graphics hardware and OpenGL library.

The following software modules can be distinguished:

- the ECT sensor modeling with FEM mesh generator,
- the FEM solver for ECT measurement simulation,
- the sensitivity matrix calculation,
- the image reconstruction.

The control panel lists the application modules cited above. Thanks to them it is possible to modify the individual parameters of the whole reconstruction process as: Mesh density, electrodes number, phantom of permittivity distribution as boundary conditions for the simulations, measuring capacitances, adding the Gauss' noise and its variance value to the simulated data; the whole mesh can be exported: nodes coordinates, triangular connections of the nodes, material value in each triangle), voltage on a sender and receiver electrodes, maximum and minimum of the permittivity values; the potential values at the nodes of the mesh as well as the vector of the calculated capacitances for the given ECT sensor model can be exported, exporting the sensitivity matrix to file, reconstruction algorithm, relaxation parameter; exporting the reconstructed image as a bitmap file and as a text in "m"- file format for Matlab.

The flow chart of the application is shown in Figure 101. In the figure the mutually dependences of the modules and the multithreading was marked.

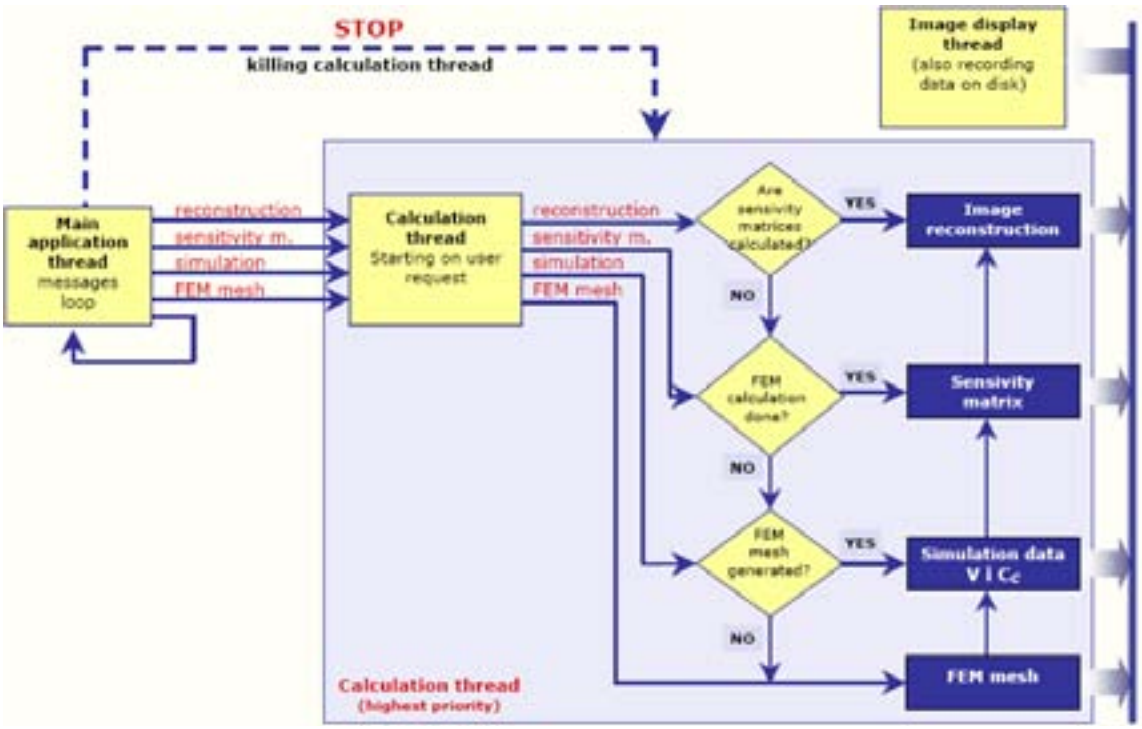

FIG. 101. The application flow diagram.

6.4. CALIBRATION OF CT SYSTEMS

6.4.1. Electrical capacitance tomography

The calibration process should take into account the above consideration in order to be performed precisely. This is a fundamental assumption of the electrical capacitance tomography (ECT) technique measurements. This calibration should be done both for the sensor and the measurement unit and should precede the right measuring process for the given object. The following calibration steps are performed in order to correctly prepare the ECT equipment:

Usually this calibration process consists of two steps. In the first one the pipe with the sensor volume is filled out with the material of low electrical permittivity. For the most common processes it is air with the permittivity equal to one. It is worth to mention that the pipe should be carefully emptied what in the industrial circumstances is hardly to achieve. As a result of measurement the vector of measured capacitances $\mathbf{c}_{min}$ is given:

$$\mathbf{c}_{min} = \begin{bmatrix} c_{0min} \\ c_{1min} \\ \vdots \\ c_{(N-1)min} \end{bmatrix}$$

where N is the number of independent measurements (for n electrodes system it is calculated as $n(n-1)/2$).

In the next step the sensor volume must be filled with the material with the possible higher permittivity. In case of having the loose material it is hardly to fill the sensor exclusively with the material. Those materials are usually in the form of the porous grains mixed with air or water. Therefore the real value of permittivity depends on the concentration and the humidity of the material. Similarly, we had a problem with the tested phantom when we had to fill the holes with the oil which is a different material then the whole phantom. After the pipe is filled out the vector of capacitances for maximal permittivity values is measured and saved as $\mathbf{c}_{max}$:

$$\mathbf{c}_{max} = \begin{bmatrix} c_{0max} \\ c_{1max} \\ \vdots \\ c_{(N-1)max} \end{bmatrix}$$

Now every measured capacitance c_i must be normalized using values $c_{i\,min}$ and $c_{i\,max}$ as components of the vectors $\mathbf{c}_{min}$ and $\mathbf{c}_{max}$ are respectively producing the value $c_{i\,n}$ according to the equation:

$$c_{i\,n} = \frac{c_i - c_{i\min}}{c_{i\max} - c_{i\min}}$$

Such normalization causes that for completely filled sensor the relative measured capacitances are close to 1 and for empty one close to 0. The vector of all values is called as a “raw data” despite of its normalization. Only normalized data can be analyzed or reconstructed, otherwise the changes of the capacitances will not take into account the different distances between the electrodes. The capacitance of the neighbored pair of electrodes is much higher than of the opposite ones. Additionally, in the ECT system with the charge – discharge circuit the last electrode stands never as a sender.

6.4.2. Gamma CT

1. Normalization CT calibration

For each and every source and detector position the attenuation of a mono-energetic gamma-ray beam is given by Lambert Beer's exponential decay law:

$$I = I_0 \exp\left[-\int \mu(r)dr\right]$$

where I is the transmitted beam, I_0 is the incident beam, μ is the linear attenuation coefficient of the sample to be imaged, and r is the path length through the sample. The raysum p_j is the average linear attenuation along the beam path, r:

$$p_j = \overline{\mu}_j = \int \mu(r_j)dr = \ln\left(I_{0j} \middle/ I_j\right)$$

The subscript j denotes the ray or projection, and for each ray there are normally two calibration measurements, p_{Ej} and p_{Fj}, representing materials with the lowest (empty vessel) and highest (full vessel) attenuation coefficient, respectively:

$$p_{Ej} = \mu_{Ej} = \frac{1}{d}\ln\left(I_{0j} \middle/ I_{Ej}\right)$$

$$p_{Fj} = \mu_{Fj} = \frac{1}{d}\ln\left(I_{Ej} \middle/ I_{Fj}\right)$$

These calibration measurements should be carried out with a long acquisition time to reduce errors due to statistical errors. Noise due to the environment of the measurement system and the aging effect on detectors can influence the performance and the resolution of the system. New calibrations should always be done after system reinstallation.

All raysums are normalized with respect to these calibration measurements so that the normalized raysum is between zero and unity:

$$p_j^N = \frac{p_j}{p_{Fj}} = \frac{\overline{\mu_j}}{\mu_{Fj}} = \frac{-\int \mu(r_j)dr}{\frac{1}{r}\ln\left(I_E \middle/ I_F\right)} = \frac{\ln\left(I_{Ej} \middle/ I_j\right)}{\ln\left(I_{Ej} \middle/ I_{Fj}\right)}$$

2. Effect of source properties on reconstructed image

In gamma ray CT, the reconstruction image is affected by several factors. It is not easy to evaluate how much the individual factor affects the reconstruction image quality. Nevertheless we can consider several factors to mainly influence the result. First one to consider is energy of source. In gamma transmission CT, the higher energy source tends to make blur image especially in lower dense or small object. The scattered radiation from energy scattered or direct radiation have more possibility to be detected through the shield material than the lower energy gamma ray. As a result the actual detection area of detector became wider, thus result in fuzzy image (Fig. 102).

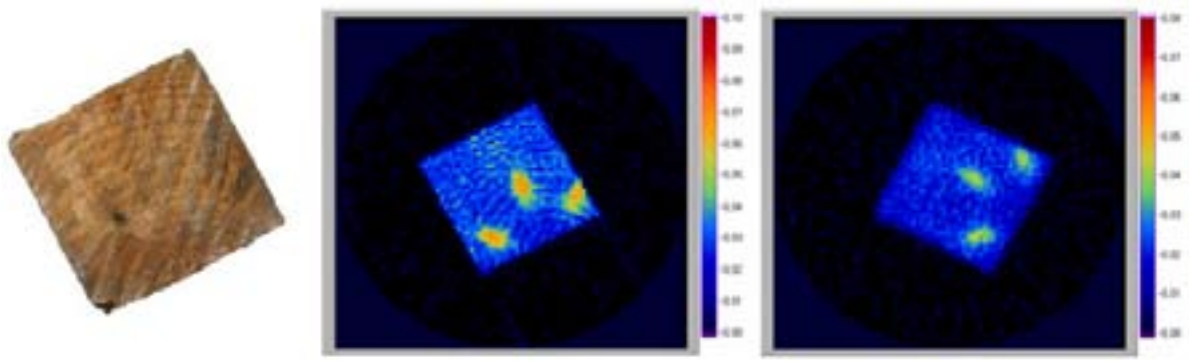

FIG. 102. Reconstructed image from different gamma energy source (left: ^{137}Cs, right: ^{60}Co).

But in many case higher energy gamma ray has good result. When the object is big enough for the detector size or the density of material is high, higher energy source can give better result (Fig.103).

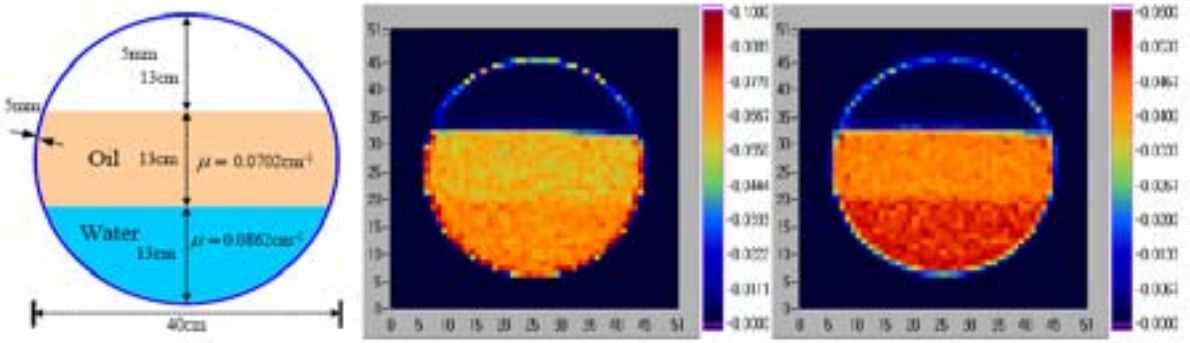

FIG. 103. The image result from different energy.

The other factor to consider is detection energy threshold setting. We can measure photon peak or full spectrum in gamma ray CT. Normally, by measuring photon peak we can get better result because it can reduce the scattered radiation. The use of collimator and full peak show the improved image (Fig. 104).

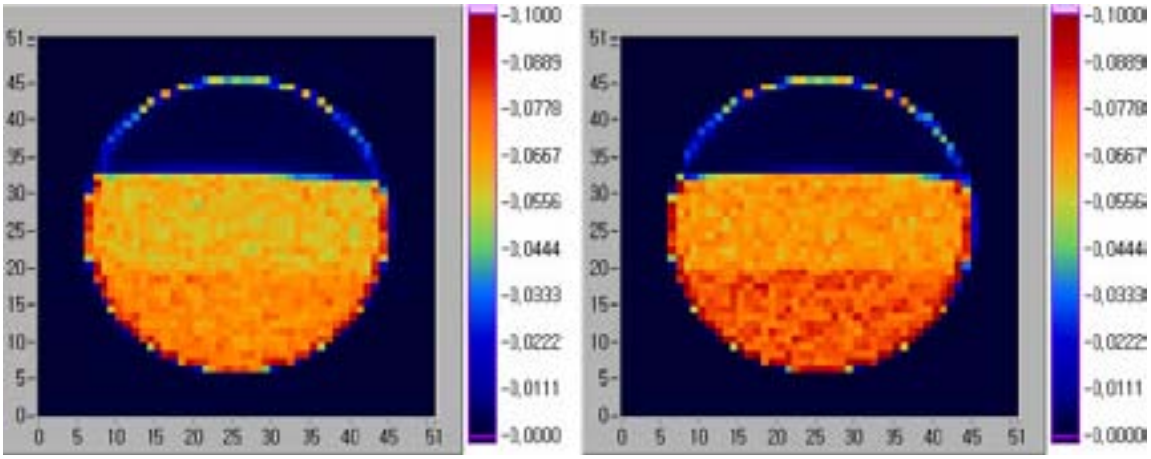

FIG. 104. Detection energy threshold level of 35keV (left) and 500keV (right).

But the count rate is inversely proportional to the aperture size of collimator. And normally the count from full peak is less than about 30% of non spectroscopic counts. The count rate is also very important factor in gamma ray measurement. It should be maintained a reasonable aperture size of collimator because low count rate results in higher statistical noise. In diagnoses of large scale industrial process column, the use of high energy gamma ray is necessary and the large sized detector is required. Sometimes there can be many cases where the detection efficiency outweighs the precise modelling especially in large scale process diagnosis.

7. AVAILABLE CT IMAGING SOFTWARE

Brief explanation of type of software

A computer controlled flexible geometry gamma-ray tomograph has been used to acquire experimental data for different measurement geometries, and these data has been used for image reconstruction with different iterative algorithms. Graphical programming software LabVIEW from National Instrument was used to develop different modules making up the total program (Fig. 105).

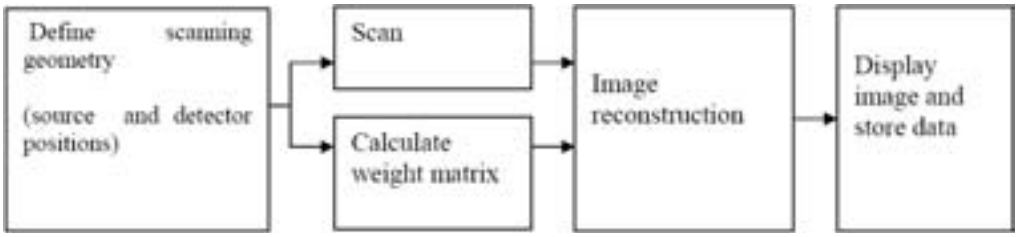

FIG. 105. The different modules making up the total program.

The defined scanning geometry module is a graphical user interface permitting to the user to set the desired optimal geometry by specifying:

- The number of sources.
- The number of detectors.
- Width of the source and the detector.
- Distance source sample.
- Distance source detector
- The position and size of the sample.
- The number of the pixels in the image to be viewed.
- The counter triggers level.
- The data acquisition time.

The Scan module automatically moves the tables in order to place the source, the detector and the sample in the desired sequence of locations and takes a measurement for each location. To reconstruct the image, we need the weight matrix, which depends on the system geometry, so the need of an automatic weight matrix generation. The weight matrix module generates the corresponding values. In the reconstruction module, different algorithms are available to the user. The last module displays the image, calculates the error and stores the data.

7.1. FEMINA SOFTWARE FOR ANALYTICAL TRANSMISSION TOMOGRAPHY

FEMINA software (prepared at Czech Technical University) is valid for analytical transmission tomography which works with limited number of gamma beams. The simplest experimental arrangement consists in using several γ emitters and collimated detectors, monitoring attenuation of rays due to absorption in material. Femina software e.g. supposes that after suitable calibration the following basic equations for volume solid fraction in suspension are:

$$\rho_v L = L\mu_s (1 - \frac{\mu_l}{\mu_s}) \ln \frac{N_{ref}}{N}$$

where N_{ref}, is number of registered pulses in calibration and N in measurements, L is distance (length of beam) , and μ_l , μ_s are linear attenuation coefficients in liquid or solid particles.

The measured signal of an arbitrary pair emitter-detector can be expressed as a mean value of the unknown volume fraction $\rho(x,y)$ along the beam. Experimental data are therefore represented by M values ρ_{m1}, ρ_{m2}, …, ρ_{mM} , which enable to identify a density distribution $\rho(x,y)$ by the model function. The model function is selected according to the presumed distribution of solid particles, and can be defined as a quite general nonlinear function of N/parameters $A_1,\ldots,A_N$ (nonlinear models based e.g. upon Bessel, exponential and harmonic functions are implemented in FEMINA in script files). However, in this contribution much more simple linear models will be presented:

$$\rho(x,y) = \sum A_i \varphi_i(x,y)$$

where A_i . are constants and φ_i (x,y) are basis function. A different pattern is used for an unknown arbitrary distribution, another for distribution, which is e.g. symmetrical around vertical axis etc. The n values of the constants A_i are determined from measured attenuation of at least n different beams.

FEMINA software starts with definition of outline and then we locate emitters and detectors as points using mouse (or by using the special command if you have already prepared the coordinates in an ASCII file.). The connecting lines emitter-detector are defined, and points of intersection with the cross-section perimeter are calculated. These new points define abscissas, along which integrals of function $\rho(x,y)$ will be calculated.

Next step is the definition of function $\rho(x,y)$ with parameters *A,B,C:*

```
FUNDEF 1,A+B*((XX-.5)**2+(YY-.5)**2)+C*(XX-.4)*(YY-.4);
```

Now the experimental data in form of a text file (free format can be used) are given to as:

N_{ref1} N_1
N_{ref2} N_2
…
N_{refN} N_N

and import them into FEMINA (for example) the 4th (N_{refi}) and 5th (N_i) columns of matrix MOP by using the special command. The mean densities are then calculated from the values recorded by detectors N_i and N_{refi}.

The model function is selected according to the presumed distribution of the density. A different pattern is used for an unknown arbitrary distribution, another for distribution, which is e.g. symmetrical around vertical axis or for discontinuous mass distributions. The *n* values of the constants A_i are determined from measured attenuation of at least $m=n$ different beams.

While this approach can be applied for quite arbitrary shape of cross section or even for an 3D case, the most frequently encountered geometries, i.e. circular and rectangular cross sections can be processed more easily using the dialog panel accessed from the menu bar cross section, shown in figure 106.

In this panel we fill the X,Y positions of emitters and detectors (assuming that the origin of the cartesian coordinate system is in the center of cross section), radius of circle or lengths of sides. At the same time measured values N_i and N_{iref} are specified for each ray together with the reference density ρ_{ref} and parameter *a*.

Several model functions were prepared and can be chosen for data evaluation. When e.g. the system under study is mechanically mixed suspension in high vessel with stirrer situated in the axis of the vessel and when a counting time is much higher than time of stirrer revolution, the rotational symmetry of concentration may be expected.

In this case the local volume fraction of solid phase ρ(x,y) depends only on the distance from the axis in the cross section plane. It is assumed that the dependence of concentration on x and y coordinates can be approximated by a finite linear combination of radial basis functions:

$$\rho(x,y) = \sum A_i [\sqrt{(x^2 + y^2)}]^{2i}$$

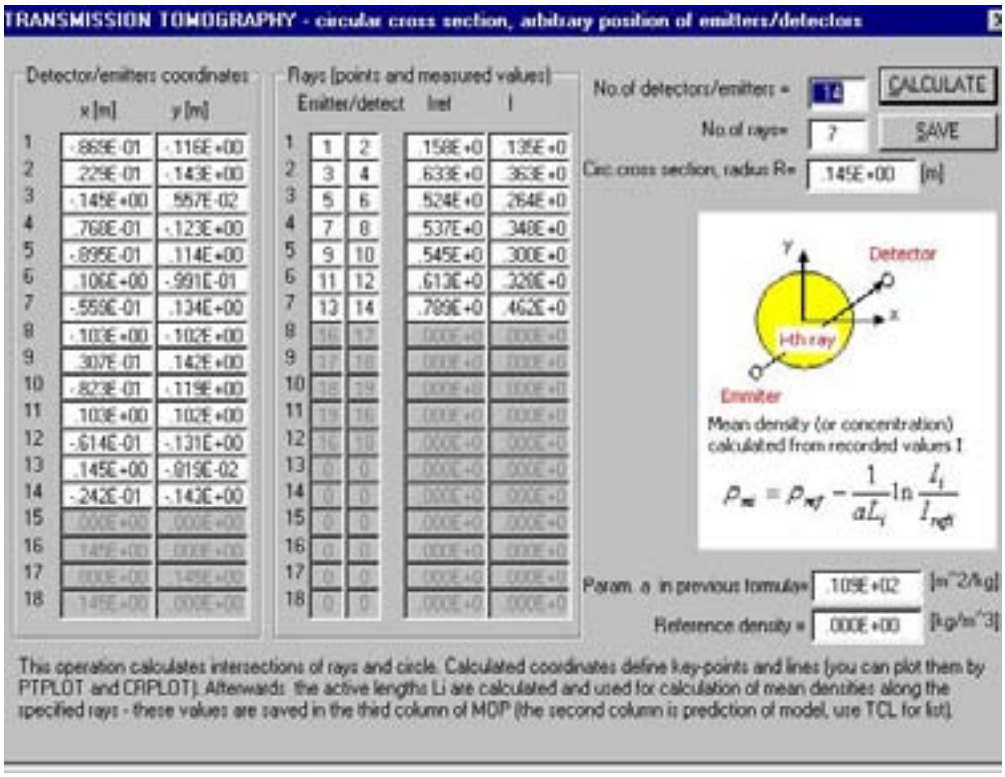

FIG. 106. Data input for transmission tomography.

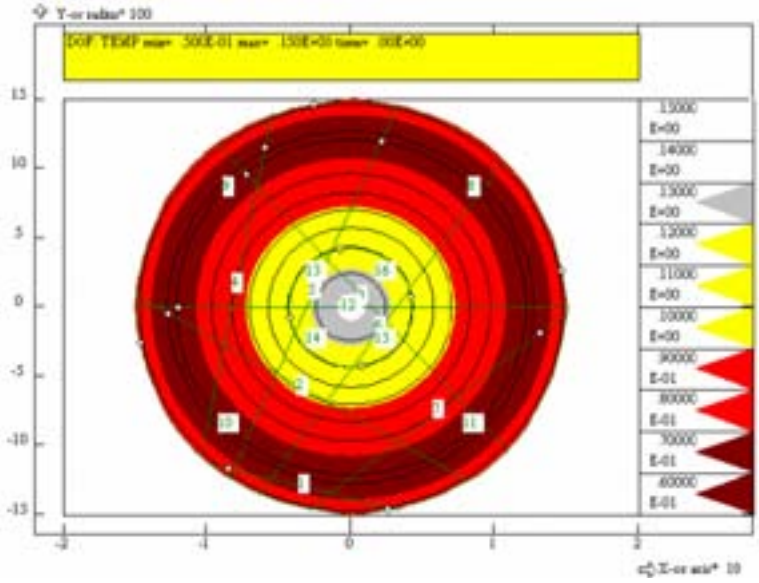

FIG. 107. Example of symmetrical distribution.

As simple basic function for asymmetry is suggested:

$$\rho(x,y) = \sum A_i \varphi_i(x,y) = A_1 + A_2 \sin\alpha + A_3 \cos\alpha$$

where $\sin \alpha = x/\sqrt{(x^2 + y^2)}$; $\cos \alpha = x/\sqrt{(x^2 + y^2)}$

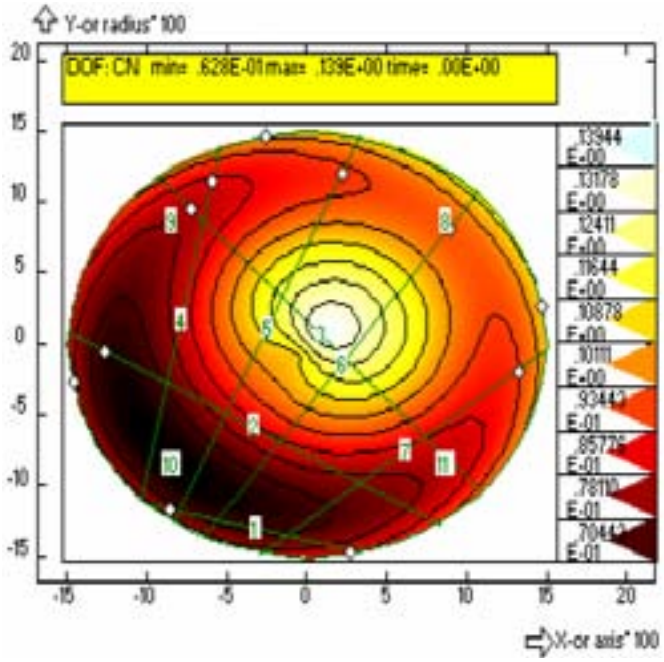

FIG. 108. Example of unsymmetrical distribution.

Quadratic polynomial can be used as well :

$$\rho(x,y) = A_1 + A_2 (x^2 + y^2) + A_3 \, x \, y$$

Of course, generally the relations of higher order with more constants can be utilised.

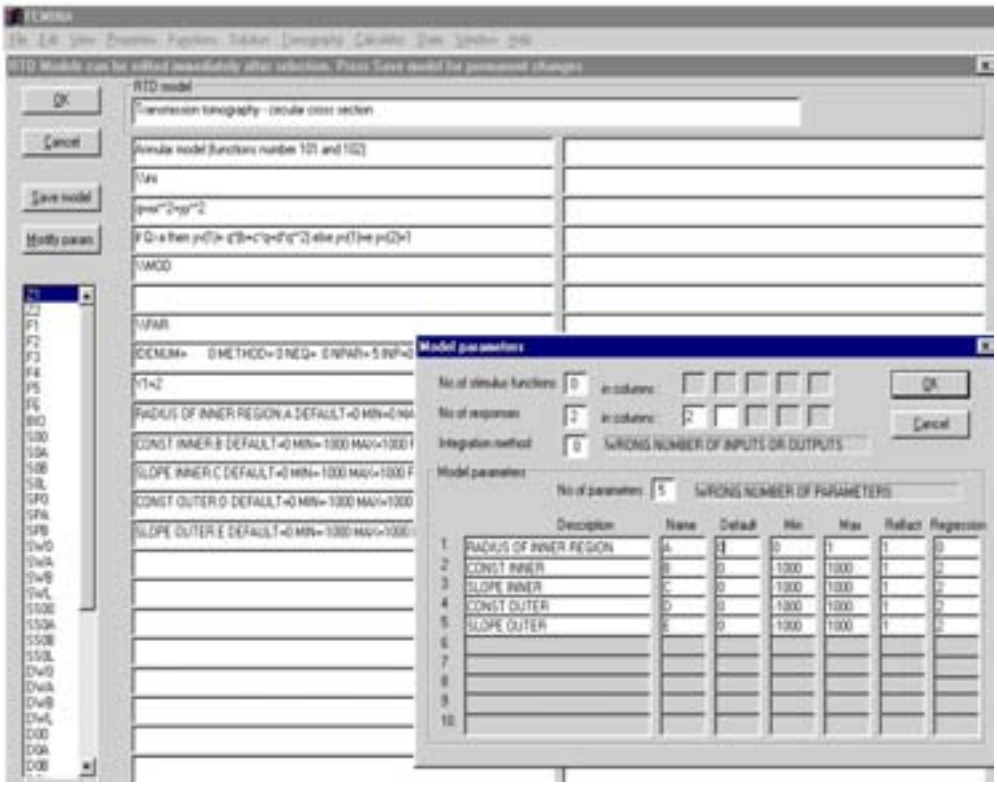

FIG. 109. The model and initial values of the parameters.

The bulk volume fraction of solid particles in the “beam” volume is evaluated from line integral on the basis of the chosen model functions. These values evaluated for all beams are used for evaluation of model parameters Ai by comparison with experimental values by iterative methods e.g. the least squares method. Two optimization procedures can be utilized in software Femina to find proper values of the constants: OPTIMA and SOMA. First one is practically the same method as Marquardt Levenberg method used for nonlinear regression. SOMA (Self Organising Migration Algorithm) belongs to the group of stochastic algorithms as MonteCarlo. (More details about procedures are given in user manuals FEM3AI1.pdf (content, introduction), FEM3AI2.pdf (tutorial), FEM3AI3.pdf (quick reference), as well as in theoretical manual FEM3AII.pdf . There is also software for ten models prepared for different distribution of mass in the object with circular or square cross section.

7.2. CEA SOFTWARE

7.2.1. Software for gamma tomography based on ILST Algorithm

A software for image reconstruction process based on the ILST (Iterative Least Square Techniques) algorithm was developed. The flowchart of the algorithm is shown in Figure 110. The software generated automatically a weight matrix based on the setup design. The weight matrix characterizes the contribution of each pixel located along each gamma-ray path. This weight matrix was used for reconstruction process. The result of the reconstruction is shown in Figure 111.

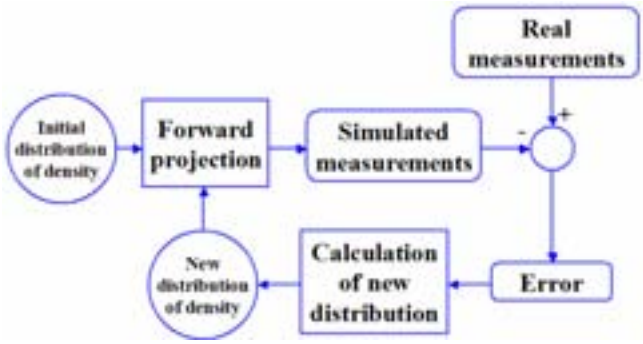

FIG. 110. The schematic of ILST algorithm.

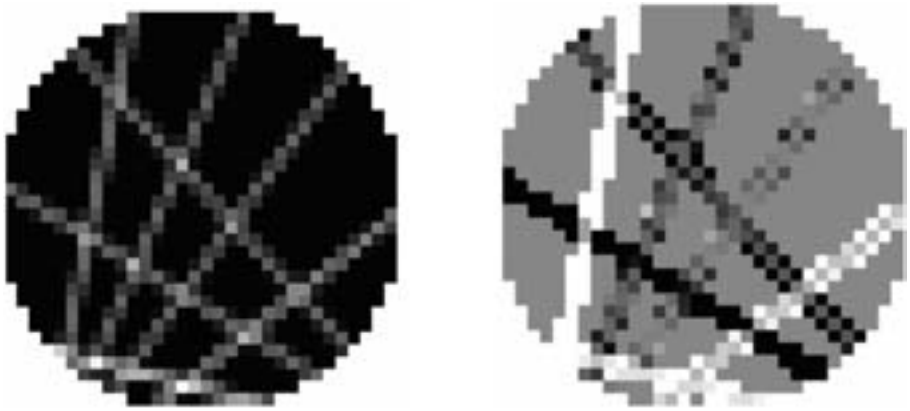

FIG. 111. Visualisation of weight matrix (l.) and reconstructed image (r.)

The quality of reconstructed image was very low, because a lot of pixels are not taken into account in the reconstruction process.

There are 2 sources and 7 detectors only, and rays do not cover the whole cross-section of the vessel. This has a major effect on the low quality of the image. One possible way to improve the quality may is by simply increasing the number of detectors (at least 30 – 40 detectors).

In order to improve the image quality, CEA has developed an original software (author PhD student S. Lewandowski) based on an interpolation approach proposed by V. Mosorov. The main window of application is presented in Figure 112.

FIG. 112. Main window of application for gamma ray tomography reconstruction.

7.2.2. Results

Reconstructed images consisting of 32x32 pixels obtained by the approach for two cases:

- water with solid particles without mixing,
- water with solid particles after mixing,

are presented in Figures 113 and 114, respectively. The number of iterations for the ILST algorithm was equal to 10.

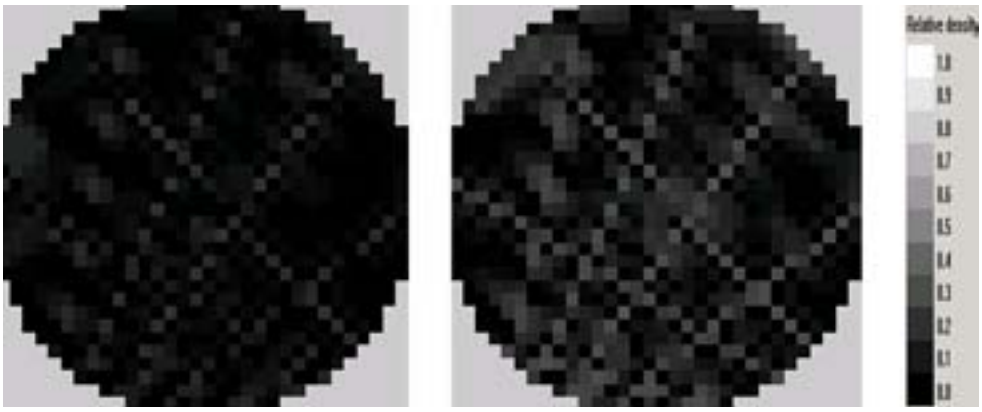

FIG. 113. Reconstructed image of water with solid particles without mixing: l.) for concentration of particles 0.1 r.) for concentration of particles 0.25.

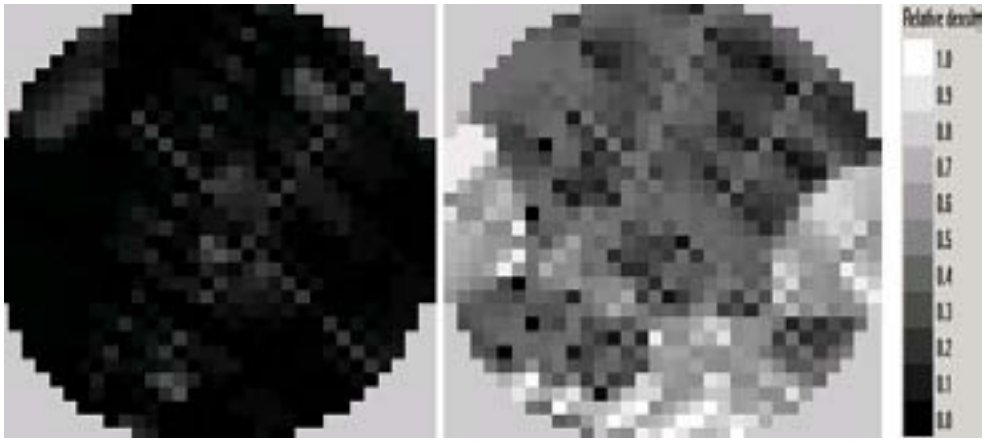

FIG. 114. Examples of reconstructed images of water with solid particles after mixing.

It is very difficult to extract any information about investigated suspension from obtained reconstructed images. One can see that the image quality is not homogeneous. In the bottom part of the image where more beams are crossing and therefore the data reconstruction is improved, the quality of image is just a little better than in upper part.

7.2.3. Conclusion

The quality of reconstructed images is better than previous classical approach but not satisfactory enough. The future work will be concentrated on the development of new theoretical approach for image reconstruction with limited number of gamma beams.

7.3. IRREGULAR PIXELS [REXELS]

7.3.1. Introduction

The measured values (from tomograph's detectors) are a function of the distribution of the physical property (density in gamma CT) of the measured system. Reconstruction algorithms solve the inverse problem i.e. determination of the distribution of density from measured values. There are several approaches to image reconstruction. The most common algorithms in gamma CT method are iterative algorithms. The approach of iterative reconstruction techniques is to apply correction to image of the process. This procedure is repeated until a satisfactory accuracy is achieved. There are several types of iterative algorithms: ART (Algebraic Reconstruction Technique), SIRT (Simultaneously Iterative Reconstruction Technique) etc. Because of numerical calculation, before reconstruction the area under examination must be discretized (divided into finite number of elements).

7.3.2. Classical approach

In classical approach the area is divided into *N* identical elements (so-called rexels). This approach is shown in Figure 115.

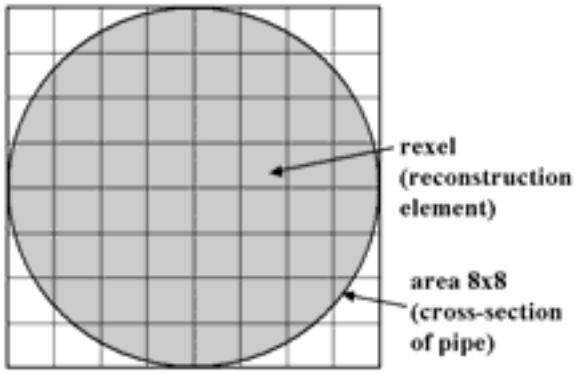

FIG. 115. Classical approach to discretization.

In classical approach the grid is regular and shape of the rexel is always the same. It causes that boundaries of grid (rexels) are not match to boundaries of rays. The second problem is determination of optimal grid resolution. For low grid resolution image will be unclear, for high resolution image will be blurred (Figure 116).

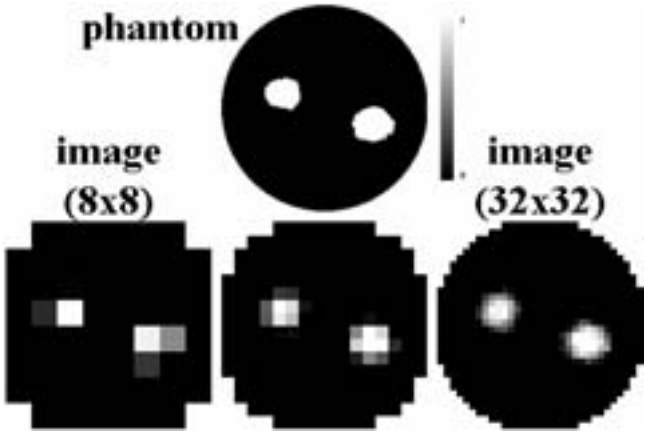

FIG. 116. Examples of image reconstruction for different resolution.

7.3.3. Proposed approach

The new approach is based on the idea that the area under examination is divided by boundary of rays. In this case resolution of image (i.e. number of rexels) is strictly determined. The idea of this approach is presented in Figure 117.

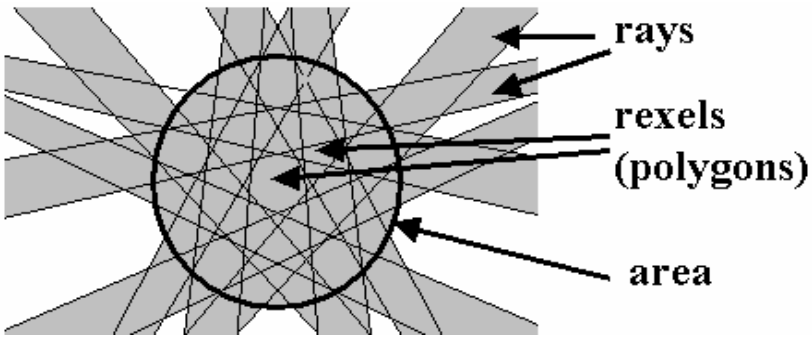

FIG. 117. Irregular discretization of the area.

To determine the shape of the rexels (polygons) thick grid (*nxn* elements) is superimposed into area under examination. For each element of thick grid, it is determined if individual element is included in individual ray. Elements include to the same rays are merged in one rexel. In Figure 118, three exemplary rexels are distinguished.

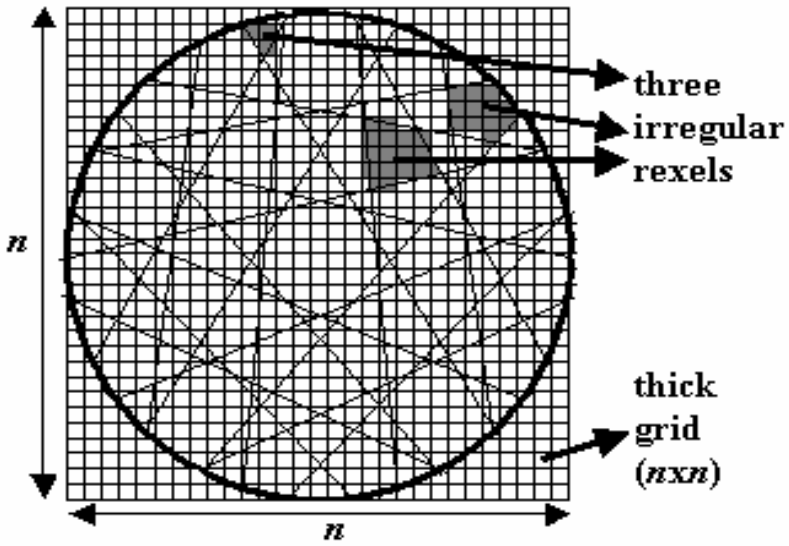

FIG. 118. Determination of irregular rexels.

In this approach very important question is how thick the grid should be (i.e. value of *n*). Figure 119 shows dependence between value of *n* and number of irregular rexels for two cases: for 85 detectors and for 35 detectors. Above this value, number of rexels is approximately constant. It means that all possible rexels are determined.

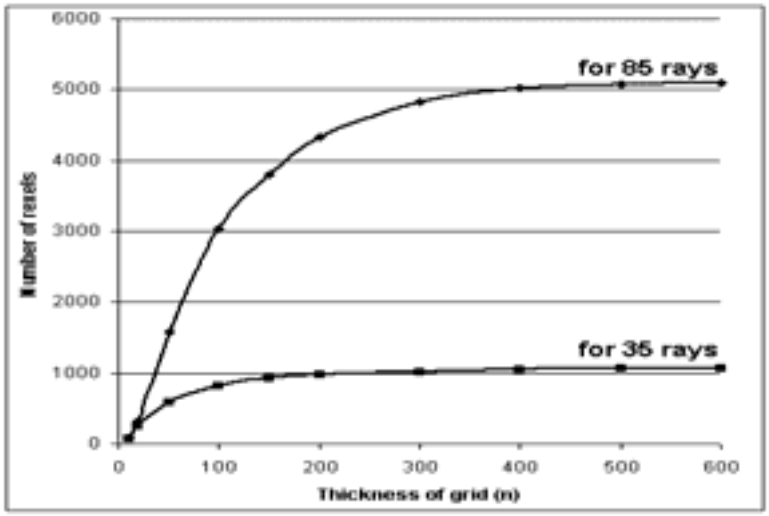

FIG. 119. Number of rexels vs. thickness of grid (n)

7.3.4. Results

Preliminary results of image reconstruction are shown in Figures 120 and 121. Images were reconstructed using ILST (Iterative Least Square Technique) algorithm for 35 measurements (Figure 120) and for 85 measurements (Figure 121), number of iterations was 100.

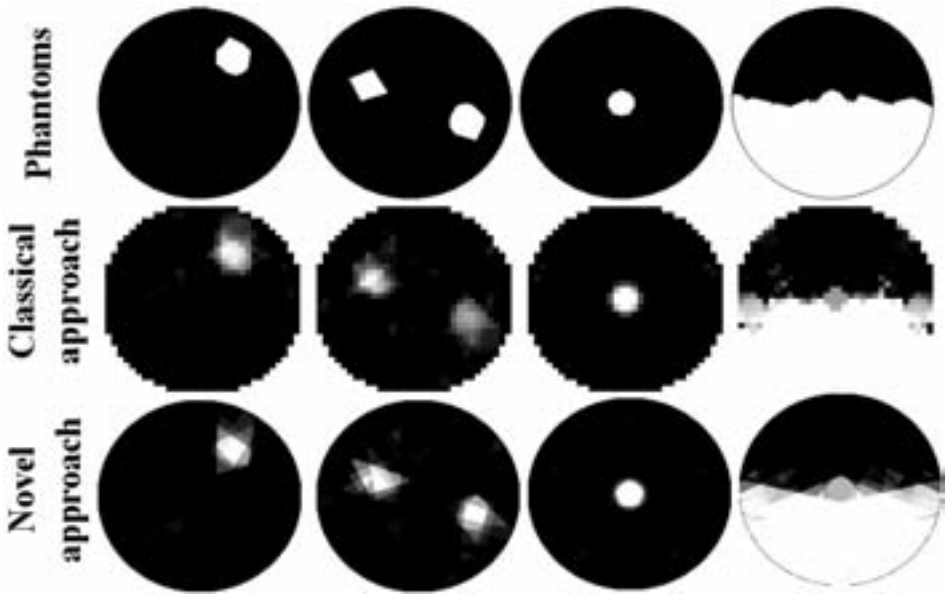

FIG. 120. Results of image reconstruction for 35 measurements.

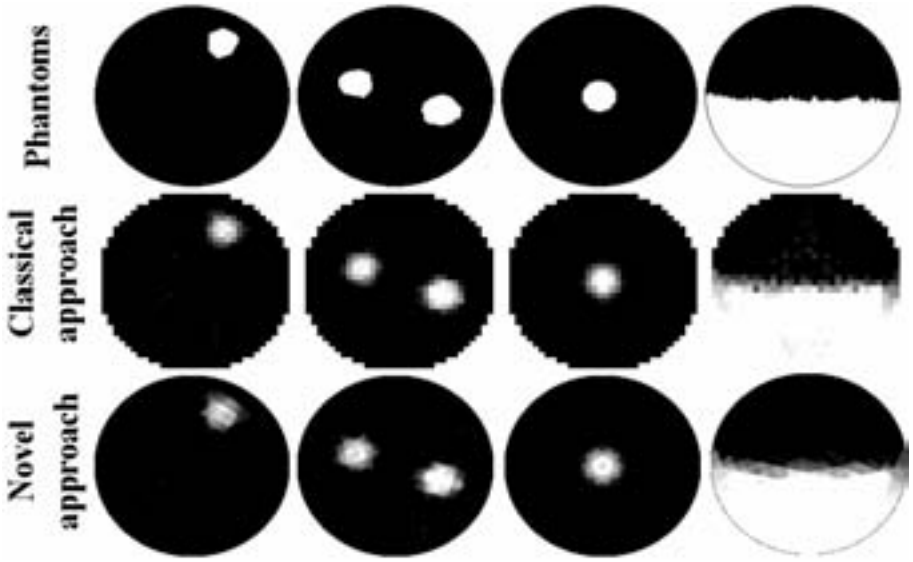

FIG. 121. Results of image reconstruction for 85 measurements.

7.4. IMAGE RECONSTRUCTION ALGORITHM SOFTWARE DEVELOPED BY THE REPUBLIC OF KOREA

The Korean CRP team carried out a lot of preliminary works on gamma ray tomography and developed its own software for image reconstruction of gamma-ray CT. It is developed using LabVIEW programming language and based on iterative reconstruction algorithm.

7.4.1. A set of linear equations

Iterative reconstruction technique solving a set of linear equations that consist of unknown variable, weight matrix and ray-sum. The ray-sum is determined by the measurement data. Weight matrix can be calculated from the geometry. And pixel values are the unknown variable to be determined. Therefore image reconstruction can lead to solving the unknown variable from ray-sum an weight matrix. The linear equation can be denoted as following.

$$\begin{bmatrix} H_{11} & H_{12} & H_{13} & . & . & H_{1N} \\ H_{21} & H_{22} & H_{23} & . & . & H_{2N} \\ . & . & . & . & . & . \\ H_{i1} & . & . & H_{ij} & . & H_{iN} \\ . & . & . & . & . & . \\ H_{M1} & H_{M2} & H_{M3} & . & . & H_{MN} \end{bmatrix} \begin{bmatrix} f_1 \\ f_2 \\ . \\ . \\ . \\ f_N \end{bmatrix} = \begin{bmatrix} g_1 \\ g_2 \\ . \\ . \\ . \\ g_M \end{bmatrix}$$

i=1~M: M total number of raysums

J=1~N: N: total number of pixels

Where f is unknown pixel, h is weight matrix and g is ray-sum measured.

7.4.2. Weighted matrix calculation

For the image reconstruction with iterative method, weighted matrix calculation is required. The weight matrix can be determined from geometry and normally is singular matrix. The weight matrix is impact factor that how the specific pixels interact with beam trajectory. There are several ways to determine the weight matrix. Six methods are introduced in the bibliography (G.A Johansen, "Gamma ray tomography software and image reconstruction" IAEA/RCA Regional training course on Industrial Process Gamma Tomography , Korea, October 11-15, 2004).

- 1/0 : beam crossing pixel; weight =1, otherwise 0
- Measurement path length in one pixel divided by the total measurement length
- Distance of measurement area to the pixel centre
- Measurement path length in one pixel divided by the pixel hypotenuse
- Measurement area inside a pixel divided by the total pixel area
- Measurement volume inside a voxel divided by the total volume

Among the six methods, "Measurement path length in one pixel divided by the total measurement length" and "Measurement area inside a pixel divided by the total pixel area" are developed using LabVIEW programming language by Korean CRP team.

Fig.122 shows the automatic weight matrix program by pixel intersection length. The more precise model of weight matrix we can set up, the better result we can have. But precise model need complex and much calculation time. We should compromise between complexity and accuracy.

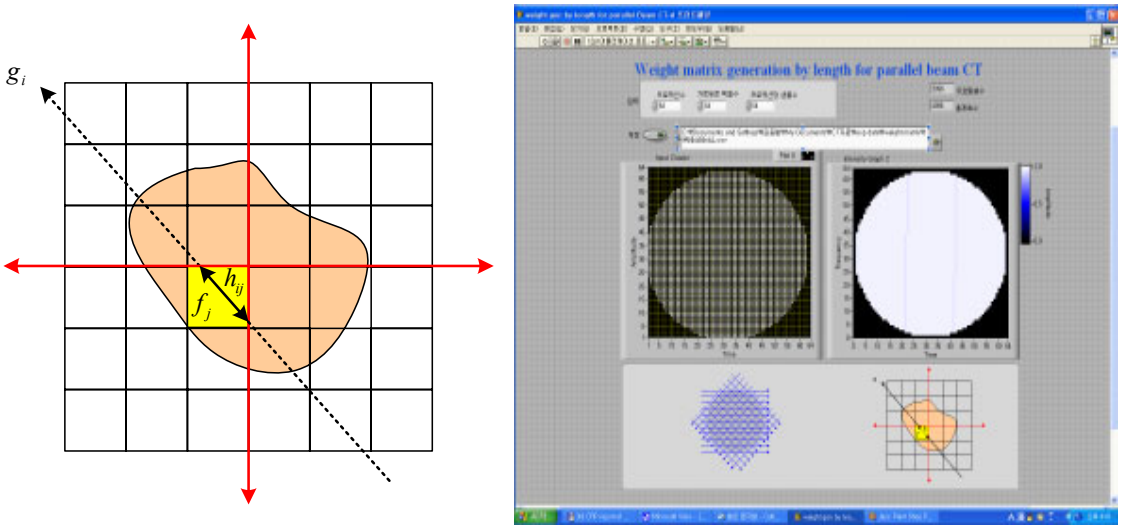

FIG. 122. Weight matrix determine from pixel intersection length.

Fig. 123 shows the result from the different weight matrix calculation methods. Weight matrix is dependant on geometry of tomography system. If the CT hardware is changed, the weight matrix should be recalculated.

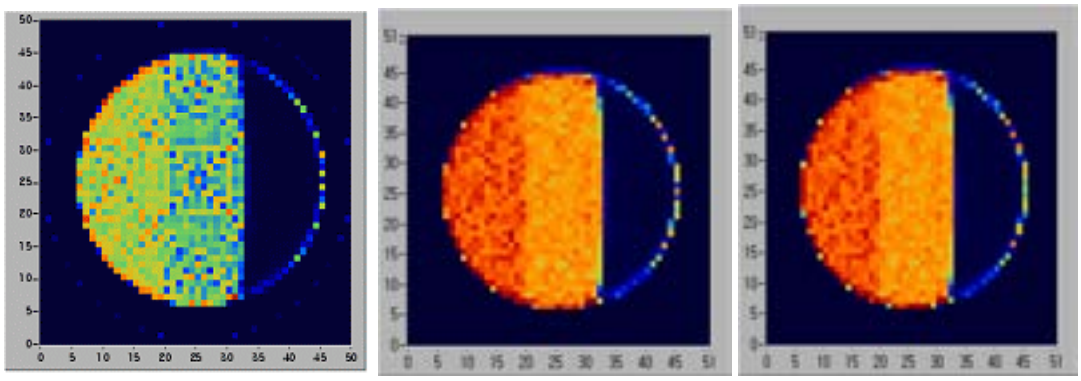

FIG. 123. Result from weighted matrix determined by 0/1(left), length(center) and area(right).

7.4.3. Iterative reconstruction technique

If we know ray-sum and weight matrix, we can solve the linear equation. There are known several ways to solve the set of equation with singular matrix. In algebraic reconstruction technique(ART) and its variation, there are ART, SIRT, MART and etc. ML-EM algorithm which is based on Poison model has been also popularly used. Korean CRP team has developed image reconstruction program baed on SIRT and ML-EM which are programmed using LabVIEW software. Simultaneous iterative reconstruction technique (SIRT) is a variation of ART. In SIRT, the projections are all performed simultaneously and then averaged. The equation below shows the SIRT algorithm. δ is relaxation number which controls convergence.

$$f_j^{(n+1)} = f_j^{(n)} + \delta \sum_{i=1}^{M} h_{ij} \frac{(g_i - \sum_{k=1}^{N} h_{ik} f_k^{(n)})}{\sum_{k=1}^{N} h^2_{jk}}$$

The sum of power of row in weight matrix is dividend. When a line of ray-sum doesn't interact ROI circle, the value of sum is zero. For this reason, when power sum of row is zero, it is deleted from the set of equations in the program. Its convergence is faster than EM but it has tendency to be often divergent when the relaxation number is too big.

The reference (Kenneth Lange and Richard Carson, EM reconstruction Algorithms for Emission and Transmission Tomography, Journal of Computer Assisted Tomography,1984) introduced the another equation:

$$f_j^{(n+1)} = \frac{f_j^{(n)}}{\sum_{i=1}^{M} h_{ij}} \sum_{i=1}^{M} h_{ij} \frac{g_i}{\sum_{k=1}^{N} h_{ik} f_k^{(n)}}$$

The Expectation Maximization algorithm has been widely used in a medical emission CT such as a single photon emission tomography (SPECT) and a positron emission tomography (PET). One of shortcoming of EM algorithm is slow convergence which normally takes 30~50 iterations for image result. And as the iteration numbers increase, the reconstruction noise arises. So the early termination is required for the better result.

In transmission tomography, the EM equation can be modified as equation:

$$f_j^{(n+1)} = f_j^{(n)} \frac{\sum_{i=1}^{M} (I_0 e^{(-\sum_{k=1}^{N} h_{ik} f_k^{(n)})} \cdot h_{ij})}{\sum_{i=1}^{M} I_i \cdot h_{ij}}$$

In spite of above-mentioned short-coming, the EM algorithm shows good result enough. Fig. 124 shows the ML-EM image reconstruction program and Fig. 125 shows example of images reconstructed from the different algorithms. The noise is more visible in FBP and EM than in SIRT but overall image quality is good in EM.

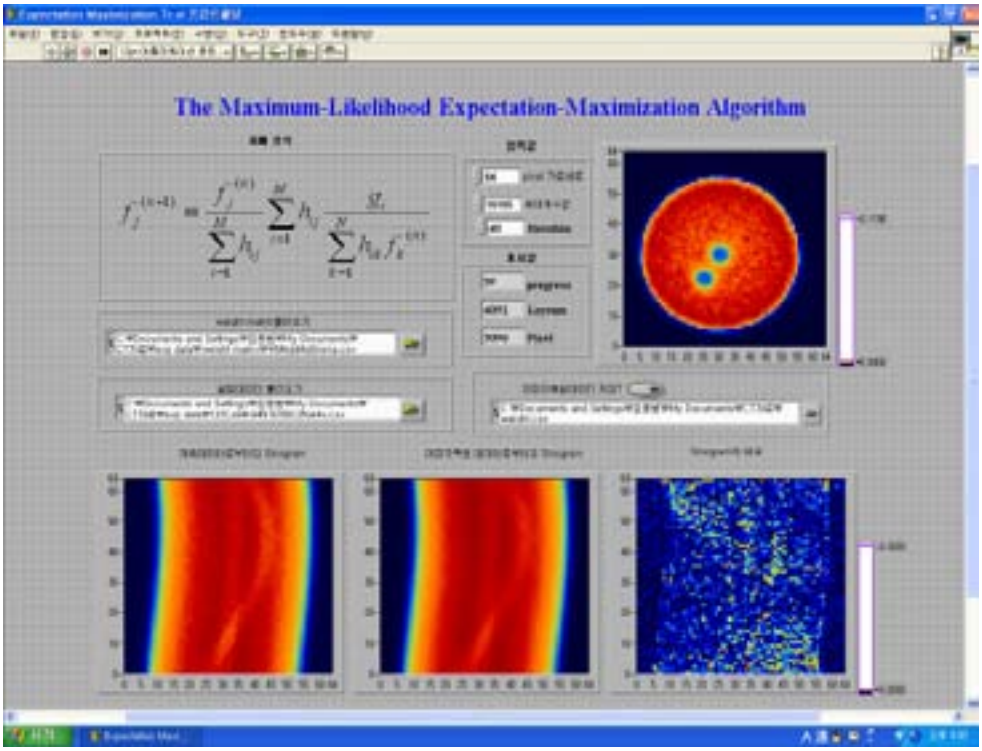

FIG. 124. Image reconstruction software based on ML-EM algorithm.

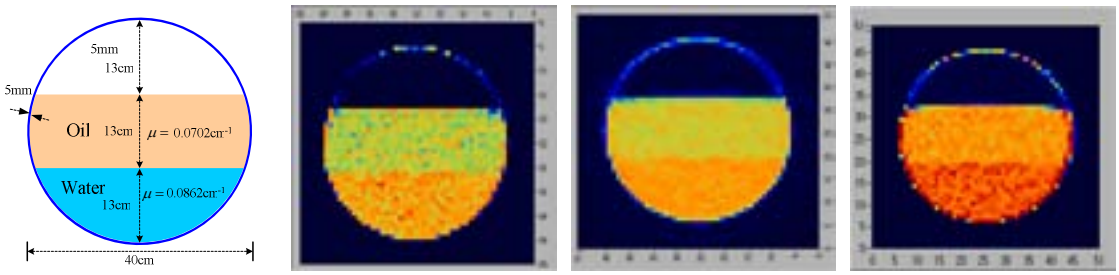

FIG. 125. The visual evaluation of algorithm by FBP(left), SIRT(centre) and EM(right).

7.5. ECT RECONSTRUCTION SOFTWARE

The aim of image reconstruction process for Electrical Capacitance Tomography – ECT is to reconstruct the electrical permittivity distribution of the material inside the sensor.

This process usually called as “Inverse Problem” is ill-posed and ill-conditioned. The solution of it is very susceptible to the error and to the measurement noise. Relationship between the electrical permittivity and measured capacitance is strongly non-linear. The electrical field is disturbed by the material distribution. This is mostly called as “soft - field” effect. The measured capacitance value depends strongly on the surface of the electrode and on the diameter of the ECT sensor. The length of the electrodes is usually the same as a diameter of the sensor and the width is determined by the total number of electrodes located on a ring. Designing too long layers of the electrodes makes that the final image of the cross-section can be a great averaging of the reality. Simultaneously too short layers affect the small capacitance values and the measurement is susceptible to noise.

The calibration process should take into account the above consideration in order to be performed precisely as a result from the measurement specificity of the ECT technique. This calibration should be done both for the sensor and the measurement unit and should precede the right measuring process for the given phantom. The following calibration steps are performed in order to correctly prepare the ECT equipment:

The measurement channel amplitudes gains adjustment. The profile of the ECT measurement is as follows:

- the value of the capacitance for the neighbored pair of electrodes is much higher than for the opposite one and the same measurement system in both cases is used,
- the higher permittivity value of the phantom affects the higher capacitance values.
- the maximum and minimum capacitances calibration for the specific sensor and for maximum and minimum permittivity of the phantom.

The tomography team of the Computer Engineering Department (CED) of Technical University of Lodz (TUL) carried out a lot of preliminary experiments with its own phantoms before the experiments with the phantom provided for the project was started. CED has developed its own software for image reconstruction of ECT. It is developed using C++ programming language and works under Microsoft Windows operating system. The software uses the multithreaded character of the system which allows the full control of the reconstruction process by the user. Additionally the separation of the calculation and visualization modules allows maximizing computing power. Image visualization is powered with the modern 3D graphics hardware and OpenGL library.

The following software modules can be distinguished:

- the ECT sensor modeling with FEM mesh generator,
- the FEM solver for ECT measurement simulation,
- the sensitivity matrix calculation,
- the image reconstruction.

Figure 126 shows the interface of the application given as a ECT reconstruction library attached on a CD. The control panel lists the application modules cited above. Thanks to them it is possible to modify the individual parameters of the whole reconstruction process as:

- mesh density, electrodes number, phantom of permittivity distribution as boundary conditions for the simulations, measuring capacitances, adding the Gauss’ noise and its variance value to the simulated data; the whole mesh can be exported: nodes coordinates, triangular connections of the nodes, material value in each triangle)
- voltage on a sender and receiver electrodes, maximum and minimum of the permittivity values; the potential values at the nodes of the mesh as well as the vector of the calculated capacitances for the given ECT sensor model can be exported,
- exporting the sensitivity matrix to file,
- reconstruction algorithm, relaxation parameter; exporting the reconstructed image as a bitmap file and as a text in “m”- file format for Matlab.

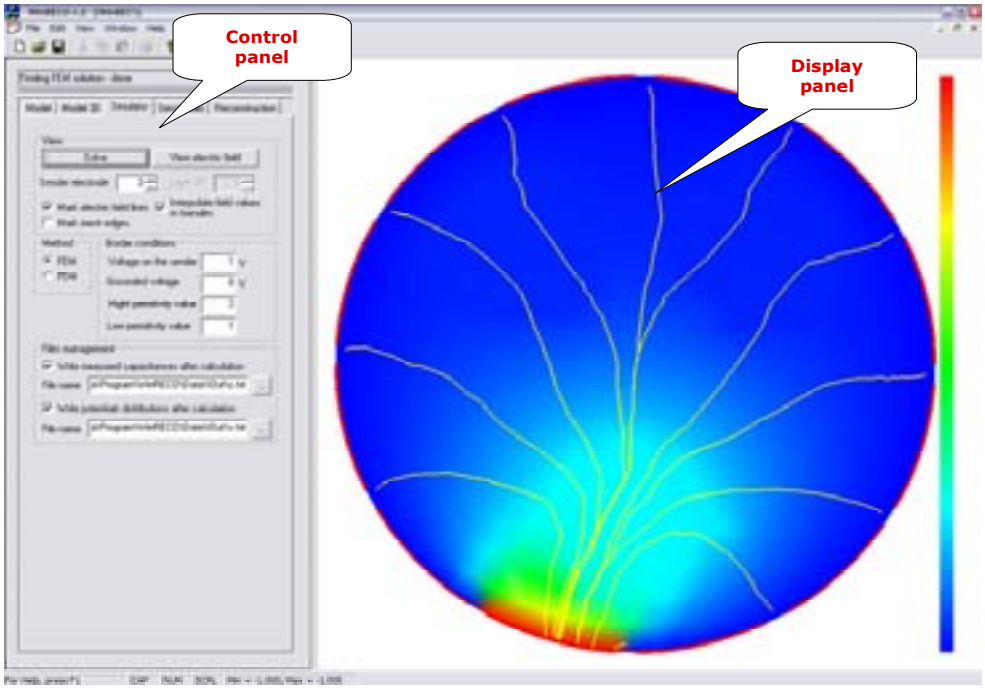

FIG. 126. Main interface of the ECT software. The control and display panels are shown.

For each of the application modules the control panel is given. Thanks to them it is possible to modify the individual parameters of the whole reconstruction process including mesh density, electrodes number, phantom of permittivity distribution as a boundary conditions for the simulations, measured capacitances, adding the Gauss' noise and its variance value to the simulated data; the whole mesh can be exported to the files.

The stored whole grid is kept into 4 files:

- g_nodes.txt the coordinates of the triangle nodes,
- g_simples.txt: the 3 nodes combination (indexes from the g_nodes.txt file) as a product for one element – triangle,
- g_electr.txt: every row of the file is given for a single electrode description. Every electrode is kept as a set of lines segments (i.e. one side of the triangle). Therefore the groups of two nodes can be seen. The value of zero is used for filling the null elements in the electrodes array.
- g_materials.txt: the normalized permittivity values of the material. The indexes of the values are compatible with the indexes from g_simples.txt file.

For each file the first row includes a number of elements except for g_electrodes.txt where additionally the number of electrodes can be found. For boundary conditions there are additional data that are useless for image reconstruction, so WinRECO is not able to export them.

Additionally for simulation proposes, the initial phantom of permittivity distribution can be imported from PRT file. This file consists of 32x32 values of image matrix. Some examples of such files can be found in DATA/PERMIT folder enclosed with WinRECO.

- voltage on a sender and receiver electrodes, maximum and minimum of the permittivity values; the potential values at the nodes of the mesh as well as the vector of the calculated capacitances for the given ECT sensor model can be exported to files (Fig. 127),
- export of the sensitivity matrix to file,
- reconstruction algorithm, relaxation parameter; export of the reconstructed image as a bitmap file and as a text in "m"-file for Matlab (Fig. 128).

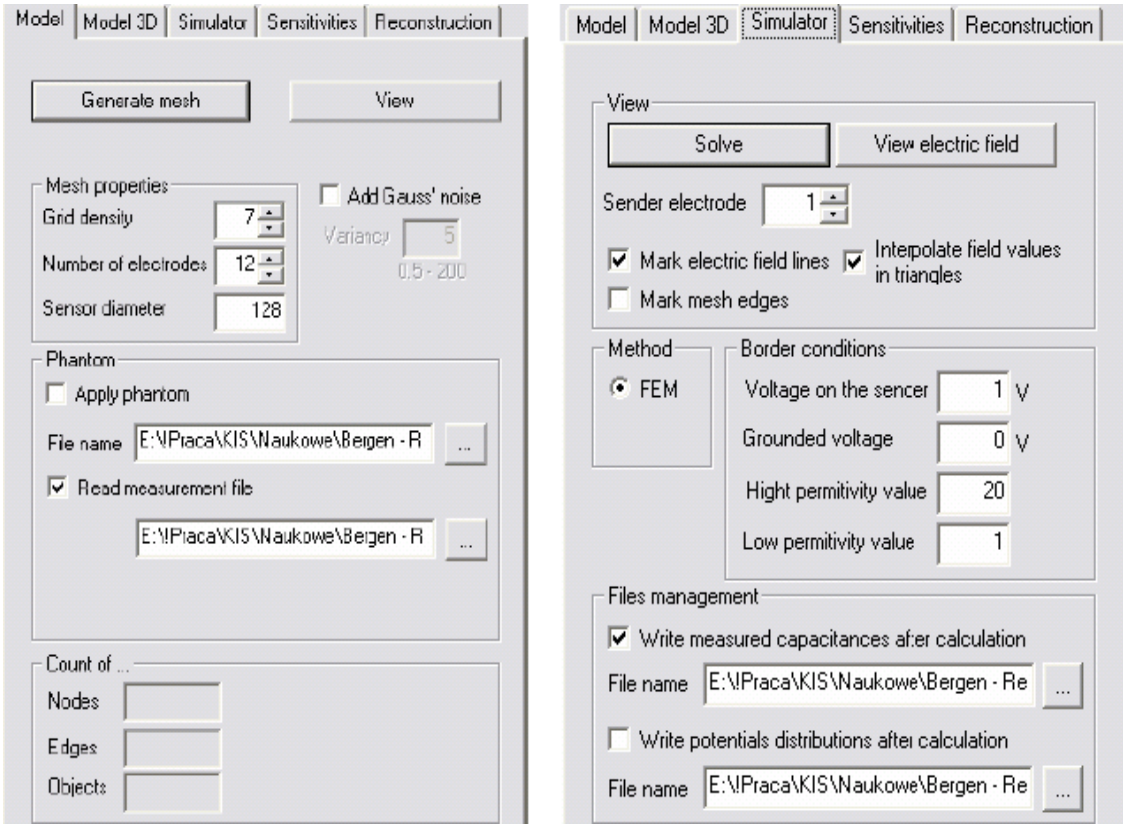

FIG. 127. The ECT sensor modelling panel (left) and FEM solver panel for ECT measurement simulation (right).

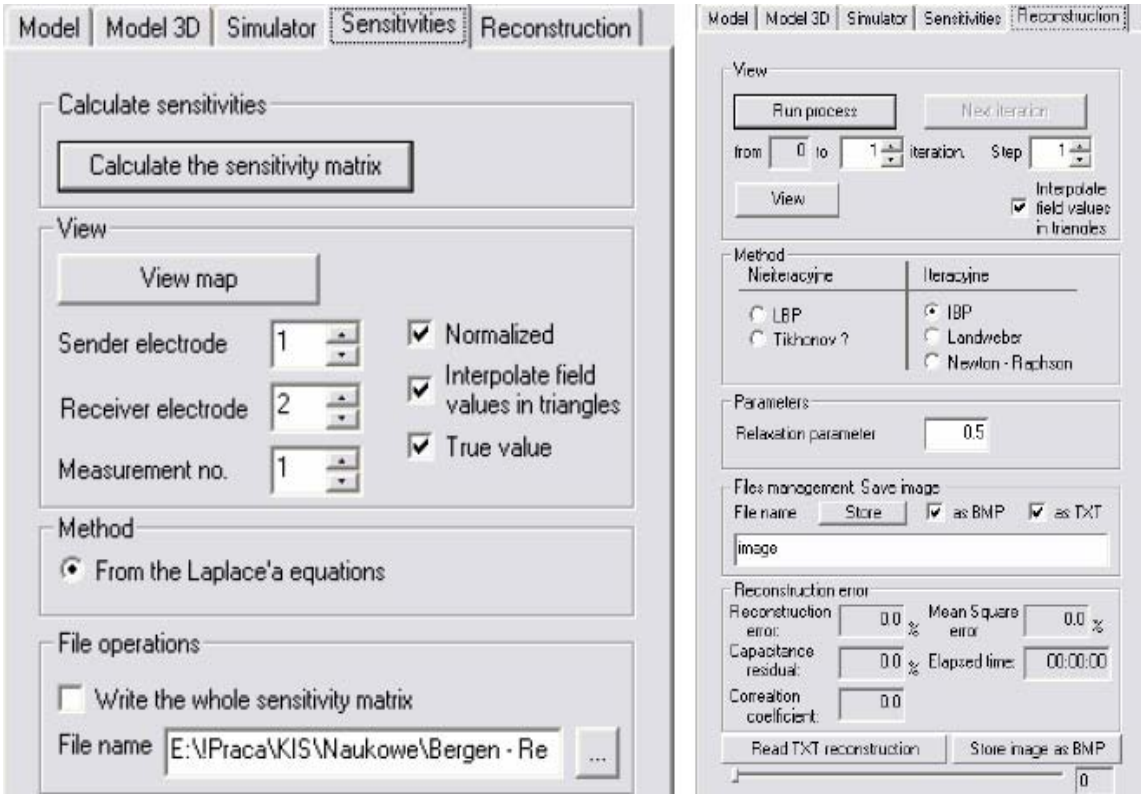

FIG. 128. The sensitivity matrix calculation panel and the image reconstruction panel.

BIBLIOGRAPHY

ABDULLAH, J., AFERKA, S., CRINE, M., TOYE, D., MARCHOT, P., Investigating the liquid distribution in a reactive distillation packing using high energy x-ray tomography, The 5th International Symposium on Measurement Techniques for Multiphase Flows (ISMTMF 2006), Macau, China, 10th to 13th December 2006.

ABDULLAH, J., RAHIM, R.A., Computed Tomography for Industrial Imaging and Process Investigation, IAEA/RCA Regional Training Course (RAS/8/091) on Industrial Process Gamma Tomography, Daejon, Korea, 11th to 15th October 2004.

ABDULLAH, J., MOHAMAD, G. H. P., HAMZAH, M. A., YUSOF, M. S. M., RAHMAN, M. F. A., ISMAIL, F., ZAIN, R. M., Development of a portable computed tomographic scanner for on-line imaging of industrial piping systems, Proceedings the 5th national seminar on non-destructive testing (NDT), Shah Alam, Malaysia (2003) ISBN 983-3006-00-0

ABDULLAH, J., SIPAUN, S. M., X-ray and Gamma-Ray Transmission Computed Tomographic Imaging of Archaeological Objects, Persidangan Kebangsaan Sains dan Teknologi Dalam Pemuliharaan Warisan Negara, Melaka, Malaysia, 16th to 19th August 2004.

ABOUELWAFA, M.S.A. AND KENDALL, E.J.M., The measurement of component ratios in multiphase systems using γ-ray attenuation, J. Phys. E: Sci. Instrum. 13 (1980) 341.

ÅBRO, E., JOHANSEN, G. A., Low noise gamma-ray and X ray detectors based on CdTe-materials, Nucl. Instr. Meth. A377 (1996) pp. 470-474.

AFERKA S., ABDULLAH J., CRINE M., OLUJIC Z., SAROHA A.K., TOYE D., MARCHOT P., Liquid distribution study in a KATAPAK-SP12 column using X ray tomography, Submitted for publication in Journal of Nuclear and Related Technologies, September 2006.

ANDERSEN A.H., KAK A.C., Simultaneous algebraic reconstruction technique (SART): a superior implementation of the art algorithm, Ultrasonic Imaging, 6:81-94, 1984.

BAROUCH G., LEGOUPIL S. AND CHEVALIER E., Détecteur linéaire pour la tomographie, 3ème Colloque Interdisciplinaire en Instrumentation C2I-2004-Cachan, Actes du Colloque, 93 (Hermès-Science 2004)

BAYTAS, F.; GECKINLI M., An alternative approach to direct Fourier reconstruction in parallel-bean tomography, Meas. Sci. Technol., 7, pp.556-563 (1996).

BENAC J. Alternating minimization algorithms for X-ray computed tomography: multigrid acceleration and dual energy application D.Sc. thesis Washington University- St. Louis, USA (2005).

BHUSARAPU, S., Solids Flow Mapping in Gas-Solid Risers, D.Sc. Thesis, Washington University, St. Louis, Missouri, USA (2005).

BHUSARAPU, S., CASSANELLO, M. C., AL-DAHHAN, M., DUDUKOVIC, M. P., TRUJILLO, S., O'HERN, T. J., Dynamical Features of the Solid Motion in Gas-Solid Risers, Int. Journal of Multiphase Flow, in press.

CASSANELLO, M., LARACHI, F., MARIE, M. N., GUY, C., CHAOUKI, J. Experimental Characterization of the Solid Phase Chaotic Dynamics in Three-Phase Fluidization, Ind. & Eng. Chem. Res., **34** (1995) 2971-2980.

CASSANELLO, M., LARACHI, F., CHAOUKI, J., GUY, C., Solids Mixing in Gas-Liquid-Solid Fluidization: Experiments and Modeling, Chem. Eng. Science, 51 (1996) 2011-2020.

CASSANELLO, M. C., LARACHI, F., LEGROS, R., CHAOUKI, J., Solid Dynamics from Experimental Trajectory Time-Series of a Single Particle Motion in Gas-Spouted Beds, Chem. Eng. Science, 54 (1999) 2545-2554.

CASSANELLO, M., LARACHI, F., KEMOUN, A., AL-DAHHAN, M. H., DUDUKOVIC, M. P., Inferring liquid chaotic dynamics in bubble columns using CARPT, Chem. Eng. Science, 56 (2001) 6125-6134.

CASSANELLO, M., LARACHI, F., CHAOUKI, J., Dynamical features extracted from the solids circulation trajectories in gas-liquid-solid fluidized bed, Proc. of Tracer 3, Conference on Tracers and Tracing Methods, Ciechocinek, Poland, June 2004. p.68-73, ISBN 83-909690-2-5.

CESAREO, R. AND MASCARENHAS S., A new tomographic device based on the detection of fluorescent X-rays, Nucl. Instr. Meth. A277 (1989) 669.

CHAOUKI, J., LARACHI, F., DUDUKOVIC, M.P. (Editors), Non-Invasive Monitoring of Multiphase Flows, Elsevier, Amsterdam (1997).

CHAOUKI, J., LARACHI, F., DUDUKOVIC, M. P., Non-Invasive Tomographic and Velocimetric Monitoring of Multiphase Flows, Ind. & Eng. Chem. Research 36 (1997a) 4476-4503.

COUTIER-DELGOSHA O., STUTZ B., VABRE A. AND LEGOUPIL. S, Analysis of the cavitating flow structure by experimental and numerical investigations, accepted to Journal of Fluid Mechanics.

CSISZÁR I. Why Least Squares and Maximum Entropy? An Axiomatic Approach to Inference for Linear Inverse Problems. Annals of Statistics No. 19 (1991) 2033-2066.

DEGALEESAN, S., DUDUKOVIC, M., PAN, Y., Fluid Mechanics and Transport Phenomenon. Experimental study of gas-induced liquid-flow structures in bubble columns, AIChE J., 47 (2001) 1913-1931

DEGALEESAN, S., Fluid Dynamic Measurements and Modeling of Liquid Mixing in Bubble Columns, D.Sc. Thesis, Washington University, St. Louis, Missouri, USA (1997).

DEMPSTER AP, LAIRD NM, RUBIN DB. Maximum Likelihood for Incomplete Data via the EM Algorithm. J. R Stat Soc Series B, (1977) 39 1-38.

DE MESQUITA, C.H.; LEGOUPIL, S.; HAMADA, M.M. Development of an industrial computed tomography designed with a plastic scintillator position sensitive detector. Nuclear Science Symposium Conference Record, 2005 IEEE, Volume 1, 23-29 Oct. 2005 Page(s):540 – 544. Digital Object Identifier 10.1109/NSSMIC.2005.1596310

DEVANTHAN, N., Investigation of Liquid Hydrodynamics in Bubble Columns via Computer-Automated Radioactive Particle Tracking (CARPT), D.Sc. Thesis, Washington University, St. Louis, Missouri, USA (1991).

DEVANATHAN, N., MOSLEMIAN, D., DUDUKOVIC, M. P., Flow mapping in bubble columns using CARPT, Chem. Eng. Science, 45 (1990), 2285-2291

DUDUKOVIC, M. P., Opaque multiphase flows: Experiments and modelling, Experimental Thermal & Fluid Science, 26 (2002) 747-761

FRAGUÍO, M. S., CASSANELLO, M. C., LARACHI, F., CHAOUKI, J., Flow Regime Transition Pointers in Three Phase Fluidized Beds Inferred from a Solid Tracer Trajectory, Chem. Eng. and Process., 45 (2006) 350-358.

FRAGUÍO, M. S., CASSANELLO, M. C., LARACHI, F., CHAOUKI, J., Flow Regime Transition Pointers in Three Phase Fluidized Beds Inferred from a Solid Tracer Trajectory, Chem. Eng. and Process., 45 (2006) 350-358.

FRAGUÍO, M. S., CASSANELLO, M. C., LARACHI, F., Flow regime diagnosis of a three phase fluidized bed inferred from the comparison of attractors reconstructed from solid tracer trajectories obtained by RPT, Proc. of the 4th Int. Conf. on Tracers and Tracing Methods – Tracer4, Autrans/Grenoble, France, October 2006.

FRAGUÍO, M. S., CASSANELLO, M. C., CARDONA, M. A., HOJMAN, D., SOMACAL, H., Alternative methods for extracting dynamic information from a bubble column, Proc. of the 4th Int. Conf. on Tracers and Tracing Methods – Tracer4, Autrans/Grenoble, France, October 2006.

FRAGUÍO, M. S., CASSANELLO, M. C., LARACHI, F., CHAOUKI, J., Indicators of Flow Regime Transitions in Three Phase Fluidized Beds Inferred from a Solid Tracer Trajectory, Proc. of the 2nd Mercosur Congress on Chemical Engineering ENPROMER 2005, Rio de Janeiro, Brasil, August 2005.

FRØYSTEIN, T., KVANDAL, H. AND AAKRE, H., Dual energy gamma tomography system for high pressure multiphase flow, Flow Meas. Instr., 16, Iss. 2-3, (2005) 99-112.

GODFROY, L., LARACHI, F., CHAOUKI, J., Position and velocity of a large particle in a gas/solid riser using the radioactive particle tracking technique, The Canadian J. of Chem. Eng., 77 (1999).

GODFROY, L., LARACHI, F., KENNEDY, G., GRANDJEAN, B. P. A., CHAOUKI, J., Online flow visualization in multiphase reactors using neural networks, Appl. Radiat. Isotop., 48(2) (1997) 225-235.

GRAVITIS, V. L. WATT, J. S., MULDOON L. J. AND COCHRANE, E. M., Long-term trial of a dual energy γ-ray transmission gauge determining the ash content of washed coking coal on a conveyer belt, Nucl. Geophys. 1, No. 2 (1987) 111.

GUPTA, P., Churn-turbulent bubble columns: experiments and modeling, D. Sc. Thesis, Washington University, St. Louis, Missouri, USA (2002).

HASSAN W., BARRE S., LEGOUPIL S., REBATTET C., Dynamic vapour fraction measurement in Ariane 5 inducer by X-rays, Proceedings of FEDSM2005, ASME Fluids Engineering Division Summer Meeting and Exhibition, June 19-23, 2005, Houston, TX, USA.

HASSAN W., CHAMBELLAN D., LEGOUPIL S., Industrial X-ray generator in dynamic multi-phase flow measurements. Accepted to IEEE TNS.

HERMAN G.T., LENT A., Iterative reconstruction algorithms, Computers in biology and medicine, 6:273-294, 1976.

HERMÈS SCIENCE, librairie LAVOISIER, Traité IC2 (Information, commande, communication), Série Traitement du Signal et de l'Image. ISBN: 2-7462-0356-1, 2002.

HJERTAKER, B. T., TJUGUM, S.-A., HAMMER, E. A. AND JOHANSEN, G. A. Multi modality tomography for multiphase hydrocarbon flow IEEE Sensors Journal, 5 No 2 (2005) 153-160.

HJERTAKER, B. T., TJUGUM, S.-A., HAMMER, E. A. AND JOHANSEN, G. A. Multi modality tomography for multiphase hydrocarbon flow IEEE Sensors Journal, 5 No 2 (2005) 153-160.

ISAKSEN Ø. A review of reconstruction techniques for capacitance tomography, Meas. Sci. Technol., Vol. 7 (1996) 325-337.

JIANG M. AND WANG G., Convergence of the simultaneous algebraic reconstruction technique (SART). IEEE Transactions on image processing, 12:957-961, 2003.

JOHANSEN, G. A., FRØYSTEIN, T., HJERTAKER, B. T. AND OLSEN, Ø. A dual sensor flow imaging tomographic system. Meas. Sci. Techn. 7, No. 3 (1996) 297-307.

JOHANSEN, G. A., FRØYEN, S. AND HANSEN, T. E. Gamma-ray detection with an UV-enhanced photodiode and scintillation crystals emitting at short wavelengths. Nucl. Instr. Meth. A387 (1997) 239-242.

JOHANSEN, G.A. AND JACKSON, P., Salinity independent measurement of gas volume fraction in oil/gas/water pipe flow, Appl. Rad. Isotop., 53, (2000) 595.

JOHANSEN, G. A. AND JACKSON, P. Radioisotope gauges for industrial process measurements ISBN 0471 48999 9, John Wiley & Sons, Ltd. (2004) 336pp (www.wileyeurope.com/go/radioisotope).

JOHANSEN, G. A., FRØYSTEIN, T., HJERTAKER, B. T. AND OLSEN, Ø. A dual sensor flow imaging tomographic system. Meas. Sci. Techn. 7, No. 3 (1996) 297-307.

JOHANSEN, G. A., FRØYEN, S. AND HANSEN, T. E. Gamma ray detection with an UV enhanced photodiode and scintillation crystals emitting at short wavelengths. Nucl. Instr. Meth. A387 (1997) 239-242.

JOHANSEN, G.A. AND JACKSON, P. Salinity independent measurement of gas volume fraction in oil/gas/water pipe flow, Appl. Rad. Isotop., 53, (2000) 595.

JOHANSEN, G. A. Nuclear tomography methods in industry, Nucl. Phys. A752 (2005) 696c.

KANTZAS, A., WRIGHT, I. AND KALOGERAKIS, N., Quantification of channelling in polyethylene resin fluid beds using x-ray computer assisted tomography (CAT), Chem. Eng. Sci. 52 No. 13 (1997) 2023-2035.

LANGE K., CARSON R. EM reconstruction algorithms for emission and transmission tomography. J. Comput. Assist. Tomogr. 8 (1984): 306-316

LARACHI, F., KENNEDY, G.. AND CHAOUKI, J., A γ-ray Detection System for 3D Particle Tracking in Multiphase Reactors, Nucl. Intr. & Meth., A338 (1994), 568-576.

LARACHI, F., CASSANELLO, M., CHAOUKI, J. AND GUY, C., Flow structure of the Solids in a Three-Dimensional Gas-Liquid-Solid Fluidized Bed, AIChE J., 42 (1996) 2439-2452.

LEGOUPIL S., PASCAL G., La tomographie d'émission appliquée à la visualisation d'écoulements Industriels dans l'ouvrage: La tomographie: Fondements mathématiques, imagerie microscopique, imagerie industrielle. Ouvrage réalisé sous la direction de Pierre Grangeat. Éditions

LEGOUPIL, S., PASCAL, G., CHAMBELLAN, D., BLOYET, D. Determination of the detection process in an experimental tomograph for industrial flow visualization using radioactive tracers. IEEE Transactions on Nuclear Science, Volume 43, Issue 2, Part 2, April 1996 Page(s):751 – 760. Digital Object Identifier 10.1109/23.491525.

LEGOUPIL, S. Tomographie d'Emission Gamma appliquée à partir d'un nombre limité de détecteur appliquée à la visualisation d'écoulements, thèse de doctorat, Université de Caen-France, 1999. Rapport CEA-R-5866 (http://www-ist.cea.fr/publicea/exl-doc/00000037289.pdf)

LIMTRAKUL, S., Hydrodynamics of liquid fluidized beds and gas-liquid fluidized beds, D.Sc. Thesis, Washington University, Saint Louis, Missouri, USA (1996).

LIN, J. S., CHEN, M. M., AND CHAO, B. T., A novel radioactive particle tracking facility for measurement of solids motion in gas fluidized beds, AIChE J., 31 (1985) 465-473.

MELCHER, C. L. Perspectives of the future development of new scintillators, Nucl. Instr and Meth. A537 (2005) 6-14

MILLER M.I., SNYDER D.L. AND MILLER T.R. Maximum- Likelihood reconstruction for Single-Photon Emission Computed-Tomography. IEEE Trans. Nucl. Sci. **NS-32 (1985)**:769-778.
Mohamad, D. et.al., Nuclear Science and Technology, MINT Publication (2005), ISBN 983-99341-6-3
MOSLEMIAN, D., DEVANATHAN, N., DUDUKOVIC, M. P., Radioactive particle tracking technique for investigation of phase recirculation and turbulence in multiphase systems, Review of Scientific Instruments, 63 (1992) 4361-4372.

MOSTOUFI, N. AND CHAOUKI, J., Flow structure of the solids in gas–solid fluidized beds, Chem. Eng. Science, 59 (2004) 4217-4227.

MUZEN, A., CASSANELLO, M. C., Liquid Holdup in Columns Packed with Structured Packings: Countercurrent vs. Cocurrent Operation, Chem. Eng. Science, 60 (2005) 6226-6234.

MUZEN, A., VALLEJOS, R., SOBRAL, S., CASSANELLO, M., Local Hydrodynamics during Flow Regime Transition in a Trickle Bed Reactor with Structured Parking, Proc. of the 58th Annual Congress of Indian Chemical Engineering, CHEMCON-2005, Delhi, India, December 2005.

MUZEN, A., CASSANELLO, M., Obstructions in the Liquid Circulation within a Trickle Bed Reactor with Stuctured Packings as "Observed" from the Wall, Proc. of the 2nd Mercosur Congress on Chemical Engineering ENPROMER 2005, Rio de Janeiro, Brasil, August 2005.

MUSTAPHA, I. AND ABDULLAH, J., Development of a Large-Scale Experimental Flow Loop for Three Phase Systems, The 5th International Symposium on Measurement Techniques for Multiphase Flows (ISMTMF 2006), Macau, China, 10th to 13th December 2006.

OLSZEWSKI T., BRZESKI P., MIRKOWSKI J., PLĄSKOWSKI A., SMOLIK W. AND SZABATIN R. Modular Capacitance Tomograph, 4th International Symposium on Process Tomography in Poland, Warsaw (2006).

O'SULLIVAN, J. A., BENAC, J. Alternating Minimization Algorithms for Transmission Tomography. IEEE Transactions on Medical Imaging, resubmitted (July 2006).

PARKER, D.J., MCNEILL, P.A., Positron emission tomography for process applications, Meas. Sci. Technol. 7, No. 3 (1996) 287.

RADOS, N., Slurry bubble column hydrodynamics: experimentation and modeling, D.Sc., Thesis, Washington University, Saint Louis, Missouri, USA (2003).

RAMMOHAN, A., Characterization of Single and Multiphase Flows in Stirred Tank Reactors, D.Sc. Thesis, Washington University, St. Louis, USA (2002).

REINECKE, N. AND MEWES, D., Recent developments and industrial/research applications of capacitance tomography, Meas. Sci. Technol., 7 (1996) 233-246.

ROY, S., LARACHI, F., AL-DAHHANA, M. H. AND DUDUKOVIC, M. P., Optimal design of radioactive particle tracking experiments for flow mapping in opaque multiphase reactors, Appl. Radiat. Isotop., 56 (2002) 485-503.

SANKOWSKI, D., ZAIN, R. M. AND MOSOROV, V., Image fusion for dual tomography, Proceeding of the 1st International Conference of Young Scientists (MEMSTECH 2006): Perspective Technologies and Methods in MEMS Design, Lviv-Polyana, Ukraine, 2006.

SHEPP L.A. AND VARDI Y. Maximum Likelihood Reconstruction for Emission Tomography. IEEE Trans. Med. Imaging **MI-1** (1982) :113-121.

SNYDER DL, SCHULZ TJ AND SULLIVAN JO. Deblurring Subject to Nonnegativity Constraints. IEEE transactions on signal processing No.40(5) (1992)1143-1150.

SOWERBY, B.D., NGO, V.N., Determination of the ash content of coal using annihilation radiation, Nucl. Instr. Meth. 188 (1981) 429.

STITT, H., JAMES, K., Process tomography and particle tracking: research and commercial diagnostic tool Proceedings of the 3rd World congress on industrial process tomography, Banff, Canada, 2-5 September (2003) 2.

THORN, R., JOHANSEN, G.A. AND HAMMER, E.A., Recent developments in three-phase flow measurement, Meas. Sci. Technol. 8 (1997) 691.

THYN, J. AND ZITNY, R. Analysis and Diagnostics of Industrial Processes by Radiotracers and Radioisotope Sealed Sources I. CTU Faculty of Mechanical Engineering, Prague 2000

THYN, J. AND ZITNY, R. Analysis and Diagnostics of Industrial Processes by Radiotracers and Radioisotope Sealed Sources II. CTU Faculty of Mechanical Engineering, Prague 2002.

TOYE, D., ABDULLAH, J. B., CRINE, M. AND MARCHOT, P., 3D imaging of reactive packings with a new high energy x-ray tomography, Proceedings of 4th World Congress on Industrial Process Tomography, Aizu, Japan, 5th to 8th September 2005b.

TOYE, D., LETRONG, E., ABDULLAH, J.B., CRINE, M. AND MARCHOT, P., Analysis of liquid distribution in catalytic distillation packings, Proceedings of 7th Conference on Gas-Liquid and Gas-Liquid-Solid Reactor Engineering, Strasbourg, France, 21st to 24th August 2005a.

TSOULFANIDIS, N., Measurement and detection of radiation, McGraw Hill, New York (1983).

VABRE A. AND LEGOUPIL S., X ray imaging of the filling of "T" shaped microchannel using a MEDIPIX2 detector, Pub n°A4001836 du 15-Oct-2004.

VABRE A. ET AL, X-ray phase contrast imaging of a fluid flow meniscus in micro-channels, 3ème Congrès de Microfluidique (µFlu'06), Toulouse, 12-14 dec. 2006.

VAN EIJK, C. W. E. Inorganic scintillators in medical imaging detectors, Nucl. Instr and Meth. A509 (2003) 17-25.

VAN EIJK, C. W. E. Inorganic Scintillator Research, Principles and New Materials, Workshop on Use of Monte Carlo Techniques for Design and Analysis of Radiation Detectors, Coimbra, September 15, 2006

VARMA R., BHUSARPU S., O'SULLIVAN J.A. AND AL-DAHHAN M.A. Comparison of Alternating Minimization and Estimation Maximization algorithms for imaging two phase systems, Measurement science and Technology , Submitted December 2006.

WEBER, M. J. Inorganic scintillators: today and tomorrow, J. Lumin. 100 (2002) 35-45.

XUAN, P. AND THYN, J., Space Distribution of Particulate Materials, Isotopenpraxis 26, (1990) 445-448.

YANG W.Q. AND YORK T.A. New AC-based capacitance tomography system, IEE Proc.-Sci. Meas. Technol., vol. 146, No. 1, (1999) 47-53.

YUSOFF, W. R. AND ABDULLAH, J., Advanced non-disruptive evaluation technology: Computed tomography simulation of industrial process columns, Proceedings of NDT and Corrosion Management Asia Conference, Kuala Lumpur, Malaysia, 21st to 22nd September 2005.

ZAIN, R. M., RAHIM, R. A. AND ABDULLAH, J., Image fusion of dual modality electrical capacitance and optical tomography in industrial solid/gas flow, Findings of the Young Researchers on Applied Science 2006 (CAS 2006), Volume 1: Physics and Material Science, Kuala Lumpur, Malaysia, 13th and 14th June 2006.

ZHU, P., DUVAUCHELLE, P., PEIX, G. AND BABOT, D., X ray Compton backscattering techniques for process tomography: imaging and characterization of materials, Meas. Sci. Technol. 7 (1996) 281.

ZELINKA, I., Umela inteligence v problemech globalni optimalizace, BEN Praha 2002

ZITNY, R., THYN. J., Application of analytical transmission tomography with limited number of detectors in analysis of two phases flow in tube Proc. of the 4th Int. Conf. on Tracers and Tracing Methods – Tracer 4, Autrans/Grenoble, France, October 2006.

ABBREVIATIONS

ADC	Analog digital converter
AM	Alternating minimization
ART	Algebric reconstruction technique
ATT	Analytical transmission tomography
CARPT	Computer assisted radioactive particle tracking
CT	Computed tomography
ECT	Electrical capacitance tomography
ERT	Electrical capacitance tomography
EMT	Electromagnetic tomography
EM	Estimation maximization
FBP	Filtered back projection
FWHM	Full width at half maximum
ILST	Iterative least square technique
IPT	Industrial process tomography
MART	Multiplicative algebric reconstruction technique
MC	Monte Carlo
ML-EM	Maximum likelihood – Expectation maximization
MRI	Magnetic resonance imaging
NCS	Nucleonic conmtrol system
PET	Positron emission tomography
PEPT	Positron emission particle tracking
SART	Simultaneous algebric reconstruction technique
SIRT	Simultaneous iterative reconstruction technique
SMART	Simultaneous multiplicative algebric reconstruction technique
SOMA	Self organising migration algorithm
SPECT	Single photon emission computed tomography
RMSE	Root mean square error
RPT	Radioactive particle tracking
RTD	Residence time distribution

ANNEX 1
SUMMARY OF CRP PARTICIPANTS' REPORTS

ARGENTINA

The activities of the Argentinean research group participating in the CRP can be briefly summarized in the following items:

- Implementation of algorithms to extract dynamical features of the liquid and solid motion in multiphase systems. Particularly, analysis of radioactive tracer trajectories moving freely in 3D mock-ups of different multiphase reactors.
- Development and implementation of algorithms capable of classifying flow regimes and diagnosing flow regime transitions in multiphase contactors, particularly bubble columns, three-phase fluidized beds and circulating fluidized beds.
- Development, mounting and implementation of a Computer Automated Radioactive Particle Tracking (CARPT) facility in Argentina in collaboration with a group of the National Commission of Atomic Energy (CNEA).

Multiphase systems are ubiquitous in industrial practice, either in pipes, operation units and multiphase reactors (MPR). MPR are vessels where two or more phases are brought together for a chemical transformation to take place. They are extensively used for quite diverse applications ranging from the upgrading and conversion of petroleum feed-stocks, with a huge installed capacity, to the manufacture of pharmaceuticals or fine-chemicals, and ever present in biotechnological processes. The gamma emission tomography of a single radioactive tracer, frequently called Computer Automated Radioactive Particle Tracking (CARPT), provides a massive amount of information on the traced phase motion, which has been used to determine characteristic features, like Eulerian velocity fields, turbulence intensities, dispersion coefficients, phase distribution, etc.

The fluid dynamics in MPR is extremely complex due to interaction of the coexisting phases, particularly for fluidized systems or gas-liquid systems at high gas velocities. Moreover, these systems dynamics frequently have chaotic features and are far from being understood. Hence, further insights on fundamentals of the motions are always desirable, since no mechanistic model can still describe them.

For this reason, it is interesting to pursue in the analysis of experimental data gathered by CARPT, so as to improve the data analysis tools already available, and to apply and develop non-conventional analysis to identify features of MPR dynamics related to the solid or liquid motion, which lead to distinct characteristics of the flow pattern and flow regime transitions. The project in Argentina was strongly oriented to analyze the trajectories of radioactive solid tracers, obtained by CARPT in fluidized systems (three-phase and circulating fluidized beds) and bubble columns. A data-mining approach was applied to recover some features of the solids actual motion from the long tracing periods of observation.

Algorithms to get dynamical features by data mining the 3D trajectories of radioactive tracers obtained by CARPT in different types of multiphase contactors have been written in Fortran language. Data has been analyzed using tools of the theory of nonlinear dynamics, conventional statistical methodologies and symbolic dynamics. By directly inspecting the trajectories measured during prolonged periods, some characteristics were also inferred by data mining the data, observing particularly the fast ascending and descending paths of the tracer while freely wandering within the multiphase emulsions. Particularly, definitions of flow regime classifiers and indexes that can be used as pointers of the flow regime transition in different multiphase systems have been proposed.

Finally, the CRP triggered the interaction between PINMATE from the Department of Industry, Faculty of Science, University of Buenos Aires and a group of nuclear spectroscopy from Tandar Laboratory at the National Commission of Atomic Energy (CNEA) and University of San Martín. This interaction of groups with quite different backgrounds allowed the implementation of a Computer Automated Radioactive Particle Tracking facility in Argentina, which is now being used in cooperation for research and it is expected to be used for technological assistance to the local industry. The implemented facility consists in a pilot scale vessel that can be used as a bubble column or a three-phase fluidized bed, surrounded by an array of 8 NaI(Tl) scintillation detectors and the required nuclear instrumentation to register the photon counts with appropriate frequency. The tracer path is determined by inverse reconstruction methods implemented in Fortran language. Improvements to the reconstruction procedure so as to consider dynamic information in the calibration step are within the objective of a thesis work starting on April 2007. In addition, within the CRP, three PhD thesis works have been developed, two of them already finished and one ongoing. Publications and conference presentations arising from the project, which illustrates applications of the different analysis procedures, are listed below.

Publications and presentations from the CRP

Journals

Alejandra Muzen, Miryan C. Cassanello. Flow regime transition in a trickle bed with structured packing examined with conductimetric probes, Chemical Engineering Science, submitted.

S. Bhusarapu, M.C. Cassanello, M. Al-Dahhan, M. P. Dudukovic, S. Trujillo, T. O'Hern. Dynamical features of the solid motion in gas-solid risers. International Journal of Multiphase Flow. In press.

M.S. Fraguío, M.C. Cassanello, F. Larachi, J. Chaouki. Flow Regime Transition Pointers in Three Phase Fluidized Beds Inferred from a Solid Tracer Trajectory, Chemical Engineering and Processing, 45, 350–358 (2006).

A. Muzen, M.C. Cassanello. Liquid Holdup in Columns Packed with Structured Packings: Countercurrent vs. Concurrent Operation, , Chemical Engineering Science, 60, 6226–6234 (2005)

Presentations

Alternative Methods for Diagnosing the Flow Regime in a Bubble Column, M.S. Fraguío, M.C. Cassanello, M.A. Cardona, D. Hojman, H. Somacal, XXII Interamerican Congress of Chemical Engineering and V Argentinean Congress of Chemical Engineering, Buenos Aires, Argentina, October 2006.

Flow regime diagnosis of a three phase fluidized bed inferred from the comparison of attractors reconstructed from solid tracer trajectories obtained by RPT, M.S. Fraguío, M.C. Cassanello, F. Larachi, 4th International Conference on Tracers and Tracing Methods – Tracer4, Autrans/Grenoble, France, October 2006.

Alternative methods for extracting dynamic information from a bubble column, M.S. Fraguío, M.C. Cassanello, M.A. Cardona, D. Hojman, H. Somacal, 4th International Conference on Tracers and Tracing Methods – Tracer4, Autrans/Grenoble, France, October 2006.

Local Hydrodynamics during Flow Regime Transition in a Trickle Bed Reactor with Structured Parking, A. Muzen, R. Vallejos, S. Sobral, M. Cassanello, 58th Annual Congress of Indian Chemical Engineering, CHEMCON-2005, Delhi, India, December 2005. Award from the Conference as the best work on multiphase reactors.

Indicators of Flow Regime Transitions in Three Phase Fluidized Beds Inferred From a Solid Tracer Trajectory, M.S. Fraguío, M.C. Cassanello, F. Larachi, J. Chaouki, 2nd Mercosur Congress on Chemical Engineering ENPROMER 2005, Rio de Janeiro, Brasil, August 2005.

Obstructions in the Liquid Circulation within a Trickle Bed Reactor with Stuctured Packings as "Observed" from the Wall, A. Muzen, M.C. Cassanello, 2nd Mercosur Congress on Chemical Engineering ENPROMER 2005, Rio de Janeiro, Brazil, August 2005.

Dynamical features extracted from the solids circulation trajectories in gas-liquid-solid fluidized bed, M. Cassanello, F. Larachi, J. Chaouki, Tracer 3, Conference on Tracers and Tracing Methods, Ciechocinek, Poland, June 2004. p.68-73.

BRAZIL

For the last years, industrial computed tomography (CT) in Brazil has had its application in non-destructive testing, for scientific studies. Today, the interest of a wide range of industries, such as chemical and oil sectors in the use of computed tomography began to appear in large number, for improving design, operation and troubleshooting of industrial processes. Computerized tomography for multiphase processes is now a promising technique and has been studied for advanced research centres. To follow this trend and to keep update, the IPEN laboratory began a study for the development the computed tomography methodology. Firstly, a tomography of first generation one detector-one source was developed using a NaI(Tl) detector, 2" x 2, for comparison. The data acquisition board and the mechanical control interface were specially developed in our laboratory to be used in our Computed Tomography system. For testing these developments the tomography of the first generation one NaI(Tl) detector-one 60Co source was used to carry out the TC experiments using the hardware and software developed.

The data acquisition board is constituted of two 8 bit ADC with corresponding to 256 channels positions (0 to 5V) for each one. It is versatile for multipurpose applications, so that, it can be used for one detector (CT1) version, a multi-detector array (1 board for each 2 detectors) or as well as in linear detector CT with a position sensitive detector.

A good resolution was observed for all images reconstructed from the first generation one detector-one source using a NaI (Tl) detector CT system. The attenuation coefficient found for the different density materials used to fill the phantom holes are comparable to the theoretical values described in the literature for these materials. The development and the studies carried out with tomography of first generation one detector-one source using a NaI (Tl) detector give us valuable experience to start the design and development of other tomographic systems.

A linear detector tomography system was also developed using a unique cylinder of plastic scintillator (PS) as a position sensitive detector to the radiation interaction. This kind of detector can be useful mainly in the case of industrial CT applications for large objects because it uses only two photomultiplier, thus require more simplified electronics, compared with those used in multiple detectors version.

Previously, the light attenuation in the plastic scintillator along the plastic scintillator length was evaluated. Thus, in order to know the light auto-absorption (self-quenching), a 100 cm cylinder with 4 cm diameter of PS made with PPO (0.5%w/v) and POPOP (0.05% w/v) in a polystyrene matrix was prepared. Two photomultipliers (Hamamatsu Model R329-02) were coupled to the cylinder extremities of the PS detector. According to this study, the plastic scintillator cylinder can be used up to 80 cm in order to work suitably as a linear detector tomography system.

For the linear detector CT mounting, a plastic scintillator cylinder of 4 cm diameter and 40cm high was used as position sensitive detector. The schematic drawing of the plastic scintillator linear detector CT is showed in Figure 129. The plastic was coupled to two photomultipliers (Hamamatsu Model R329-02) in each extremity and collimated with 5 mm lead slices placed each 10 mm along the detector. A ^{60}Co source of 12 MBq was used in this experiment.

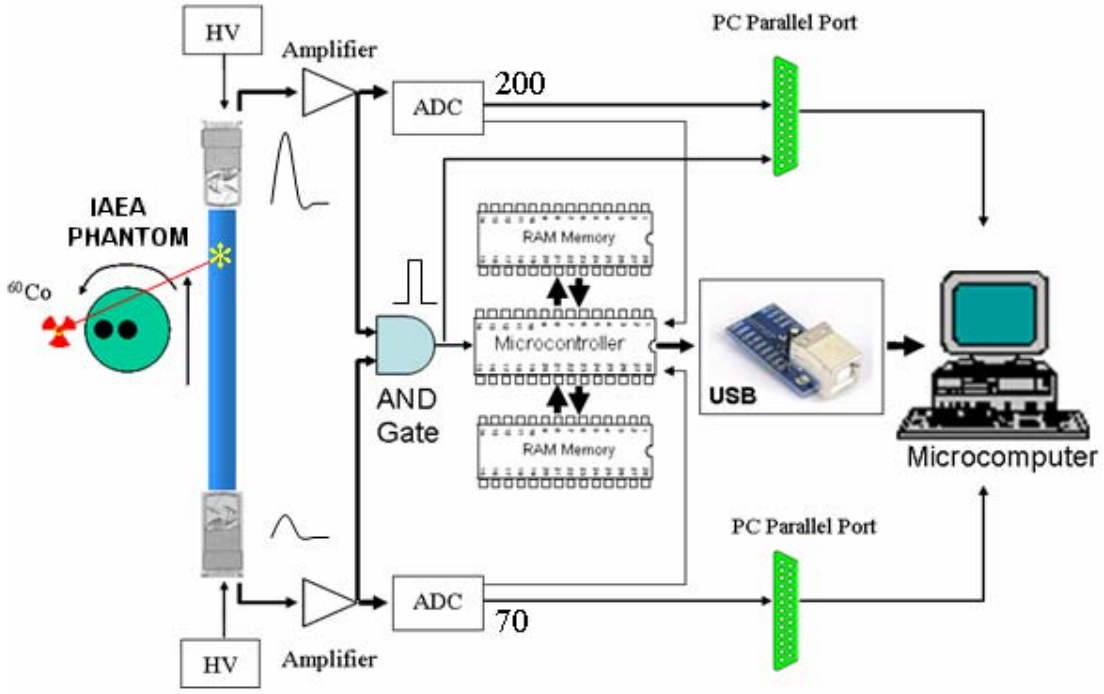

FIG. 129. Basic diagram of a data acquisition board for a linear tomography system.

The reconstructed image was not as good as that found for first generation CT system using NaI(Tl) detector. There are several reasons for that. The dimensions of the detector used could be considered one of causes. It was used PS cylinder of small size ϕ= 4cm against an ideal value of 10 to 15 cm with respect to minimum statistical noise. A code (software) was developed to simulate the gamma-ray photon interactions in the scintillator detectors by the Monte Carlo method in order to determine the ideal dimension. Absorption of 42% of the incident 60Co whole energy spectrum is foreseen for a 5x5 cm NaI(Tl) crystal. Considering this value (42%) suitable to be obtained for the plastic scintillator, then a sequence of several simulations using the Monte Carlo method was carried out for different PS rectangular bars. Dimensions between 10x10x5 to 15x15 x5 cm is foreseen to be capable to absorb 38% to 48% respectively of the incident ^{60}Co whole energy spectrum, suggesting that in this dimension range of the plastic scintillator is capable to work similarly to a NaI crystal detector. Dimensions between 10x10x5 to 15x15 x5 cm is foreseen to be capable to absorb 38% to 48% of the incident ^{60}Co whole energy spectrum, suggesting that in this dimension range the plastic scintillator is capable to work similarly to a NaI crystal detector.

A plastic scintillator of 12x12x80 cm dimension was prepared in our laboratory and it is being cut to be polished subsequently. Using the plastic in the suitable dimension, the quality of the image is expected to improve.

PUBLICATIONS RELATED TO CRP

Mesquita, C.H. ; Legoupil, S.; Hamada, M.M. *Development of an Industrial Computed Tomography Designed with a Plastic Scintillator Position Sensitive Detector*, Nuclear Science Symposium Conference Record, 2005 IEEE, Volume 1, 23-29 Oct. 2005 Page(s):540 – 544. Digital Object Identifier 10.1109/NSSMIC.2005.1596310.

Vasquez, P. A. S.; Costa, F. E.; Rela, P. R., Calvo; W. A. P.; Leroux, G. A.; Hamada, M. M. *Gamma scanning evaluation for random packed columns,* Nuclear Science Symposium Conference Record, 2005 IEEE, Volume 1, 23-29 Oct. 2005 Page(s):514 – 519. Digital Object Identifier 10.1109/NSSMIC.2005.1596310.

Vasquez, P. A. S.; Leroux, G. A. C.; Hamada, M. M. *Simulated Study Study of Parallel-Beam Gamma*. Proceedings of International Nuclear Atlantic Conference - VII ENAN. Rio de Janeiro: Associação Brasileira de Energia Nuclear, 2005. v.01. p.01 – 09.

Vasquez, P. A. S.; Costa, F.E.; Calvo, W.A.P.; Hamada, M. M. *Development of a Scintillator Detector System from Gamma Scan Measurements of Industrial Distillation*. Nucl. Instr. and Meth. in Physics Research A, 537, 458 – 461 (2005).

Mesquita, C. H., Fernandes Neto, J. M., Hamada, M. M. The Target Theory Applied to the the Radation Analysis Damage in the Organic Detectors. (In Portuguese) Proceedings of International Nuclear Atlantic Conference - VII ENAN.. Rio de Janeiro: Associação Brasileira de Energia Nuclear, 2005. v.01. p.01 – 09

CZECH REPUBLIC

1. Mass distribution analyzed by analytical transmission tomography with limited number of detectors.

Tomography is method**,** which acquired detailed image of cross section of the object. Method presented several years ago, which can be called as analytical transmission tomography (ATT), use**s** analytical function to describe 2D distribution of the matter on the basis of measurement of narrow gamma beams absorption in the object. In comparison with CT this classical method offer**s** simple evaluation, with simple detection techniques, which can use limited number of gamma beams. For different reasons only a limited number of detectors can be applied in the field and also more information about the system cannot be obtained e.g. by rotation of detectors or even by rotation of the system as it is common in laboratory tests. It is therefore supposed that some attention still should be devoted to the application of relatively cheap measured systems with only small number of beams. This technique has chance for success in industrial applications because of their simplicity and relatively cheap measured equipments, however some information about the measured system received with another method is required.

Basic steps used in the data treatment are presented in the literature [Thyn et. al., 2002]. Several analytical models used or recommended for different continuous or discontinuous distribution of the matter were prepared for application by FEMINA software.

There was achieved good progress in the following topics:

(a) two phase flows in tube,
(b) distribution of solid particles in mixed vessel,
(c) determination of dimension and localities of density discontinuities.

(a) The distribution of the gas-liquid phase during transport in the horizontal or vertical tube can be specified on the basis of measurement with only two or three detectors as soon as the flow regime can be deduced, for example from the measured mass flow-rates of individual phases. The basic density distribution models and procedures are presented as contribution to these specific phenomena [Zitny et. al., 2006]. The mean velocity of the phases can be then evaluated from the distribution of density in cross section area of the tube and from the flow rates of phases.

(b) The distribution of suspension was analyzed in a circulator that is in a mixed vessel with stirrer in the draft tube. The concentration of solid particles in the draft tube is important for estimation of required power input and it is evident that it is important information for designing optimal configuration of the circulator. Distribution of solid particles in liquid in mixed vessel is very complicated phenomena especially for the high concentration of suspension. However semi-prediction of concentration in the draft tube and in the rest of vessel can be done for working conditions, which suppose holding particle in suspension and for the known flow rate of liquid in

the draft tube. Suggested prediction is verified by gamma transmission tomography with using only seven detectors and two radioactive sources.

Their configuration and number of detectors utilize the recommendation done on the basis of numerical analysis [Xuan et. al., 1990]. Method of analytical tomography is used for cross sectional distribution of particles in the draft tube as well in the annulus part of the circulator. The radial profiles of concentration for different total volume concentration <0.025-0.40> for two diameters of ballotiny in water were evaluated.

(c) Often in industry there are problems with deformation, or changing position of some materials, which has different density than the rest of material in the object. The position of two empty tubes in continuous phase in cylindrical vessel can be one example of this situation, and a concentration in the tube situated in the middle of the vessel with lower or higher density than in the rest of the vessel is another example.

Estimation of dimension and positions of these discontinuous regions or their densities can be done again by ATT. Analysis of circular polypropylene phantom (d = 0.3 m) with two holes was used for procedure testing. If we can assume that the shape of cross section area of these holes are circles, their positions and diameters can be determined by proper analytical model used in ATT.. Comparison with known reality were done with experiments realized for different counting time and different sequence of rotation of basic system with seven detectors and two collimated sources. Also the phantom with known position and dimension of tube in cylindrical vessel with different density were analysed with basic configuration of seven detectors and two sources in one position. Again the procedure of ATT has been successfully applied FEMINA software, which use for identification of model parameters two optimization operation OPTIMA and SOMA was complemented with suitable models of mass distributions and was successfully applied in all evaluations of experiments mentioned above. Seven collimated scintillation detectors with Nucleus Digital Multiplexer Router II system enable to evaluate an energy spectrum of detected radiation and measurement could be done in given ”window” to eliminate the scattering radiation. Only single radioactive source ^{137}Cs (460 MBq i.e. ~ 13 mCi) was used separately in two positions.

2. Conclusions

- Methodology of analytical transmission tomography with limited number of detectors in two phase systems with continuous as well as discontinuous mass distribution was suggested.
- Methodology was used for evaluation of experiments which analyzed the distribution of suspension in the mechanically mixed vessel with draft tube, as well as for determination of mass discontinuity of two regions; two regions were: two empty circular holes in the cylindrical vessel from the polypropylene; and water or ballotiny in tube or in annulus of circular vessel.
- Femina program prepared for IAEA with special model and macros was tested as friendly used software for data evaluation.
- ATT procedure with algebraic models with some information about system (as diameter of the draught tube e.g.) provides acceptable results for evaluation of solid concentration ratio in draught tube and annual part of mechanically mixed vessel.
- For application of ATT procedure in transport gas-liquid system in tube simple measurement with small number of detectors was suggested and reconstruction method of evaluation was prepared and tested.

FRANCE

Industrial tomography at CEA-LIST France

First developments in tomography in CEA-LIST have been conducted in the field of medical imaging for osteoporosis. First generation of scanner was based on bi-energy measurement in order to measure mineral weight independently to the morphology of the patient. Second generation of scanner was a tomo-osteodensitometer which allowed having cross section view of vertebra. This technology has been derived afterwards to oil recovery process to monitor 3 phase flows in rock sample (gas, oil and water). A gamma scanner dedicated to fixed bed and fluidized bed reactors has been designed in 1998-1999 for French Institute of Petroleum (IFP). The scanner is based on 32 BGO detectors and a 13 GBq ^{137}Cs source. Detectors can be shifted so that the system is equivalent to 64 detectors. Two rotations of the scanner are thus required to achieve the CT scan, which takes between 20 and 30 minutes. Mono or bi-energy CT systems, based on sealed source or filtered X ray generator, have been developed for different purposes such that 3 phases flow mixing monitoring, flows in rock sample or liquid-vapor distribution in space rocket pump. A new CT system based on 10 detectors for low resolution imaging of gas/liquid distribution is under development for small reactors with diameter ranging between 50 and 200 mm.

For the last 2 years now, efforts are focused on the development of micro imaging technology. Due to the development of micro technology, new systems involving flows in micro structures like canal, porous media, foams, micro reactors or lab-on-chip are of prime interests. As flows in meso-scale reactors in heavy industry, there is a need to understand the flow's behavior in these structures, where capillary forces are dominant to gravitation. In addition, nature of material, surface aspect, coatings have a major role in the system properties. A μ-CT based on micro focus X-ray source generator, a flat panel or silicon detector (Medipix2 detector) is used to make 3D high resolution imaging of the structure of high porosity foams and water distribution in the foam. Spatial resolution as low as 5 to 10 μm has been obtained. CEA-LIST is going on improving this resolution with an objective of 1 μm, which requires a very good control of the acquisition process and more specially the geometry and also the development of algorithms for local tomography approach. In transmission CT, the laboratory is strongly involved in cavitation phenomena analysis in space rocket cryogenic pump. Another important field of research is the analysis of foams; both structure analysis and liquid behavior in the structure.

First research in industrial emission tomography (SPECT) started in 1994. Initial objective of SPECT was to provide complementary information to the residence time distribution approach, developed and applied in CEA for more than 30 years. First industrial application of SPECT was conducted in 1999 for the control of flow in a nuclear power plant in France. The objective was to understand the flow patterns in a T-shape mixer of flows of different temperatures. Results showed that part of the pipe was submitted to periodic thermal fluctuations due to the alternative presences of flows. This was validated by CFD, and leads to modify the management of this critical part of the circuit. Experiments have also been conducted on trickle bed reactor and fluidized bed reactor at laboratory scale. Measurements with SPECT system located at 2 positions have realized so that pseudo velocity field and diffusion field have been estimated for the reactor, showing an unbalance of the flow's behavior. Most important and recent developments have been carried in SPECT for the thermal flow stratification measurement in primary circuit of a French nuclear plant. In transmission CT, the laboratory is strongly involved in cavitation phenomena analysis in space rocket cryogenic pump. Another important field of research is the analysis of foams; both structure analysis and liquid behavior in the structure.

KOREA, REPUBLIC

1. Introduction

The preliminary results from a lab scale CT system have been promising. The system introduced here has a 1st generation scanning mechanism that is a parallel beam scanning. The parallel beam transmission CT is most basic geometry for tomography but it is still useful for industrial purpose. By the Monte Carlo simulation, the CT geometry and selection of source have been decided. The CT uses a higher energy gamma ray source as ^{137}Cs and ^{60}Co for transmission modalities aimed at large scale industrial objects whose sizes are relatively larger than those of the conventional NDT technique. As long as the development of hardware, image reconstruction software which is based on Filtered Back Projection (FBP), SIRT ad EM reconstruction methods are programmed with LabVIEW. Various phantoms similar to industrial object are designed and tested at different counting time, scanning grid and sources. The measurement data was reconstructed by different algorithm

2. Hardware

Figure 130 shows the detail of hardware configuration of CT for object size of 50 cm (diameter). The system is a parallel beam type in which one radiation source and one detector see each other. ^{137}Cs and ^{60}Co gamma source activity of 740 MBq are used as a gamma emitter. A replaceable (in normal case 2 inches) detector is used for gamma ray detection. Basically any number can be selected as projection number and sample per projection within the scanning range. But the normal scanning grids are 16×16, 32×32 and 64×64.

FIG. 130. Hardware configuration for 1st generation CT.

3. Image reconstruction algorithm

The fundamental of image reconstruction algorithm of gamma ray CT is identical to other CT methods. There are two kinds of algorithm for image reconstruction. One is transform based method such as “Filtered back projection”, the others are iterative reconstruction method. The relationship between FBP and iterative method is efficiency vs accuracy. FBP are efficient for large number of ray-sums.

The normal scanning grids of the gamma-ray CT introduced here are 16 ×16, 32 ×32 and 64×64 data. Those measurements numbers are fewer ray-sum where iterative method has advantage over transform-based algorithm. And fewer ray-sum can be sufficiently meaningful data for the plant engineer in industrial plant when other methods are not applicable. Iterative reconstruction techniques solve a set of linear equations that consist of one unknown vector, weight matrix and ray-sum.

The ray-sum is the measurement data. Pixels are the unknown variable to be reconstructed. And weight matrix can be determined from geometry. Normally the direct weight matrix inversion technique is not applicable because the number of row and column are not equal.

There are several ways to solve the set of equation. In algebraic reconstruction technique (ART) and its variation, there are ART, SIRT, MART and etc. ML-EM algorithm which is based on Poison model has been also popularly used.

In the petrochemical industry, the materials most frequently encountered are oil and plastics. To estimate the contrast of water and oil, the phantom shown in figure 131 was designated. The linear attenuation coefficient was 0.0862 cm^{-1} for water and 0.0702 cm^{-1} for oil and the oil-water ratio was 0.815 (μ_{oil}/μ_{water}). Fig. 132 shows the experimental results with Cs-137 (20 mCi) and water-oil-air layer phantom. In this case, SIRT gave a better image.

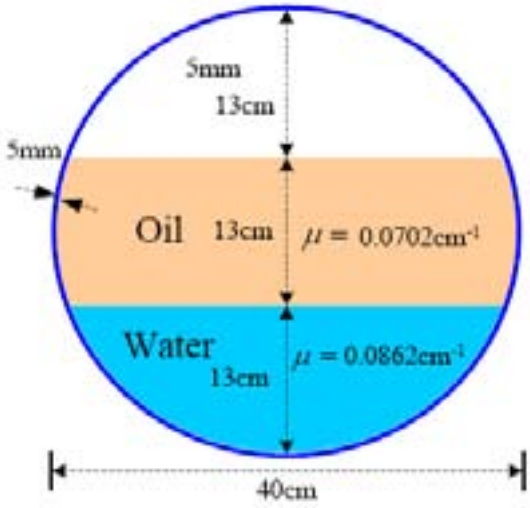

FIG. 131. Phantom simulating water –oil-air layers.

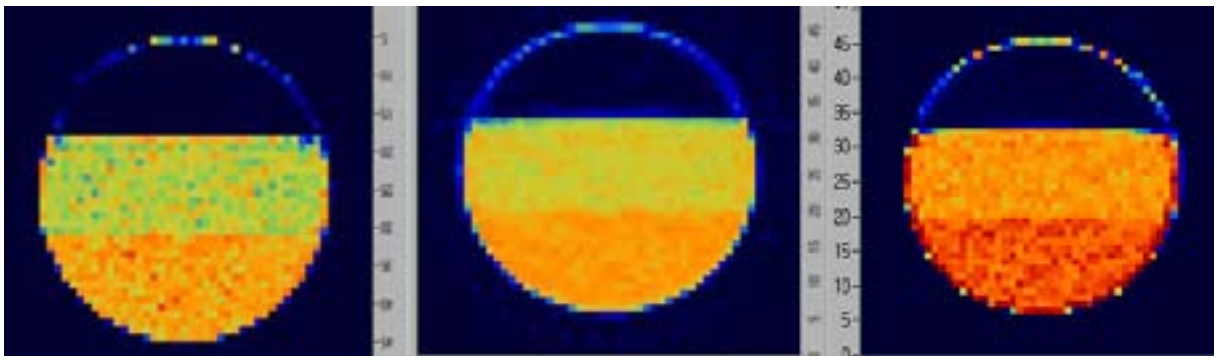

FIG. 132. The visual evaluation of algorithm by FBP (left), SIRT(center) and EM (right).

4. Weight matrix calculation

For the image reconstruction with iterative method, weighted matrix calculation is required (Fig. 133). Several ways are known to determine the weight matrix. An automatic weight matrix calculation program with LabVIEW has been created by Korean group. “Measurement path length in one pixel divided by the total measurement length” and “Measurement area inside a pixel divided by the total pixel area” were selected for main algorithm for weight matrix calculation.

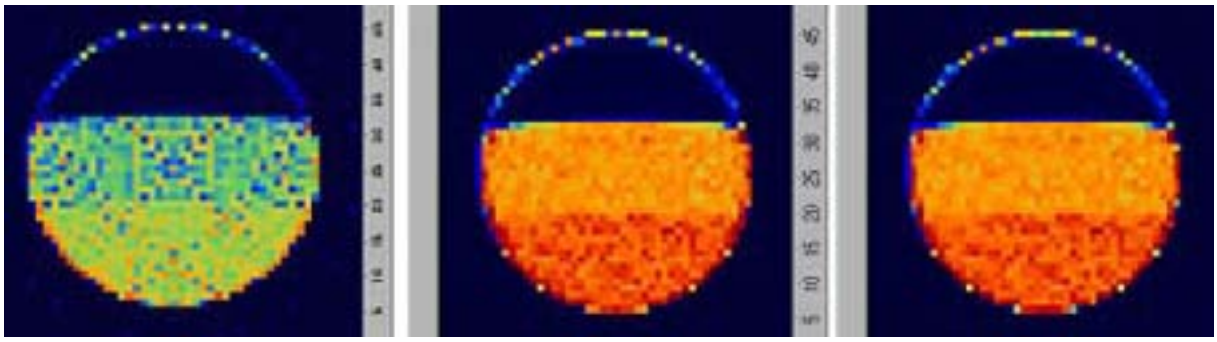

FIG. 133. Result from weighted matrix determined by 0/1 (a), length (b) and area (c).

5. Conclusion

During the CRP, the hardware of CT and software has been developed successfully. We have use Monte Carlo code to reduce trial error in designing the tomograph system. Study of tomography needs various techniques on radioisotope handling, radiation measurement, image processing, electronics and mathematics. So there should be cooperation among nuclear research institute and academic institute. In geometry design, field demonstration should be accompanied with lab scale experiment for practical solution. For this we should also have good cooperation with industries.

MALAYSIA

One of the emerging technologies of advanced measurement and imaging in Malaysia is computed tomography. In particular, all aspects of research and development of industrial process gamma tomography are being actively pursued at the Agensi Nuklear Malaysia (Nuklear Malaysia). Through close collaboration with universities, research institutes and industries in Malaysia and abroad, research and development of different modality tomographic systems are continuously being carried out. The first program on industrial CT was started in 80’s where a second-generation gamma-ray CT was designed and manufactured. Today, the development of industrial CT with various measurement modalities has expanded. Among others, the systems being developed include gamma ray process tomography, capacitance and optical tomography, portable gamma tomography and x-ray tomography. To support research works and testing, a multi-phase flow facility, lab-scale industrial process columns and special tomographic exposure rooms for high-energy radiation were constructed in Nuklear Malaysia, financially supported by the 8th and 9th Malaysian Plan (RMK8 and RMK9). In addition, a micro X ray tomographic system is being planned through the support of the IAEA. On-going research and development efforts for the various systems and facilities are briefly described in the following paragraphs.

A third generation gamma-ray process tomography system is currently being developed in Nuklear Malaysia to study and investigate multiphase processes occurring in a bubble column, trickle column, packed column etc [Yusoff and Abdullah, 2005].

The design and development of this system are divided into three main parts, a lab-scale industrial process column and its mechanical assembly, process tomography hardware (source and detector) and image reconstruction software. The basic design of mechanical and electronic systems for this gamma-ray CT is developed through close consultation from the University of Washington, USA. For the design and development of the laboratory-scale industrial process column in Nuklear Malaysia, it is being carried out in collaboration with Universiti Kebangsaan Malaysia (UKM). An empirical development of a computer simulation and image reconstruction of the cross-sectional views of industrial process columns using gamma-ray computed tomography was carried out. In developing the software, simulation for different configurations of gamma-ray source and detectors were used to study the spatial resolution and other characteristics of the reconstructed images and their sensitivity to the number of projections and ray-sums.

One new project has just started for a tomography system that combines the electrical capacitance and optical sensor in one sensor plane [Zain *et al*, 2006, Sankowski *et al*, 2006]. The combination of these two sensors shall give a full range distribution of the industrial solid/gas flow. With the cooperation of the Technical University of Lodz, Poland, a software development project based on a new algorithm for the combination images or fusions of image in full range distribution for investigation of an industrial solid/gas flow has been executed. Apart from non-nuclear CT modalities in Nuklear Malaysia, the Universiti Teknologi Malaysia (UTM) are also carries out research projects on electrical capacitance, electrical resistance, optical and ultrasonic tomography [Abdullah and Rahim, 2004]. Close cooperation between these two organisations allows project collaboration and post-graduate programs in the field of industrial process tomography are smoothly carried out.

The development of a portable computed tomographic scanner, specifically for non-destructive inspection and on-line imaging of industrial pipelines [Abdullah *et al*, 2003]. Within the constraints of size and weight, there is a trade-off between the radiation source strength, scanning time and spatial and density resolution of the resulting image. The system consists of five CsI(Na) detectors, ^{137}Cs gamma-ray source and mechanical gantry system. On-going testing and design improvement is being carried out.

A third generation X ray CT system is currently being configured in our laboratory [Abdullah and Sipaun, 2004]. With the availability of commercial array detectors and high precision manipulators, the selection of suitable hardware components was made, to build a CT system for non-destructive evaluation of industrial and archaeological objects. The industrial X ray CT system consists of these main components: 160kV/10mA constant potential X ray generating system with specified focal spots of 1.5 and 0.4 (IEC336), linear array detector and linear, elevator and rotary stage with controller. High energy X ray CT to study various processes in industrial columns using 450kV X ray source is being planned. The initial development of this system received strong support from the University of Liege, Belgium [Toye at al., 2005a, Toye at al., 2005b, Aferka et al., 2005, Abdullah et al., 2006].

Construction of a low temperature and low-pressure multi-phase flow rig (gas-water-oil system) was completed in December 2005 [Mustapha and Abdullah, 2006]. The basic design of the system is based on a similar system that has been developed at Christian Michelsen Research AS (CMR), Bergen, Norway. The test facility shall provide the necessary environment and access for industrial radioisotope R&D activities as well as to facilitate in the development of process tomography systems in the country. In particular, the flow rig will be used as a test station for the development of process tomography for multiphase flow system. This facility is open for use by researcher from national and international organizations. With the Malaysian government commitment, through research funding and human capital building, and the continuous support from the IAEA, research and development of industrial process tomography systems are to be continued. The availability and access to resulting systems shall open up opportunities for this technique to be applied in the industrial sector such as, in oil refineries and petrochemical installations.

MEXICO

The gamma CT was applied to investigate the geometrical cross section distribution of the catalyst in a reactor of the FCC Plant, denominated “Riser”. The Riser’s geometry is very particular since is a vertical tube that has three different diameters, that are increased as the high raise, see figure 134.

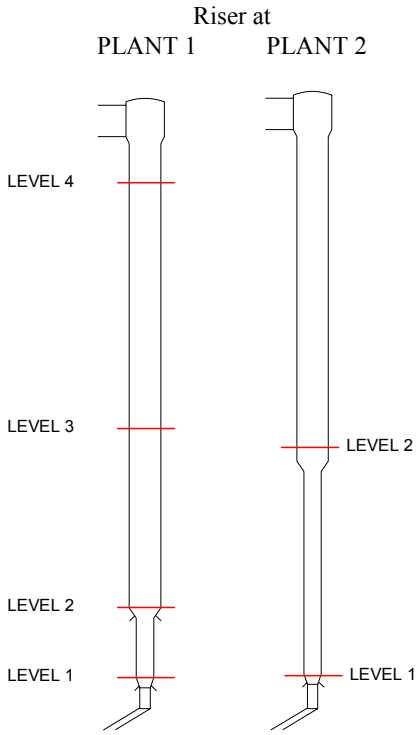

FIG. 134. Diagrams of the two risers showing the levels at which the tomographs were made.

The internal diameters of the Riser are for Plant 1: 813 mm, 1016 mm and 1219 mm, and for Plant 2: 813 mm, 1270 mm and 1600 mm. The total high of each riser are 33922 mm and 34823 mm, respectively. The properties of the catalyst were: density between 0.79 and 0.99 g/cm^3 with avoid fraction of 0.42. The charge had a density between 19.5 and 24.9ºAPI. Some of the operational conditions were:

The gamma CT technique employed was based on a procedure developed at the Mexican Petroleum Institute (IMP, “Instituto Mexicano del Petróleo”). This procedure has a fan-beam scanning geometry that includes one ^{137}Cs source with activity of 2.22 GBq and five or seventh INa(Tl) of 51x51 mm, with 50 mm thick lead collimators (Fig. 135). The procedure for moving for the detectors and source is the source is move to next position and the nearest detector to the source is moved to the farther position. The reconstruction algorithm uses a polynomial of maximum 6th order power. But from experience was found that the maximum order needed is 5.

The measurements were done under the assumption that the flow is under steady state regime, which means that the interest is in the temporal average of the flow.

The work parameters for Plant 1 and Plant 2 were:

- Fresh Charge (1000m^3/1000BPD): 5.07/31.9 and 6.53/41.1
- Catalyst circulation Mg/min: 22.9 and 27.8
- Relation Cat/Oil kg/kg: 7.2 and 6.8.

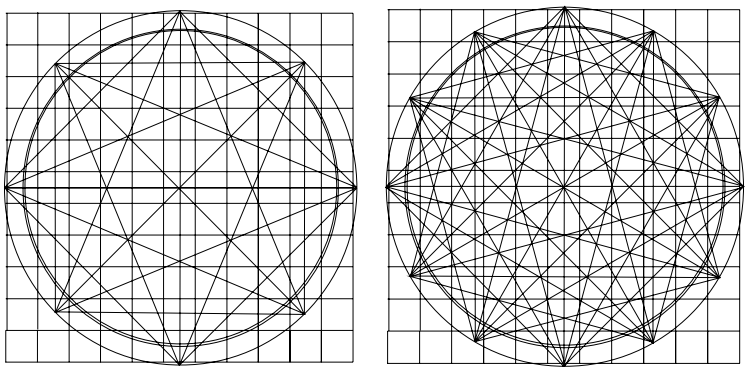

FIG. 135. Diagrams of the geometrical fan-beam for five detectors (l.) and seven detectors (r.).

Some of the tomographs obtained are shown in figures 136&137, which were made at the Riser Plant 1 and 2, respectively. The tomographic image corresponds to the levels at the RISER shown in figure 134.

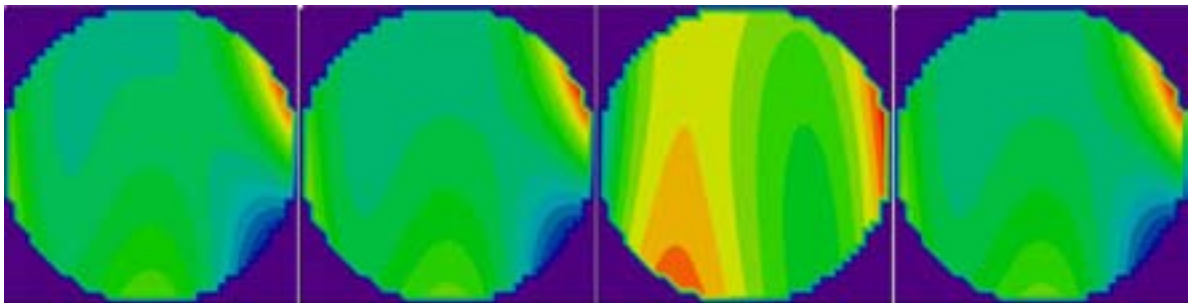

FIG. 136. Tomographs obtained at level 1, 2, 3 and 4 at the riser Plant 1.

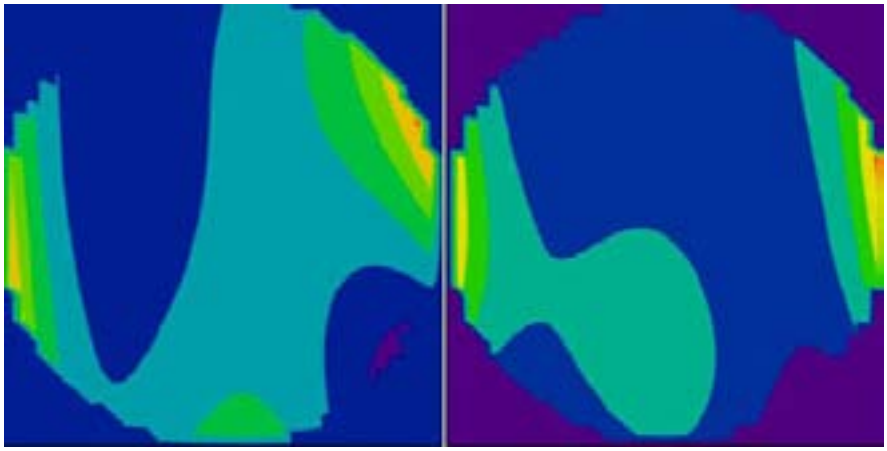

FIG. 137. Tomographs obtained at level 1 and 2 at the riser Plant 2.

NORWAY

The first gamma-ray tomography systems in Norway were developed in the late 1980s at the University of Bergen (UoB). These were mechanical scanning systems with one source and one detector, and they were developed for imaging of oil and water flows in porous rocks and for multiphase (gas, oil and water) pipe flows, respectively. Due to the high flow rates in the latter case, the development of the UoB high speed gamma-ray tomography with five ^{241}Am sources and 85 CZT detectors, was started in 1992 and finished three years later. This was a dual modality tomograph with an integrated 8-electrode capacitance tomograph [1]. In this period industrial process tomography received an increased attention in Europe through the European Concerted Action on Process Tomography in which the Bergen group was actively involved. UoB also developed in the detector system of a mechanical scanning gamma-ray tomograph using one ^{137}Cs source and 40 BGO scintillation detectors with photodiode read-out. Its application is imaging of flow in porous rocks [2]. The final large tomography development by UoB was a flexible gamma-ray tomograph; a one source, one detector, computer controllable system with one swing table and one rotational table [3]. This is used for experimental evaluation of any multiple source and detector fan-beam geometry.

The software for the high speed tomography was initially developed in C++ under DOS. This was first ported to LabWindows, and finally to LabVIEW under Windows NT and Windows XP. So was the software for the flexible gamma-ray tomograph. All this software is based on LabVIEW VIs and is thus modular so that new algorithms easily can be interchanged. The high speed tomograph was designed with a parallel data acquisition bus using a proprietary expansion PC-card. This system is now being replaced with a new USB2 solution which is faster a far more versatile. The capacitance tomograph in the dual modality system, which cannot be used with water continuous flows, has also been replaced with a high magnetic field probe which measures the water content in the pipe cross section and compensates for this under the reconstruction [4]. The most recent work of the UiB group has been experimental evaluation of reconstruction algorithms by using phantoms and calculating the pixel error in the reconstructed images.

The oil company Hydro has developed a dual energy gamma-ray tomograph (^{133}Ba; ~31 keV and 81 keV) for imaging of the gas, oil and water distribution of pipe flows. This is a one source and one detector mechanical system where the feasibility of dual energy imaging is, to our knowledge, demonstrated for the first time [5].

REFERENCES FOR NORWAY

[1] JOHANSEN G A, FRØYSTEIN T, HJERTAKER B T AND OLSEN Ø *A dual sensor flow imaging tomographic system*. Meas. Sci. Techn. **7**, No. 3 (1996) 297-307.

[2] JOHANSEN G A, FRØYSTEIN T AND URSIN J R: *A gamma detector system for tomographic imaging of porous media*. Proc. ECAPT '93 (European Concerted Action on Process Tomography), ISBN: 0952316501, Karlsruhe, Germany, March 24-27 (1993) 177-180.

[3] JOHANSEN, G A, FRØYSTEIN T, PEDERSEN H AND MCKIBBEN B. *A Flexible Test Platform for Investigating Gamma ray Tomography Geometries and Applications* Proc. Frontiers in Industrial Process Tomography II, Delft 8-12 April (1997) 365-369.

[4] HJERTAKER B T, TJUGUM S-A, HAMMER E A AND JOHANSEN G A. *Multi modality tomography for multiphase hydrocarbon flow* IEEE Sensors Journal, **5** No 2 (2005) 153-160.

[5] FRØYSTEIN T, KVANDAL H AND AAKRE H. *Dual energy gamma tomography system for high pressure multiphase flow* Flow Meas. Instr. **16** (2005) 99–112.

POLAND

Computer Engineering Department (CED), Lodz, Poland contribution to the project was focused on the following items:

- phantom tests
- software development for ECT tomography,
- software for gamma tomography
- software for dual modality (electrical capacitance and gamma tomography)

1. Software development for ECT tomography

The tomography team of the Computer Engineering Department has developed its own software for image reconstruction of ECT. It is developed using C++ programming language and works under Microsoft Windows operating system. The software uses the multithreaded character of the system which allows the full control of the reconstruction process by the user. Additionally the separation of the calculation and visualization modules allows maximizing computing power. Image visualization is powered with the modern 3D graphics hardware and OpenGL library. The following software modules can be distinguished:

- ECT sensor modeling with FEM mesh generator,
- FEM solver for ECT measurement simulation,
- sensitivity matrix calculation,
- image reconstruction.

Modularity of developed software allows modifying the individual parameters of the whole reconstruction process as:

- Mesh density, electrodes number, phantom of permittivity distribution as boundary conditions for the simulations, measuring capacitances, adding the Gauss' noise and its variance value to the simulated data; the whole mesh can be exported: nodes coordinates, triangular connections of the nodes, material value in each triangle)
- Voltage on a sender and receiver electrodes, maximum and minimum of the permittivity values; the potential values at the nodes of the mesh as well as the vector of the calculated capacitances for the given ECT sensor model can be exported,
- Exporting the sensitivity matrix to file,
- Reconstruction algorithm, relaxation parameter; exporting the reconstructed image as a bitmap file and as a text in "m"- file format for Matlab.

The following reconstruction algorithms were implemented in the software:

- Iterative Back Projection (IBP) with forward problem calculated using FEM simulation
- Landweber Iterations where instead of FEM simulation the linearized calculation was performed
- Newton – Raphson as an Iterative Tikhonov Regularization technique with FEM forward problem.

2. Software for gamma-ray tomography

Computer Engineering Department developed its own software for image reconstruction process based on the ILST (Iterative Least Square Techniques) algorithm. This software was developed to reconstruct image from measurement data from limited number of gamma beams, what can be applied to the measurements performed in The Technical University in Prague. The software generates automatically a weight matrix based on the measurement setup.

The weight matrix characterizes the contribution of each pixel located along each gamma-ray path. The example of results of the reconstruction is shown in Figure 138.

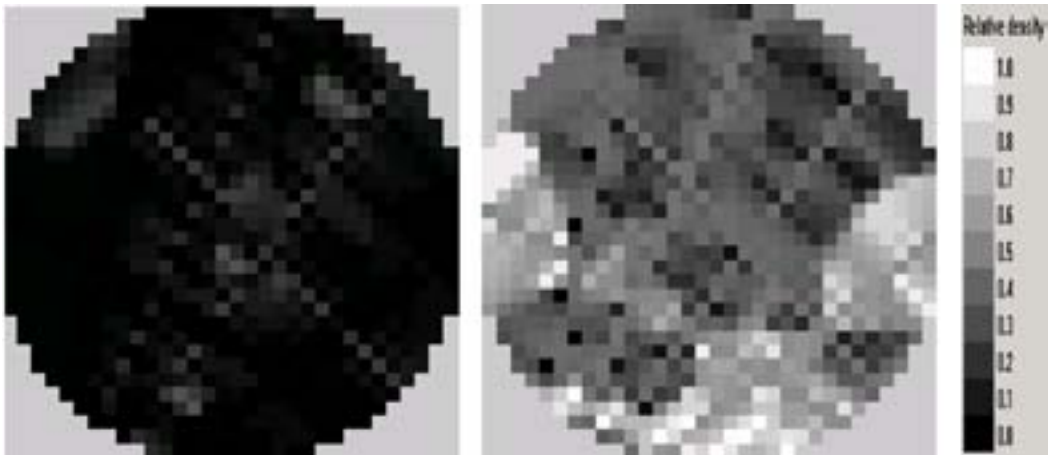

FIG. 138. Reconstructed image of glass particles in water.

3. Software for dual modality tomography (electrical capacitance and gamma)

For image reconstruction, which can be applied to dual modality tomography, new algorithm was developed, which uses a priori knowledge provided by gamma-ray and capacitance tomography and it should be emphasized that the DMR (Dual Mode Reconstruction) algorithm is a mixture of deterministic and stochastic approaches.

On the basis of the ILST (Iterative Least Square Technique) pixel values, the set is calculated, which consists of the pixel values which meet three criterions. The average of pixels values must be more or less equal to ILST pixel the improved pixel values obtained by means of the DMR algorithm should not significantly differ from the value of the equivalent pixel obtained using the IBP algorithm (IBP criterion), the calculated pixel values should not significantly differ from the neighboring pixels, obtained using the k-NN rule (neighborhood criterion). The DMR algorithm was also applied to imaging a gas/solid flow in a vertical channel. The images obtained by means of the DMR algorithm are characterized by a greater sharpness than those obtained from the IBP (Iterative Back Projection) algorithm. In addition, the effect of blurring that occurs in IBP images has significantly been reduced.

UNITED STATES OF AMERICA

1. Research

At the Chemical Reaction Engineering Laboratory (CREL) at Washington University in 2005-2006 we continued the development and extended use of computer assisted radioactive particle tracking (CARPT) and gamma ray computer tomography (CT) in various studies for sponsors (companies and government agencies), such as:

- Evaluation of performance of different liquid distributor configurations in trickle bed reactor using gamma ray CT (proprietary results)
- Performing reduced tomography experiments to minimize quantity of transmission data and by extension the scan time for the use of CT for diagnostic applications in the field.
- Porosity distribution studies using CT in 6 in. trickle bed reactor packed with 3mm catalyst particles.
- Evaluation of solids holdup in solid-liquid stirred tank reactor with CT.
- Solids velocity measurements in solid-liquid stirred tank rectors.

- Experiments to determine the solids holdup in gas-liquid-solid bubble columns with a dual modal technique that involves the use of CT (CREL) and electrical resistance tomography (ECT)-Ohio State University.
- Work on use of CT for flow regime demarcation in bubble columns. A flow regime indicator was developed and tested for effect of operating pressure on regime transition in bubble columns.

2. Key related new publications

"Hydrodynamics of slurry bubble column during dimethyl ether (DME) synthesis: Gas-liquid recirculation model and radioactive tracer studies", Chen, P., Gupta, P., Dudukovic, M. P., Toseland, B. A., Chemical Engineering Science, 61(19), 6553-6570 (2006).

"Gas Holdup in Trayed Bubble Column Reactors", Alvare, Javier, Al-Dahhan, Muthanna H., Industrial & Engineering Chemistry Research, 45(9), 3320-3326 (2006).

"Phase distribution in an upflow monolith reactor using computed tomography", Al-Dahhan, M. H., Kemoun, A., Cartolano, A. R., AIChE Journal , 52(2), 745-753 (2006).

"Solids flow mapping in a gas-solid riser: Mean holdup and velocity fields", Bhusarapu, Satish, Al-Dahhan, Muthanna H., Dudukovic, Milorad P., Powder Technology, 163(1-2), 98-123 (2006).

3. Development of training material

A detailed operational manual for gamma ray CT has been developed. The manual is presented in the Annex 1.

4. Cooperation efforts

CREL is currently housing the graduate student Maria Sol Fraguio from Cassanello's group in Argentina.

CREL has invited Pablo Vasquez-Salvador from Hamada's group in Brazil to specialize here in gamma ray tomography reconstruction in 2007.

LIST OF PARTICIPANTS

Abdullah J.
Malaysian Institute for Nuclear Technology Research (MINT)
Industrial Technology Division
Plant Assessment Technology Group
4300 Bangi, Selangor, MALAYSIA
E-mail: abdullah@mint.gov.my
Tel.+603 892 50510; Fax. +603 892 50907

Cassanello M.C.F.
Dep. Industrias, Universidad de Buenos Aires
Facultad de Ciencias Exactas y Naturales
Departamento de Industrias
Ciudad Universitaria – Pab. Industrias
C1428BGA – Buenos Aires, ARGENTINA
E-mail: miryan@di.fcen.uba.ar
Tel. +54 11 457 63383; Fax.+54 11 457 63366

Dudukovic M.P.
Chemical Reaction Engineering Laboratory (CREL)
Washington University
Box 1198, One Brookings Drive
St. Louis, Missouri 63130-4899, USA
E-mail: DUDU@CHE.WUSTL.EDU
Tel. +1 314 935 6021; Fax. 314 935 4832

Dyakowski T.
Department of Chemical Engineering
University of Manchester Institute of Science and Technology
PO Box 88 Sackville Street ,
M60 1DP, Manchester, UNITED KINGDOM

Hamada M.M.
Comissão Nacional de Energia Nuclear
Instituto de Pesquisas Energeticas e Nucleares (IPEN)
Centro de Technologia das Radiaçoes
São Paulo, BRAZIL
E-mail: mmhamada@ipen.br
Fax. +55 11 381 69186

Jin, J.H
(Project Officer/Scientific Secretary)
Industrial Applications & Chemistry Section
NAPC Division
International Atomic Energy Agency
Wagramer Strasse 5, P.O. Box 100,
A-1400 Vienna, AUSTRIA
E-mail: J-H.Jin@iaea.org
Tel. +43 1 2600 21745, Fax. +43-1- 26007

Johansen G.A.
Department of Physics and Technology
University of Bergen
Allegaten 55, N-5007 Bergen, NORWAY
E-mail:GEIR.JOHANSEN@IFT.UIB.NO
Tel. +47 5558 2745; Fax. +47 5558 9440

Kim J.B.
Korea Atomic Energy Research Institute (KAERI)
P.O. Box 7, Daeduk-Danji
Taejon 305-606, KOREA, REPUBLIC OF
E-mail:JONG@KAERI.RE.KR
Tel.+82 42 8688050; Fax. +82 42 8626980

Legoupil S.A.	Commissariat à l'Energie Atomique CEA-LIST , DETECS/SSTM/LID BP No. 52 91191 Gif-sur-Yvette, FRANCE E-mail: samuel.legoupil@cea.fr Tel. +33 1 690 84313; Fax +33 1 690 86030
Maad, R.	Sogn og Fjordane University College Engineering Department P.O.Box 523 N-6801 Førde , NORWAY E-Mail: RACHID.MAAD@HISF.NO
Mesquita, C.H	Comissão Nacional de Energia Nuclear, Instituto de Pesquisas Energeticas e Nucleares (IPEN) Centro de Technologia das Radiaçoes, São Paulo, BRAZIL E-mail:chmesqui@usp.br. Fax No.+55 11 381 69186
Nowakowski J.	Technical University of Lodz Computer Engineering Department 90-924 Lodz, POLAND
Ramirez-Garcia, F.P.	Universidad Nacional Autonoma de Mexico, Facultad de Ciencias Ciudad Universitaria, Delg. Coyoacan, Mexico, D.F. MEXICO EMail FCOPABLORAMIREZ@TONATIU.NET Tel/Fax. No.+52 55 5534 5036
Sankowski D.	Technical University of Lodz Computer Engineering Department 90-924 Lodz, POLAND E-mail:dsan@kis.p.lodz.pl Tel.+4842631 2750; Fax. +48426312755
Sipaun, S.M.	Malaysian Institute for Nuclear Technology Research (MINT) Industrial Technology Division Plant Assessment Technology Group 4300 Bangi, Selangor, MALAYSIA E-mail: susan@mint.gov.my Tel. +603 892 50510; Fax. +603 892 50907
Thyn J.	Czech Technical University of Prague Faculty of Mechanical Engineering Department of Process Engineering, FSI 16000 Prague 6, CZECH REPUBLIC E-mail: THYN@FSID.CVUT.CZ Tel. +420 2 2435 2559; Fax. +420 2 2431 0292

No. 21, July 2006

IAEA
International Atomic Energy Agency

Where to order IAEA publications

In the following countries IAEA publications may be purchased from the sources listed below, or from major local booksellers. Payment may be made in local currency or with UNESCO coupons.

Australia
DA Information Services, 648 Whitehorse Road, Mitcham Victoria 3132
Telephone: +61 3 9210 7777 • Fax: +61 3 9210 7788
Email: service@dadirect.com.au • Web site: http://www.dadirect.com.au

Belgium
Jean de Lannoy, avenue du Roi 202, B-1190 Brussels
Telephone: +32 2 538 43 08 • Fax: +32 2 538 08 41
Email: jean.de.lannoy@infoboard.be • Web site: http://www.jean-de-lannoy.be

Canada
Bernan Associates, 4611-F Assembly Drive, Lanham, MD 20706-4391, USA
Telephone: 1-800-865-3457 • Fax: 1-800-865-3450
Email: order@bernan.com • Web site: http://www.bernan.com

Renouf Publishing Company Ltd., 1-5369 Canotek Rd., Ottawa, Ontario, K1J 9J3
Telephone: +613 745 2665 • Fax: +613 745 7660
Email: order.dept@renoufbooks.com • Web site: http://www.renoufbooks.com

China
IAEA Publications in Chinese: China Nuclear Energy Industry Corporation, Translation Section, P.O. Box 2103, Beijing

Czech Republic
Suweco CZ, S.R.O. Klecakova 347, 180 21 Praha 9
Telephone: +420 26603 5364 • Fax: +420 28482 1646
Email: nakup@suweco.cz • Web site: http://www.suweco.cz

Finland
Akateeminen Kirjakauppa, PL 128 (Keskuskatu 1), FIN-00101 Helsinki
Telephone: +358 9 121 41 • Fax: +358 9 121 4450
Email: akatilaus@akateeminen.com • Web site: http://www.akateeminen.com

France
Form-Edit, 5, rue Janssen, P.O. Box 25, F-75921 Paris Cedex 19
Telephone: +33 1 42 01 49 49 • Fax: +33 1 42 01 90 90 • Email: formedit@formedit.fr

Lavoisier SAS, 145 rue de Provigny, 94236 Cachan Cedex
Telephone: + 33 1 47 40 67 02 • Fax +33 1 47 40 67 02
Email: romuald.verrier@lavoisier.fr • Web site: http://www.lavoisier.fr

Germany
UNO-Verlag, Vertriebs- und Verlags GmbH, August-Bebel-Allee 6, D-53175 Bonn
Telephone: +49 02 28 949 02-0 • Fax: +49 02 28 949 02-22
Email: info@uno-verlag.de • Web site: http://www.uno-verlag.de

Hungary
Librotrade Ltd., Book Import, P.O. Box 126, H-1656 Budapest
Telephone: +36 1 257 7777 • Fax: +36 1 257 7472 • Email: books@librotrade.hu

India
Allied Publishers Group, 1st Floor, Dubash House, 15, J. N. Heredia Marg, Ballard Estate, Mumbai 400 001,
Telephone: +91 22 22617926/27 • Fax: +91 22 22617928
Email: alliedpl@vsnl.com • Web site: http://www.alliedpublishers.com

Bookwell, 2/72, Nirankari Colony, Delhi 110009
Telephone: +91 11 23268786, +91 11 23257264 • Fax: +91 11 23281315
Email: bookwell@vsnl.net

Italy
Libreria Scientifica Dott. Lucio di Biasio “AEIOU”, Via Coronelli 6, I-20146 Milan
Telephone: +39 02 48 95 45 52 or 48 95 45 62 • Fax: +39 02 48 95 45 48

Japan
Maruzen Company, Ltd., 13-6 Nihonbashi, 3 chome, Chuo-ku, Tokyo 103-0027
Telephone: +81 3 3275 8582 • Fax: +81 3 3275 9072
Email: journal@maruzen.co.jp • Web site: http://www.maruzen.co.jp

Korea, Republic of
KINS Inc., Information Business Dept. Samho Bldg. 2nd Floor, 275-1 Yang Jae-dong SeoCho-G, Seoul 137-130
Telephone: +02 589 1740 • Fax: +02 589 1746
Email: sj8142@kins.co.kr • Web site: http://www.kins.co.kr

Netherlands
De Lindeboom Internationale Publicaties B.V., M.A. de Ruyterstraat 20A, NL-7482 BZ Haaksbergen
Telephone: +31 (0) 53 5740004 • Fax: +31 (0) 53 5729296
Email: books@delindeboom.com • Web site: http://www.delindeboom.com

Martinus Nijhoff International, Koraalrood 50, P.O. Box 1853, 2700 CZ Zoetermeer
Telephone: +31 793 684 400 • Fax: +31 793 615 698 • Email: info@nijhoff.nl • Web site: http://www.nijhoff.nl

Swets and Zeitlinger b.v., P.O. Box 830, 2160 SZ Lisse
Telephone: +31 252 435 111 • Fax: +31 252 415 888 • Email: infoho@swets.nl • Web site: http://www.swets.nl

New Zealand
DA Information Services, 648 Whitehorse Road, MITCHAM 3132, Australia
Telephone: +61 3 9210 7777 • Fax: +61 3 9210 7788
Email: service@dadirect.com.au • Web site: http://www.dadirect.com.au

Slovenia
Cankarjeva Zalozba d.d., Kopitarjeva 2, SI-1512 Ljubljana
Telephone: +386 1 432 31 44 • Fax: +386 1 230 14 35
Email: import.books@cankarjeva-z.si • Web site: http://www.cankarjeva-z.si/uvoz

Spain
Díaz de Santos, S.A., c/ Juan Bravo, 3A, E-28006 Madrid
Telephone: +34 91 781 94 80 • Fax: +34 91 575 55 63 • Email: compras@diazdesantos.es
carmela@diazdesantos.es • barcelona@diazdesantos.es • julio@diazdesantos.es
Web site: http://www.diazdesantos.es

United Kingdom
The Stationery Office Ltd, International Sales Agency, PO Box 29, Norwich, NR3 1 GN
Telephone (orders): +44 870 600 5552 • (enquiries): +44 207 873 8372 • Fax: +44 207 873 8203
Email (orders): book.orders@tso.co.uk • (enquiries): book.enquiries@tso.co.uk • Web site: http://www.tso.co.uk

On-line orders:
DELTA Int. Book Wholesalers Ltd., 39 Alexandra Road, Addlestone, Surrey, KT15 2PQ
Email: info@profbooks.com • Web site: http://www.profbooks.com

Books on the Environment:
Earthprint Ltd., P.O. Box 119, Stevenage SG1 4TP
Telephone: +44 1438748111 • Fax: +44 1438748844
Email: orders@earthprint.com • Web site: http://www.earthprint.com

United Nations (UN)
Dept. I004, Room DC2-0853, First Avenue at 46th Street, New York, N.Y. 10017, USA
Telephone: +800 253-9646 or +212 963-8302 • Fax: +212 963-3489
Email: publications@un.org • Web site: http://www.un.org

United States of America
Bernan Associates, 4611-F Assembly Drive, Lanham, MD 20706-4391
Telephone: 1-800-865-3457 • Fax: 1-800-865-3450
Email: order@bernan.com • Web site: http://www.bernan.com

Renouf Publishing Company Ltd., 812 Proctor Ave., Ogdensburg, NY, 13669
Telephone: +888 551 7470 (toll-free) • Fax: +888 568 8546 (toll-free)
Email: order.dept@renoufbooks.com • Web site: http://www.renoufbooks.com

Orders and requests for information may also be addressed directly to:

Sales and Promotion Unit, International Atomic Energy Agency
Wagramer Strasse 5, P.O. Box 100, A-1400 Vienna, Austria
Telephone: +43 1 2600 22529 (or 22530) • Fax: +43 1 2600 29302
Email: sales.publications@iaea.org • Web site: http://www.iaea.org/books

08-16791